universität wien

DISSERTATION

Titel der Dissertation

Density Functional Theory applied to liquid metals and the Adjacent Pairs Exchange correction to the Random Phase Approximation

verfasst von

Dipl.-Ing. Felix Alfred Hummel

angestrebter akademischer Grad

Doktor der Naturwissenschaften (Dr. rer. nat.)

Wien, Oktober 2015

Studienkennzahl lt. Studienblatt:	A 796 605 411
Dissertationsgebiet lt. Studienblatt:	Physik
Betreut von:	Univ.-Prof. Dipl-Ing. Dr. Georg Kresse

to my father, who sparked my interest for science and engineering

Abstract

In the first part, the so-called simple liquids conjecture is tested. Simple liquids posses distinct state points in the thermodynamic phase diagram that can be transformed into each other by the choice of units, also referred to as scaling invariance. This allows, for instance, an accurate extrapolation of the melting line to high pressures from a calculation at ambient pressure. Melting rules, such as the Lindemann melting criterion also follow from the scaling invariance.

It has been conjectured that the metal melts are simple to a large degree while melts of non-metallic elements are not, based on classical molecular dynamics calculations using various models. Experimentally, simplicity is hard to test due to the large pressure range required. To test the conjecture using a quantum mechanical description of the atomic interactions, Density Functional Theory (DFT) calculation have been conducted within this work, confirming the conjecture at this level of theory.

The second part proposes a correction to the systematic error of the Random Phase Approximation (RPA), a widely employed post Hartree-Fock/DFT method, capable of capturing, for instance, van der Waals interactions at relatively low costs. However, since it neglects antisymmetrization, RPA overestimates correlation energies and bond lengths in general.

The proposed method exchanges adjacent particle/hole pairs in the RPA diagrams – hence its name – offering similar accuracy than the Second Order Screened Exchange (SOSEX) correction but at lower memory requirements of only $\mathcal{O}(N^2)$. The correction is calculated from imaginary time propagators in $\mathcal{O}(N^5)$ steps. If the propagators can be stored in memory it can also be calculated in $\mathcal{O}(N^4)$ steps. It improves on SOSEX in the uniform electron gas for low densities, where correlation effects are stronger, and first calculations of lattice constants in solids are in excellent agreement with experiment.

Zusammenfassung

Im ersten Teil wird die sogenannte „Einfache–Flüssigkeits–Vermutung“ getestet. In einfachen Flüssigkeiten gibt es thermodynamische Zustände, die sich nur in der Wahl der Einheiten unterscheiden. Dies wird auch als Skalierungsinvarianz bezeichnet. In einfachen Flüssigkeiten kann, unter Anderem, die Schmelzkurve bis zu hohen Drücken extrapoliert werden, ausgehend von einer Rechnung bei Umgebungsdruck. Auch Schmelzkriterien, wie das Lindemann Kriterium, finden eine Erklärung in der Skalierungsinvarianz.

Bisher ließen Molekulardynamik-Rechungen mit verschiedenen klassischen Modellen vermuten, dass die Schmelzen von Metallen in hohem Maße einfache Flüssigkeiten sind, während die Schmelzen von Nichtmetallen diese Eigenschaft nicht aufweisen. Experimentall ist diese Vermutung schwer zu testen aufgrund des großen Bereichs an notwendigen Drücken. In dieser Arbeit wurden Dichtefunktionaltheorie (DFT) Rechnungen durchgeführt, die die Vermutung ohne Annahme von klassischen Modellen bestätigen, zumindest im Rahmen der DFT.

Der zweite Teil schlägt eine Korrektur zur Random Phase Approximation (RPA) vor, einer verbreiteten post Hartree-Fock/DFT Methode, die etwa van der Waals Kräfte erfasst und mit verhältnismäßig niedrigem Aufwand berechnet werden kann. Allerdings vernachlässigt RPA die anti-Symmetrie der Wellenfunktion und überschätz dadurch im Allgemeinen Korrelationsenergien und Bindungslängen.

Die vorgeschlagene Methode tauscht benachbarte Teilchen/Loch Paare in den RPA Diagrammen aus – daher der Name Adjacent Pairs Exchange (APX) – und bietet vergleichbare Genauigkeit zur bestehenden Second Order Screened Exchange (SOSEX) Korrektur bei niedrigerem Speicherbedarf von nur $\mathcal{O}(N^2)$. APX wird mit Propagatoren in imaginärer Zeit in $\mathcal{O}(N^5)$ Schritten berechnet. Wenn die Propagatoren gespeichert werden können, ist die Berechnung in $\mathcal{O}(N^4)$ Schritten möglich. Sie verbessert die Korrelationsenergie im Vergleich zu SOSEX im homogenen Elektronengas bei niedigen Dichtigen, wo die Korrelation stärker ist. Erste Berechnungen von Gitterkonstanten zeigen ausgezeichnete Übereinstimmung zum Experiment.

Contents

1 Introduction **1**
1.1 Organization of this work . . . 2

2 Electronic structure calculation **3**
2.1 Notation and units . . . 3
2.2 The Schrödinger equation in condensed matter . . . 3
2.3 The Hartree-Fock approximation . . . 5
2.4 Density Functional Theory . . . 6
2.5 Hartree Fock and DFT in periodic systems . . . 7

I DFT applied to liquid metals **9**

3 Melting point calculations with Interface Pinning **11**
3.1 *Ab-initio* at finite temperature . . . 11
3.2 Free energy . . . 12
3.3 The Interface Pinning method . . . 14
3.4 Melting point of Na, Mg, Al and Si . . . 19
3.5 Interface mobility . . . 22
3.6 Summary and discussion . . . 26

4 Isomorphs in metal melts **29**
4.1 Isomorphs . . . 31
4.2 The Inverse Power Law ansatz . . . 34
4.3 Isomorph properties of 58 elements . . . 36
4.4 Summary and discussion . . . 38

II The Adjacent Pairs Exchange correction to the RPA **41**

5 Many-Body Perturbation Theory **43**
5.1 Time dependent perturbation theory . . . 44
5.2 The Gell-Mann–Low theorem . . . 47
5.3 Wick's theorem . . . 48
5.4 Goldstone diagrams . . . 51
5.5 The Linked-Cluster theorem . . . 57
5.6 Hartree-Fock reference . . . 58

5.7 Propagators . . . 59
5.8 Feynman diagrams . . . 61

6 The Random Phase Approximation 65
6.1 RPA in the frequency domain . . . 66
6.2 Direct Ring Coupled Cluster Doubles . . . 69
6.3 RPA from the Adiabatic Connection . . . 72
6.4 RPA for the uniform electron gas . . . 77

7 Second Order Screened Exchange 87
7.1 SOSEX from Direct Ring Coupled Cluster Doubles . . . 88
7.2 Adiabatic Connection-SOSEX . . . 90
7.3 Difference between drCCD SOSEX and AC-SOSEX . . . 92

8 Adjacent Pairs Exchange 99
8.1 Drivation of the Adjacent Pairs Exchange correction . . . 99
8.2 APX for the uniform electron gas . . . 104
8.3 APX for solids . . . 111
8.4 Summary and discussion . . . 116

III Appendices 121

A Periodic Table of Simple Liquids 123

B Total energies in G_0W_0 from connected diagrams 125

Acknowledgements 137

List of publications and Curriculum Vitae 139

Chapter 1

Introduction

Most materials properties are governed by the behavior of its electrons. The Schrödinger equation describes this behavior sufficiently well (when including relativistic corrections) but unfortunately it cannot be solved exactly for more than a few electrons, not even numerically. Computational physics tries to find suitable simplifications of the Schrödinger equation that can be applied to a considerable number of electrons – typically a few 100 – and tests them either against experiment or against other methods. These methods can then be applied to find answers to physical questions that are hard to access by other means, such as the melting behavior of iron under earth core pressures. Since no experimental input is required for such calculations apart from physical constants they are referred to as first principles or *ab-initio* calculations. Clearly, developing and applying *ab-initio* methods does not take place independently.

Various approximations have been developed for the Schrödinger equation especially for numerical evaluation on the computer. Density Functional Theory (DFT) is among the most widely used ones. Instead of finding one many particle wave function $\Psi(\mathbf{x}_1, \ldots, \mathbf{x}_N)$ depending on all N electron positions, it finds N one-electron wave functions $\psi_i(\mathbf{x})$ depending only on the position of one electron and the density $n(\mathbf{x})$ of all electrons. The former requires $\mathcal{O}(e^N)$ calculations while the latter can be performed in $\mathcal{O}(N^3)$ steps. The ground state energy is a functional solely of the electron density $n(\mathbf{x})$, so this approximation – crude as it might seem – is well-founded and could be exact in theory. Unfortunately, only the existence of such a functional is predicted, lacking an algorithm to construct it on the computer. Still, the effort of more than four decades turned DFT into a well researched and fast method with a laudable accuracy sufficient for many applications.

There are also various methods for reaching higher accuracy which are based on DFT's one-electron wave functions $\psi_i(\mathbf{x})$, collectively called post-DFT methods. The Random Phase Approximation (RPA) is one of its most applied representative. It captures, for instance, dispersion interactions and works well in a large set of chemical environments at relatively moderate computational costs. Recent developments allow the RPA to be calculated in $\mathcal{O}(N^3)$ steps, just as DFT but with a considerably higher prefactor compared to DFT (Kaltak, Klimeš, and Kresse 2014b).

1.1 Organization of this work

The first part of this thesis applies DFT to monatomic liquids. In Chapter 3 a recently developed method for finding the melting point is tested for four elements, where the melting point has been previously calculated *ab-initio* by different methods. In Chapter 4 the so-called simple liquid conjecture of metal melts is verified for 58 elements using *ab-initio* calculations. The conjecture explains empirical melting rules such as the Lindemann melting criterion and it allows to accurately extrapolate the melting line to high pressures. Direct experimental verification of this conjecture would require experiments under very high pressure for a broad set of elements which is hard to conduct.

The second part is dedicated to developing an improvement of the RPA which partially cures its systematic errors. The method is closely related to the Second Order Screened Exchange (SOSEX) method but it is considerably easier to calculate regarding its memory usage of $\mathcal{O}(N^2)$ compared to $\mathcal{O}(N^4)$ of SOSEX. Chapter 5 contains an overview of standard many-body perturbation theory and its representation in terms of Goldstone and Feynman diagrams. Less standard but equally important symmetry considerations connecting the two types of diagrams are also discussed. In Chapter 6 it is shown that the Random Phase Approximation derived from many-body perturbation theory is formally equivalent to the standard derivation in the Adiabatic Connection framework. Chapter 7 discusses two of the existing corrections to the RPA, derived in different frameworks: the Second Order Screened Exchange (SOSEX) from many-body perturbation theory and the AC-SOSEX from the Adiabatic Connection. Finally, Chapter 8 introduces the proposed Adjacent Pairs Exchange (APX) correction, solely based on many-body perturbation theory and discusses its differences, advantages and disadvantages compared to SOSEX and AC-SOSEX.

Chapter 2 briefly introduces Hartree-Fock and Density Functional Theory as the foundation of both parts. Appendix A presents the simple liquid results for the studied elements in form of a periodic table. Appendix B proposes the application of the symmetry considerations discussed in the second part to the diagrams comprising the total energy in the G_0W_0 approximation, which would circumvent the Galitsky–Migdal formula.

Chapter 2

Electronic structure calculation

2.1 Notation and units

In the condensed phase, matter is organized in atoms bound by the interplay of their electrons. This work is mainly concerned with the consequences of this interplay, referred to as electronic structure. It is therefore natural to choose units where the Schrödinger equation for electrons appears as simple as possible. This is accomplished by atomic units where the numerical values of the electron mass m_e, the elementary charge e, Coulomb's constant $1/4\pi\epsilon_0$ and the reduced Planck's constant $\hbar$ are set to unity. This renders the electronic Schrödinger equation for the hydrogen atom in a particularly simple form:

$$\left(\frac{-\nabla^2}{2} - \frac{1}{r}\right)\Psi = E\Psi.$$

The dimensions of the respective quantities must still be kept in mind although they do not appear explicitly. All energies are given in *Hartrees* unless noted otherwise. The notation employed within this work is listed in Table 2.1.

2.2 The Schrödinger equation in condensed matter

A system of M atomic nuclei and N electrons can be described non-relativistically by a single wave function obeying the Schrödinger equation, assuming each nucleus can be treated as a single quantum object. The full wave function is a function of the coordinates of all M nuclei $\mathbf{X}_1, \ldots, \mathbf{X}_M$ and of the coordinates of all N electrons $\mathbf{x}_1, \ldots, \mathbf{x}_N$. The coordinates $\mathbf{x}_n = (\mathbf{r}_n, \alpha_n)$ and $\mathbf{X}_m = (\mathbf{R}_m, A_m)$ contain spatial and spin coordinates of the electrons and nuclei, respectively. Since the nuclei are considerably heavier than the electrons their respective dynamics takes place at quite different time scales. To a good approximation the full wave function can be separated into wave functions of only the atomic and only the electronic positions, which is referred to as the Born-Oppenheimer approximation. The positions of the nuclei $\mathbf{R}_1, \ldots, \mathbf{R}_M$ enter the Schrödinger equation of the electronic wave function $\Psi(\mathbf{x}_1, \ldots, \mathbf{x}_N)$ merely as parameters. In the adiabatic approximation they are further assumed to vary slowly enough to keep the electronic wave function in an eigenstate with a single instantaneous energy E. The electronic wave function satisfies the stationary Schrödinger equation

$$\hat{H}_{\mathbf{R}_1,\ldots,\mathbf{R}_M}\Psi(\mathbf{x}_1, \ldots, \mathbf{x}_N) = E\Psi(\mathbf{x}_1, \ldots, \mathbf{x}_N)$$

Quantity	Symbol
scalars	$a, b, \ldots$
3-vectors	$\mathbf{r}, \mathbf{r}', \ldots$
spin and position combined $(\alpha, \mathbf{r})$, where $\alpha \in \{\uparrow, \downarrow\}$	$\mathbf{x}, \mathbf{x}', \ldots$
matrices	$\mathbf{A}, \mathbf{B}, \ldots$
operators	$\hat{A}, \hat{B}, \ldots$
many-body wave function	Ψ
ground state Slater determinant	Φ
spin orbital	ψ_p
index of general spin states (excited or unexcited)	$p, q, r, \ldots$
index of unexcited states	$i, j, k, \ldots$
index of excited states	$a, b, c, \ldots$
electron creation and annihilation operator for spin state p	$\hat{c}_p^\dagger, \hat{c}_p$
hole creation and annihilation operator for spin state i	$\hat{\imath}^\dagger, \hat{\imath}$
particle creation and annihilation operator for spin state a	$\hat{a}^\dagger, \hat{a}$
creation and annihilation operator for a hole or a particle	$\hat{p}^\dagger, \hat{p}$
normal ordering operator	$N[\hat{A}\hat{B}\ldots]$
time ordering operator	$T[\hat{A}\hat{B}\ldots]$
imaginary unit $\sqrt{-1}$	i
Euler's constant	e
integral over entire domain, e.g. $\int_{-\infty}^{\infty} \mathrm{d}t$, $\int_{\mathbb{R}^3} \mathrm{d}^3\mathbf{r}$	$\int \mathrm{d}t$, $\int \mathrm{d}\mathbf{r}$

Table 2.1: Notation used herein

with the electronic Hamiltonian given by

$$\hat{H}_{\mathbf{R}_1,\ldots,\mathbf{R}_M} = \underbrace{\sum_{n=1}^{N} \frac{-\nabla_n^2}{2}}_{\hat{T}} \underbrace{- \sum_{n=1}^{N} \sum_{m=1}^{M} \frac{Z_m}{|\mathbf{R}_m - \mathbf{r}_n|}}_{\hat{V}_{\mathrm{ne}}} \underbrace{+ \frac{1}{2} \sum_{n \neq n'}^{N} \frac{1}{|\mathbf{r}_n - \mathbf{r}_{n'}|}}_{\hat{V}_{\mathrm{ee}}}, \tag{2.1}$$

where ∇_n denotes the Nabla operator with respect to the coordinate $\mathbf{r}_n$ and Z_m is the nuclear charge of the m-th atom in units of the positive elementary charge. The electronic Hamiltonian is composed of the kinetic energy operator $\hat{T}$, the operator for the nucleus-electron interaction $\hat{V}_{\mathrm{ne}}$ and the electron-electron interaction $\hat{V}_{\mathrm{ee}}$. The latter couples the coordinates of different electrons. The Hamiltonian is assumed to be independent of the spin coordinates and the explicitly denoted dependence of the Hamiltonian on the coordinates of the nuclei will be dropped from now on.

2.3 The Hartree-Fock approximation

Despite all previous approximations, the electronic Schrödinger equation is still a partial differential equation in the coordinates of all contained electrons, evading analytic solutions even for the helium atom with only two electrons. Finding a numerical solution is possible but scales like $\mathcal{O}(\mathrm{e}^N)$ in time and memory with respect to the number of electrons N. Systems of interest in the condensed phase comprise several dozens to several hundreds of electrons, rendering a direct numerical solution intractable.

We can, however, limit the *Hilbert space* of all possible wave functions $\Psi(\mathbf{x}_1, \ldots, \mathbf{x}_N)$ in N coordinates to the space of functions $\Phi(\mathbf{x}_1, \ldots, \mathbf{x}_N)$, which can be expressed by an anti-symmetrized product of N functions $\psi_i(\mathbf{x}_n)$ in one coordinate:

$$\Phi(\mathbf{x}_1, \ldots, \mathbf{x}_N) = \mathcal{A}\psi_1(\mathbf{x}_1) \ldots \psi_N(\mathbf{x}_N) = \frac{1}{\sqrt{N!}} \begin{vmatrix} \psi_1(\mathbf{x}_1) & \psi_2(\mathbf{x}_1) & \ldots & \psi_N(\mathbf{x}_1) \\ \psi_1(\mathbf{x}_2) & \psi_2(\mathbf{x}_2) & \ldots & \psi_N(\mathbf{x}_2) \\ \vdots & \vdots & \ddots & \vdots \\ \psi_1(\mathbf{x}_N) & \psi_2(\mathbf{x}_N) & \ldots & \psi_N(\mathbf{x}_N) \end{vmatrix}$$

where the operator $\mathcal{A}$ sums all permutations of the coordinates $\mathbf{x}_1, \ldots, \mathbf{x}_N$ with the respective sign. Even permutations enter with a positive sign, odd permutations with a negative sign. The normalization is chosen such that $\langle\Phi|\Phi\rangle = 1$ if the functions $\psi_i(\mathbf{x})$ are orthonormal. The product ansatz assumes that the electronic coordinates are uncorrelated, i.e. the choice of one electronic coordinate $\mathbf{x}_1$ does not affect the probability amplitude of the other coordinates. Written as a determinant, Φ is referred to as *Slater determinant*. The functions $\psi_i(\mathbf{x})$ in one combined spatial and spin coordinate $\mathbf{x}$ are referred to as *(spin) orbitals*. In the unrestricted Hartree-Fock approximation each spin orbital can only host an electron of suitable spin, depending only on the spin orbital index i. For the sake of simplicity only unrestricted Hartree-Fock is discussed here.

The true ground state solution Ψ of the stationary Schrödinger equation has the lowest eigenenergy E. The best approximation in the space of Slater determinants, Φ, minimizes

$$E_0 = \frac{\langle\Phi|\hat{H}|\Phi\rangle}{\langle\Phi|\Phi\rangle}. \tag{2.2}$$

The approximate ground state energy E_0 cannot be lower than the exact ground state energy E and the difference $E_c = E - E_0$ is called *correlation energy*. The minimization of (2.2) leads to the Hartree-Fock equation

$$\hat{F}\psi_i(\mathbf{x}) = \varepsilon_i \psi_i(\mathbf{x}) \tag{2.3}$$

where the *Fock operator* $\hat{F}$ is given by

$$\hat{F} = \hat{T} + \hat{V}_{\text{ne}} + \hat{V}_{\text{eff}}. \tag{2.4}$$

The Fock operator bears resemblance to the Hamiltonian operator. However, it operates on functions in one coordinate rather than in N coordinates and it contains an effective interaction $\hat{V}_{\text{eff}}$ in place of the electron-electron interaction $\hat{V}_{\text{ee}}$. The effective interaction of the Fock operator depends recursively on the N eigenfunctions $\psi_1(\mathbf{x}), \ldots, \psi_N(\mathbf{x})$ of the Fock operator from (2.3) with the lowest eigenenergies ε_j:

$$\hat{V}_{\text{eff}}\,\psi_i(\mathbf{x}) = \sum_{j=1}^{N} \int \mathrm{d}\mathbf{x}' \, \frac{\psi_j^*(\mathbf{x}')\psi_j(\mathbf{x}')}{|\mathbf{r} - \mathbf{r}'|}\,\psi_i(\mathbf{x}) - \sum_{j=1}^{N} \int \mathrm{d}\mathbf{x}' \, \frac{\psi_j^*(\mathbf{x}')\psi_i(\mathbf{x}')}{|\mathbf{r} - \mathbf{r}'|}\,\psi_j(\mathbf{x}). \tag{2.5}$$

The first term is called *Hartree term* and it is a local, potential, depending on the density of the N electrons $n_0(\mathbf{x}') = \sum_j \psi_j^*(\mathbf{x}')\psi_j(\mathbf{x}')$. The second term is called *Fock term* or *exchange term*. It cannot be written in terms of a local potential. Since the Fock operator depends on its own lowest N eigenfunctions, the solution can only be retrieved self-consistently by iteration. For the first iteration the orbitals $\psi_i(\mathbf{x})$ are, for instance, assumed constant. For every further iteration, the Fock operator is calculated from the orbitals $\psi_i(\mathbf{x})$, found in the previous iteration. For sufficiently non-degenerate systems the iteration converges quickly and the Slater determinant Φ, built from the converged orbitals $\psi_i(\mathbf{x})$ is called *Hartree-Fock (HF) approximation*. The approximate ground state energy E_0 is an upper bound for the true ground state energy E and it is given by the sum of the lowest N converged eigenenergies, corrected for double counting:

$$E_0 = \sum_i \varepsilon_i - \frac{1}{2}\sum_i \langle \psi_i | \hat{V}_{\text{eff}} | \psi_i \rangle.$$

In this work, sums over lower case indices $i, j, k, \ldots$ will always cover the range of orbitals occupied by an electron in the Hartree-Fock ground state, i.e. $i = 1$ to N.

2.4 Density Functional Theory

The total energy is an expectation value of the many-body wave function $\Psi(\mathbf{x}_1, \ldots, \mathbf{x}_N)$, which is a very complicated object. The true ground state energy E, solving the stationary Schrödinger equation can be brought into a simpler form. It is the minimum of a functional $E[n(\mathbf{x})]$ solely of the ground state electron density $n(\mathbf{x})$ (Hohenberg and Kohn 1964). The (spin) density is given by

$$n(\mathbf{x}) = N \int \mathrm{d}\mathbf{x}_2 \ldots \mathrm{d}\mathbf{x}_N \Psi^*(\mathbf{x}, \mathbf{x}_2, \ldots, \mathbf{x}_N)\Psi(\mathbf{x}, \mathbf{x}_2, \ldots, \mathbf{x}_N).$$

Expressing the ground state energy in this form is exact although only the existence of the functional $E[n(\mathbf{x})]$ has been proven. There is no recipe to calculate the exact $E[n(\mathbf{x})]$ for a

given function $n(\mathbf{x})$, which could, in turn, be minimized. It is not even known how to calculate the kinetic energy as a functional of the density only. In practice, one needs to approximate the functional $E[n(\mathbf{x})]$ in order to find an approximate ground state energy E_0.

In Kohn-Sham DFT, the true density $n(\mathbf{x})$ is expressed as the density $n_0(\mathbf{x})$ of a Slater determinant, $\Phi(\mathbf{x}_1, \ldots, \mathbf{x}_N) = \mathcal{A}\psi_1(\mathbf{x}_1) \ldots \psi_N(\mathbf{x}_N)$, formed by orthonormal *Kohn-Sham orbitals* $\psi_i(\mathbf{x})$. The kinetic energy can then be retrieved from the expectation value of the kinetic operator $\langle\Phi|\hat{T}|\Phi\rangle$ for the above Slater determinant. Minimizing this functional leads to an eigenvalue equation for $\psi_i(\mathbf{x})$, analogous to that in the HF approximation (2.3), but with a different effective interaction which is given by

$$\hat{V}_{\text{eff}}^{\text{KS}}\psi_i(\mathbf{x}) = \underbrace{\int \mathrm{d}\mathbf{x}' \frac{n_0(\mathbf{x}')}{|\mathbf{r} - \mathbf{r}'|}}_{v_{\text{H}}(\mathbf{x})} \psi_i(\mathbf{x}) + v_{\text{xc}}(\mathbf{x})\psi_i(\mathbf{x}). \tag{2.6}$$

The first term is the Hartree term also occurring in the HF effective interaction. The second term contains the *exchange-correlation potential* v_{xc}, chosen such that

$$\underbrace{\langle\Phi|\tfrac{1}{2}\textstyle\sum_i v_{\text{xc}}(\mathbf{x}_i)|\Phi\rangle}_{E_{\text{xc}}[n_0(\mathbf{x})]} = E[n(\mathbf{x})] - \langle\Phi|\hat{T} + \hat{V}_{\text{ne}} + \tfrac{1}{2}\textstyle\sum_i v_{\text{H}}(\mathbf{x}_i)|\Phi\rangle. \tag{2.7}$$

The energy $E_{\text{xc}}[n_0(\mathbf{x})]$ is referred to as exchange-correlation energy. Unlike the exchange term in the Hartree-Fock approximation, the exchange-correlation potential is local, justified by the sole dependence of the ground state wave function on the electron density. This allows a faster calculation of the DFT ground state compared to the HF approximation, given an efficient algorithm to evaluate the exchange-correlation potential from the electron density. However, the exchange-correlation potential is as unknown as the functional $E[n(\mathbf{x})]$ and thus subject to approximation.

In the *Local Density Approximation (LDA)* the Uniform Electron Gas (UEG) serves as the model system for this approximation. In the UEG the density n is constant for all $\mathbf{x}$, making the ground state energy $E(n)$ merely a function of the density. $E(n)$ has been calculated by Ceperley and Alder 1980 and parametrized by Perdew and Zunger 1981; Perdew and Wang 1992 for a wide range of uniform densities n. The other terms occurring on the right side of (2.7) can be calculated analytically for the UEG, yielding an explicit expression for the exchange-correlation potential $v_{\text{xc}}^{\text{UEG}}$ in the UEG. In the Local Density Approximation, the exchange-correlation potential for an arbitrary, usually inhomogeneous, system is then approximated by

$$v_{\text{xc}}(\mathbf{x}) \approx v_{\text{xc}}^{\text{UEG}}(n_0(\mathbf{x})),$$

where $n_0(\mathbf{x})$ is the density of the Kohn-Sham system. More sophisticated approximations use more local information of the density function $n(\mathbf{x})$, such as its gradient, and a non-uniform electron gas as its model. The Perdew-Burke-Enzerhof exchange-correlation potential belongs to this class of approximations and it is among the most commonly used potentials for solids or liquids (Perdew et al. 2008).

2.5 Hartree Fock and DFT in periodic systems

In a crystal the nuclear potential is periodic. In this case the solutions $\psi_i(\mathbf{x})$ of the eigenvalue equations of Hartree-Fock or Density Functional Theory have a particular form:

$$\psi_{n\mathbf{k}}(\mathbf{x}) = e^{\mathbf{i}\mathbf{k}\cdot\mathbf{r}} u_{n\mathbf{k}}(\mathbf{x}),$$

where the functions $u_{n\mathbf{k}}(\mathbf{x})$ have the same periodicity as the nuclear potential (Floquet 1883; Bloch 1929). Instead of a single index i, each orbital is identified by a discrete *band index* n and a continuous $\mathbf{k}$-*vector*, within the first *Brillouin zone*. For a one dimensional nuclear potential with period length a the first Brillouin zone satisfies $-\pi/a < k \leq \pi/a$. The functions $u_{n\mathbf{k}}(\mathbf{x})$ can be found for each $\mathbf{k}$-vector independently as the solution of

$$\left(\hat{T}_{\mathbf{k}} + \hat{V}_{\text{ne}} + \hat{V}_{\text{eff}}\right) u_{n\mathbf{k}}(\mathbf{x}) = \varepsilon_{n\mathbf{k}} u_{n\mathbf{k}}(\mathbf{x}),$$

where $\hat{T}_{\mathbf{k}} = (-\nabla^2 + \mathbf{k}^2)/2$. In practice, the $\mathbf{k}$-vectors are sampled at discrete points within the first Brillouin zone. For large systems, comprising many atoms in the periodic boundary, it may be sufficient for many properties to sample at $\mathbf{k} = \mathbf{0}$ only. This $\mathbf{k}$-point is referred to as the Γ *point*.

Part I

Density Functional Theory applied to liquid metals

Chapter 3

Melting point calculations with Interface Pinning

Calculating thermodynamical quantities, such as thermal expansion coefficients or even melting temperatures, requires a large number of atoms in the calculations for sufficient accuracy. Modern Density Functional Theory implementations are fast enough to conduct *ab-initio* calculation of such properties from a quantum mechanical description of the involved interactions. The following two sections give an intuitive, but by no means rigorous, introduction to methods and concepts involved in *ab-initio* calculations of thermodynamical properties. Section 3.3 then discusses a recently developed method to calculate melting points, a non-trivial task due to the hysteresis of the solid/liquid phase transition.

3.1 *Ab-initio* at finite temperature

In single *ab-initio* calculations using Hartree-Fock or Density Functional Theory the positions of the atomic nuclei are usually fixed. Therefore, the resulting quantities, such as lattice constants or atomization energies refer to zero temperature, even excluding the zero point energy of the atomic vibrations. HF or DFT merely provide a function $U(\mathbf{R})$ to retrieve the energy of the system including its electrons, given the positions of the atomic nuclei $\mathbf{R}$. To calculate temperature dependent quantities, such as thermal expansion coefficients or melting temperatures, we can treat the motion of the nuclei classically and evaluate thermal expectation values of quantities of interest $X(\mathbf{R}, \dot{\mathbf{R}})$:

$$\langle X \rangle = \frac{\sum_{\mathbf{R},\dot{\mathbf{R}}} X(\mathbf{R}, \dot{\mathbf{R}})\, \mathrm{e}^{-\beta H(\mathbf{R},\dot{\mathbf{R}})}}{\sum_{\mathbf{R},\dot{\mathbf{R}}} \mathrm{e}^{-\beta H(\mathbf{R},\dot{\mathbf{R}})}}\,, \quad \text{with } H(\mathbf{R}, \dot{\mathbf{R}}) = T(\dot{\mathbf{R}}) + U(\mathbf{R})\,. \tag{3.1}$$

$T(\dot{\mathbf{R}})$ is the classical kinetic energy of the nuclei and $\beta = 1/k_{\mathrm{B}}T$ is the inverse temperature in units of the Boltzmann constant. $H(\mathbf{R}, \dot{\mathbf{R}})$ is the classical Hamiltonian of the nuclei, depending on its positions $\mathbf{R}$ and velocities $\dot{\mathbf{R}}$. If the quantities of interest can be separated into a kinetic and a potential part the sums can be separated as well. The kinetic part can often be evaluated analytically, since it is of a Gaussian form, however, the integral over all configurations $\mathbf{R}$, given the potential energy landscape $U(\mathbf{R})$, is not trivial.

One way of evaluating this integral is by means of a Metropolis Monte Carlo algorithm (Metropolis et al. 1953; Hastings 1970), which generates (pseudo) random samples $\mathbf{R}_i$ of

configurations that are asymptotically distributed with a probability density function (PDF) proportional to $e^{-\beta U(\mathbf{R}_i)}$. Thus, the thermal expectation value of a quantity X is approximately given by the average of the values $X(\mathbf{R}_i)$. The application of the Metropolis Monte Carlo algorithm to a potential energy landscape $U(\mathbf{R})$ calculated by an *ab-initio* method is, however, limited. The sampling algorithm places atoms at random positions, which can impede the convergence of the self-consistent calculation considerably. It also takes a large number of iterations until the sampling algorithm has covered a sufficiently large portion of the configuration space for an accurate result. Finally, a considerable amount of samples $\mathbf{R}$ is rejected from participating in the average, which can only be done after the costly evaluation of $U(\mathbf{R})$ from HF or DFT.

Another method to sample the configuration space is by means of a molecular dynamics simulation. Given the initial positions and velocities of the atomic nuclei, the Hamiltonian equations of motions are solved numerically, yielding a trajectory of configurations at discrete times $\mathbf{R}(i\Delta t)$, where Δt is the time step. The thermal average of a quantity X can then be approximated by the average over the trajectory $X(\mathbf{R}(i\Delta t))$. The entire relevant phase space is eventually covered by the trajectory of the system, regardless of the initial positions and velocities of the nuclei. In each iteration, $U(\mathbf{R})$ and its gradient have to be evaluated from a Hartree-Fock or DFT calculation. Unlike in the case of the Metropolis algorithm, none of the calculated energies or forces have to be discarded. Additionally, the quadratic equation of motion of the nuclei permits an estimation of the HF or DFT wave function for the next iteration from the previous two iterations, which considerably speeds up the convergence of the self-consistent iterations in the respective *ab-initio* calculation. Finally, HF and DFT are both variational methods such that the gradient of $U(\mathbf{R})$ can be calculated analytically at hardly any extra costs employing the Güttinger 1932 theorem, also known as Hellman–Feynman theorem.

Although the nuclei are heavy compared to electrons, a classical treatment of their dynamics is not always justified, even at room temperature. The frozen vibrational mode of N_2 and tunneling of protons are important counterexamples. A path-integral molecular dynamics approach can be chosen in these cases, of course at considerably higher computational costs (Catlow, Parker, and Allen 1989; Cao and Voth 1994).

3.2 Free energy

There are cases where the relevant configuration space can by no means be visited by the trajectory of a single molecular dynamics simulation on the computer, not even a very long one. Crystallization or melting at a state point of temperature and pressure close to the melting line are an example. In such a first order phase transition there are two regions in configuration space that are likely to be visited. In the example of melting, one region in configuration space is where the atoms are in a crystalline configuration, the other region is where the atoms are in a liquid configuration. One region, the liquid, has a continuous rotational and translation symmetry on average, while the other region has a discrete rotational and possibly[1] a discrete translational symmetry. Therefore, the two regions of the configuration space are not directly connected and a transition from one region to the other region of configuration space can only occur collectively. This makes a thermal transition very unlikely. For instance, a simulation at the melting point, which starts from a crystalline configuration will never melt and vice

[1] A quasi-crystal does not exhibit translational symmetry.

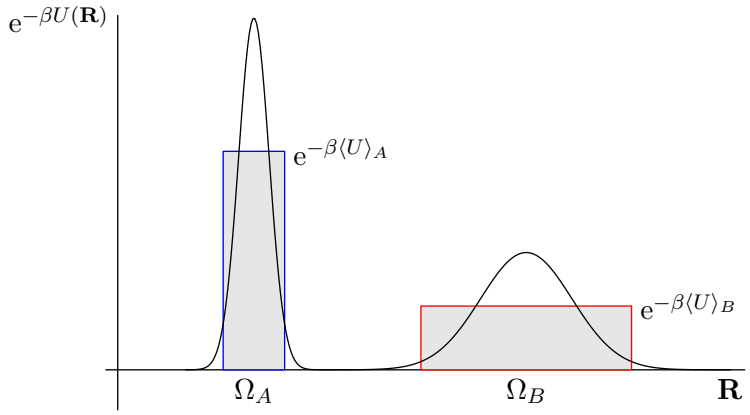

Figure 3.1: A schematic plot of the configuration space for two phases A and B at coexistence. It is equally likely to find the system in either phase, indicated by the area under each peak. The effective support Ω is defined here such that the area of the supported rectangle equals that under the respective peak.

versa. Even in experiment, a liquid can be supercooled to several degrees below freezing point, if it is sufficiently free of impurities. It does not freeze due to the thermal motion of its atoms until crystallization is induced externally, for instance by a shock.

The separation of regions in the configuration space can be thought of as deep basins in the potential energy landscape that are only connected by saddle points high above the bottom of the respective basins. The Boltzmann factor $e^{-\beta U}$ on the bottom of the basins is orders of magnitude higher than that at the saddle points, which makes a spontaneous phase transition very unlikely. If the system starts in any configuration it will evolve towards one of the deep basins in the potential energy landscape and stay in the region of the respective basin for a very long time. However, it will eventually pass the saddle points, exploring another basin in the configuration space and so forth. Two such regions A and B are in *coexistence* if the system spends equally much time in region A as it spends in region B, on a very long time scale. In other words, after a very long time T, the probability of finding the system in region A is the same as finding it in region B:

$$P(\mathbf{R}(T) \in A) = P(\mathbf{R}(T) \in B), \tag{3.2}$$

where we assume that the two trajectories are independent. The time T is usually much larger than possible in practice. An algorithm to determine whether a configuration is an element of either region will be discussed in Section 3.3. Figure 3.1 sketches the configuration space and the respective Boltzmann factors at coexistence. The integral of the Boltzmann factors in a region corresponds to the probability of finding the system in the respective region. In order to relate the probability to quantities which can be measured, we introduce the *effective support* Ω_A of a region A, defined here such that the integral of the Boltzmann factors in that region equals the product of the effective support and the Boltzmann factor using the thermal average $\langle U\rangle_A$ of U restricted to the region A. In practice, these are the thermal averages of the potential energy when measured or calculated for a finite time t, since a spontaneous transition to another region is very unlikely to occur within that time. We can then rewrite (3.2) to

$$\Omega_A\, e^{-\beta\langle U\rangle_A} = \Omega_B\, e^{-\beta\langle U\rangle_B}. \tag{3.3}$$

Finally, a probability is not a practical quantity to work with since it is not extensive. Having a system consisting of two parts, the probability of finding both for instance in the crystalline phase is the product of the probabilities of finding each part in the crystalline phase, assuming that the configurations of the two parts are sufficiently uncorrelated. Taking the logarithm of (3.3) gives an extensive quantity and we obtain

$$\langle U \rangle_A - TS_A = \langle U \rangle_B - TS_B, \tag{3.4}$$

where $S_A = k_\mathrm{B} \log \Omega_A$ is called *entropy* of the system in a region A. The discussion of indistinguishability in the context of entropy is omitted here. It can be found, for instance, in Cates and Manoharan 2015. Equation (3.4) has the dimension of energy and the quantity on either side is called *Helmholtz free energy*. The *Gibbs free energy* is the pendant of the Helmholtz free energy at constant pressure, rather than constant volume, such that (3.4) becomes

$$\underbrace{\langle U \rangle_A + p\langle V \rangle_A - TS_A}_{=: G_A} = \underbrace{\langle U \rangle_B + p\langle V \rangle_B - TS_B}_{=: G_B}. \tag{3.5}$$

Conversely, we can also express the probability in terms of the free energy. In case of constant pressure, this gives

$$P(\mathbf{R}(T) \in A) = \mathrm{e}^{-\beta G_A}. \tag{3.6}$$

Thus, free energies are the thermal analog to the potential energy since preferred regions have lowest free energy as preferred configurations have lowest potential energy at $T = 0\,\mathrm{K}$. The above equations still do not provide an algorithm of how to compute the free energy difference between two phases. The previously discussed means of evaluating thermal averages only allows us to evaluate the thermal averages of the potential energies and the volume for each phase. For the solid/liquid phase transition, Interface Pinning can be employed to evaluate the difference of the Gibbs free energy per atom between the two phases directly. This is described in the next section.

3.3 The Interface Pinning method

In direct methods for finding coexistence states, the two phases are brought in contact, having a mono-crystalline part, a liquid part and interfaces between the phases, all in one simulation under periodic boundary conditions as shown in Figure 3.2. This places the system on a saddle point between the two phases of interest. Starting at roughly half solid, half liquid, the system will either entirely melt or solidify at constant temperature and pressure, depending on whether the temperature is above or below the melting line, respectively. Assuming an interface perpendicular to the z direction, the size of the simulation cell must be kept fixed in the x and y direction in order to keep the crystal free from strain. This ensemble is herein referred to as Np_zT ensemble. The average velocity of the interface will be zero at coexistence. However, the simulation is not at equilibrium and a single calculation can only be carried out until the system is entirely liquid or solid (Zykova-Timan, Horbach, and Binder 2010).

Interface Pinning improves on this method by imposing an additional bias potential, coupled to an order parameter $Q(\mathbf{R})$ which should be proportional to the size of the crystalline phase:

$$U'(\mathbf{R}) = U(\mathbf{R}) + \frac{\kappa}{2} \left(Q(\mathbf{R}) - a\right)^2. \tag{3.7}$$

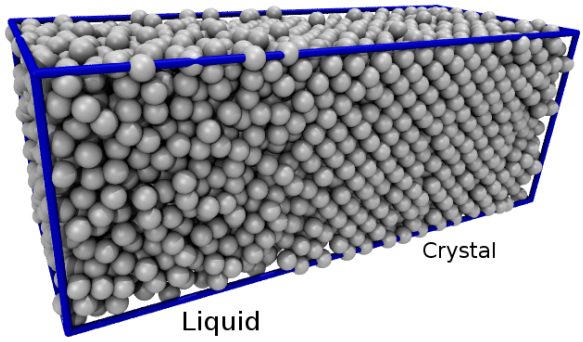

Figure 3.2: Direct calculations of the solid/liquid coexistence bring a crystalline and a liquid slab in contact. At constant temperature and hydrostatic pressure the preferred slab will grow until the entire cell either liquid or solid. Interface Pinning imposes an additional penalty energy for deviations from the initial half-half configuration, effectively pinning the position of the interface. Image from Pedersen 2013.

The strength of the bias potential is given by κ and the desired value of the order parameter is given by a, which is chosen close to the order parameter of the initial half liquid, half solid configuration. In a simulation above coexistence temperature, the system will melt until the penalty energy imposed by the bias potential is in balance with the free energy gained from melting. If κ is chosen strong enough, this balance will occur before the system is entirely liquid and the system will stay in this equilibrium for all practical considerations. The situation is almost analogous at temperatures below coexistence, however, it is preferable to simulate above coexistence temperature for reasons discussed in Subsection 3.3.3. The bias converts the non-equilibrium situation of the two phase system into an equilibrium situation, allowing to evaluate the thermal average $\langle Q \rangle'$ of the order parameter $Q(\mathbf{R})$ in the biased dynamics, where the potential energy U is replaced by the biased potential energy U'. The average of the order parameter Q will be below the desired value a, if the system is simulated at temperatures above the melting line and the difference of $\langle Q \rangle' - a$ is related to the difference of the Gibbs free energy per atom, $\Delta\mu$ called *chemical potential* difference.

3.3.1 Free energy of the two phase system

We model the Gibbs free energy G of the simulated system without the bias potential as a function of crystalline atoms assuming that the number of atoms in the planar interface N_i as well as its free energy G_i is constant and independent of N_c and N_l:

$$G(N_\mathrm{c}) = N_\mathrm{c}\mu_\mathrm{c} + N_\mathrm{l}\mu_\mathrm{l} + G_\mathrm{i}. \tag{3.8}$$

N_c and μ_c are the number of atoms and the chemical potential in the crystalline phase and N_l and μ_l are the number of atoms and the chemical potential in the liquid phase. $N = N_\mathrm{c} + N_\mathrm{l} + N_\mathrm{i}$ is the total number of atoms, which is constant. The surface tension of the interface conserves the planar interface as initially prepared. To justify the assumption of a constant average number of atoms in the interface, the crystal must be allowed to grow and melt due to thermal fluctuations by at least one full layer of atoms. Thus, the strength of the bias potential κ must be low enough to allow that. Given an order parameter $Q(\mathbf{R})$, which is

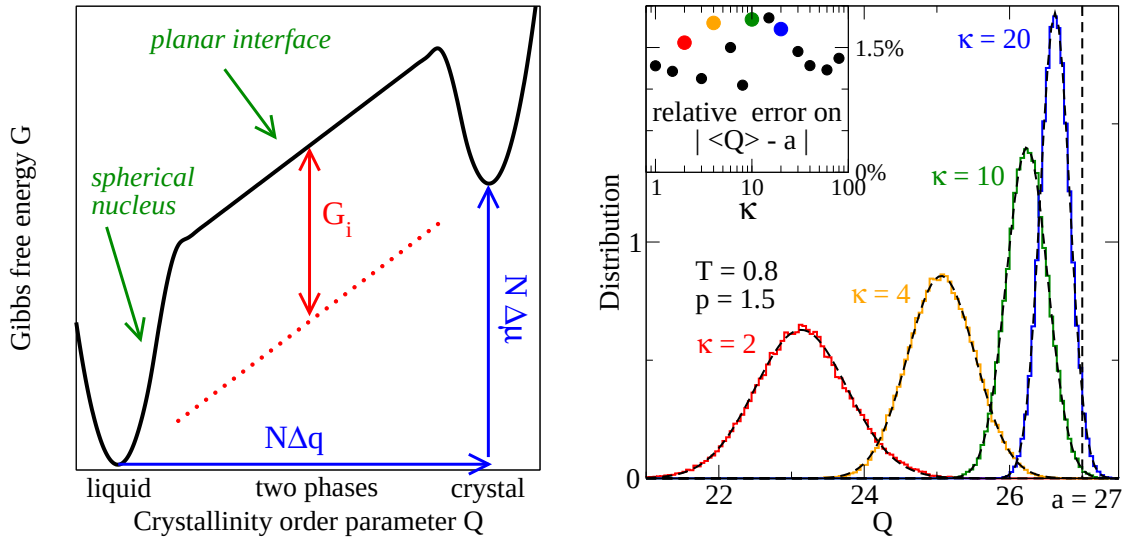

Figure 3.3: (a) Sketch of the Gibbs free energy of the two phase system. The free energy of the interface G_i is assumed constant as long as the interface is planar. This allows the Gibbs free energy difference per atom $\Delta\mu$ to be estimated from the slope of $G(Q)$ at one value of Q only. (b) Measured distributions of the order parameter Q in the Lennard-Jones system for different strengths κ of the applied bias potential. Temperature and pressure are given in reduced units. The inset shows that the relative error is largely independent of κ in a wide range. Modified images from Pedersen et al. 2013.

linear in the number of crystalline atoms, we can express the number of crystalline particles by

$$N_\mathrm{c} = \frac{Q(\mathbf{R})}{\Delta q} + \text{const.}\,, \tag{3.9}$$

where $\Delta q = \langle q \rangle_\mathrm{c} - \langle q \rangle_\mathrm{l}$ is the difference of the average order parameter per atom between the liquid and the crystalline phase. We will generally denote differences of thermal averages between the phases by

$$\Delta X = \langle X \rangle_\mathrm{c} - \langle X \rangle_\mathrm{l}\,.$$

Figure 3.3(a) sketches the Gibbs free energy as a function of a crystallinity order parameter Q. Inserting (3.9) into (3.8) yields the Gibbs free energy without the bias potential as a function of the order parameter Q:

$$G(Q) = \frac{\Delta\mu}{\Delta q} Q + \text{const.} \tag{3.10}$$

The above equation holds as long as the interface is planar on average and still present in the system. Adding the bias potential changes the potential energy of the system. However, it hardly changes the number of available configurations of the system since the bias potential is relatively shallow compared to the deep basins of either the fully crystalline or fully liquid regions. Thus, the change of the Gibbs free energy in the biased ensemble is equivalent to the

change of the potential energy. From (3.7) and (3.10), we obtain

$$G'(Q) = \frac{\Delta\mu}{\Delta q} Q + \frac{\kappa}{2}(Q-a)^2. \tag{3.11}$$

Finally, we can retrieve the probability distribution of Q from the free energy of the biased system as a function of Q by using (3.6) for the region of constant Q, giving:

$$\mathrm{PDF}(Q) \propto \exp\left(-\beta G'(Q)\right) \propto \exp\left(-\beta\kappa\left(Q - a + \Delta\mu/\kappa\Delta q\right)^2/2\right). \tag{3.12}$$

Thus, the order parameter $Q(\mathbf{R})$ with the bias potential enabled is Gaussian distributed. Its expectation value and its variance are

$$\langle Q\rangle' = a - \frac{\Delta\mu}{\kappa\Delta q}, \qquad \langle Q^2\rangle' - \langle Q\rangle'^2 = \frac{k_\mathrm{B}T}{\kappa}. \tag{3.13}$$

The former gives a direct relation between the thermal average of the order parameter in the biased simulation and the Gibbs free energy difference per atom $\Delta\mu = \mu_\mathrm{c} - \mu_\mathrm{l}$ between the liquid and the crystalline phase. The latter is the statement of the equipartition theorem that the average energy contained in the degree of freedom offered by the bias potential is $k_\mathrm{B}T/2$.

3.3.2 Computing coexistence points with Interface Pinning

Figure 3.3(b) shows the distribution of the order parameter Q for the Lennard-Jones system simulated at a temperature slightly above coexistence at $T = 0.8$ and $p = 1.5$ in reduced units, respectively. The desired order parameter was set to $a = 27$ and the strength of the bias potential κ was varied over a wide range. In the superheated regime the expectation value of Q is below a, depending on the strength of the bias potential κ according to (3.13). The measured histograms of Q are shown in color, while the Gaussians fitted to *one* value of κ are drawn in black. The difference $\langle Q\rangle' - a$ between the desired order parameter and the average order parameter in the biased system is the key quantity required for determining $\Delta\mu$. The insert of Figure 3.3(b) shows that the relative error of this quantity hardly depends on the choice of κ over a wide range of bias potential strengths. If only the difference of the chemical potential is to be calculated in an Interface Pinning simulation, it is sufficient to choose κ large enough that the system is prevented from entirely melting or freezing and small enough that the interface can fluctuate at least by one full layer of atoms. Interface Pinning also allows for an evaluation of the interface mobility requiring additional constraints on the strength of the bias potential κ, which are discussed in Section 3.5.

To correct for finite size errors $\Delta\mu$ should be evaluated at the same temperature and pressure for different sizes of the simulation cell N. An extrapolation with $1/N$ finally yields the difference of the chemical potential $\Delta\mu$ for an infinite system. Additionally, the liquid to solid ratio can be varied for each size by varying the desired order parameter a. This gives an error estimate for each size N and subsequently for the extrapolated value of $\Delta\mu$. Note that the interface itself requires space in the amount of several layers of the crystalline phase. Thus, the extrapolation with $1/N$ requires the size N to be large enough. A more detailed discussion of finite size effects is found in Pedersen 2013.

The difference of the chemical potential is the difference of the Gibbs free energy per atom. From (3.5) follows that

$$\Delta\mu = \Delta u + p\Delta v - T\Delta s, \tag{3.14}$$

where $\Delta u = (\langle U\rangle_\mathrm{c} - \langle U\rangle_\mathrm{l})/N$, $\Delta v = (\langle V\rangle_\mathrm{c} - \langle V\rangle_\mathrm{l})/N$ and $\Delta s = (S_\mathrm{c} - S_\mathrm{l})/N$. Δv and Δs are the *latent volume* and the *latent entropy* per atom, respectively. At the same temperature but at coexistence pressure p_m the difference of the chemical potential must vanish

$$0 = \Delta u + p_\mathrm{m}\Delta v - T\Delta s,$$

where we assume that Δu, Δv and Δs do not change when changing the pressure to p_m. From above equations we can then estimate a state point on the coexistence line (T, p_m) at the same temperature, or analogously (T_m, p) at the same pressure as used in the simulation to retrieve $\Delta\mu$:

$$p_\mathrm{m} = p - \frac{\Delta\mu}{\Delta v}\,, \qquad T_\mathrm{m} = T + \frac{\Delta\mu}{\Delta s}\,. \tag{3.15}$$

Knowing the difference of the chemical potential $\Delta\mu$ from the Interface Pinning calculation allows us to calculate the latent entropy Δs per atom from (3.14). Note that the latent entropy is negative as defined here. Subsequently, the Interface Pinning calculation can be repeated at the estimated state point (T, p_m) or (T_m, p) until $\Delta\mu$ is zero within statistical accuracy.

3.3.3 Order parameter for crystallinity

Interface Pinning requires an *order parameter* that is linear in the number of crystalline atoms in the simulation as long as a planar interface is present. For applicability in a molecular dynamics simulation, we also require the order parameter to be continuous in all components of $\mathbf{R}$ to yield finite forces. One possible order parameter is the intensity of one of the peaks in the phase factor of the atom positions

$$Q(\mathbf{R}) = |\rho_\mathbf{k}|, \quad \text{with } \rho_\mathbf{k} = \frac{1}{\sqrt{N}}\sum_i \mathrm{e}^{\mathrm{i}\mathbf{k}\cdot\mathbf{r}_i}$$

and where $\mathbf{k}$ is a Bragg peak of the crystal structure in consideration. Note that $\mathbf{k}$ must be parallel to the interface since the length of the simulation cell fluctuates in the direction perpendicular to the interface, herein referred to as z direction. The normalization is chosen such that the order parameter of the liquid phase is on average 1, irrespective of the system size, which is not necessary but helpful. This order parameter is fast and can be evaluated in $\mathcal{O}(N)$ steps. Furthermore, it is continuous and the forces are easy to retrieve. However, this order parameter exhibits a particular caveat in the supercooled regime, where the order parameter is supposed to prevent the system from crystallizing by enforcing a low value of $Q(R)$. Given the positions of the atoms $\mathbf{r}_i$ in the perfectly crystalline structure with a Bragg peak $\mathbf{k}$ perpendicular to z, the following configuration $\mathbf{r}'_i$ has an order parameter of zero although it is a crystalline configuration with only a triangular distortion along the z direction:

$$\mathbf{r}'_i = \mathbf{r}_i + \mathbf{k}\frac{\pi}{k^2}\,\mathrm{tri}\left(\frac{2\pi}{L_z}\,\mathbf{z}\cdot\mathbf{r}_i\right).$$

$\mathbf{z}$ is the unit vector in the z direction and L_z is the average length of the simulation cell in that direction. tri is the function of the periodic triangular wave between -1 and $+1$ with period 2π. This distortion corresponds to a superposition of sinusoidal acoustic modes. Truncating this Fourier series still lowers the order parameter considerably, however, the energy to form it from the perfect crystal decreases with the wavelength L_z. Thus, a system can crystallize

assuming a low order parameter by forming such a distortion if sufficiently supercooled, which has also been observed in practice.

The orientational order parameter proposed by Steinhardt, Nelson, and Ronchetti 1983 is more robust in that regard but more expensive to evaluate and to implement. Analogous to the translational order parameter, projecting atom positions on spatial harmonics, the orientational order parameter projects bond directions onto spherical harmonics. This makes the order parameter rotationally invariant. Different degrees can be used to discriminate the discrete rotational symmetries of the crystal in consideration from the liquid. The degree six, Q_6, has proven to be a reliable order parameter for many common crystal structures, especially for the ones of the studied elements Na, Mg, Al and Si, which are listed in Table 3.1. The order parameter is given by

$$Q_l = \sqrt{\frac{4\pi}{2l-1}\sum_{m=-l}^{l} Q_l^m Q_l^{m*}} \quad \text{with } Q_l^m = \frac{1}{M}\sum_{\text{bond } (ij)} Y_l^m(\vartheta_{ij}, \varphi_{ij}),$$

where M is the number of bonds between nearest neighbors and Y_l^m is the spherical harmonic of degree l and order m. The angles ϑ_{ij} and φ_{ij} respectively denote the angle to the positive z axis and the azimuthal angle of the bond between atom i and j. This definition is not continuous, as the number of bonds can only assume integer values, however, we can introduce a continuous and smooth weighting function $w(r)$ for bonds of length r:

$$w(r) = \begin{cases} 1 & \text{for } r \leq n, \\ \dfrac{\left(f^2 - r^2\right)^2 \left(f^2 - 3n^2 + 2r^2\right)}{\left(f^2 - n^2\right)^3} & \text{for } n < r < f, \\ 0 & \text{for } f \leq r. \end{cases}$$

The distances n and f can be chosen from the radial distribution function $g(r)$ of the crystal phase. The first peak in the radial distribution function should be fully counted, the second peak should not be counted at all. Furthermore, $g(r)$ should be small where the weighting function has a high derivative to avoid spurious stress when the bias potential applies a force on the order parameter. Thus, the distance n where $g(r)$ goes below 1 for the first time and the distance f where $g(r)$ goes above 1 again before the second peak, provide a reasonable choice for the distances n and f, respectively. The orientational order parameter employed by the Interface Pinning method is then given by

$$Q_l = \sqrt{\frac{4\pi}{2l-1}\sum_{m=-l}^{l} Q_l^m Q_l^{m*}} \quad \text{with } Q_l^m = \frac{\sum_{i<j} w(r_{ij})\, Y_l^m(\vartheta_{ij}, \varphi_{ij})}{\sum_{i<j} w(r_{ij})}, \tag{3.16}$$

where $r_{ij} = |\mathbf{r}_i - \mathbf{r}_j|$ is the distance between the atoms i and j. At the time of publication, Q_6 is implemented in `VASP`, which is sufficient to discriminate common crystal structures with four and six fold symmetries from the liquid phase.

3.4 Melting point of Na, Mg, Al and Si

The Interface Pinning method was employed to calculate the melting point of Na, Mg, Al and Si at ambient pressure to verify its applicability and efficiency in *ab-initio* calculations.

These elements crystallize into four of the most common crystal structures, namely body centered cubic, hexagonal close packed, face centered cubic and cubic diamond, respectively. Furthermore, they are sufficiently well described on the level of Density Functional Theory to allow comparison with experiment in the cases of Na, Mg and Al. The calculations were conducted with the Vienna Ab-initio Simulation Package (`VASP`), which is a DFT solver using a plane wave basis set. In the regions close to the nuclei the basis set is augmented with atom centered basis functions by the Projector Augmented Wave (PAW) method to improve its accuracy at a given number of basis functions (Kresse and Furthmüller 1996; Blöchl 1994). To gain further efficiency, the *frozen core approximation* was applied, where the chemically inactive core electrons are only considered by means of the effective potential and are taken out of the self-consistent calculation. This leaves only one to four electrons per atom to be calculated self-consistently. Considering the large number of atoms there are still literally thousands of electrons to be calculated self-consistently.

In the case of Na, Mg and Al the used exchange-functional was the Perdew, Burke, Enzerhof functional optimized for solids (PBEsol), which gives good agreement between DFT and experimental densities. For silicon it has been shown that LDA does not yield good agreement of the melting temperature with experiment. To allow comparison with with previous publications (Sugino 1995) we decided to use LDA since no PBEsol reference has been found.

3.4.1 Interface preparation

All finite temperature molecular dynamics calculations were carried out using a Langevin thermostat with a coupling time of 1 ps. To simulate at constant pressure, the barostat proposed by Parrinello and Rahman 1981 was employed with a fictitious mass of 100 atomic mass units and a coupling to the heat bath with a time constant of 1/3 ps. A time step of 3 fs was chosen for the molecular dynamics simulations of Mg, Al and Si. For sodium the time step was 4 fs.

First, the maximum size of the system and the orientation of the interface must be chosen. In the cubic systems bcc, fcc and cd, this is straight forward. In the hexagonal close packed system of Mg the orientation of the interface was chosen to be perpendicular to the hexagonal layers to enforce crystal growth in the layer stacking of hcp, $ABAB\ldots$ Table 3.1 lists the largest super cells for the molecular dynamics simulations of the calculated elements. The trial temperature for the first Interface Pinning calculation was chosen slightly above the experimental melting temperature to avoid the supercooled regime with its associated difficulties mentioned in Subsection 3.3.3. For silicon the melting temperature found in Sugino 1995 was taken instead of the experimental one.

Subsequently, each system was set up in a perfectly crystalline configuration of the chosen size and split into two cells of equal size along the z direction. One part is used to evaluate the DFT density and the average Q_6 order parameter of the crystalline phase at the selected temperature. The angles of the simulation cell were fixed in this simulation. The other part was set up at the DFT density found for the crystalline phase and molten at about twice the selected temperature in the Np_zT ensemble, where the size of the simulation cell is only allowed to vary along the z axis. After melting, the system was slowly cooled to the selected trial temperature. Once at equilibrium, the density and the average Q_6 order parameter were evaluated for the liquid phase.

In the last phase, the final configurations of the two prepared parts were concatenated along the z direction. As a result of this procedure the atoms might be unusually close in

	unit cell	super cell	inter-face	N	T [K]	T_m [K]	$-\Delta s$ [k_B]	$\mathrm{d}T_m/\mathrm{d}p$ [K/GPa]	M [Å/ps eV]
Na	bcc	$5 \times 5 \times 10$	(100)	500	400	354(21)	1.19(15)	120(30)	250(50)
Mg	hcp	$4 \times 6 \times 8$	$(2\bar{1}\bar{1}0)$	768	960	920(20)	1.05(16)	55(8)	—
Al	fcc	$4 \times 4 \times 8$	(100)	512	1000	985(30)	1.44(14)	70(9)	—
Si	cd	$3 \times 4 \times 7$	(100)	672	1400	1241(20)	3.61(11)	-35(5)	30(15)

Table 3.1: Results from the Interface Pinning calculations of the elements Na, Mg, Al and Si. The listed system sizes are the largest sizes considered for each element and the listed temperatures correspond to the temperature of the last state point iteration. The numbers in parenthesis give the expected error on the last digits of the number to its left. The slope of the melting line was retrieved from the Clausius–Clapeyron relation and the interface mobilities M are discussed in Section 3.5.

the interface region which was corrected manually if the distances were particularly small. Finally, the atoms at the two interfaces were relaxed at constant volume to yield the initial configuration for Interface Pinning.

Interface Pinning calculation

Before initiating the Interface Pinning molecular dynamics simulation the strength κ and the desired order parameter a of the bias potential must be determined. The strength κ was chosen to allow fluctuations of the crystal size by at least 2 layers and the desired order parameter was set to the Q_6 order parameter of the configuration resulting from the interface preparation phase. Starting from that configuration, the Interface Pinning simulation was run with the biased potential. After a warm up time, the trajectory of $Q_6(t)$ was recorded until its variance reached the theoretical value of $k_\mathrm{B}T/\kappa$ to a sufficiently degree of statistical uncertainty. These fluctuations originate from thermal vibrations of the atoms as well as from much slower crystal growth and shrinking. The time of the latter determines the required duration of the Interface Pinning simulation to a large extent. The recorded trajectories were between 30 ps and 60 ps long.

From the average order parameter over the whole recorded trajectory $\langle Q(t) \rangle'$ the difference in the chemical potential $\Delta\mu$ and subsequently the predicted melting temperature T_m was evaluated according to (3.13) and (3.15), respectively. If T_m differed from the simulated temperature T by more than 10%, the whole procedure was repeated at $T = T_\mathrm{m}$, including the interface preparation. Note that in the case of Na and Si, 11% were tolerated due to the large computational costs of the whole procedure and the small correction expected.

Statistical uncertainties were estimated by splitting the entire trajectory into blocks of equal and sufficient length, such that the average over each block can be regarded an independent random variable. The length of the blocks was assessed by inspecting the autocorrelation of the order parameter $\langle Q(t), Q(t+\tau) \rangle'$. For silicon the finite size effect was estimated as described in Subsection 3.3.2. The error found for smaller systems was too large to allow a reliable extrapolation to infinite system size. However, the finite size error was found to be of the same order of magnitude as the statistical error. For this reason finite size extrapolations were not conducted. The results reported in Table 3.1 were taken from the largest simulated cell and the reported errors include the statistical error with a confidence interval of 95% and

the expected finite size error. The reported errors do not contain systematic errors expected from the DFT calculations. They are, for instance, discussed in Alfè 2003.

3.5 Interface mobility

To calculate the free energy difference between the solid and the liquid phase, it is sufficient to use average quantities of the biased simulation containing both phases. Fluctuation properties of the order parameter Q may provide additional information. From (3.13) we have already seen that the variance of the order parameter should fulfill the equipartition theorem so we can only use it for testing whether the system can be considered equilibrated or not. The fluctuations of the order parameter arise from the thermal motion of the atoms, as well as from growth and shrinking of the crystalline part. Thus, the trajectory of the order parameter from a molecular dynamics simulation of the two phases in contact may indeed provide information on the growth dynamics of the crystal in the direction perpendicular to the interface. Specifically, we want to retain information on the interface mobility M, which relates the crystal growth velocity $\dot{z}(t)$ of the interface in an unbiased system to the difference in chemical potential per atom between the solid and the liquid phase

$$\dot{z}(t) = -M\Delta\mu. \tag{3.17}$$

We assume that the order parameter $Q(t)$ can be decomposed into a contribution proportional to the amount of crystal $c(t)$ and a contribution from the comparatively fast thermal vibrations $f(t)$ such that

$$Q(t) = c(t) + f(t).$$

In the previous sections, we were not required to make this distinction between the two contributions, since we only needed the expectation value of the amount of the crystal $c(t)$, which is proportional to $\langle Q(t)\rangle'$ as long as $\langle f(t)\rangle' = \text{const}$. In an Interface Pinning simulation, we can relate the growth velocity of the two interfaces to the time derivative of the amount of crystal $\dot{c}(t)$ as follows

$$2XY\dot{z}(t)\langle\rho\rangle_\mathrm{s}\Delta q = \dot{c}(t), \tag{3.18}$$

where X and Y are the lengths of the simulation cell parallel to the interface. $\langle\rho\rangle_\mathrm{s}$ is the average number density in the solid phase and $\Delta q = (\langle Q\rangle_\mathrm{s} - \langle Q\rangle_\mathrm{l})/N$. The Interface Pinning simulation provides information on the dynamics of $Q(t)$ rather than $c(t)$. To extract information on $c(t)$ we model the dynamics of $c(t)$ and $f(t)$ with a simplified effective Hamiltonian, where $c(t), f(t)$ and $\dot{f}(t)$ are the only dynamical variables. Subsequently, we can compare the modeled dynamics of $c(t) + f(t)$ to the actual dynamics of $Q(t)$ from the Interface Pinning simulation to estimate the model parameters, including the interface mobility.

The dynamics of $c(t)$ and $f(t)$ is modeled by the following effective Hamiltonian:

$$H(c, f, \dot{f}) = \alpha c + \frac{\kappa}{2}(c + f - a)^2 + \frac{\kappa_f}{2}f^2 + \frac{m_f}{2}\dot{f}^2. \tag{3.19}$$

The first term reflects the free energy gain from growing or shrinking the amount of crystal $c(t)$, where $\alpha = \Delta\mu/\Delta q$. κ and a are the parameters of the bias potential in an Interface Pinning simulation according to (3.7), coupled to the order parameter $Q = c + f$ as given by the second term. The last two terms model the atomic vibrations by a single harmonic oscillator with the spring constant κ_f and the fictitious mass m_f. We assume an overdamped

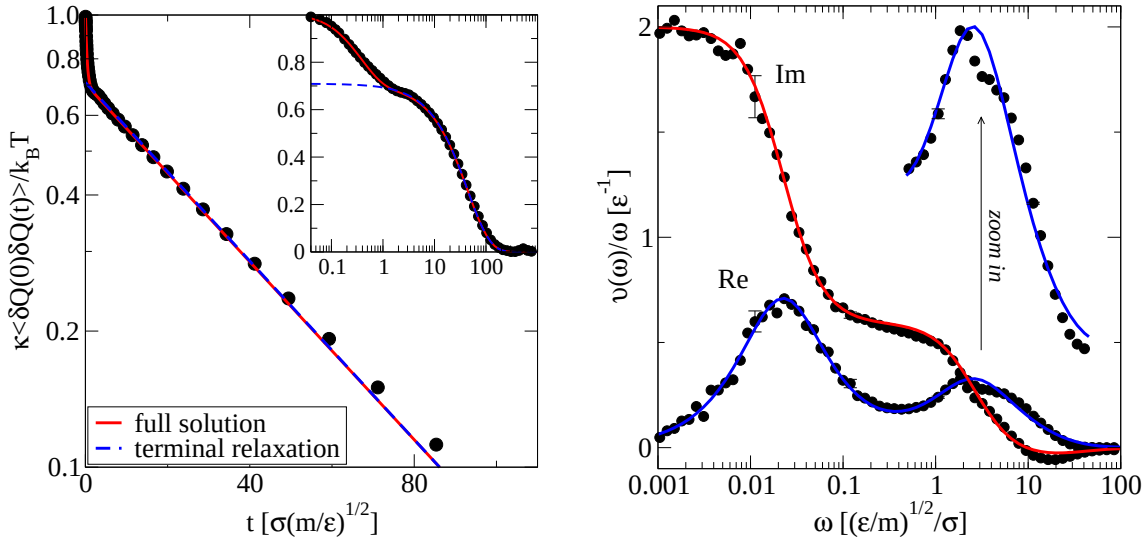

Figure 3.4: (a) autocorrelation function of the order parameter Q in units of $k_\mathrm{B}T/\kappa$, which is the variance of Q. It is compared to the fit of the full solution of the Langevin equations of motion and to the terminal relaxation. (b) the frequency dependent admittance retained from the autocorrelation reveals more on the quality of model. The model parameters were determined from a fit to the real part only. The zoom on the high frequency part exhibits more details on the thermal vibrations than modeled by a single harmonic oscillator.

dynamics in the amount of crystal $c(t)$ relieving the effective Hamiltonian from a mass term coupled to the growth velocity $\dot{c}(t)$. In the presence of a heat bath, a set of Langevin equations of motion can be derived for $c(t)$ and $f(t)$ from the effective Hamiltonian (3.19):

$$\alpha + \kappa\left(c(t) + f(t) - a\right) = \eta_c(t) - \gamma\,\dot{c}(t) \tag{3.20}$$

$$m_f\ddot{f}(t) + \kappa_f f(t) + \kappa\left(c(t) + f(t) - a\right) = \eta_f(t) - \gamma_f\dot{f}(t). \tag{3.21}$$

γ and γ_f are the friction constants associated with the amount of crystal and the thermal vibrations, respectively, and $\eta_c(t)$ and $\eta_f(t)$ are δ-correlated Gaussian forces such that the average kinetic energy corresponds to the chosen constant temperature.

3.5.1 Solving the equations of motion

We can solve the above Langevin equations of motion and analytically calculate the autocorrelation function of the modeled $Q(t)$. This is done in Pedersen, Hummel, and Dellago 2015, particularly in the Appendix, and it turns out to be a sum of three complex exponentials. We are only interested in the long time scales of the overdamped growth and shrinking of the crystal. Furthermore, we cannot expect the fast thermal vibrations to be well described by a single effective harmonic oscillator only. For long time scales the autocorrelation[2] of the

[2] The autocorrelation function in the biased dynamics is given by $\langle \delta f(0), \delta g(t)\rangle' = \lim_{T\to\infty}\frac{1}{T}\int_0^T \mathrm{d}t'\,(f(t') - \langle f\rangle')^*\,(g(t'+t) - \langle g\rangle')$.

model is given by

$$\langle \delta Q(0), \delta Q(t) \rangle' \sim \frac{k_\mathrm{B} T}{\kappa} A \mathrm{e}^{-t/\tau}, \tag{3.22}$$

where $A = \kappa_f/(\kappa+\kappa_f)$ is the strength and $\tau = \gamma\,(1/\kappa + 1/\kappa_f)$ is the characteristic time of the terminal relaxation. Figure 3.4(a) shows the autocorrelation function for the Lennard-Jones system in comparison to the full solution of the Langevin equations of motion and to the terminal relaxation of (3.22). The quality of the model can be better assessed by comparison of the frequency dependent admittance $\upsilon(\omega)$, retrieved by the fluctuation dissipation theorem

$$\upsilon(\omega) = \frac{\mathrm{i}\omega}{k_\mathrm{B} T} \int_0^\infty \mathrm{d}t \langle \delta Q(0), \delta \dot{Q}(t) \rangle' \mathrm{e}^{-\mathrm{i}\omega t}.$$

Figure 3.4(b) compares the admittance from the Interface Pinning simulation with the admittance of the stochastic model. The model parameters were retrieved from a least squares fit to the real part only. The zoomed part of the high frequency peak indicates that the thermal vibrations actually exhibit more features than can be modeled by a single harmonic oscillator, due to the different vibrations in the liquid and in the solid phase. They are, however, irrelevant for the interface mobility which requires only the zero frequency limit to be accurately described by the model. The applicability of the model is further discussed in Pedersen, Hummel, and Dellago 2015.

3.5.2 Estimating the interface mobility

Using this model, we can estimate the friction constant γ, associated with the amount of crystal $c(t)$, from a fit of A and τ in the long time behavior of the autocorrelation function of the actual trajectory of $Q(t)$, calculated from the Interface Pinning simulation:

$$\gamma = A\tau\kappa.$$

In the absence of the bias potential the crystal growth or shrinking is simply determined by the first of the two Langevin equations of motion (3.20), $\alpha = \eta_c(t) - \gamma\,\dot{c}(t)$, allowing us to express the average crystal growth velocity in terms of the fitted parameters

$$\dot{c}(t) = -\frac{\alpha}{\gamma},$$

where $\alpha = \Delta\mu/\Delta q$. Finally, (3.18) relates the friction constant γ, to the interface mobility M as defined in (3.17), arriving at

$$M^{-1} = 2XY \langle \rho \rangle_\mathrm{s} \Delta q^2 A \tau \kappa, \tag{3.23}$$

which can – in principle – be evaluated from an Interface Pinning simulation *a posteriori*. In the following subsection practical considerations are discussed for retrieving sufficiently accurate results.

3.5.3 Interface mobility of Na and Si

Figure 3.5 shows the autocorrelation functions of the order parameter $Q(t)$ for Na and Si along with their fits, once to the full model and once to the terminal relaxation only. For an accurate fit of the characteristic time τ and the strength A of the terminal relaxation the

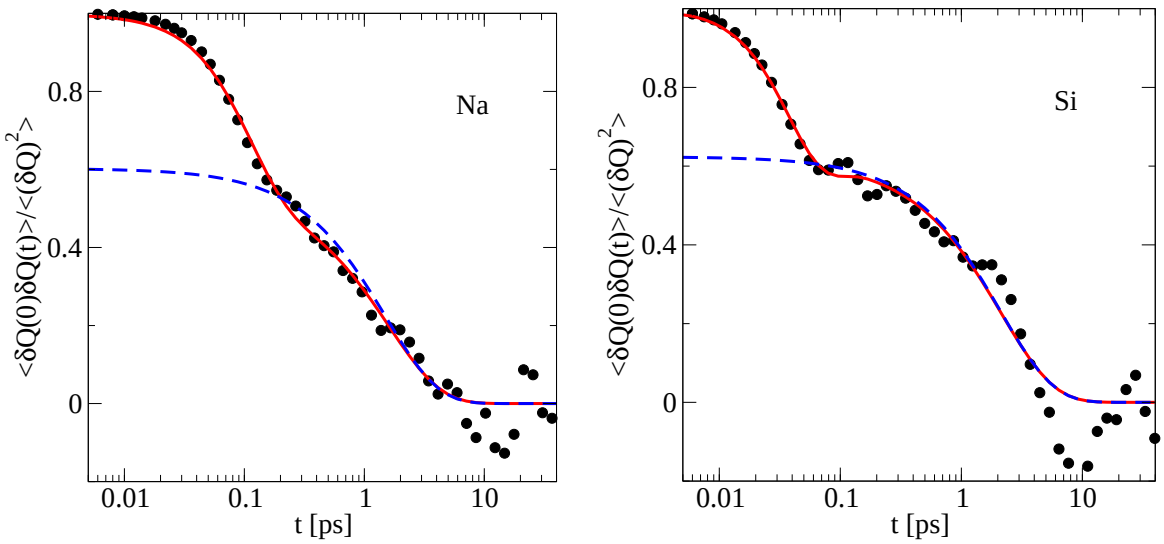

Figure 3.5: The dots show the autocorrelation function of the order parameter $Q(t)$ in the Interface Pinning calculations of Na and Si. It is compared to fits of the full stochastic model, given by the Langevin equations of motion, and of the terminal relaxation given by (3.22). A good fit requires different time scales for the terminal relaxation and the faster thermal vibration, such that the kink is clearly pronounced, where the terminal relaxation starts to dominate.

kink where the terminal relaxations starts to dominate must be sufficiently pronounced. It is therefore relevant that the time scale of the characteristic time τ is different from that of the thermal vibrations. Both, $A = \kappa_f/(\kappa + \kappa_f)$ and $\tau = \gamma(1/\kappa + 1/\kappa_f)$ depend on the strength of the bias potential κ, allowing an adjustment of τ by an appropriate choice of κ. The lower the strength, the better the contrast between the fast thermal vibrations and the slow interface fluctuations. On the other hand, a lower strength also results in a longer equilibration time until the fluctuations of the interface have explored the full magnitude $k_\mathrm{B}T/\kappa$, as given by the equipartition theorem, according to (3.13). Note that also the characteristic time scales of the Langevin thermostat and the Parinello-Rahman barostat should be chosen different from that of τ.

In the cases of Na and Si, κ had to be reduced from the initial Interface Pinning calculation of the melting point to allow a fit of the terminal relaxation parameters A and τ. With up to 120 ps the trajectories required for a sufficiently accurate fit were at least twice as long as in the Interface Pinning calculation of the melting point only. In the case of Mg and Al the finite size effects were too dominant at the lower strengths of the bias potential, required for a well pronounced kink in the autocorrelation function. A setup closer to the theoretical melting temperature would be required in these cases to retain a sufficient amount of crystal during the entire Interface Pinning calculation. Due to the high computational effort, this was not done in the course of demonstrating this approach for calculating the interface mobility. Table 3.1 lists the calculated mobilities for Na and Si. The given statistical 95% confidence intervals were estimated by splitting the trajectory in blocks of equal size, sufficiently large to be considered independent and fitting A and τ in for each block. Note that the trajectory was too short that each block exhibited the full variance of the order parameter $k_\mathrm{B}T/\kappa$. Assuming that the

terminal relaxation of the autocorrelation is faster than and independent of the exploration of the full variance of the order parameter, the sample variance σ_Q^2 was used instead of the infinite time variance $k_\mathrm{B}T/\kappa$ for estimating τ and A:

$$\langle \delta Q(0), \delta Q(t) \rangle' = \sigma_Q^2 A \mathrm{e}^{-t/\tau}.$$

3.6 Summary and discussion

Interface Pinning is a direct method for computing the Gibbs free energy difference between the liquid and the crystalline phase at a given temperature and pressure. In turn, state points of coexistence can be estimated assuming the same latent entropy and latent volume at the coexistence point and at the state point simulated. Interface Pinning brings the two phases in contact, such that there is a liquid and a crystalline slab in the hydrostatic Np_zT ensemble, where only the z direction perpendicular to the interface is allowed to vary. A bias potential, coupled to an order parameter linear in the number of crystalline atoms, keeps the two phase system in equilibrium allowing the simulation to be conducted *ad-infinitum*. From a single simulation of the two phase system, the difference in the Gibbs free energy can be retrieved by comparing the average order parameter to the desired order parameter where the bias potential is vanishes. If the average order parameter is for instance below the desired order parameter, the liquid phase is preferred and the melting temperature is below the simulation temperature.

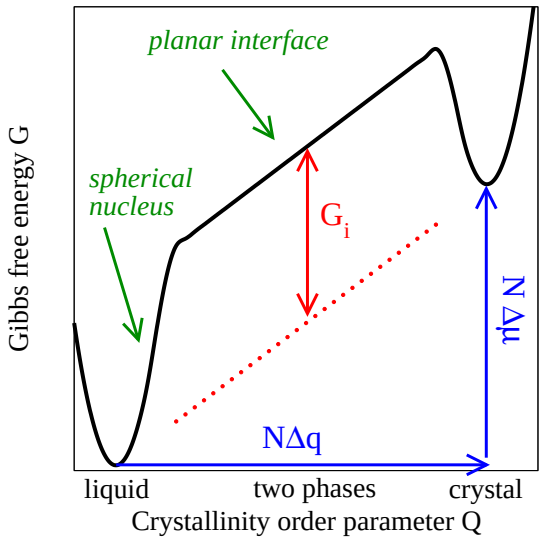

Compared to umbrella sampling or meta dynamics, Interface Pinning does not require one reaction coordinate along the entire liquid to crystal transition. It is sufficient to have an order parameter linear in the number of crystalline atoms when the planar interface is already fully formed. Interface pinning merely determines the slope $\Delta\mu/\Delta q$ of the free energy $G(Q)$ as a function of the order parameter Q at the average order parameter $\langle Q \rangle'$ in the biased dynamics. To calculate $\Delta\mu$, Interface Pinning relies on the fact that the free energy invested in the formation of the two planar interfaces starting from the fully liquid phase equals the free energy gain when this interface is finally dissolved in the fully solid phase, as indicated in the figure below. Furthermore, the free energy of the interface is assumed constant over the

whole range where a planar interface exists, which is validated up to statistical inaccuracies in Pedersen 2013.

Interface Pinning directly yields the Gibbs free energy difference between the phases of interest. Indirect methods, such as thermodynamic integration, require a common starting system to integrate from, for instance the ideal gas, and they arrive at two free energies, one for the liquid and one for the solid. The free energy difference is therefore subject to the sum of the statistical inaccuracies of both quantities. Interface Pinning can also be used for solid-solid transitions, by calculating the free energy differences of each solid phase to the liquid phase. Clearly, Interface Pinning is also subject to the sum of statistical inaccuracies in this case. Furthermore, indirect methods are not required to host an interface, which requires space. Their finite size errors are therefore smaller for the same number of simulated atoms. The equilibration times without an interface are also shorter since there are no slow fluctuations due to the growth and shrinking of the crystal. Finally, an Interface Pinning calculation requires one single simulation of $2N$ atoms, while indirect methods conduct two calculations of N atoms for comparable finite size effects. If the computation time scales worse than linear with the number of atoms, as for instance in DFT, an Interface Pinning calculation will be more expensive. However, although the computation time may be longer, Interface Pinning requires less human time, which is useful for (semi) automatic mapping of the phase diagram.

The slow fluctuations from growing and shrinking of the amount of crystal provide additional information on the interface mobility M in the direction perpendicular to the interface. The mobility is inversely proportional to the energy loss when freezing or melting at finite speed, rather than adiabatically slow. Although the interface mobility can be calculated *a posteriori* from the terminal relaxation behavior of the autocorrelation function of the order parameter Q, this is only applicable if the time scales of the crystal fluctuations are sufficiently distinct from other time scales, such as thermal vibrations and time scales of the thermo- and barostat. This often requires tuning of the bias strength κ after a considerable simulation time. Estimating M from fluctuation quantities also bears considerable statistical inaccuracies for trajectory lengths achievable by *ab-initio* calculations. Still, the presented results are the first interface mobilities calculated from *ab-initio* simulations for the given elements. In Pedersen, Hummel, and Dellago 2015 Interface Pinning is also compared to other methods for calculating the interface mobility.

To improve the accuracy of the Interface Pinning method for calculating the interface mobility, a driven dynamics could be applied by a bias potential with a time dependent desired order parameter:

$$U'(\mathbf{R}) = U(\mathbf{R}) + \frac{\kappa}{2}\left(Q(\mathbf{R}) - a(t)\right)^2,$$

where $a(t) = a_0 + a_1 \cos(\omega t)$. This bias potential drives the crystal growth directly, such that one does not have to rely on fluctuations to retrieve information on dissipative quantities, much like an alternating current probing an electric circuit. However, this gives yet another time scale to choose and it needs to be tested regarding its accuracy and applicability.

Chapter 4

Isomorphs in metal melts

A system that can exchange heat and particles with the environment is in equilibrium if the average energy per degree of freedom and the average energy density are constant throughout the system, i.e. temperature and pressure are constant. For each temperature T and pressure p a given substance exhibits a thermodynamically stable phase as the phase with the lowest Gibbs free energy. The whole map of stable phases is referred to as *phase diagram*. It usually comprises a solid, a liquid and a gaseous phase at temperatures below the ionization energy of the considered atoms.

Distinct states point usually exhibit distinct properties, such as the distribution of the inter atomic distances. In the liquid phase the properties vary continuously dependent on both, temperature and pressure. However, some liquids exhibit scale invariance where there are distinct state points in the phase diagram that can be transformed into each other solely by rescaling length and time scales. Such states are referred to as as *isomorphic* and they are thermodynamically identical for most properties differing only by the choice of units (Gnan et al. 2009). The equivalence of such states reduces the effective dimension of the phase diagram by one dimension. Instead of temperature and pressure it is sufficient to know which equivalence class a state belongs to or – in other words – on which isomorph it lies. Figure 4.1 demonstrates that the radial distribution function and the mean square displacements of liquid magnesium is almost equivalent for isomorphic states. They can be compared in dimensionless reduced units as specified in the plots.

Liquids that show such a scale invariance are called *(Roskilde) simple liquids*. A scale invariance at higher pressures is already suggested by the Grüneisen equation of states, relating temperature and pressure. At ambient pressure, scale invariance is motivated by melting or freezing rules involving relative length or time scales, such as the Lindemann melting criterion, stating that melting occurs when the vibrational atomic displacement reaches about 10% of the inter atomic distance (Gilvarry 1956). Pedersen, Schrøder, and Dyre 2010 conjecture that van der Waals bonded liquids and metal melts are simple liquids also at the triple point. Experimentally, this conjecture is hard to test as it requires to scan the phase diagram in a wide range of pressures comparing quantities such as the heat capacity, the radial distribution function and the self diffusion constant. In a molecular dynamics (MD) simulation, however, the degree of simplicity can be directly calculated from the fluctuations of the virial. An *ab-initio* study of 58 elements, conducted in the scope of this work, indicates that most metal melts are indeed simple to a considerable degree, at least at the level of DFT. Section 4.3 gives details on this study. Its results will be used as examples throughout this chapter.

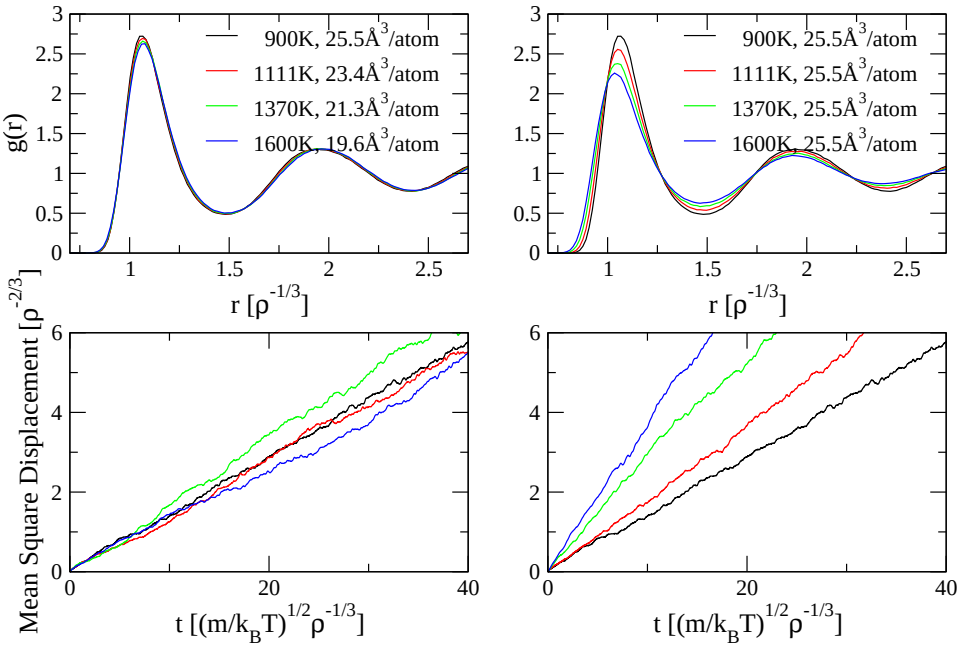

Figure 4.1: Comparison between isomorphic and isochoric states of magnesium. The radial distribution function on the top panels and the mean square displacement on the bottom panels are compared in reduced units, as indicated on the axes. The scale invariance can clearly be seen for state points on the isomorph shown on the left panels.

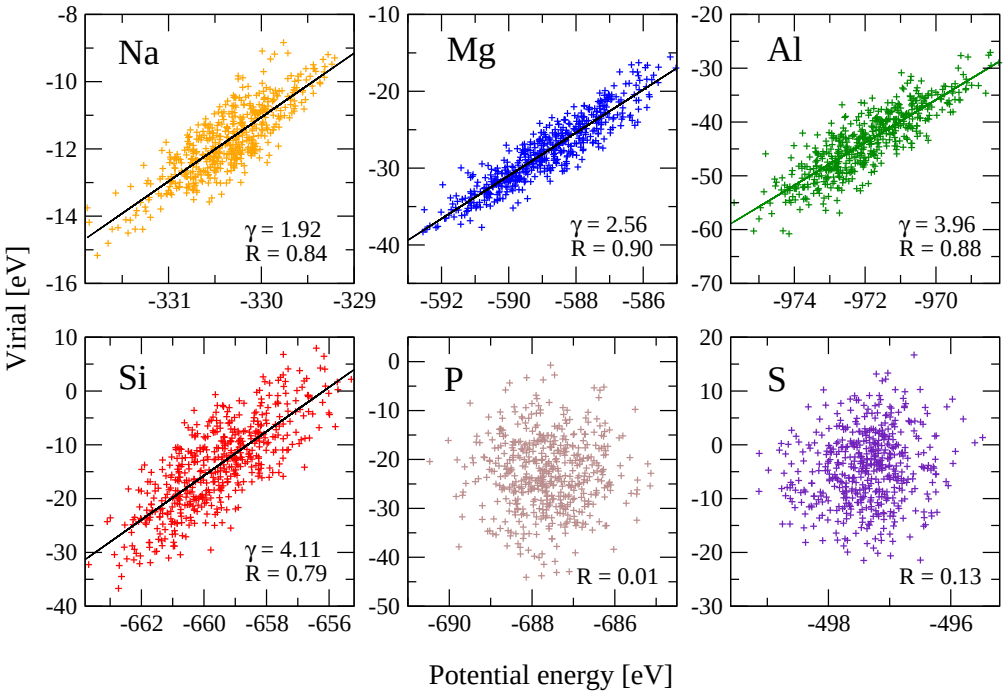

Figure 4.2: Correlation between the fluctuations of the virial W and the potential energy U. The metallic elements show a strong correlations and therefore exhibit isomorphic states.

4.1 Isomorphs

From now on, we will use density and temperature as state point coordinates since it directly reflects scale invariance features of the potential energy landscape $U(\mathbf{R})$, mapping lengths to energies. We will also give the density on the abscissa since it corresponds to the scaling of the argument of $U(\mathbf{R})$. Let us first assume that the potential energy landscape $U(\mathbf{R})$ is a homogeneous function

$$U(\mathbf{R}/\alpha) = \alpha^{3\gamma} U(\mathbf{R}).$$

I.e. a density scaling by the factor $\beta = \alpha^3$ scales the energy by the factor β^γ for all configurations and factors. In this case, we can scale the temperature by β^γ to arrive at the same Boltzmann factor for an arbitrary configuration compared to the unscaled case:

$$\exp\left(-\frac{U(\mathbf{R}\beta^{-1/3})}{k_\mathrm{B}T\beta^\gamma}\right) = \exp\left(-\frac{U(\mathbf{R})}{k_\mathrm{B}T}\right).$$

Since the Boltzmann factors are the same for the scaled and for the unscaled system they exhibit the same thermodynamical properties when translating units of length and energy of the scaled system accordingly. Thus, all states (ρ, T) with

$$\frac{T}{\rho^\gamma} = \text{const.}, \quad \text{with } \rho = \frac{N}{V} \tag{4.1}$$

are identical modulo the respective choice of units. The curve defined by this equation for each value on the right hand side is called *isomorph* and the exponent γ is solely a feature of the potential energy landscape $U(\mathbf{R})$ and independent of the state point.

Next, we generalize the condition on the potential energy surface, assuming only that the density and the coordinates are separable:

$$U(\mathbf{R}) = h(\rho)\tilde{\Phi}(\tilde{\mathbf{R}}) + Ng(\rho). \tag{4.2}$$

The entire density ρ now assumes the role of the density scaling factor β of the previous example and the dimensionless configuration $\tilde{\mathbf{R}} = \mathbf{R}\rho^{1/3}$ takes the role of the unscaled configuration. The intensive functions $h(\rho)$ and $g(\rho)$ have both the dimension of an energy, while $\tilde{\Phi}(\tilde{\mathbf{R}})$ is dimensionless, involving no lengths or energies. Instead of one global scaling exponent γ, as in the case of a homogeneous function, we can define a local scaling exponent $\gamma(\rho)$ by the logarithmic derivative of $h(\rho)$:

$$\gamma(\rho) = \frac{\mathrm{d}\log h(\rho)}{\mathrm{d}\log\rho}. \tag{4.3}$$

The concept of isomorphs still holds in the case of general functions $h(\rho)$ although not to the full degree as in the case of $h(\rho) = \rho^\gamma$ (Dyre 2014). The curves along which thermodynamic properties are invariant to a good degree are given locally by the slope

$$\frac{\mathrm{d}\log T}{\mathrm{d}\log\rho} = \gamma(\rho). \tag{4.4}$$

4.1.1 Energy-virial fluctuations

The pressure p can be split into a kinetic and a potential part

$$pV = Nk_{\mathrm{B}}T + W,$$

where $W(\mathbf{R})$ is the *virial*, given by[1]

$$W(\mathbf{R}) = -V\,\frac{\partial U(\tilde{\mathbf{R}}\rho^{-1/3})}{\partial V}.$$

At constant volume and temperature the instantaneous potential energy $U(\mathbf{R})$ and the instantaneous virial $W(\mathbf{R})$ fluctuate around their respective average value. Gnan et al. 2009 show that the existence of isomorphs is equivalent to correlated fluctuations of the instantaneous potential energy $U(\mathbf{R})$ and the instantaneous virial $W(\mathbf{R})$ at constant volume:

$$\delta W(\mathbf{R}) = \gamma\,\delta U(\mathbf{R}), \tag{4.5}$$

where $\delta A(\mathbf{R}) = A(\mathbf{R}) - \langle A\rangle$ and γ is the density scaling exponent defining the logarithmic slope of the isomorph according to (4.4). While a change of the average potential energy is correlated to a change of the average virial when changing the density, this is not necessarily the case for the respective *fluctuations* at constant volume. Dangling atoms on molecules, for instance, hardly contribute to the virial fluctuations while they do contribute to the potential energy fluctuations, lowering the correlation between them. Indeed, such atoms introduce their bond length as a characteristic length scale to the system, breaking the scale invariance (Bailey et al. 2008).

To which degree a given potential energy landscape exhibits scale invariance can be quantified by the correlation coefficient R of the virial and the potential energy fluctuations, given by

$$R = \frac{\langle \delta W(\mathbf{R})\delta U(\mathbf{R})\rangle}{\sqrt{\langle \delta W^2(\mathbf{R})\rangle\,\langle \delta U^2(\mathbf{R})\rangle}}, \tag{4.6}$$

where $\langle . \rangle$ denotes the average in the NVT ensemble. If the fluctuations are not fully correlated the isomorphic behavior will only be approximate. The density scaling exponent γ can still be estimated by the slope of the linear regression

$$\gamma = \frac{\langle \delta W(\mathbf{R})\delta U(\mathbf{R})\rangle}{\langle \delta U^2(\mathbf{R})\rangle}. \tag{4.7}$$

Figure 4.2 plots the instantaneous virial over the instantaneous potential energy for configurations $\mathbf{R}$ from a trajectory of about 10 ps in an NVT calculation. For the metallic elements a clear correlation is visible and the density scaling exponent $\gamma = \mathrm{d}\log T/\mathrm{d}\log\rho$, specifying the logarithmic slope of the isomorph, can be directly retrieved at the simulated state point (ρ, T).

[1] Note that the potential energy could be explicitly dependent on the volume V if the system is not fully described by the configuration $\mathbf{R}$. In principle, this is the case for electronic structure calculation, however, we omit this dependence for simplicity.

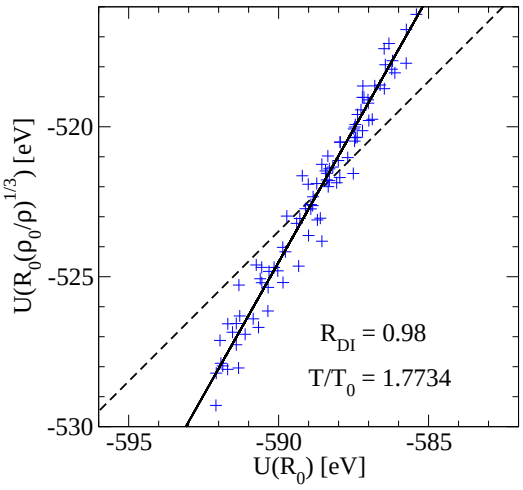

Figure 4.3: Calculating isomorphic temperatures: the ratio T/T_0 follows from the ratio of the fluctuations of the potential energy of the scaled and unscaled configurations.

4.1.2 Direct isomorph check

How can we find isomorphic state points to a given reference state point (ρ_0, T_0)? Unless $U(\mathbf{R})$ is a homogeneous function, the density scaling exponent γ, found from the fluctuations of W and U is state point dependent and only specifies the local logarithmic slope of the isomorph. Thus, an estimate of T according to (4.1) is only accurate to first order for a finite density change to a chosen density ρ. However, we can directly relate the Boltzmann factors at the two densities. First, we take configurations $\mathbf{R}_0$ from the reference state point (ρ_0, T_0) and scale them to the chosen density ρ. If the system exhibit isomorphs, the fluctuations of the scaled potential energy $U\left(\mathbf{R}_0(\rho_0/\rho)^{1/3}\right)$ are correlated with the fluctuations of the potential energy at the reference state $U(\mathbf{R}_0)$. Figure 4.3 demonstrates this correlation of 100 independent configurations of magnesium at the DFT triple point (ρ_0, T_0), scaled to a density ρ, 30% above ρ_0. The ratio of the temperatures T/T_0 follows from the ratio of the fluctuations of the potential energy to yield proportional Boltzmann factors.

This procedure is referred to as *direct isomorph check* and the correlation coefficient R_{DI} between the scaled and the unscaled potential energies is related to the correlation coefficient R between the fluctuations of the virial W and the potential energy U to first order by: (Gnan et al. 2009)

$$\frac{1}{R_{\mathrm{DI}}} - 1 = \left(\frac{1}{R} - 1\right) \log^2\left(\frac{T}{T_0}\right).$$

The isomorphic state points in Figure 4.1 were found according to this procedure for a density increase of 9%, 20% and 30% relative to the DFT triple point of magnesium, listed in Table 4.2. At these state points thermodynamic properties such as the radial distribution function can be directly compared to each other when they are transformed to common units.

4.1.3 The solid-liquid coexistence line

Albrechtsen et al. 2014 show that the logarithmic derivative of the melting temperature with respect to the density is identical to the density scaling exponent $\gamma(\rho)$, making the melting

	R	$\gamma(\rho)$	$\mathrm{d}\log T_\mathrm{m}/\mathrm{d}\rho$
Na	0.84 ± 0.02	1.9 ± 0.1	1.8 ± 0.5
Mg	0.90 ± 0.01	2.6 ± 0.2	2.6 ± 0.5
Al	0.88 ± 0.05	4.0 ± 0.2	4.6 ± 0.8

Table 4.1: The density scaling exponent $\gamma(\rho)$ of the isomorph at the melting point compared to the scaling exponent of the melting line, $\mathrm{d}\log T_\mathrm{m}/\mathrm{d}\log\rho$, calculated by Interface Pinning using the Clausius–Clapeyron relation.

line an isomorph. To verify this directly, $\mathrm{d}\log T_\mathrm{m}/\mathrm{d}\log\rho$ was calculated from the slope of the melting line $\mathrm{d}T_\mathrm{m}/\mathrm{d}p$, retrieved from the Interface Pinning results of Table 3.1. The two scaling exponents are compared in Table 4.1. Thus, the melting line can be traced over a wide range of densities following the isomorph from a state point on the melting line. For any given density, the isomorphic temperature can be found as described in the previous subsection. This provides a good initial guess for the melting temperature as input for further melting temperature calculations and should significantly accelerate mapping the melting line in the phase diagram of simple liquids, such as iron.

4.2 The Inverse Power Law ansatz

Let us consider a system where the potential energy is given by a repulsive inverse power law (IPL)

$$U_\mathrm{IPL}(\mathbf{R}) = \frac{k_\mathrm{B}T}{\rho^\gamma}\sum_{i<j}\left(\frac{\sigma}{r_{ij}}\right)^{3\gamma} + Ng(\rho), \tag{4.8}$$

with r_{ij} denoting the distance between the atoms i and j. The dimensionless constants σ and γ specify strength and the steepness of the repulsive part of the potential. This system exhibits fully correlated fluctuations of the virial and the potential energy. The scaling exponent is given by γ and it is independent of the density. The isomorphs are curves of constant T/ρ^γ.

The IPL potential is among the simplest potentials to study on the computer allowing for extensive studies of thermodynamic properties including solid-solid phase boundaries. The question is, how well can a real liquid be described by a potential with merely two parameters. This can be addressed by fitting the parameters σ and γ to best reproduce the fluctuations of a studied liquid at constant volume. The scaling exponent γ can be directly retrieved from the fluctuations of the virial and the potential energy, given in (4.7). The parameter σ can be fitted by relating the variance of $U_\mathrm{IPL}(\mathbf{R})$ to the variance of the true potential energy $U(\mathbf{R})$ of the system. Thus, σ is estimated such that

$$\left\langle \delta U^2(\mathbf{R})\right\rangle = \left(\frac{k_\mathrm{B}T}{\rho^\gamma}\sigma^{3\gamma}\right)^2 \left\langle \delta S^2(\mathbf{R})\right\rangle, \tag{4.9}$$

where $S(\mathbf{R}) = \sum_{i<j} r_{ij}^{-3\gamma}$. Figure 4.4(a) compares radial distribution functions of Na, Mg and Al, obtained from the DFT NVT molecular dynamics and obtained from a molecular dynamics solely using the fitted inverse power law. As demonstrated, the structure is represented well for these elements by an IPL in the liquid phase. Figure 4.4(b) shows the correlation between the DFT potential energy $U(\mathbf{R})$ and the fitted inverse power law $U_\mathrm{IPL}(\mathbf{R})$ of magnesium for

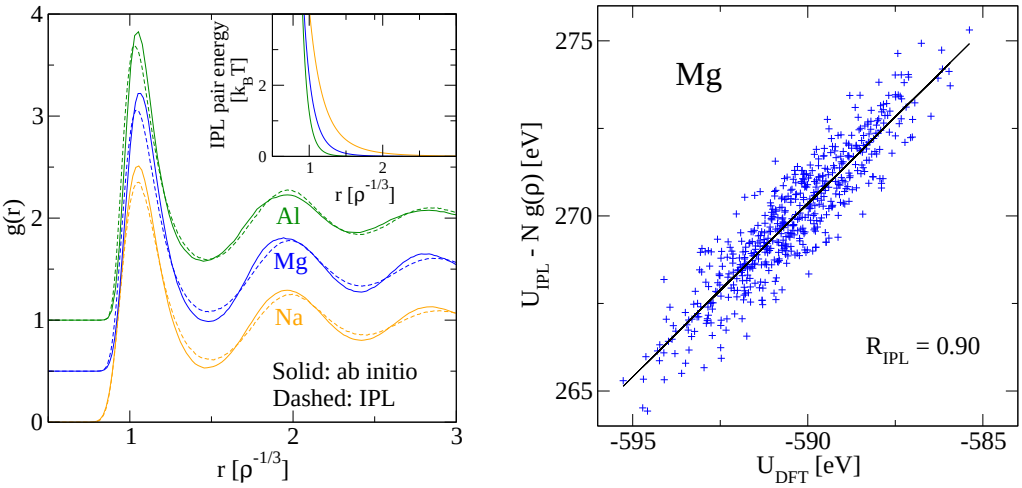

Figure 4.4: (a) Radial distribution functions of IPL liquids compared to the DFT liquids. The IPL parameter σ and γ were retrieved from Table 4.2. The inset shows the steepness of the repulsive pair potential for the different elements. (b) Correlation between the potential energies of DFT and IPL for configurations from a DFT molecular dynamics calculation.

configurations $\mathbf{R}$ from the DFT molecular dynamics trajectory. The correlation coefficient R_{IPL} can be used as a measure for how well the DFT constant volume dynamics is described by a simple inverse power law.

Table 4.2 lists the fitted parameters for all studied elements that have sufficiently strong W and U correlation, allowing to estimate γ according to (4.7), along with the correlation coefficient R_{IPL} between the DFT and the IPL potential energies. A high IPL correlation coefficient R_{IPL} implies a high correlation coefficient R between the virial and potential energy fluctuations, since a liquid that is well described by an inverse power law exhibits isomorphs. The converse case does not need to hold. However, at least at the level of Density Functional Theory no liquids were found that exhibit isomorphs but are not well described by an IPL at constant volume.

4.2.1 Predicting the crystal structure from the liquid

For the considered simple liquids, the potential energy, containing complex many-body interactions, can be well approximated by an inverse power law, at least in the liquid phase. Travesset 2014 calculated that at the triple point, an inverse power law liquid crystallizes into a body centered cubic structure if the scaling exponent γ is below ≈ 2.5. Above this limit the IPL potential is sufficiently hard that the liquid crystallizes into a close packed structure, fcc or hcp. Can this limit be applied to the scaling exponents γ, found from the fluctuations of the virial and the potential energy in the liquid phase? This question was addressed previously by Hoover 1972 and can be answered quite extensively with the calculations conducted at the level of Density Functional Theory. Figure 4.5 colors all simple liquids according to whether the scaling exponent γ predicts the correct experimental crystal structure at the triple point or not. The experimental structures were retrieved from Grimvall 2012; Tonkov and Ponya-

H																	He
Li	Be											B	C	N	O	F	Ne
Na	Mg											Al	Si	P	S	Cl	Ar
K	Ca	Sc	Ti	V	Cr	Mn	Fe	Co	Ni	Cu	Zn	Ga	Ge	As	Se	Br	Kr
Rb	Sr	Y	Zr	Nb	Mo	Tc	Ru	Rh	Pd	Ag	Cd	In	Sn	Sb	Te	I	Xe
Cs	Ba	La	Hf	Ta	W	Re	Os	Ir	Pt	Au	Hg	Tl	Pb	Bi	Po	At	Rn

Figure 4.5: Green elements have a crystal structure at the triple point predicted by assuming inverse power law interactions with parameters fitted from the DFT liquid. The distorted hcp crystal structures of Zn and Cd cannot be predicted by IPL, however a close packed structure is correctly prediced. All colored elements exhibit isomorphs.

tovsky 2005; Barrat and Hansen 2003. They are given in the Periodic Table of Simple Liquids in Appendix A.

4.3 Isomorph properties of 58 elements

Which liquids do exhibit isomorphs and are therefore simple and which do not? At high pressures, all atoms are close enough to interact with all neighbors. Thermal vibrations leading to fluctuations of the potential energy also lead to correlated fluctuations of the virial and make the liquid simple. At lower pressures there is no such simple reason. Bailey et al. 2008 found that Lennard-Jones type liquids exhibit isomorphs also close to the triple point, such that van der Waals bonded liquids are expected to be simple throughout the entire pressure range. Water, on the other hand, is not simple at low pressures where hydrogen bonds can form small chains breaking the scale invariance. Empirical melting and freezing rules suggest that metal melts are simple liquids also at low pressures. Pedersen et al. 2008 have shown that pure copper, as well as a magnesium alloy exhibit isomorphs according to the Effective Medium Approximation. While this approximation does not assume pair potentials, it still makes assumptions on the potential energy landscape.

An *ab-initio* calculation makes no such assumptions, describing the complex many-body interactions of the atoms at a quantum-mechanical level. Although Density Functional Theory is also a mean field theory, it applies its approximation at the level of single electrons rather than atoms. DFT provides accurate predictions of crystal structures, densities and melting points for a broad range of materials. In this work, the monatomic liquids of 58 elements have been studied at a state point close to the triple point. The degree of simplicity at that state point can be directly found from the fluctuations of the virial and the potential energy in an NVT calculation according to (4.7). Elements, where DFT is not expected to be accurate enough were not studied. This includes noble gas and dimer forming liquids, where van der Waals interactions are relevant. For heavy elements, such as mercury, DFT is also not expected to provide an accurate description due to missing treatment of relativistic effects beyond the contraction of the core electrons (Calvo et al. 2013). They are still provided for later reference.

The calculations were conducted using the Vienna Ab-initio Simulation Package (`VASP`) employing the projector augmented wave (PAW) method with the frozen-core assumption and the Perdew-Burke-Enzerhof exchange-correlation functional optimized for solids (PBEsol) (Kresse and Furthmüller 1996; Blöchl 1994; Perdew et al. 2008). Dispersion corrections were not included, but they are not expected to be important for metals near the melting point (Pedersen et al. 2013). Constant temperature was obtained with the Langevin thermostat with a coupling time of 1 ps. The initial equilibration trajectories cover between 9 to 24 ps corresponding to several structural relaxation times. The number of atoms contained in the periodic simulation cell is listed in Table 4.2. In most cases 125 atoms were used. Table 4.2 also contains the electronic configurations of the calculated electrons of the employed potentials as well as the cutoff energy of the plane wave basis set. All calculations were done non-spin polarized and at the Γ point only. Statistical uncertainties were estimated by dividing the MD trajectories into statistically independent blocks.

4.3.1 Determining the DFT triple point

The correlations between the virial and the potential energy are expected to increase at increasing pressure. This is discussed by Weeks, Chandler, and Andersen 1971 and demonstrated for phosphorus in Subsection 4.3.2. Thus, a liquid exhibiting isomorphic states already at the triple point is expected to be simple throughout the entire liquid phase, making the triple point the most reasonable state point for an *ab-initio* study. The theoretical triple point of DFT is difficult to locate, however, the pressure and temperature dependence of the correlation coefficient R is low as long as the pressure is high enough to form a liquid. Therefore the DFT triple point was estimated by performing an NpT computation at a state point close to, but slightly above, the experimental melting temperature and at ambient pressure. Constant pressure was realized with the barostat proposed by Parrinello and Rahman 1981 with a fictitious mass of 100 atomic units and a thermal coupling time of 1/3 ps. The finite cutoff of the plane wave basis set requires the exertion of an additional pressure to compensate for the missing basis set functions. This pressure is referred to as *Pulay stress* and it was estimated in a separate calculation.

If the system froze at the initially chosen temperature, for instance due to finite size effects, the temperature was risen until the system stayed liquid throughout the entire trajectory. For some systems, such as Ti, Ga, Sn and Hg the temperature had to be risen significantly compared to the experimental melting temperature. However, only a small temperature dependence of R was found in this temperature range. For Mn, Fe and Co the computed melting density was 25%, 16% and 15% higher than the experimental density. The reason for this is to be investigated in the future. Simulations of these elements at experimental density exhibited cavities between the atoms. Table 4.2 lists the state points (ρ, T) found for all studied elements and the average pressure p during the subsequent constant volume calculation, which is within the accuracy of DFT of about 2 GPa.

4.3.2 Elevated pressure behavior

Phosphorus does not exhibit strong correlations between the virial and potential energy fluctuations making it a non-simple liquid. The tetrahedral P_4 molecules, present in the liquid, introduce a typical length scale breaking the scale invariance. At elevated pressures the repulsive forces become more and more dominant increasing the correlations between W and U

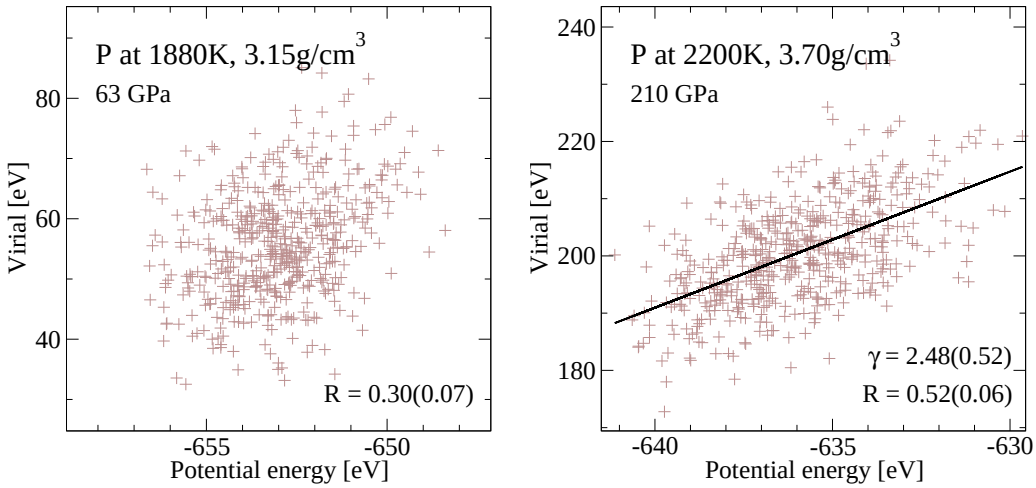

Figure 4.6: Phosphorus is not a simple liquid close to the triple point. At elevated pressures and temperatures, however, the virial and potential energy fluctuations become more and more correlated.

as demonstrated in Figure 4.6 for two state points. The temperatures had to be risen to keep the system sufficiently liquid.

4.3.3 Dependence on the exchange-correlation functional

For metals the correlation coefficient between the virial and the potential energy fluctuations hardly depends on whether the Local Density Approximation (LDA) or the Perdew-Burke-Enzerhof exchange-correlation functional is employed. For silicon or other semiconductors, however, LDA yields lower correlations than PBEsol, used throughout this survey.

4.4 Summary and discussion

Simple liquids posses distinct state points in the phase diagram that can be transformed into each other to a good approximation by the choice of units. When increasing the density, the fluctuations of the potential energy $U(\mathbf{R})$ also increase. Rising the temperature accordingly yields Boltzmann factors that are proportional to those of the original state point. Thus, scaling the units of length and energy accordingly transforms the two states points into each other. States that can be transformed into each other lie on curves called isomorphs, along which structure, dynamics and some thermodynamic properties, such as the excess entropy S_{ex}, are invariant in reduced units.

A liquid is simple if and only if the fluctuations of the instantaneous virial $W(\mathbf{R})$ and the instantaneous potential energy $U(\mathbf{R})$ are correlated at constant volume and temperature. The correlation coefficient states to which degree a liquid exhibits isomorphic state points and can be readily retrieved from a molecular dynamics calculation at a single state point. Experimentally, the instantaneous potential energy and the instantaneous virial are not accessible. The degree of simplicity can only be assessed by comparing quantities, such as the radial distribution function and the self diffusion constant over a wide range of pressures, which is hard to

Element	N	Electrons	$E_{\max}$ [eV]	T [exp.] [K]	ρ [exp.] [g/cm^3]	p [GPa]	R	γ	σ	R_{IPL}
3 Li	256	$2s^1$	140.0	470 [454]	0.534 [0.512]	0.29	0.72(0.04)	1.0(0.1)	2.03(0.27)	0.75(0.04)
4 Be	125	$2s^2$	308.8	1850 [1560]	1.570 [1.690]	-0.27	0.75(0.03)	1.8(0.3)	1.16(0.09)	0.50(0.13)
5 B	125	$2s^2 2p^1$	318.6	2400 [2349]	2.245 [2.08]	-1.69	0.10(0.12)	—	—	—
6 C	125	$2s^2 2p^2$	273.9	6000 [4800]	1.514 [1.37]	-1.04	-0.04(0.18)	—	—	—
11 Na	250	$3s^1$	62.1	370 [371]	0.941 [0.927]	-0.02	0.84(0.02)	1.9(0.1)	1.25(0.05)	0.89(0.01)
12 Mg	384	$3s^2$	98.5	900 [923]	1.581 [1.584]	0.07	0.90(0.01)	2.6(0.2)	1.13(0.03)	0.83(0.08)
13 Al	256	$3s^2 3p^1$	116.4	1000 [933]	2.352 [2.375]	-0.27	0.88(0.05)	4.0(0.2)	1.02(0.01)	0.91(0.02)
14 Si	125	$3s^2 3p^2$	245.3	1700 [1687]	2.827 [2.57]	0.51	0.79(0.03)	4.1(0.2)	0.94(0.02)	0.79(0.04)
15 P	125	$3s^2 3p^3$	255.0	650 [317]	1.850 [1.74]	-0.43	0.01(0.17)	—	—	—
16 S	125	$3s^2 3p^4$	258.7	550 [388]	1.784 [1.819]	0.07	0.13(0.12)	—	—	—
19 K	125	$3p^6 4s^1$	116.7	350 [337]	0.815 [0.828]	0.07	0.86(0.11)	1.6(0.4)	1.40(0.21)	0.87(0.20)
20 Ca	125	$3p^6 4s^2$	266.6	1200 [1115]	1.378 [1.378]	-0.44	0.80(0.06)	1.9(0.1)	1.20(0.03)	0.83(0.04)
21 Sc	125	$4s^2 3d^1$	154.8	1900 [1814]	2.800 [2.80]	-0.38	0.63(0.24)	1.4(0.5)	1.43(0.56)	0.81(0.19)
22 Ti	125	$4s^2 3d^2$	178.3	3900 [1941]	4.161 [4.11]	-0.48	0.78(0.08)	2.0(0.2)	0.96(0.04)	0.88(0.06)
23 V	125	$3p^6 4s^2 d^3$	263.7	2500 [2183]	5.773 [5.5]	-0.13	0.81(0.07)	2.6(0.6)	1.02(0.12)	0.81(0.05)
24 Cr	125	$3p^6 4s^1 d^5$	265.7	2600 [2180]	6.735 [6.3]	-1.55	0.90(0.04)	3.3(0.9)	0.98(0.07)	0.83(0.07)
25 Mn	125	$4s^2 3d^5$	269.9	2400 [1519]	7.973 [5.95]	0.66	0.93(0.02)	3.6(0.2)	0.95(0.03)	0.72(0.08)
26 Fe	125	$3p^6 4s^2 3d^6$	267.9	2400 [1811]	8.338 [6.98]	0.03	0.95(0.02)	3.6(0.1)	1.00(0.01)	0.90(0.04)
27 Co	125	$4s^2 3d^7$	268.0	1870 [1768]	8.924 [7.75]	0.22	0.93(0.01)	3.5(0.1)	1.06(0.01)	0.94(0.01)
28 Ni	125	$4s^2 3d^8$	269.5	2000 [1728]	8.189 [7.81]	-0.17	0.92(0.03)	3.5(0.3)	1.03(0.02)	0.96(0.02)
29 Cu	125	$4s^1 3d^{10}$	295.4	1480 [1358]	8.020 [8.02]	-0.72	0.90(0.02)	4.1(0.2)	1.01(0.01)	0.94(0.01)
30 Zn	125	$4s^2 3d^{10}$	276.7	760 [693]	6.570 [6.57]	-0.61	0.53(0.12)	3.3(0.9)	1.03(0.04)	0.43(0.17)
31 Ga	125	$4s^2 4p^1$	134.7	500 [303]	5.967 [6.095]	-0.41	0.74(0.09)	3.3(0.5)	1.09(0.04)	0.65(0.09)
32 Ge	125	$4s^2 3d^{10} 4p^2$	310.3	1250 [1211]	5.600 [5.60]	-1.46	0.82(0.15)	4.8(1.1)	0.91(0.02)	0.80(0.15)
33 As	125	$4s^2 4p^3$	208.7	1300 [1090]	5.220 [5.22]	0.58	-0.04(0.08)	—	—	—
34 Se	125	$4s^2 4p^4$	211.6	550 [494]	3.838 [3.99]	0.16	-0.02(0.21)	—	—	—
37 Rb	125	$4p^6 5s^1$	121.9	340 [312]	1.460 [1.46]	0.01	0.80(0.03)	2.3(0.6)	1.12(0.16)	0.91(0.02)
38 Sr	125	$4s^2 4p^6 5s^2$	229.4	1100 [1050]	2.375 [2.375]	-0.24	0.88(0.14)	1.9(0.7)	1.19(0.22)	0.89(0.14)
39 Y	125	$4s^2 4p^6 5s^2 4d^1$	202.6	1850 [1799]	4.359 [4.24]	-0.47	0.60(0.09)	1.3(0.2)	1.47(0.25)	0.82(0.07)
40 Zr	125	$4s^2 4p^6 5s^2 4d^2$	229.9	2500 [2128]	6.305 [5.8]	0.01	0.82(0.07)	2.2(0.5)	1.13(0.11)	0.93(0.03)
41 Nb	125	$4p^6 5s^1 4d^4$	208.6	2900 [2750]	7.669	0.96	0.89(0.04)	3.2(0.2)	1.01(0.02)	0.91(0.01)
42 Mo	125	$5s^1 4d^5$	224.6	3000 [2896]	9.330 [9.33]	0.42	0.89(0.03)	3.2(0.4)	0.98(0.04)	0.77(0.10)
43 Tc	125	$5s^2 4d^5$	228.7	2500 [2430]	10.606	-0.43	0.87(0.09)	4.0(0.4)	0.94(0.02)	0.65(0.18)
44 Ru	125	$5s^1 4d^7$	213.3	2800 [2607]	11.200 [10.65]	1.18	0.94(0.05)	4.6(0.5)	0.97(0.02)	0.85(0.07)
45 Rh	125	$5s^1 4d^8$	229.0	2400 [2237]	10.807 [10.7]	-1.86	0.88(0.07)	5.2(0.4)	0.96(0.01)	0.89(0.03)
46 Pd	125	$5s^1 4d^9$	250.9	1900 [1828]	10.380 [10.38]	-1.32	0.92(0.04)	4.9(0.5)	0.98(0.01)	0.94(0.01)
47 Ag	125	$5s^1 4d^{10}$	249.8	1350 [1235]	9.320 [9.320]	0.98	0.90(0.03)	4.8(0.4)	1.00(0.01)	0.96(0.01)
48 Cd	125	$5s^2 4d^{10}$	274.3	650 [594]	7.996 [7.996]	0.61	0.78(0.07)	5.5(0.6)	0.99(0.02)	0.84(0.04)
49 In	125	$5s^2 5p^1$	95.9	600 [430]	6.859 [7.02]	0.28	0.90(0.05)	4.2(0.5)	1.02(0.04)	0.88(0.08)
50 Sn	125	$5s^2 5p^2$	103.2	900 [505]	6.685 [6.99]	-0.89	0.88(0.06)	4.7(0.9)	0.99(0.03)	0.83(0.04)
51 Sb	125	$5s^2 5p^3$	172.1	950 [904]	6.530 [6.53]	0.68	0.40(0.15)	3.0(1.7)	1.03(0.33)	0.41(0.09)
52 Te	125	$5s^2 5p^4$	175.0	750 [723]	5.700 [5.70]	-0.64	0.03(0.22)	—	—	—
55 Cs	125	$5s^2 5p^6 6s^1$	220.3	330 [302]	1.826 [1.843]	0.04	0.90(0.22)	1.7(0.6)	1.33(0.77)	0.96(0.45)
56 Ba	125	$5s^2 5p^6 6s^2$	187.2	1050 [1000]	3.338 [3.338]	-0.41	0.64(0.24)	1.0(0.4)	1.89(1.15)	0.69(0.29)
57 La	125	$5s^2 5p^6 6s^2 5d^1$	219.3	1280 [1193]	5.940 [5.94]	-1.86	0.72(0.23)	1.7(0.6)	1.25(0.30)	0.86(0.16)
72 Hf	125	$5p^6 6s^2 5d^2$	220.3	2600 [2506]	12.349 [12]	-1.92	0.83(0.03)	2.2(0.3)	1.16(0.07)	0.91(0.02)
73 Ta	125	$5p^6 6s^2 5d^3$	223.7	3450 [3290]	15.000 [15]	0.45	0.90(0.03)	3.3(0.3)	1.02(0.02)	0.91(0.06)
74 W	125	$5p^6 6s^2 5d^4$	223.1	3900 [3695]	16.803 [17.6]	-0.78	0.86(0.08)	3.7(0.6)	0.99(0.03)	0.88(0.06)
75 Re	125	$6s^2 5d^5$	226.2	3650 [3459]	18.787 [18.9]	0.98	0.82(0.09)	4.5(0.7)	0.97(0.02)	0.81(0.10)
76 Os	125	$6s^2 5d^6$	228.0	3450 [3306]	19.741 [20]	0.46	0.86(0.06)	5.1(0.4)	0.97(0.01)	0.85(0.04)
77 Ir	125	$6s^1 5d^8$	210.9	2900 [2719]	19.275 [19]	-0.91	0.71(0.07)	5.1(0.4)	0.96(0.01)	0.83(0.05)
78 Pt	125	$6s^1 5d^9$	230.3	2200 [2041]	18.532 [19.77]	-1.00	0.87(0.06)	6.0(1.4)	0.97(0.02)	0.94(0.03)
79 Au	125	$6s^1 5d^{10}$	229.9	1470 [1337]	16.690 [17.31]	1.06	0.86(0.14)	7.9(1.6)	0.95(0.02)	0.92(0.06)
80 Hg	125	$6s^2 5d^{10}$	233.2	470 [234]	11.917	0.48	0.84(0.13)	4.4(1.9)	1.00(0.07)	0.67(0.19)
81 Tl	125	$6s^2 6p^1$	90.1	600 [577]	11.220 [11.22]	0.53	0.90(0.09)	3.7(0.2)	1.06(0.02)	0.86(0.12)
82 Pb	125	$6s^2 6p^2$	98.0	900 [601]	10.671 [10.66]	0.48	0.90(0.10)	4.1(0.7)	1.03(0.03)	0.94(0.09)
83 Bi	125	$6s^2 6p^3$	105.0	580 [545]	10.050 [10.05]	-0.27	0.10(0.19)	—	—	—
84 Po	125	$6s^2 6p^4$	159.7	850 [527]	9.039	-0.01	0.36(0.21)	2.5(1.7)	1.13(0.40)	0.35(0.23)

Table 4.2: Parameters and results of the liquid elements. The degree of simplicity is characterized by R according to (4.6). The IPL parameters γ, σ are fitted according to (4.7) and (4.9), respectively. Values in parenthesis are the statistical uncertainties corresponding to a confidence interval of 95%. N is the number of atoms in the periodic simulation cell. The electronic configuration of the calculated electrons as well as the plane wave cutoff energies $E_{\max}$ are listed. Experimental values of T and ρ at the triple points are given in square brackets where available (*CRC handbook of chemistry and physics* 2014; Assael et al. 2012; Savvatimskiy 2005; Haaland 1976). In Appendix A the results are also presented in form of a Periodic System.

conduct. In the scope of this work the degree of simplicity has been evaluated for the melts of 58 elements without an assumption on the functional form of the potential energy landscape, such as approximate pair potentials, but rather from a quantum-mechanical description of the chemically active electrons. Density Functional Theory currently provides the best means to do so, and although DFT can only approximate the true electronic behavior, it is expected to provide sufficient accuracy for many elements at the considered temperature.

The calculations show that the majority of the metal melts are simple liquids, while non-metallic liquids, such as phosphorus, are not. As a consequence, melting and freezing rules for metals find a concise explanation. Since the melting line is an isomorph, the structure along the melting line in relative length scales is invariant along the melting line. The Lindemann melting criterion, for instance, states that a crystal melts when the thermal vibrational atomic displacement reaches about 10% of the inter atomic distance[2]. While simplicity does not explain a universal value of 10%, it does predict a constant value along the melting line of the substance.

[2] Note that melting rules require the crystalline phase to be simple. Albrechtsen et al. 2014 show that the simplicity of a crystal follows from that of the liquid.

Part II

The Adjacent Pairs Exchange correction to the Random Phase Approximation

Chapter 5

Many-Body Perturbation Theory

Density Functional Theroy (DFT) calculations are sufficiently accurate for many applications. However, its description of electronic correlation is just approximated locally from the uniform electron gas. It lacks, for instance, non-local effects of the electron-electron interaction, such as Van der Waals forces, where electrostatic repulsion deforms the distribution of electrons and the polarized electron distributions in turn can attract each other. This effect can not be captured by DFT or HF as they only take the instantaneous electrostatic interaction into consideration. The missing descriptions beyond the instantaneous electrostatic interaction is referred to as dynamical correlation (Shavitt and Bartlett 2009).

Static correlation occurs when the single Slater determinant approximation of DFT or HF is not appropriate for the chemical environment *per se*; for instance in the dissociation of H_2^+ when the protons are already at a large distance. The single electron should be in a superposition of two states, quite localized at each respective proton. DFT, however, places one half of an electron on each proton and yields just one orbital spanning both protons.

Perturbation theory expands properties of the exact solution of the Schrödinger equation in terms of the orbitals and orbital energies of the corresponding Hartree-Fock approximation. One can also start from DFT orbitals or from an another reference which can be solved. It is mostly the dynamic correlation that is captured by the perturbation expansion but it can also include some static correlation when going to sufficiently many terms. In cases where the static correlation is large, multi reference perturbation theory may be required. Not unlike a Taylor expansion, a perturbation expansion is not guaranteed to converge or may converge slowly with the number of terms included. The convergence also strongly depends on the quality of the reference state.

We will use time dependent many-body perturbation theory following the derivation of Goldstone 1957 as it is independent of the reference system (DFT or HF) and it is extensive. Extensivity means that for two systems A and B the energy of the combined system equals the sum of the energy of the individual constituents

$$E(AB) = E(A) + E(B),$$

assuming an identical chemical environment. The time dependent formulation of perturbation theory also lends itself naturally to Goldstone diagrams to visualize terms occurring in the perturbation expansion.

Complementary treatments can be found in Kutzelnigg 2009; Lancaster and Blundell 2014; Shavitt and Bartlett 2009; Fetter and Walecka 2003; Coleman 2015.

5.1 Time dependent perturbation theory

In perturbation theory, the exact Hamiltonian is split into the unperturbed part $\hat{H}_0$, that can be solved exactly, and the perturbation $\hat{H}_1$, which contains the full Coulomb electron-electron interaction:

$$\hat{H} = \underbrace{\hat{T} + \hat{V}_{\text{ne}} + \hat{V}_{\text{eff}}}_{\hat{H}_0} + \underbrace{\hat{V}_{\text{ee}} - \hat{V}_{\text{eff}}}_{\hat{H}_1}.$$

$\hat{V}_{\text{eff}}$ is the effective interaction employed by the reference, e.g. the Hartree-Fock approximation. Note that this effective interaction included in $\hat{H}_0$ must be subtracted again by the perturbation to arrive at results of the full Hamiltonian.

Let ψ_p be the spin-orbitals of the unperturbed Hamiltonian of the HF or DFT reference and let $|\Phi\rangle$ denote the Slater determinant of the ground state, where the lowest N states are occupied by the N electrons present in the system. These states are called *unexcited states* while the states that are unoccupied in $|\Phi\rangle$ are called *excited* states. We will use the letters $i, j, k, \ldots$ to label unexcited states, $a, b, c, \ldots$ to label excited states and $p, q, r, \ldots$ to label general states. We can write $|\Phi\rangle$ in second quantization as the result of applying the electron creation operator $\hat{c}_i^\dagger$ for all unexcited states i on the vacuum state, $|\,\rangle$ without any electrons:

$$|\Phi\rangle = \prod_i \hat{c}_i^\dagger \,|\,\rangle = \hat{c}_1^\dagger \ldots \hat{c}_N^\dagger \,|\,\rangle\,.$$

Note that each application of $\hat{c}_i^\dagger$ changes the number of particles. The states of second quantization are elements of the union of all Hilbert spaces of zero particles, one particle, two particles and so forth, which is called *Fock-space*. The beauty of second quantization is that it hides all the tedious footwork of anti-symmetrization in the algebra of the creation and annihilation operators, which is completely given by the anti-commutator relations:

$$\{\hat{c}_p^\dagger, \hat{c}_q^\dagger\} = 0 \qquad \{\hat{c}_p, \hat{c}_q\} = 0 \qquad \{\hat{c}_p^\dagger, \hat{c}_q\} = \delta_{pq}, \tag{5.1}$$

where $\{\hat{A}, \hat{B}\} = \hat{A}\hat{B} + \hat{B}\hat{A}$. One immediate consequence of the these relations is the Pauli exclusion principle disallowing two fermions in the same state:

$$\hat{c}_p^\dagger \hat{c}_p^\dagger \,|\,\rangle = \frac{1}{2}\{\hat{c}_p^\dagger, \hat{c}_p^\dagger\} \,|\,\rangle = 0.$$

Note that the vacuum, $|\,\rangle$ is a state while the number 0 is not.

The Fock-space used for the creation and annihilation operators is spanned by the Slater determinants of the eigenfunctions ψ_p of the unperturbed Hamiltonian $\hat{H}_0$. Therefore, $\hat{H}_0$ is diagonal and given by

$$\hat{H}_0 = \sum_p \varepsilon_p \hat{c}_p^\dagger \hat{c}_p. \tag{5.2}$$

5.1.1 Particle/hole picture

Let us now introduce the particle/hole picture where we want to consider the non-interacting ground state $|\Phi\rangle$ as the new vacuum state instead of the true vacuum, $|\,\rangle$ without any electrons. In this picture, we care about the difference to the non-interacting ground state $|\Phi\rangle$, and we only count excited states that are now occupied called *particles*, and unexcited states that are

no longer occupied called *holes*. While $\hat{c}_a^\dagger$ indeed creates a particle in an excited state, a hole in an unexcited state has to be created by annihilating a formerly occupied state by $\hat{c}_i$. For unexcited states below the Fermi energy the meaning of creation and annihilation has to be reversed. We define the creation and annihilation operators for particles $(\hat{a}^\dagger, \hat{a})$ and for holes $(\hat{i}^\dagger, \hat{i})$:

$$\begin{array}{llll} \hat{a}^\dagger = \hat{c}_a^\dagger & \hat{a} = \hat{c}_a & \text{for} & \varepsilon_a > \varepsilon_\mathrm{F} \\ \hat{i}^\dagger = \hat{c}_i & \hat{i} = \hat{c}_i^\dagger & \text{for} & \varepsilon_i \leq \varepsilon_\mathrm{F} \end{array} \tag{5.3}$$

The anti-commutator relations for these operators follow directly from (5.1) and the only non-vanishing relations are

$$\{\hat{i}^\dagger, \hat{j}\} = \delta_{ij} \qquad \{\hat{a}^\dagger, \hat{b}\} = \delta_{ab}. \tag{5.4}$$

Inserting the particle/hole operators into (5.2) splits the sum over states p into a sum over holes i and a sum over particles a, giving

$$\begin{aligned} \hat{H}_0 &= \sum_i \varepsilon_i \hat{i}\hat{i}^\dagger + \sum_a \varepsilon_a \hat{a}^\dagger \hat{a} \\ &= \underbrace{\sum_i \varepsilon_i}_{=E_0} - \sum_i \varepsilon_i \hat{i}^\dagger \hat{i} + \sum_a \varepsilon_a \hat{a}^\dagger \hat{a}, \end{aligned} \tag{5.5}$$

where we have used the anti-commutator relation to put the operators into normal order, such that all annihilation operators appear on the right.

Next, we need to translate the perturbation $\hat{H}_1$ into the particle/hole formalism. We start with its second quantized representation using the electron creation and annihilation operators $\hat{c}_p^\dagger$ and $\hat{c}_p$:

$$\hat{H}_1 = \frac{1}{2} \sum_{pqrs} V_{sr}^{pq} \hat{c}_p^\dagger \hat{c}_q^\dagger \hat{c}_r \hat{c}_s - \sum_{pq} v_q^p \hat{c}_p^\dagger \hat{c}_q, \tag{5.6}$$

where V_{sr}^{pq} and v_q^p are the matrix elements of the first quantized operators $\hat{V}_\mathrm{ee}$ and $\hat{V}_\mathrm{eff}$, given by

$$V_{sr}^{pq} = \langle pq|\hat{V}_\mathrm{ee}|sr\rangle = \iint \mathrm{d}\mathbf{x}\, \mathrm{d}\mathbf{x}'\, \psi_p^*(\mathbf{x}) \psi_q^*(\mathbf{x}') \frac{1}{|\mathbf{r} - \mathbf{r}'|} \psi_r(\mathbf{x}') \psi_s(\mathbf{x}) \tag{5.7}$$

$$v_q^p = \langle p|\hat{V}_\mathrm{eff}|q\rangle = \int \mathrm{d}\mathbf{x}\, \psi_p^*(\mathbf{x}) \left(\hat{V}_\mathrm{eff} \psi_q\right)(\mathbf{x}), \tag{5.8}$$

with $\int \mathrm{d}\mathbf{x} = \sum_\alpha \int \mathrm{d}\mathbf{r}$. The factor $\frac{1}{2}$ in (5.6) accounts for double counting.

Unfortunately, it is not as straightforward to translate $\hat{H}_1$ into the particle/hole picture as it was for $\hat{H}_0$ since there are now up to 4 different indices that can be either holes or particles. If, for example, p, q, r are particle indices a, c, b and s is a hole index i, $\hat{V}_\mathrm{ee}$ creates the particles a, c and the hole i while it destroys the particle b, as shown in Figure 5.1. The electron creation and annihilation operators $\hat{c}^\dagger$ and $\hat{c}$ always occur in pairs thus keeping the number of electrons constant. However, particle and hole creation and annihilation operators are in general not normal ordered and occur in any constellation. The number of particles and holes is therefore not necessarily constant. Figure 5.1 also shows a particle/hole pair created by the action of $\hat{V}_\mathrm{eff}$ indicated by a shaded circle.

$V_{ib}^{ac}\hat{c}_a^\dagger\hat{c}_c^\dagger\hat{c}_b\hat{c}_i = V_{ib}^{ac}\hat{a}^\dagger\hat{c}^\dagger\hat{b}\hat{i}^\dagger =$ 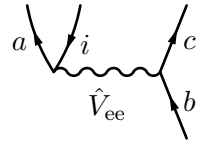

$v_i^a\hat{c}_a^\dagger\hat{c}_i = v_i^a\hat{a}^\dagger\hat{i}^\dagger =$ 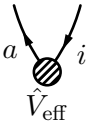

Figure 5.1: Examples of terms occurring in $\hat{H}_1$ and their respective diagrammatic representation

5.1.2 Interaction picture

So far, all operators were given in the Schrödinger picture, where all time evolution takes place in the states ψ_p and the operators are time independent. The Heisenberg picture, on the other hand, keeps the states time independent and all time evolution is put into the operators. In order to do time dependent perturbation theory, it is convenient to use the interaction picture, which is a hybrid of the Schrödinger and the Heisenberg picture. In the interaction picture, the operators evolve according to a time evolution solely based on the unperturbed part of the Hamiltonian $\hat{H}_0$, while the states evolve only due to the action of the perturbation $\hat{H}_1$.

Given a state in the Schrödinger picture $|\Psi(t)\rangle$ we define the corresponding state in the interaction picture $|\Psi_I(t)\rangle$ by "undoing" the time evolution which originates from $\hat{H}_0$:

$$|\Psi_I(t)\rangle = \mathrm{e}^{\mathrm{i}\hat{H}_0 t}\,|\Psi(t)\rangle\,. \tag{5.9}$$

To find the equation of motion for states in the interaction picture we derive with respect to time, yielding

$$\begin{aligned}
\mathrm{i}\frac{\partial}{\partial t}|\Psi_I(t)\rangle &= -\hat{H}_0\mathrm{e}^{\mathrm{i}\hat{H}_0 t}\,|\Psi(t)\rangle + \mathrm{e}^{\mathrm{i}\hat{H}_0 t}\mathrm{i}\frac{\partial}{\partial t}|\Psi(t)\rangle \\
&= -\mathrm{e}^{\mathrm{i}\hat{H}_0 t}\hat{H}_0\,|\Psi(t)\rangle + \mathrm{e}^{\mathrm{i}\hat{H}_0 t}(\hat{H}_0+\hat{H}_1)\,|\Psi(t)\rangle \\
&= \underbrace{\mathrm{e}^{\mathrm{i}\hat{H}_0 t}\hat{H}_1\mathrm{e}^{-\mathrm{i}\hat{H}_0 t}}_{=\hat{H}_{1I}(t)}|\Psi_I(t)\rangle\,.
\end{aligned} \tag{5.10}$$

So the time evolution of $|\Psi_I(t)\rangle$ is determined by the perturbation $\hat{H}_{1I}(t)$ only. The time dependence of $\hat{H}_{1I}(t)$, on the other hand, solely depends on the unperturbed part of the Hamiltonian $\hat{H}_0$. We are now interested in the time evolution operator $\hat{U}_I(t,t_0)$ that evolves a state in the interaction picture from the time t_0 to the time t:

$$\hat{U}_I(t,t_0)\,|\Psi_I(t_0)\rangle = |\Psi_I(t)\rangle\,. \tag{5.11}$$

Operating with $\mathrm{i}\partial/\partial t$ on both sides and using (5.10) gives

$$\mathrm{i}\frac{\partial}{\partial t}\hat{U}_I(t,t_0)\,|\Psi_I(t_0)\rangle = \hat{H}_{1I}(t)\hat{U}_I(t,t_0)\,|\Psi_I(t_0)\rangle\,,$$

which must hold for all $|\Psi_I(t_0)\rangle$ thus leading to the equation of motion for the time evolution operator in the interaction picture

$$\mathrm{i}\frac{\partial}{\partial t}\hat{U}_I(t,t_0) = \hat{H}_{1I}(t)\hat{U}_I(t,t_0). \tag{5.12}$$

Integrating both sides of the above equation with respect to the first argument from t_0 to t yields

$$\hat{U}_I(t,t_0) = 1 - \mathrm{i}\int_{t_0}^{t} \mathrm{d}t'\, \hat{H}_{1I}(t')\hat{U}_I(t',t_0), \tag{5.13}$$

where we have used $\hat{U}_I(t_0,t_0) = 1$, which follows from (5.11). This integral equation can be solved by iteratively applying the above equation to each occurrence of $\hat{U}_I(t',t_0), \hat{U}_I(t'',t_0)$ and so forth, giving

$$\begin{aligned}\hat{U}_I(t,t_0) &= 1 - \mathrm{i}\int_{t_0}^{t} \mathrm{d}t'\, \hat{H}_{1I}(t') + \mathrm{i}^2 \int_{t_0}^{t} \mathrm{d}t' \int_{t_0}^{t'} \mathrm{d}t''\, \hat{H}_{1I}(t')\hat{H}_{1I}(t'') - \mathrm{i}^3 \ldots \\ &= \sum_{n=0}^{\infty} (-\mathrm{i})^n \int\limits_{t>t_1>\ldots>t_n>t_0} \mathrm{d}t_1 \ldots \mathrm{d}t_n\, \hat{H}_{1I}(t_1)\ldots\hat{H}_{1I}(t_n). \end{aligned} \tag{5.14}$$

This means that the time evolution operator in the interaction picture can be constructed by applying the perturbation $\hat{H}_{1I}$ any number of times and at all possible times between t_0 and t in a time ordered manner. The number of applications of $\hat{H}_{1I}$ is called the *order* in the perturbation expansion of the time evolution operator. The perturbation expansion for the time evolution operator can be truncated at a finite order. However, the truncated expansion is not guaranteed to converge at any finite order. In metals, for example, no truncation is convergent beyond first order. This is a considerable drawback for finite order perturbation methods, such as second order Møller–Plesset perturbation theory (MP2).

5.2 The Gell-Mann–Low theorem

In the previous section, we have seen how to evolve any given state from t_0 to t. We are, however, interested in eigenstates of the full Hamiltonian, most importantly in its ground state $|\Psi\rangle$. All we have are eigenstates of the non-interacting Hamiltonian $\hat{H}_0$, which we can evolve from. In general, such an evolved state $\hat{U}_I(t,t_0)\,|\Phi(t_0)\rangle$ will be neither an eigenstate of the non-interacting Hamiltonian $\hat{H}_0$ nor of the full Hamiltonian $\hat{H}$. We can, however, introduce a time dependent perturbation

$$\hat{H}(t) = \hat{H}_0 + \mathrm{e}^{\eta t}\hat{H}_1 \tag{5.15}$$

for $t \leq 0$, slowly turning on the electron-electron interaction for small $\eta > 0$. The system starts with the unperturbed Hamiltonian $\hat{H}_0$ at $t = -\infty$ and at $t = 0$ the interaction is fully turned on, giving $\hat{H}$. According to the adiabatic theorem, the system will stay in an eigenstate of $\hat{H}(t)$ at all times when starting from an eigenstate of $\hat{H}_0$ at $t = -\infty$, if the transition is sufficiently slow. This holds for

$$\eta \ll \Delta E.$$

ΔE is the energy change of the ground state when turning on the interaction. Note that starting in the ground state of $\hat{H}_0$ at $t = -\infty$ does not guarantee that the evolved eigenstate at $t = 0$ is indeed the ground state of the full Hamiltonian $\hat{H}$. Level crossings may occur. We will, however, assume that they do not occur for the ground state and that the ground state $|\Phi\rangle$ of $\hat{H}_0$ evolves adiabatically into the ground state $|\Psi\rangle$ of $\hat{H}$:

$$|\Psi\rangle = \hat{U}_\eta(0,-\infty)\,|\Phi\rangle\,, \tag{5.16}$$

where we drop the explicit denotation of the interaction picture in favor of denoting the dependence on the parameter η of the transition speed, writing from now on

$$\hat{U}_\eta(t,t_0) = \sum_{n=0}^{\infty}(-\mathrm{i})^n \int\limits_{t>t_1>\ldots>t_n>t_0} \mathrm{d}t_1 \ldots \mathrm{d}t_n \, \hat{H}_1(t_1)\ldots\hat{H}_1(t_n) \tag{5.17}$$

and

$$\hat{H}_1(t) = \mathrm{e}^{\mathrm{i}\hat{H}_0 t}\mathrm{e}^{\eta t}\hat{H}_1\mathrm{e}^{-\mathrm{i}\hat{H}_0 t}. \tag{5.18}$$

Although $\hat{U}_\eta$ and $\hat{H}_1$ depend on η we hope that the results are, in the end, independent of η, if η is chosen sufficiently small. The quantity we are now most interested in is the energy difference ΔE between the ground state energy of the non-interacting Hamiltonian $\hat{H}_0$ and the ground state energy of the fully interacting Hamiltonian $\hat{H} = \hat{H}_0 + \hat{H}_1$. The fully interacting ground state $|\Psi\rangle$ satisfies the Schrödinger equation

$$(\hat{H}_0 + \hat{H}_1)\,|\Psi\rangle = (E_0 + \Delta E)\,|\Psi\rangle\,.$$

Multiplying both sides with $\langle\Phi|$ from the left and using (5.16) gives

$$\begin{aligned} E_0 + \Delta E &= \frac{\langle\Phi|\hat{H}_0|\Psi\rangle}{\langle\Phi\,|\Psi\,\rangle} + \frac{\langle\Phi|\hat{H}_1|\Psi\rangle}{\langle\Phi\,|\Psi\,\rangle} \\ &= \frac{\langle\Phi|\hat{H}_0\hat{U}_\eta(0,-\infty)|\Phi\rangle}{\langle\Phi|\hat{U}_\eta(0,-\infty)|\Phi\rangle} + \frac{\langle\Phi|\hat{H}_1(0)\hat{U}_\eta(0,-\infty)|\Phi\rangle}{\langle\Phi|\hat{U}_\eta(0,-\infty)|\Phi\rangle}\,. \end{aligned} \tag{5.19}$$

The last equation now relates the ground state energy of the fully interacting system to vacuum expectation values (VEV) of the non-interacting system in the particle/hole picture, where $|\Phi\rangle$ is the vacuum state without any particle or hole excitations. In principle, these expectation values can be evaluated despite the infinite sums hidden in the time evolution operators $\hat{U}_\eta$.

5.3 Wick's theorem

Equation (5.19) still has two practical drawbacks. First, there is yet no systematic recipe how to approximate the time evolution operator $\hat{U}_\eta$, consisting of an infinite sum, and second, one still needs to show that ΔE does not depend on the choice of η if it is chosen sufficiently small. We start with the diagrammatic representation of the terms occurring in (5.19), where we need to evaluate terms of the form

$$\langle\Phi|\hat{A}\hat{B}\ldots|\Phi\rangle.$$

$\hat{A}, \hat{B}, \ldots$ are arbitrary creation or annihilation operators. If these operators were normal ordered, such that all annihilation operators are on the right side of all creation operators, its vacuum expectation value (VEV) would simply be 0, given there is at least one creation or annihilation operator. A relation between the VEV of the operators in one specific order and the VEV in normal order is therefore desired. Let $N[\hat{A}\hat{B}\ldots]$ denote normal ordering of the operators where in the case of fermions the sign changes for each transposition. For two creation or annihilation operators, there is only one non-trivial case

$$N[\hat{p}\hat{q}^\dagger] = -\hat{q}^\dagger\hat{p},$$

in the other three cases the operators are already in normal order. Since the vacuum expectation value of two operators in normal order is 0, we can rewrite a given VEV of two operators

$$\langle\Phi|\hat{A}\hat{B}|\Phi\rangle = \langle\Phi|\hat{A}\hat{B}|\Phi\rangle - \langle\Phi|N[\hat{A}\hat{B}]|\Phi\rangle = \langle\Phi|\hat{A}\hat{B} - N[\hat{A}\hat{B}]|\Phi\rangle = \langle\Phi|\overbrace{\hat{A}\hat{B}}|\Phi\rangle, \tag{5.20}$$

defining the *contraction* of two operators $\hat{A}$ and $\hat{B}$ by[1]

$$\overbrace{\hat{A}\hat{B}} := \hat{A}\hat{B} - N[\hat{A}\hat{B}].$$

This may seem arbitrary, however, it turns out that the contraction of two operators is simply a scalar. For two creation or annihilation operators there are four possible contractions

$$\overbrace{\hat{p}\hat{q}} = 0 \qquad \overbrace{\hat{p}\hat{q}^\dagger} = \{\hat{p}, \hat{q}^\dagger\} = \delta_{pq} \qquad \overbrace{\hat{p}^\dagger\hat{q}} = 0 \qquad \overbrace{\hat{p}^\dagger\hat{q}^\dagger} = 0. \tag{5.21}$$

Since the contraction of two operators is a scalar it is unaffected by normal ordering. This allows us to make the desired connection between the given order and the normal order of two operators $\hat{A}\hat{B}$:

$$\hat{A}\hat{B} = N[\hat{A}\hat{B}] + \overbrace{\hat{A}\hat{B}} = N[\hat{A}\hat{B} + \overbrace{\hat{A}\hat{B}}]$$

This result can be generalized to more than two operators by the virtue of Wick's theorem (Wick 1950; Peskin and Schroeder 1995):

$$\hat{A}\hat{B}\hat{C}\ldots = N\left[\hat{A}\hat{B}\hat{C}\ldots + \text{all possible contractions of } \hat{A}\hat{B}\hat{C}\ldots\right]. \tag{5.22}$$

For a sequence of four operators this gives for instance

$$\begin{aligned}\hat{A}\hat{B}\hat{C}\hat{D} \;=\; & N[\hat{A}\hat{B}\hat{C}\hat{D}] + N[\overbrace{\hat{A}\hat{B}}\hat{C}\hat{D}] + N[\hat{A}\overbrace{\hat{B}\hat{C}}\hat{D}] + N[\overbrace{\hat{A}\hat{B}\hat{C}\hat{D}}] + N[\hat{A}\overbrace{\hat{B}\hat{C}}\hat{D}] + \\ & N[\hat{A}\overbrace{\hat{B}\hat{C}\hat{D}}] + N[\hat{A}\hat{B}\overbrace{\hat{C}\hat{D}}] + N[\overbrace{\hat{A}\hat{B}}\overbrace{\hat{C}\hat{D}}] + N[\overbrace{\hat{A}\hat{B}\hat{C}}\hat{D}] + N[\overbrace{\hat{A}\hat{B}\hat{C}\hat{D}}],\end{aligned} \tag{5.23}$$

where we can now reorder the operators, changing the sign appropriately, to pull contracted operators out of the normal ordering operator. For example

$$N[\overbrace{\hat{A}\hat{B}\hat{C}\hat{D}}] = -\overbrace{\hat{A}\hat{C}} \times N[\hat{B}\hat{D}].$$

Since vacuum expectation values of normal ordered operators vanish, only the fully contracted terms survive in a VEV. The VEV of the four operators in (5.23) thus evaluates to

$$\langle\Phi|\hat{A}\hat{B}\hat{C}\hat{D}|\Phi\rangle = \overbrace{\hat{A}\hat{B}}\overbrace{\hat{C}\hat{D}} - \overbrace{\hat{A}\hat{C}}\overbrace{\hat{B}\hat{D}} + \overbrace{\hat{A}\hat{D}}\overbrace{\hat{B}\hat{C}}. \tag{5.24}$$

[1] Note that contractions are usually defined by $\overbrace{\hat{A}\hat{B}} = T[\hat{A}\hat{B}] - N[\hat{A}\hat{B}]$, where $T[\hat{A}\hat{B}]$ denotes time ordering of the operators, such that the time increases from right to left. In our case, the terms occurring in (5.19) are already time ordered by the constraints of the integrals so we will drop the time ordering symbol.

5.3.1 Application to the perturbation

We can now apply this algebra to a simplified case without an effective interaction, $\hat{V}_{\text{eff}}$ where the perturbation is given by

$$\hat{H}_1(t) = \mathrm{e}^{\mathrm{i}\hat{H}_0 t}\mathrm{e}^{\eta t}\frac{1}{2}\sum_{pqrs} V_{sr}^{pq}\hat{c}_p^\dagger\hat{c}_q^\dagger\hat{c}_r\hat{c}_s\mathrm{e}^{-\mathrm{i}\hat{H}_0 t}. \tag{5.25}$$

The electron creation and annihilation operators $\hat{c}_p^\dagger$ and $\hat{c}_p$ have to be expressed in terms of particle and hole creation and annihilation operators $\hat{p}^\dagger$ and $\hat{p}$, since we want to use the non-interacting ground state $|\Phi\rangle$ as the vacuum state. From (5.3) we get

$$\hat{c}_p^\dagger = \begin{cases} \hat{p}^\dagger & \text{for } \varepsilon_p > \varepsilon_\mathrm{F} \\ \hat{p} & \text{otherwise,} \end{cases} \qquad \hat{c}_p = \begin{cases} \hat{p} & \text{for } \varepsilon_p > \varepsilon_\mathrm{F} \\ \hat{p}^\dagger & \text{otherwise.} \end{cases} \tag{5.26}$$

We start with evaluating the numerator of the right term in (5.19) in zeroth order of the expansion of the time evolution operator, where $\hat{U}_\eta^{(0)}(0,-\infty) = 1$:

$$\langle\Phi|\hat{H}_1(0)|\Phi\rangle = \frac{1}{2}\sum_{pqrs} V_{sr}^{pq}\hat{c}_p^\dagger\hat{c}_q^\dagger\hat{c}_r\hat{c}_s + \frac{1}{2}\sum_{pqrs} V_{sr}^{pq}\hat{c}_p^\dagger\hat{c}_q^\dagger\hat{c}_r\hat{c}_s + \frac{1}{2}\sum_{pqrs} V_{sr}^{pq}\hat{c}_p^\dagger\hat{c}_q^\dagger\hat{c}_r\hat{c}_s \tag{5.27}$$

According to (5.21) the only non-vanishing contraction comes from operators of the form $\hat{p}\hat{p}^\dagger$, first creating a hole or a particle in the state p and subsequently destroying it. Thus, the first term in (5.27) must vanish. The second and the third term can only survive if p, q, r and s are hole indices i, j, k and l, giving

$$\langle\Phi|\hat{H}_1(0)|\Phi\rangle = \frac{1}{2}\sum_{ijkl} V_{lk}^{ij}\hat{i}\hat{j}\hat{k}^\dagger\hat{l}^\dagger + \frac{1}{2}\sum_{ijkl} V_{lk}^{ij}\hat{i}\hat{j}\hat{k}^\dagger\hat{l}^\dagger = -\frac{1}{2}\sum_{ij} V_{ji}^{ij} + \frac{1}{2}\sum_{ij} V_{ij}^{ij}. \tag{5.28}$$

Note that neither of the two terms individually respects the Pauli exclusion principle. However, the offending terms, where $i = j$, cancel in the sum of all terms. By the merit of Wick's theorem it is no longer necessary to keep track of disallowed states individually. They simply cancel in the sum of all contractions.

Let us now proceed evaluating the numerator of (5.19) in the simplified case of above with the perturbation given by (5.25). The next order in the expansion of the time evolution operator is

$$\hat{U}_\eta^{(1)}(0,-\infty) = -\mathrm{i}\int_{-\infty}^{0} \mathrm{d}t_1\, \hat{H}_1(t_1).$$

For the application of Wick's theorem at $t \neq 0$ it is more convenient to write the Hamiltonian of the perturbation $\hat{H}_1(t)$ in terms of time dependent creation and annihilation operators. Inserting $\hat{H}_0 = \sum_{p'} \varepsilon_{p'} |p'\rangle \langle p'|$ into (5.25) allows us to write $\hat{H}_1(t)$ in terms of time dependent creation and annihilation operators:

$$\hat{H}_1(t) = \mathrm{e}^{\eta t}\frac{1}{2}\sum_{pqrs} V_{sr}^{pq}\underbrace{\left(\hat{c}_p^\dagger\mathrm{e}^{\mathrm{i}\varepsilon_p t}\right)}_{=\hat{c}_p^\dagger(t)}\left(\hat{c}_q^\dagger\mathrm{e}^{\mathrm{i}\varepsilon_q t}\right)\left(\hat{c}_r\mathrm{e}^{-\mathrm{i}\varepsilon_r t}\right)\underbrace{\left(\hat{c}_s\mathrm{e}^{-\mathrm{i}\varepsilon_s t}\right)}_{=\hat{c}_s(t)}.$$

This can be used to evaluate the next order: $\langle\Phi|\hat{H}_1(0)\hat{U}_\eta^{(1)}(0,-\infty)|\Phi\rangle$

$$= \left\langle \Phi \left| -\mathrm{i}\int_{-\infty}^{0} \mathrm{d}t_1\, \mathrm{e}^{\eta t_1} \frac{1}{4} \sum_{pqrstuvw} V_{sr}^{pq} V_{wv}^{tu}\, \hat{c}_p^\dagger \hat{c}_q^\dagger \hat{c}_r \hat{c}_s \hat{c}_t^\dagger(t_1) \hat{c}_u^\dagger(t_1) \hat{c}_v(t_1) \hat{c}_w(t_1) \right| \Phi \right\rangle$$

There are 4 creation and 4 annihilation operators in this expression, thus there are $4! = 24$ non-vanishing ways of contractions possible. We will, for now, just look at the following:

$$\begin{aligned} & -\mathrm{i}\int_{-\infty}^{0} \mathrm{d}t_1\, \mathrm{e}^{\eta t_1} \frac{1}{4} \sum_{pqrstuvw} V_{sr}^{pq} V_{wv}^{tu}\, \overbrace{\hat{c}_p^\dagger \hat{c}_q^\dagger \hat{c}_r \hat{c}_s \hat{c}_t^\dagger(t_1) \hat{c}_u^\dagger(t_1) \hat{c}_v(t_1) \hat{c}_w(t_1)} \\ = \quad & -\mathrm{i}\int_{-\infty}^{0} \mathrm{d}t_1\, \mathrm{e}^{\eta t_1} \frac{1}{4} \sum_{pqrstuvw} V_{sr}^{pq} V_{wv}^{tu}\, \overbrace{\hat{c}_p^\dagger \hat{c}_w(t_1)} \overbrace{\hat{c}_s \hat{c}_t^\dagger(t_1)} \overbrace{\hat{c}_q^\dagger \hat{c}_v(t_1)} \overbrace{\hat{c}_r \hat{c}_u^\dagger(t_1)} \end{aligned}$$

For non-vanishing terms, p, w and q, v must be hole indices i and j, respectively. Similarly, s, t and r, u must be particle indices a and b, giving

$$-\mathrm{i}\int_{-\infty}^{0} \mathrm{d}t_1\, \mathrm{e}^{\eta t_1} \frac{1}{4} \sum_{ijab} V_{ab}^{ij} V_{ij}^{ab}\, \mathrm{e}^{-\mathrm{i}\varepsilon_i t_1} \mathrm{e}^{\mathrm{i}\varepsilon_a t_1} \mathrm{e}^{-\mathrm{i}\varepsilon_j t_1} \mathrm{e}^{\mathrm{i}\varepsilon_b t_1} = \frac{1}{4} \sum_{ijab} \frac{V_{ab}^{ij} V_{ij}^{ab}}{\varepsilon_i + \varepsilon_j - \varepsilon_a - \varepsilon_b + \mathrm{i}\eta}. \quad (5.29)$$

For a system where there exists a finite gap $E_g > 0$ such that $|\varepsilon_i - \varepsilon_a| > E_g$ for all holes i and particles a, we can simply choose $\eta \ll E_g$ to get a result independent of the choice of η. For metals with a non-degenerate ground state there is no finite $E_g > 0$ for all i and a, however, $|\varepsilon_i - \varepsilon_a| > 0$. In this case the limit $\eta \to 0$ can only be taken after summing over all states, as done in Section 6.4 for the Uniform Electron Gas. If the ground state is degenerate we have to resort to Degenerate State Perturbation Theory, which is not discussed here.

Wick's theorem provides a systematic way to evaluate the vacuum expectation values occurring in the Gell-Mann–Low theorem (5.19). Instead of keeping track of which states are occupied after each interaction, we can simply sum over contractions of the operator matrices V_{sr}^{pq} and v_q^p occurring in the perturbation, as shown in (5.28) and in (5.29). We do, however, have to sum over all possible contractions.

5.4 Goldstone diagrams

The number of possible contractions in Wick's theorem quickly becomes too large to evaluate vacuum expectation values as we did in the previous section. So far, we have used diagrams solely for depicting the action of a second quantized operator where the initial state was shown below and the final state above the operator symbol, as shown in Figure 5.1. It is time to rigorously introduce the diagrammatic notation employed by Goldstone in order to enumerate and evaluate all contractions.

Each Coulomb interaction $\hat{V}_{\mathrm{ee}}$ is represented by a horizontal wiggly line between two vertices. Each *vertex* consists of one electron creation operator and one electron annihilation operator represented by an outbound and an inbound *leg*, respectively. Without loss of generality, the outer operators $\hat{c}_p^\dagger$ and $\hat{c}_s$ are associated with the left vertex and the inner operators $\hat{c}_q^\dagger$ and $\hat{c}_r$ with the right vertex. Each effective interaction $\hat{V}_{\mathrm{eff}}$ is represented by a vertex in form of a shaded circle. Therefore, lower indices of the matrices V_{sr}^{pq} and v_q^p are from inbound legs, upper indices are from outbound legs and left indices are from left legs.

$V_{sr}^{pq}\hat{c}_p^\dagger\hat{c}_q^\dagger\hat{c}_r\hat{c}_s =$ 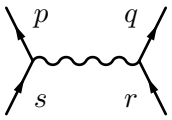

$v_q^p\hat{c}_p^\dagger\hat{c}_q =$ 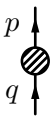

Figure 5.2: Representation of the Coulomb and effective interaction in Goldstone diagrams

Connections of these legs represent the contractions, where only outbound legs may be connected to inbound legs, as they are the only non-vanishing operator contractions. The connections are directed from an outbound to an inbound leg, indicated by an arrow. Time propagates from bottom to top and the last Coulomb or effective interaction is usually at $t = 0$. Connections directed forwards in time represent contractions of the form $\hat{c}_p \ldots \hat{c}_q^\dagger$ and are hence restricted to particles. Conversely, connections directed backwards in time are restricted to holes. Connections between legs of the same Coulomb interaction are called *non-propagating* and are also restricted to holes, since they are of the form $\hat{c}_p^\dagger\hat{c}_q^\dagger\hat{c}_r\hat{c}_s$. Each connection is labeled with a unique index, over which to contract, $a, b, c, \ldots$ for particles and $i, j, k, \ldots$ for holes.

$\frac{1}{2}\sum_{ij} V_{ji}^{ij}\hat{i}\hat{j}\hat{i}^\dagger\hat{j}^\dagger =$ 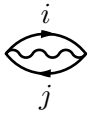

$\frac{1}{2}\sum_{ij} V_{ij}^{ij}\hat{i}\hat{j}\hat{j}^\dagger\hat{i}^\dagger =$ 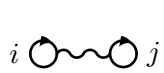

Figure 5.3: Goldstone diagrams for the terms of (5.28) with non-propagating connections

5.4.1 Symmetries

Interchanging the left and the right side of a Coulomb interaction including all its connections in the Goldstone diagram leaves the respective matrix elements V_{sr}^{pq} invariant. In general, however, we get a different contraction from the swapped connections. Since we have to sum over all possible contractions, both contributions have to be counted if they are distinct. Figure 5.4 shows all possible left/right interchanges for the diagram representing the contraction evaluated in (5.29). For the sake of simplicity the time arguments of the operators are omitted. The two cases on the left hand side have distinct contractions, so both must be counted. Both evaluate to the same value since they can be transformed into each other with an even number of operator transpositions and $V_{sr}^{pq} = V_{rs}^{qp}$. We can do that with every Coulomb interaction and from now on identify one Goldstone diagram with all contractions that arise from interchanging the left and the right side of all its Coulomb interactions. In general, this cancels the factor $\frac{1}{2}$ in all Coulomb operators for evaluating one Goldstone diagram as opposed to evaluating one single contraction, where this factor is needed according to (5.6).

If there is however a global left/right symmetry in the Goldstone diagram, interchanging all Coulomb interactions simultaneously does not give a distinct contraction. It merely interchanges the labels of the indices over which to contract, as shown in the right two cases of Figure 5.4. Thus, for a Goldstone diagram with a global left/right symmetry only half of the cases arising from interchanging each Coulomb interaction are distinct, which gives rise to a factor of 1/2 for the entire diagram. This also applies to the Hartree and exchange diagram shown in Figure 5.3.

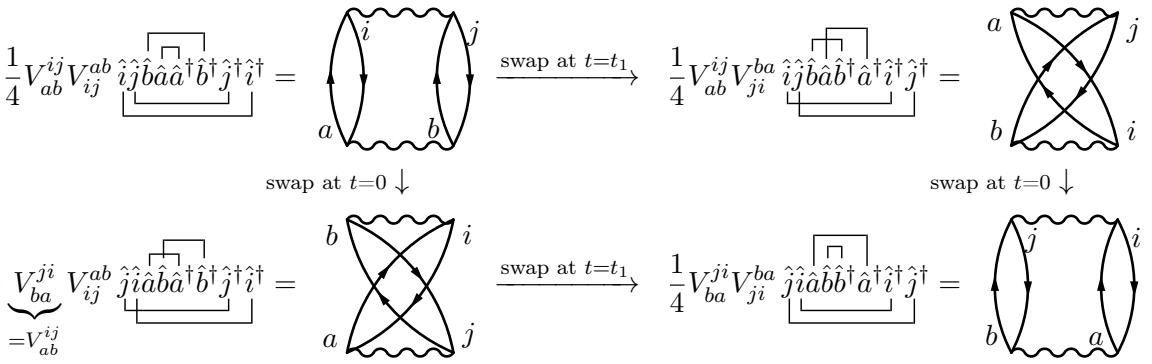

Figure 5.4: All possible left/right interchanges of Coulomb interactions for the diagram representing the contraction evaluated in (5.29). The sums and the time arguments of the operators are omitted.

5.4.2 Time integration

The number of interactions occurring in the diagram is called its *order*, which is $n+1$, where n is the order of the expansion of the time evolution operator $\hat{U}_\eta$ in (5.17). According to the expansion of $\hat{U}_\eta$, we must integrate over all times $t_1, \ldots, t_n$ of all interactions except the last one, respecting the order $0 > t_1 > \ldots > t_n$. We can make the substitutions $t_{0,1} = 0 - t_1, \ldots, t_{n-1,n} = t_{n-1} - t_n$ to integrate over the times between each interaction $t_{0,1}, t_{1,2}, \ldots, t_{n-1,n}$. For a particle state a propagating from an interaction at the time t_n to the time $t = 0$ this gives for instance

$$(-\mathrm{i})^n \int\limits_{0>t_1>\ldots>t_n} \hat{a}\mathrm{e}^{-\mathrm{i}\varepsilon_a 0} \ldots \mathrm{e}^{\eta t_1} \ldots \mathrm{e}^{\eta t_n} \hat{a}^\dagger \mathrm{e}^{\mathrm{i}\varepsilon_a t_n} \ldots =$$

$$(-\mathrm{i})^n \int_0^\infty \mathrm{d}t_{0,1} \mathrm{e}^{-\mathrm{i}(\varepsilon_a + \ldots - n\mathrm{i}\eta)t_{0,1}} \int_0^\infty \mathrm{d}t_{1,2} \mathrm{e}^{-\mathrm{i}(\varepsilon_a + \ldots - (n-1)\mathrm{i}\eta)t_{1,2}} \ldots \int_0^\infty \mathrm{d}t_{n-1,n} \mathrm{e}^{-\mathrm{i}(\varepsilon_a + \ldots - \mathrm{i}\eta)t_{n-1,n}}$$

$$\ldots \hat{a} \ldots \hat{a}^\dagger \ldots \quad (5.30)$$

So the eigenenergy ε_a appears in the exponential of each time interval where the state propagates. For hole states i the sign is inverted. Integrating out all time intervals gives an energy denominator for each interval between two interactions of the form

$$\frac{1}{\sum\limits_{i \in H_k} \varepsilon_i - \sum\limits_{a \in P_k} \varepsilon_a + k\mathrm{i}\eta},$$

where H_k and P_k are the sets of the holes and particles propagating in the respective k-th time interval. k is counted from the bottom. Figure 5.5 shows an example with two holes and two particles.

For finite orders n of the diagrams and systems with a finite energy gap E_g one can choose $n\eta \ll E_g$ to retrieve results independent of η. When going to infinite orders in the diagrams, as it is done in the Random Phase Approximation, the limit $\eta \to 0$ needs to be evaluated.

$$\frac{1}{2}\sum_{ijab}\frac{V_{ab}^{ij}V_{ij}^{ab}}{\varepsilon_i+\varepsilon_j-\varepsilon_a-\varepsilon_b+\mathrm{i}\eta} =$$

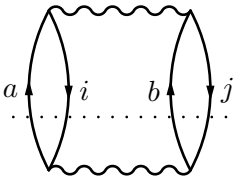

$H=\{i,j\}, P=\{a,b\}$

Figure 5.5: Evaluation of all contractions represented by the given Goldstone diagram. There is one time interval where the holes i,j and the particles a,b are propagating. The symmetry factor is $1/2$.

5.4.3 Fermion sign

Finally, we need a rule to determine the sign of all contractions arising from one Goldstone diagram in a graphical way. The sign of a contraction depends on whether an even or an odd number P of transpositions is required to reorder the contractions in pairs:

$$\overbrace{\hat{A}\hat{B}\hat{C}\ldots\hat{Z}} = (-1)^P \overbrace{\hat{A}\hat{C}}\overbrace{\hat{B}\hat{Z}}\ldots$$

Note that contracted operators must not be interchanged since that turns a particle connection into a hole connection or vice versa, representing a different diagram. In the upper example, the following reordering is therefore not allowed: $\overbrace{\hat{A}\hat{C}}\overbrace{\hat{Z}\hat{B}}\ldots$

In Goldstone diagrams the contracted operators are the operators occurring in the perturbation. They are of the general form

$$\ldots V_{sr}^{pq}\hat{c}_p^\dagger\hat{c}_q^\dagger\hat{c}_r\hat{c}_s\ldots v_{q'}^{p'}\hat{c}_{p'}^\dagger\hat{c}_{q'}\ldots$$

omitting the sums for brevity. Their respective time arguments can be integrated out according to the last section, the order of the interactions from right to left is, however, still relevant. To determine the sign of all contractions of one Goldstone diagram, we first reorder the operators such that operators of the same vertex of an interaction are grouped together:

$$\ldots V_{sr}^{pq}\underbrace{\hat{c}_p^\dagger\hat{c}_s}_{\text{vertex}}\hat{c}_q^\dagger\hat{c}_r\ldots v_{q'}^{p'}\hat{c}_{p'}^\dagger\hat{c}_{q'}\ldots$$

This only affects the Coulomb interactions and requires two transpositions for each interaction, leaving the sign invariant. The matrix elements V_{sr}^{pq} and v_q^p are complex numbers. Their order is therefore irrelevant and we will omit them from now on.

The finite set of vertices and connections form a directed graph, where each vertex has exactly one outgoing and one incoming connection. Thus, the graph consists of disconnected loops of vertices allowing one to group the vertices of each loop together as long as we do not change the order of the vertices within each loop. The sign will not be affected since we only move vertices, i.e. pairs of operators. For the diagram in Figure 5.5 this gives for instance

$$\overbrace{\hat{i}\hat{a}\hat{j}\hat{b}\hat{a}^\dagger\hat{i}^\dagger\hat{b}^\dagger\hat{j}^\dagger} = (+1)\overbrace{\hat{i}\hat{a}\hat{a}^\dagger\hat{i}^\dagger}\overbrace{\hat{j}\hat{b}\hat{b}^\dagger\hat{j}^\dagger}. \tag{5.31}$$

In a diagram we can freely move the vertices horizontally such that each loop forms a simple polygon where the connections do not intersect each other, as exemplified on the left of Figure 5.6. Without loss of generality, we choose a clockwise orientation of the directed connections in order to resemble the order of the creation operators in a vertex of the form $\hat{a}^\dagger\hat{i}^\dagger$.

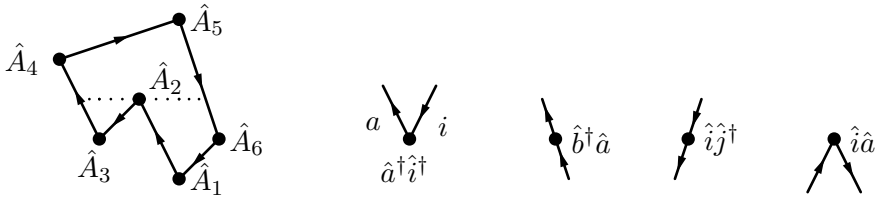

Figure 5.6: A closed loop of vertices $\hat{A}_1, \ldots, \hat{A}_6$, where each vertex operator $\hat{A}$ is of one of the four possible forms shown.

Simple polygons can be decomposed into truncated monotone polygons (Preparata and Shamos 2008). In a *monotone polygon* a horizontal line intersects the edges at most twice, such that its left side consists only of particle connections and its right side only of hole connections. In the loop in Figure 5.6 there are three monotone polygons, two starting at the vertices $\hat{A}_1$ and $\hat{A}_3$ below the dotted line and one above the dotted, ending at vertex $\hat{A}_5$.

We have already reordered the operators to group vertices and loops together, as shown in (5.31). As a last preparatory step, we will group vertices of monotone polygons together, keeping the time order within each monotone polygon. For the loop in Figure 5.6 this rearrangement from the initial time order yields

$$\hat{A}_5\hat{A}_4\hat{A}_2\hat{A}_6\hat{A}_3\hat{A}_1 = (+1)\,\hat{A}_5\hat{A}_4\hat{A}_2(\hat{A}_3)(\hat{A}_6\hat{A}_1),$$

where the operators in the left and in the right parenthesis respectively belong to the left and right monotone polygon below the dotted line.

With the operators ordered this way it is now sufficient to treat monotone polygons only. We will follow the vertices within a monotone polygon starting with a vertex of the form $\hat{a}^\dagger\hat{i}^\dagger$, as indicated on the right of Figure 5.6. Then, vertices of the form $\hat{b}^\dagger\hat{a}$ add particle connections on the left side of the monotone polygon under consideration while vertices of the form $\hat{j}\hat{i}^\dagger$ add hole connections on the right side. A vertex of the form $\hat{i}\hat{a}$ can either join two different monotone polygons, as $\hat{A}_2$ does in Figure 5.6, or it can close the loop. At each vertex we reorder the involved contractions into the general form

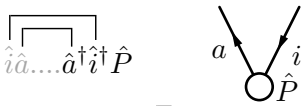

(5.32)

such that $\hat{P}$ consists only of contracted pairs $\hat{b}\hat{b}^\dagger\hat{j}\hat{j}^\dagger\ldots$ and the creation operators $\hat{a}^\dagger\hat{i}^\dagger$ of the open particle and hole connections are to the left of $\hat{P}$. All operators to the right of $\hat{a}^\dagger\hat{i}^\dagger$ are then in the desired order, denoted here by a circle in the diagram. Note that the order of the creation operators $\hat{a}^\dagger\hat{i}^\dagger$ is relevant and the particle creation operator must stand to the left of the hole creation operator.

A monotone polygon starts with a vertex of the form $\hat{a}^\dagger\hat{i}^\dagger$. This is trivially in the above form

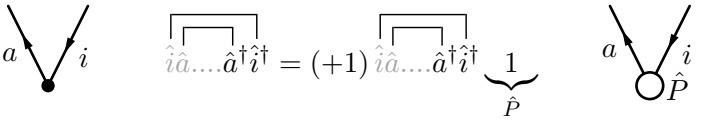

(5.33)

with no change of sign. A vertex of the form $\hat{b}^\dagger\hat{a}$ adds a particle connection on the left side of the polygon. Using two transpositions we can bring the operators into the desired form

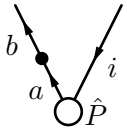

$$\hat{i}\hat{b}....\hat{b}^\dagger\hat{a}\hat{a}^\dagger\hat{i}^\dagger\hat{P} = (+1)\,\hat{i}\hat{b}....\hat{b}^\dagger\hat{i}^\dagger\underbrace{\hat{a}\hat{a}^\dagger\hat{P}}_{\hat{P}'} \tag{5.34}$$

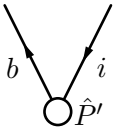

such that $\hat{a}\hat{a}^\dagger$ can be absorbed into the set of paired operators $\hat{P}'$ to continue with. The sign does not change in this case. A vertex of the form $\hat{i}\hat{j}^\dagger$ adds a hole connection on the right side of the polygon. Now, three transpositions are required to bring the operators into the form

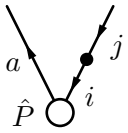

$$\hat{j}\hat{a}....\hat{i}\hat{j}^\dagger\hat{a}^\dagger\hat{i}^\dagger\hat{P} = (-1)\,\hat{j}\hat{a}....\hat{a}^\dagger\hat{j}^\dagger\underbrace{\hat{i}\hat{i}^\dagger\hat{P}}_{\hat{P}'} \tag{5.35}$$

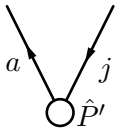

to absorb $\hat{i}\hat{i}^\dagger$ into $\hat{P}'$ and to bring the hole creation operator $\hat{j}^\dagger$ of the open connection to the right side of the particle creation operator $\hat{a}^\dagger$, as required by (5.32). In this case the sign changes.

At a vertex of the form $\hat{j}\hat{a}$ two different monotone polygons can be joined to a polygon that is monotone after this vertex. We assume that the right monotone polygon starts earlier in time, such that all its operators $\hat{a}^\dagger\hat{i}^\dagger\hat{P}$ are to the right of all operators of the left monotone polygon $\hat{b}^\dagger\hat{j}^\dagger\hat{Q}$. The converse case can be treated analogously. Bringing the operators into the desired form

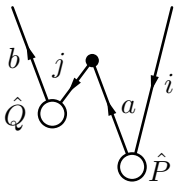

$$\hat{i}\hat{b}....\hat{j}\hat{a}\hat{b}^\dagger\hat{j}^\dagger\hat{Q}\hat{a}^\dagger\hat{i}^\dagger\hat{P} = (-1)\,\hat{i}\hat{b}....\hat{b}^\dagger\hat{i}^\dagger\underbrace{\hat{j}\hat{j}^\dagger\hat{Q}\hat{a}\hat{a}^\dagger\hat{P}}_{\hat{P}'} \tag{5.36}$$

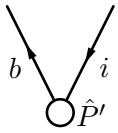

requires an odd number of transpositions and changes the sign. The last vertex of a loop is of the form $\hat{i}\hat{a}$. It closes the monotone polygon without change of sign

$$\hat{i}\hat{a}\hat{a}^\dagger\hat{i}^\dagger\hat{P} = (+1)\,\underbrace{\hat{a}\hat{a}^\dagger\hat{i}\hat{i}^\dagger\hat{P}}_{\hat{P}'}. \tag{5.37}$$

In summary, the sign changes when a contraction of hole operators $\hat{i}\hat{i}^\dagger$ is absorbed into the set of paired operators $\hat{P}'$, as in (5.35) and (5.36). When closing the loop in (5.37) there is however no change of sign although there is a pair of hole operators absorbed in $\hat{P}'$. The Fermion sign of a single loop is therefore $(-1)^{h-1} = (-1)\,(-1)^h$, where h is the number of hole connections in the loop. For a Goldstone diagram consisting of l loops and h hole connections in total the Fermion sign is thus

$$(-1)^{l+h}, \tag{5.38}$$

which can easily be determined graphically. Note that non-propagating connections, as shown in Figure 5.3 also count as holes. We left their treatment out for simplicity.

5.5 The Linked-Cluster theorem

We can now employ the framework of Goldstone diagrams to systematically evaluate the terms of the Gell-Mann–Low theorem (5.19):

$$E_0 + \Delta E = \frac{\langle\Phi|\hat{H}_0\hat{U}_\eta(0,-\infty)|\Phi\rangle}{\langle\Phi|\hat{U}_\eta(0,-\infty)|\Phi\rangle} + \frac{\langle\Phi|\hat{H}_1(0)\hat{U}_\eta(0,-\infty)|\Phi\rangle}{\langle\Phi|\hat{U}_\eta(0,-\infty)|\Phi\rangle}$$

Only fully contracted operators contribute to the vacuum expectation values which requires that all occurring diagrams are closed with no dangling connection left. In Figure 5.3 and 5.5, we have already evaluated selected diagrams of the numerator containing the final interaction $\hat{H}_1(0)$. Diagrams that are connected to the final interaction at $t = 0$ are called *connected* or, historically, *linked* diagrams. In second order there are already disconnected diagrams, such as

$\hat{H}_1(0)$ 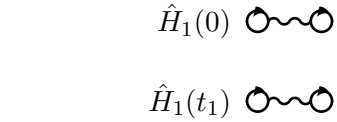
$\hat{H}_1(t_1)$

$$= \quad -\mathrm{i}\int_{-\infty}^{0} \mathrm{d}t_1 \sum_{ijkl} V_{ij}^{ij}\,\hat{i}\hat{j}\hat{j}^\dagger\hat{i}^\dagger\,\mathrm{e}^{\eta t_1}\,V_{kl}^{kl}\,\hat{k}\hat{l}\hat{l}^\dagger\hat{k}^\dagger = \left(\sum_{ij} V_{ij}^{ij}\right)\left(\sum_{ij}\frac{V_{ij}^{ij}}{\mathrm{i}\eta}\right),$$

where the lower diagram is disconnected. Since there are no contractions between disconnected diagrams by definition their vacuum expectation value decomposes into factors which can be evaluated independently. Note that each disconnected diagram comes with an additional factor of $1/\mathrm{i}\eta$ which diverges in the limit of $\eta \to 0$. In general, we get the following form for the numerator of the Gell-Mann–Low energy expression containing the final interaction:

$$\langle\Phi|\hat{H}_1(0)\hat{U}_\eta(0,-\infty)|\Phi\rangle = \Big(\sum \text{connected diagrams}\Big)\Big(\sum \text{disconnected diagrams}\Big).$$

Let us now look at the denominator $\langle\Phi|\hat{U}_\eta(0,-\infty)|\Phi\rangle$, where there is no operator at $t = 0$. Since the diagrams must be closed we simply get the same diagrams as the disconnected diagrams in the previous case, as for instance in

$t = 0$ ⋯⋯⋯
$\hat{H}_1(t_1)$

$$= \quad \left(\sum_{ij}\frac{V_{ij}^{ij}}{\mathrm{i}\eta}\right).$$

Thus, the denominator has the following general form

$$\langle\Phi|\hat{U}_\eta(0,-\infty)|\Phi\rangle = \Big(\sum \text{disconnected diagrams}\Big).$$

Finally, we need to evaluate the numerator containing $\hat{H}_0$, which is by construction diagonal and from (5.5) given by $\hat{H}_0 = E_0 - \sum_i \varepsilon_i \hat{i}^\dagger\hat{i} + \sum_a \varepsilon_a \hat{a}^\dagger\hat{a}$. Therefore, all diagrams from $\hat{U}_\eta$ must already be closed at $t = 0$ for non-vanishing contributions, just like in the denominator. In general we get

$$\langle\Phi|\hat{H}_0\hat{U}_\eta(0,-\infty)|\Phi\rangle = E_0\Big(\sum \text{disconnected diagrams}\Big).$$

Thus, all disconnected diagrams, containing diverging factors $1/\mathrm{i}\eta$, cancel, and we finally arrive at the expression for the correlation energy in many-body perturbation theory

$$\Delta E = \Big(\sum \text{connected diagrams}\Big).$$

5.6 Hartree-Fock reference

For the sake of simplicity we have not yet taken the effective interaction $\hat{V}_{\text{eff}}$ into consideration although it is an integral part of the perturbation $\hat{H}_1$. Including the effective interaction in first order gives just one additional diagram leading to three non-vanishing contributions:

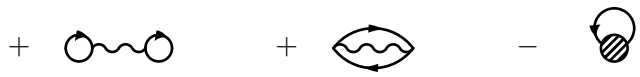

(5.39)

The perturbation $\hat{H}_1$ contains $\hat{V}_{\text{eff}}$ with a negative sign which has to be taken into account additionally to the sign of the Goldstone diagram originating from the number its loops and holes. The former is explicitly given here, the latter not.

For a Hartree-Fock Hamiltonian $\hat{H}_0$, $\hat{V}_{\text{eff}}$ can be explicitly given

$$v_q^p \hat{c}_p^\dagger \hat{c}_q \;=\; \sum_i V_{qi}^{pi} \hat{c}_p^\dagger \hat{c}_q - \sum_i V_{qi}^{ip} \hat{c}_p^\dagger \hat{c}_q,$$

or in diagrams:

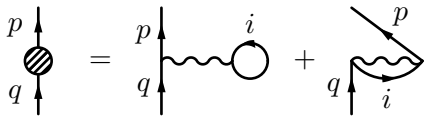

(5.40)

We can insert (5.40) into (5.39) giving

In the case of the Hartree-Fock reference, it turns out that the effective interaction contained in the perturbation exactly cancels with all Coulomb interactions containing non-propagating connections. This greatly simplifies the set of Goldstone diagrams to consider. In second order there are already 11 connected Goldstone diagrams, which are shown in Figure 5.7, and only two of them do not cancel in Hartree-Fock. Finite order many-body perturbation theory based on Hartree-Fock is referred to as Møller–Plesset perturbation theory: MP2, MP3 or MP4. The maximum order is given as suffix and in practice hardly ever exceeds four. Møller–Plesset perturbation theory was developed by Møller and Plesset 1934 well before Goldstone introduced the diagrammatic treatment of perturbation theory discussed here.

For a non-Hartree-Fock reference, such as Density Functional Theory, one must take all diagrams into consideration that contain either the effective interaction or non-propagating connections. There are nine such diagrams in second order, shown on the left in Figure 5.7. In case of Density Functional Theory, where the effective interaction consists of the Hartree contribution and an exchange-correlation interaction

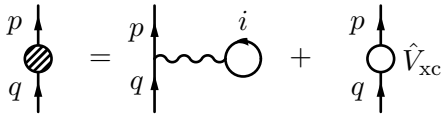

all diagrams containing the Hartree contribution cancel. This leaves only 4 of the 9 additional diagrams and they are to be evaluated with $\hat{V}_{\text{xc}}$ instead of $\hat{V}_{\text{eff}}$. Note that these diagrams are convergent in second order even for metals, offering an alternative to renormalization as done for instance by Ren et al. 2013. Unless explicitly stated, the diagrams containing the effective or the exchange-correlation interaction are only taken into account to first order according to (5.39) computing the Hartree-Fock interaction energy with the DFT orbitals.

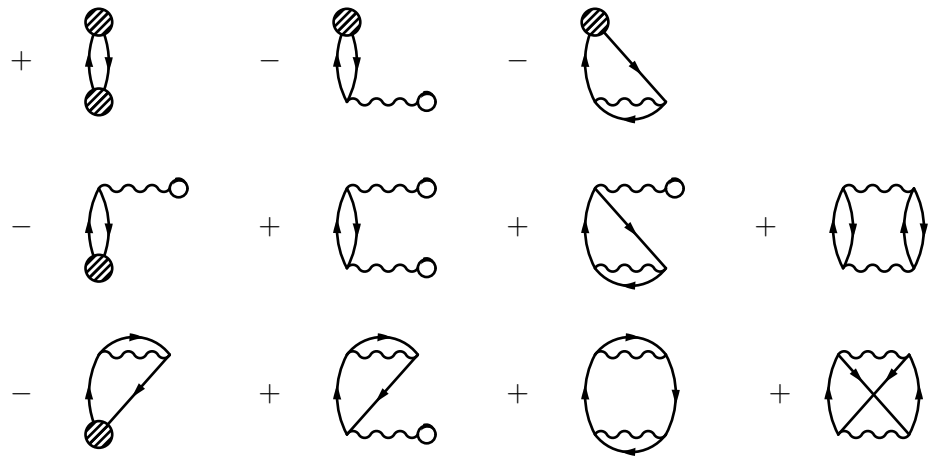

Figure 5.7: All connected Goldstone diagrams of second order. In a Hartree-Fock reference the left three columns cancel leaving only the two contributions of second order Møller–Plesset perturbation theory (MP2).

5.7 Propagators

In the current approach to many-body perturbation theory we use the matrix elements V_{sr}^{pq} and v_q^p from the second quantized representation of the interactions present in the perturbation $\hat{H}_1$. However, storing the Coulomb integrals V_{sr}^{pq} on the computer requires a large amount of memory scaling like $\mathcal{O}(N^4)$ with the size of the system since this matrix has four indices. It is also time consuming to calculate all elements of V_{sr}^{pq} scaling like $\mathcal{O}(N^5)$ with system size according to (6.19). V_{sr}^{pq} must be computed before we can even begin to evaluate any of its contractions for the diagrams in the perturbation expansion.

It can be beneficial to defer the calculation of the Coulomb integrals to a later stage, especially for diagrams where the sums of the Coulomb integrals can be factored into independent contributions, such as in the Hartree term

$$= \frac{1}{2}\sum_{ij} V_{ij}^{ij} = \frac{1}{2}\sum_{ij}\iint \mathrm{d}\mathbf{x}_1\mathrm{d}\mathbf{x}_2\, \psi_i^*(\mathbf{x}_1)\psi_j^*(\mathbf{x}_2)\frac{1}{|\mathbf{r}_1-\mathbf{r}_2|}\psi_j(\mathbf{x}_2)\psi_i(\mathbf{x}_1)$$

$$= \frac{1}{2}\iint \mathrm{d}\mathbf{x}_1\mathrm{d}\mathbf{x}_2 \left(\sum_i \psi_i^*(\mathbf{x}_1)\psi_i(\mathbf{x}_1)\right)\frac{1}{|\mathbf{r}_1-\mathbf{r}_2|}\left(\sum_i \psi_i^*(\mathbf{x}_2)\psi_i(\mathbf{x}_2)\right)$$

which can even be computed in $\mathcal{O}(N^2)$. We can rewrite the above expression to read

$$\frac{1}{2}\iint \mathrm{d}\mathbf{x}_1\mathrm{d}\mathbf{x}_2\, G_0(\mathbf{x}_1 0, \mathbf{x}_1 0)\,\frac{1}{|\mathbf{r}_1-\mathbf{r}_2|}\,G_0(\mathbf{x}_2 0, \mathbf{x}_2 0)\,,$$

defining the complex valued *propagator* or *Green's function* from the spin-position $\mathbf{x}'$ to the spin-position $\mathbf{x}$ at the same instance in time t

$$G_0(\mathbf{x}t, \mathbf{x}'t) := -\sum_i \psi_i(\mathbf{x})\psi_i^*(\mathbf{x}')\,. \tag{5.41}$$

Note that the sign in the non-propagating case for equal times is negative in accordance with the Fermion sign rules discussed in Subsection 5.4.3.

For propagating states we can use the time dependent creation and annihilation operators to express contractions over V_{sr}^{pq} and v_q^p in terms of complex valued functions of two spin, space and time coordinates. In case of the direct MP2 diagram this gives

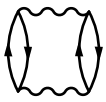

$$
\begin{aligned}
&= \frac{1}{2}(-\mathrm{i})\int_{-\infty}^{0} \mathrm{d}t\, \mathrm{e}^{\eta t} \sum_{ijab} V_{ij}^{ab} V_{ab}^{ij} \\
&= \frac{1}{2}(-\mathrm{i})\int_{-\infty}^{0} \mathrm{d}t\, \mathrm{e}^{\eta t} \iiiint \mathrm{d}\mathbf{x}_1\, \mathrm{d}\mathbf{x}_2\, \mathrm{d}\mathbf{x}_3\, \mathrm{d}\mathbf{x}_4\, \frac{1}{|\mathbf{r}_1 - \mathbf{r}_3|}\, \frac{1}{|\mathbf{r}_2 - \mathbf{r}_4|} \\
&\qquad \sum_i \psi_i^*(\mathbf{x}_1)\psi_i(\mathbf{x}_3)\mathrm{e}^{-\mathrm{i}\varepsilon_i t} \sum_a \psi_a(\mathbf{x}_1)\psi_a^*(\mathbf{x}_3)\mathrm{e}^{\mathrm{i}\varepsilon_a t} \\
&\qquad \sum_j \psi_j^*(\mathbf{x}_2)\psi_j(\mathbf{x}_4)\mathrm{e}^{-\mathrm{i}\varepsilon_j t} \sum_b \psi_b(\mathbf{x}_2)\psi_b^*(\mathbf{x}_4)\mathrm{e}^{\mathrm{i}\varepsilon_b t}\,.
\end{aligned}
$$

According to the Linked-Cluster theorem we can choose η arbitrarily small since the terms diverging with $\eta \to 0$ cancel. Therefore, the adiabatic switching function $\mathrm{e}^{\eta t}$ has no physical effect and rather serves to make the integrals convergent in the considered interval. Thus, we can as well absorb the switching function into the time dependent creation and annihilation operators. We obtain

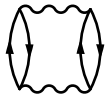

$$
\begin{aligned}
&= \frac{1}{2}(-\mathrm{i})\int_{-\infty}^{0} \mathrm{d}t \iiiint \mathrm{d}\mathbf{x}_1\, \mathrm{d}\mathbf{x}_2\, \mathrm{d}\mathbf{x}_3\, \mathrm{d}\mathbf{x}_4\, \frac{1}{|\mathbf{r}_1 - \mathbf{r}_3|}\, \frac{1}{|\mathbf{r}_2 - \mathbf{r}_4|} \\
&\qquad \sum_i \psi_i^*(\mathbf{x}_1)\psi_i(\mathbf{x}_3)\mathrm{e}^{(-\mathrm{i}\varepsilon_i + \eta)t} \sum_a \psi_a(\mathbf{x}_1)\psi_a^*(\mathbf{x}_3)\mathrm{e}^{(\mathrm{i}\varepsilon_a + \eta)t} \\
&\qquad \underbrace{\sum_j \psi_j^*(\mathbf{x}_2)\psi_j(\mathbf{x}_4)\mathrm{e}^{(-\mathrm{i}\varepsilon_j + \eta)t}}_{=-G_0(\mathbf{x}_4 t, \mathbf{x}_2 0)} \underbrace{\sum_b \psi_b(\mathbf{x}_2)\psi_b^*(\mathbf{x}_4)\mathrm{e}^{(\mathrm{i}\varepsilon_b + \eta)t}}_{=+G_0(\mathbf{x}_2 0, \mathbf{x}_4 t)}\,,
\end{aligned}
\tag{5.42}
$$

extending the definition of the propagator[2] to all cases:

$$
G_0(\mathbf{x}t, \mathbf{x}'t') := \begin{cases} -\sum_i \psi_i(\mathbf{x})\psi_i^*(\mathbf{x}')\mathrm{e}^{(-\mathrm{i}\varepsilon_i + \eta)(t-t')} & \text{for } t \leq t' \\ +\sum_a \psi_a(\mathbf{x})\psi_a^*(\mathbf{x}')\mathrm{e}^{(-\mathrm{i}\varepsilon_a - \eta)(t-t')} & \text{otherwise.} \end{cases} \tag{5.43}
$$

In other words, particle states a propagate forwards in time from t' to t, while hole states i propagate backwards in time from t' to t. Note that we have to use hole states i in the non-propagating case, where $t' = t$, to be consistent with definition (5.41). The adiabatic switching function is now part of the propagator and its sole purpose is to make positive time intervals convergent for particles and negative time intervals convergent for holes.

[2] Note that it is often $\mathrm{i}G_0$ which is defined by the right hand side of (5.43). This factor is normally introduced such that the time evolution of the propagator is compatible to that of the Hamiltonian. We omit this factor here for brevity and in accordance with Lancaster and Blundell 2014.

5.8 Feynman diagrams

Eventually, it is desirable to have a diagrammatic framework that treats space and time on equal footing. Here, we do not need it for a relativistic treatment of the many-body system, however, we want to be able to work in the frequency domain. This requires independent integrals over the whole time domain of the form $\int_{-\infty}^{\infty} \mathrm{d}t_1 \ldots \int_{-\infty}^{\infty} \mathrm{d}t_n$ rather than the dependent integrals $\int_{0>t_1>\ldots>t_n} \mathrm{d}t_1 \ldots \mathrm{d}t_n$ we have from the expansion of the time evolution operator $\hat{U}_\eta(0, -\infty)$ according to (5.17):

$$\hat{U}_\eta(t, t_0) = \sum_{n=0}^{\infty} (-\mathrm{i})^n \int\limits_{t>t_1>\ldots>t_n>t_0} \mathrm{d}t_1 \ldots \mathrm{d}t_n \, \hat{H}_1(t_1) \ldots \hat{H}_1(t_n) \,.$$

Each interaction that comes from the time evolution operator introduces a time variable to integrate over and a factor of $(-\mathrm{i})$. In connected diagrams, this applies to all interactions except the last one. We can, however, introduce the same for the last interaction and rewrite (5.42) to

$(-\mathrm{i})$ 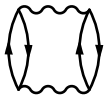

$$= \frac{1}{2} \int\limits_{t_1>t_3} \mathrm{d}t_1 \mathrm{d}t_3 \iiint \mathrm{d}\mathbf{x}_1 \, \mathrm{d}\mathbf{x}_2 \, \mathrm{d}\mathbf{x}_3 \, \mathrm{d}\mathbf{x}_4 \, \delta(t_1) \frac{(-\mathrm{i})}{|\mathbf{r}_1 - \mathbf{r}_2|} \frac{(-\mathrm{i})}{|\mathbf{r}_3 - \mathbf{r}_4|}$$
$$G_0(x_1 t_1, x_3 t_3) \, G_0(x_3 t_3, x_1 t_1) \, G_0(x_2 t_1, x_4 t_3) \, G_0(x_4 t_3, x_2 t_1)$$

Since the propagators G_0 only depend on time differences we no longer explicitly require the times to be negative and we can integrate over the whole domain instead. However, we still require the times to be ordered and we also need to anchor one of the interaction times for a convergent result. Without loss of generality, we choose to fix the last interaction at $t_1 = 0$ by including $\delta(t_1)$.

In the case of the MP2 direct diagram, we can now simply drop the constraints on the time variables taking double counting into consideration:

$(-\mathrm{i})$ 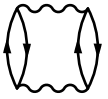

$$= \frac{1}{4} \iint_{-\infty}^{\infty} \mathrm{d}t_1 \mathrm{d}t_3 \iiint \mathrm{d}\mathbf{x}_1 \, \mathrm{d}\mathbf{x}_2 \, \mathrm{d}\mathbf{x}_3 \, \mathrm{d}\mathbf{x}_4 \, \delta(t_1) \frac{(-\mathrm{i})}{|\mathbf{r}_1 - \mathbf{r}_2|} \frac{(-\mathrm{i})}{|\mathbf{r}_3 - \mathbf{r}_4|}$$
$$G_0(x_1 t_1, x_3 t_3) \, G_0(x_3 t_3, x_1 t_1) \, G_0(x_2 t_1, x_4 t_3) \, G_0(x_4 t_3, x_2 t_1)$$

In general, most permutations of the order of the time variables will lead to distinct Goldstone diagrams that we all want to include. This will be discussed in Subsection 5.8.2.

Finally, we introduce time variables on every vertex to arrive at an expression where time and space coordinates are treated on equal footing

$(-\mathrm{i})$ 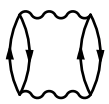

$$= \frac{1}{4} \iiiint_{-\infty}^{\infty} \mathrm{d}t_1 \mathrm{d}t_2 \mathrm{d}t_3 \mathrm{d}t_4 \iiint \mathrm{d}\mathbf{x}_1 \, \mathrm{d}\mathbf{x}_2 \, \mathrm{d}\mathbf{x}_3 \, \mathrm{d}\mathbf{x}_4$$
$$G_0(x_1 t_1, x_3 t_3) \, G_0(x_3 t_3, x_1 t_1) \, G_0(x_4 t_4, x_2 t_2) \, G_0(x_2 t_2, x_4 t_4)$$
$$\delta(t_1) \underbrace{\frac{(-\mathrm{i})}{|\mathbf{r}_1 - \mathbf{r}_2|} \delta(t_1 - t_2)}_{= V(\mathbf{x}_1 t_1, \mathbf{x}_2 t_2)} \frac{(-\mathrm{i})}{|\mathbf{r}_3 - \mathbf{r}_4|} \delta(t_3 - t_4)$$

$$= \frac{1}{4} \iiint \mathrm{d}1 \, \mathrm{d}2 \, \mathrm{d}3 \, \mathrm{d}4 \, \delta(t_1)$$
$$G_0(1,3) \, G_0(3,1) \, V(3,4) \, G_0(4,2) \, G_0(2,4) \, V(2,1) \tag{5.44}$$

defining the propagator for the Coulomb interaction

$$V(\mathbf{x}t, \mathbf{x}'t') := \frac{(-\mathrm{i})}{|\mathbf{r} - \mathbf{r}'|}\,\delta(t - t') \tag{5.45}$$

and the short forms $G_0(1,2) = G_0(\mathbf{x}_1 t_1, \mathbf{x}_2 t_2)$ and $\int \mathrm{d}1 = \int_{-\infty}^{\infty} \mathrm{d}t_1 \int \mathrm{d}\mathbf{r}_1 \sum_{\alpha_1}$. Figure 5.8 shows the coordinate labels used in (5.44) and it is called *Feynman diagram*.

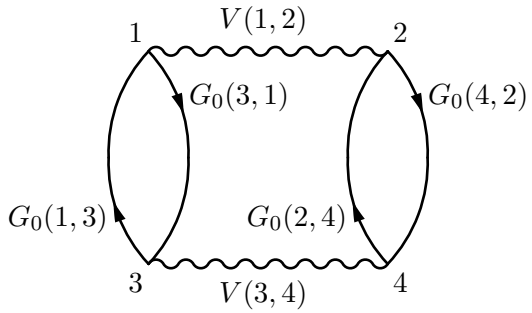

Figure 5.8: In Feynman diagrams, space and time coordinates are integrated over the entire domain and there is no required time order of the Coulomb interactions. Each vertex is given a label denoting its space and time coordinates. The propagator G_0 represents particles or holes propagating between the respective vertices and the propagator V represents Coulomb interactions between vertices. The depicted diagram is the one evaluated in (5.44).

5.8.1 Effective interaction

If the effective interaction is a multiplicative effective potential $\left(\hat{V}_{\mathrm{eff}}\psi_q\right)(\mathbf{x}) = v_{\mathrm{eff}}(\mathbf{x})\psi_q(\mathbf{x})$ we can simply use the potential $v_{\mathrm{eff}}(\mathbf{x})$ to evaluate Feynman diagrams containing effective interactions, respecting its negative sign. For a process involving a single effective interaction to be inserted between the two space-time coordinates 1 and 2 we get for instance

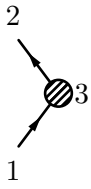

$$= -\int \mathrm{d}3\, G_0(2,3)\, v_{\mathrm{eff}}(3)\, G_0(3,1)\,.$$

5.8.2 Symmetries

When dropping the constraints on the order of the interaction times we get $n!$ permutations of the initial order. We now have to consider, how many of them lead to distinct Goldstone diagrams and in turn to distinct contractions, which we all have to count. Due to symmetries some permutations may lead to the same Goldstone diagram and must not be counted more than once. Figure 5.9 shows the case for a third order diagram, where three of the six possible permutations lead to distinct Goldstone diagrams. This is due to the reflection symmetry when swapping t_1 and t_2, indicated by the dotted line.

The product of the order of all symmetry operations on a certain Feynman diagram is called its *symmetry factor*. In the example in Figure 5.9 there is only one reflection symmetry with the order 2. Thus, the symmetry factor of the considered diagram is 2, which means that

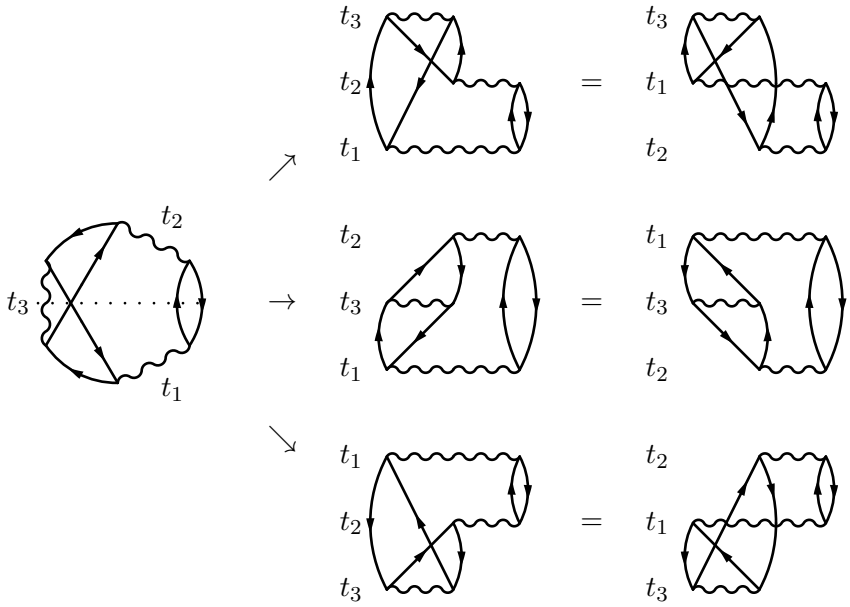

Figure 5.9: One Feynman diagram on the left represents all Goldstone diagrams originating from permutations of its interaction times t_1, t_2 and t_3. Due to the reflection symmetry when swapping t_1 and t_2, indicated by the dotted line, only three of the six permutations give rise to distinct Goldstone diagrams. The symmetry factor is 2 and the diagram must be divided by that upon evaluation.

only half of all the six permutations are distinct. The symmetry factor can be determined graphically or computer aided, considering all permutations of the vertices. For the diagram in Figure 5.8 there are 4 vertices, 2 Bosonic edges B and 4 Fermionic edges F:

$$B = \{\{1,2\},\{3,4\}\}$$
$$F = \{(1,3),(3,1),(2,4),(4,2)\}\,.$$

The Bosonic edges are undirected since swapping the left and the right side of a Coulomb interaction leads to the same Goldstone diagram. The Fermionic edges are directed. The permutation $\tau = \begin{pmatrix} 1 & 2 & 3 & 4 \\ 4 & 3 & 2 & 1 \end{pmatrix}$ is for instance one of four permutations leaving the sets B and F unaltered:

$$\tau(B) = \{\{4,3\},\{2,1\}\} = B$$
$$\tau(F) = \{(4,2),(2,4),(3,1),(1,3)\} = F\,,$$

thus being a symmetry operation. For this diagram, there are two reflection symmetries of order 2 resulting in a symmetry factor of 4. Therefore, the diagram has to be divided by 4 as done in (5.44).

5.8.3 Fermion sign

The Fermion sign of a Goldstone diagram is $(-1)^{l+h}$, where l is the number of Fermion loops and h is the number of hole connections in the entire diagram. In Feynman diagrams, the

negative sign for each hole connection is already contained in the definition of the propagator G_0 in (5.43) for the hole case. Thus, only the number of loops l still needs to be taken into consideration and the Fermion sign of a given Feynman diagram is

$$(-1)^l .$$

Summary

Many-body perturbation theory provides a recipe to approximate the ground state energy of the fully interacting Hamiltonian given the spin orbitals $\psi_p(\mathbf{x})$ and their eigenenergies ε_p of a single body reference, such as Hartree-Fock or DFT. It is derived from time dependent Rayleigh-Schrödinger perturbation theory which makes it extensive and thus applicable to molecules as well as solids. We can write the expansion of the perturbation series leading to the ground state in terms of connected diagrams and we can use either the rules of Goldstone diagrams or the ones of Feynman diagrams to evaluate the individual terms in the expansion.

One Goldstone diagram of order n expands in general to 2^n different contractions originating from swapping the two vertices at each Coulomb interaction. The time order of the interactions is fixed indicated by drawing the Coulomb interactions as parallel wiggly lines. Goldstone diagrams are evaluated by contracting the occurring matrix elements of the Coulomb integrals V_{sr}^{pq}. One Feynman diagram of order n expands in general to $n!$ different Goldstone diagrams arising from all permutations of the order of the interactions. The order of the interactions is not fixed and Coulomb interactions are normally not drawn as parallel lines. Feynman diagrams are evaluated by integrating the spin, space and time coordinates of all its vertices which are arguments to complex valued functions, the propagators, defining its connections.

The symmetry of a diagram determines how many distinct contractions arise from evaluating a single Goldstone or Feynman diagram. In a Goldstone diagram there can only be a global left/right symmetry with a symmetry factor of 2, while in a Feynman diagram more complex symmetries are possible. In both approaches we can define diagrams with open legs as building blocks to be inserted in larger diagrams. In the Goldstone approach this has to be done in a time ordered fashion while in Feynman diagrams it cannot be done in a time ordered way.

Although, many-body perturbation theory is a valuable framework for approximating the ground state energy, it also has several drawbacks. The number of diagrams is still infinite and one can only evaluate a small subset. Using building blocks iteratively allows for evaluating an infinite number of diagrams of a certain class. This improves the results in many cases but there are still infinitely many diagrams neglected that can not be constructed by iterating building blocks. The Random Phase Approximation is a prominent example for this procedure. Another drawback of MBPT is that it requires not only the reference solutions of the unexcited states $\psi_i(x)$ and ε_i but also of the theoretically infinite number of excited states $\psi_a(x)$ and ε_a, called virtual orbitals. The convergence with respect to the number of virtual orbitals if often slow and it easily exceeds twice the number of electrons. Finally, MBPT is not variational and one cannot give an upper bound for the ground state energy as it is given by the Hartree-Fock approximation. The non-variational nature of MBPT also considerably complicates the evaluation of analytic gradients, for instance with respect to the atom positions, i.e. forces.

Chapter 6

The Random Phase Approximation

The Random Phase Approximation (RPA) is one of the most prominent methods beyond Hartree-Fock or DFT. Historically, it has been derived within two different frameworks rather independently. Within Rayleigh-Schrödinger perturbation theory, Heisenberg already noticed that certain processes are diverging in the uniform electron gas due to the vanishing band gap and the sign of the divergence is alternating with the order (Ziesche 2014). In the diagrammatic notation introduced later by Feynman and Goldstone these processes are

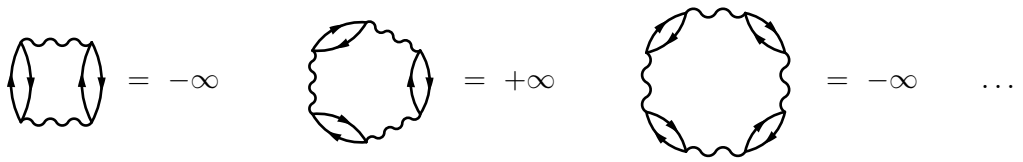

and they are referred to as *ring diagrams*. These divergencies pose serious problems as they render any finite order perturbation theory useless for metals. However, Macke 1950, a student of Heisenberg, found a finite sum of all such diagrams – later to be termed RPA – if one carries out the summation over the perturbation orders before summing over the states in the perturbation expression of each term. This reconciles the use of perturbation theory for metals again. The summation over the perturbation orders can be done by iterating the diagram  as a building block like in a geometric series. Pines and Bohm 1952 developed the RPA independently and coined the term Random Phase Approximation.

With the advent of Quantum Field Theory the procedure of redefining summation orders became more common and was termed *resummation* or *renormalization*. We will not argue in depth whether this procedure is justified. After all, the sum of a conditionally convergent series depends crucially on the order in which the individual terms are summed and – even worse – any result can be achieved just by choosing an appropriate order. However, we can argue that the notion of perturbation order is in a way arbitrary regarding that it solely originates from iteratively solving the equation of motion for the time evolution operator $\hat{U}(t, t_0)$ in (5.14). Therefore, it seems a natural choice to sum over the perturbation order first.

In the scope of Density Functional Theory, RPA has also been derived in the framework of the Adiabatic Connection (AC) (Langreth and Perdew 1977). Both frameworks, AC and many-body perturbation theory, arrive at the same result in the case of the RPA but despite the common use of diagrams in the Adiabatic Connection their meaning differs from Goldstone and Feynman diagrams of many-body perturbation theory discussed in Chapter 5.

From a more applied point of view, RPA poses an important improvement over Hartree-Fock and DFT. Just like finite order perturbation theories, such as Møller–Plesset PT, it can describe van der Waals interaction but unlike its finite order counterparts it can also be applied to metals. Recent developments allow the RPA to be calculated in $\mathcal{O}(N^3)$ steps, just as DFT but with a considerably higher prefactor compared to DFT (Kaltak, Klimeš, and Kresse 2014b).

6.1 RPA in the frequency domain

We will first derive the Random Phase Approximation using many-body perturbation theory in the frequency domain. Given the propagators $G_0(\mathbf{x}t, \mathbf{x}'t')$ and $V(\mathbf{x}t, \mathbf{x}'t')$ of a system according to (5.43) and (5.45), we introduce the matrix notation[1]

$$\mathbf{G}_{0\mathbf{x}\mathbf{x}'}(t-t') := G_0(\mathbf{x}t, \mathbf{x}'t') \quad \text{and} \quad \mathbf{V}_{\mathbf{x}\mathbf{x}'}(t-t') := \frac{(-\mathrm{i})}{|\mathbf{r}-\mathbf{r}'|}\,\delta(t-t'), \tag{6.1}$$

where $\mathbf{x} = (\alpha, \mathbf{r})$. Note that the propagators only depend on the time difference. We define the trace and the matrix product of two propagators $\mathbf{A}$ and $\mathbf{B}$ by

$$\mathrm{tr}\{\mathbf{A}\} := \int \mathrm{d}\mathbf{x}\, \mathbf{A}_{\mathbf{x}\mathbf{x}}\,, \qquad (\mathbf{A}\mathbf{B})_{\mathbf{x}\mathbf{x}''} := \int \mathrm{d}\mathbf{x}'\, \mathbf{A}_{\mathbf{x}\mathbf{x}'}\mathbf{B}_{\mathbf{x}'\mathbf{x}''}\,.$$

Next, we define the *independent particle polarizability* χ_0 as the first building block of the ring diagrams and we let $\mathbf{X}_0$ denote its matrix representation

$$= \chi_0(\mathbf{x}t, \mathbf{x}'t') := -G_0(\mathbf{x}t, \mathbf{x}'t')\, G_0(\mathbf{x}'t', \mathbf{x}t)\,, \quad \mathbf{X}_{0\mathbf{x}\mathbf{x}'}(t-t') := \chi_0(\mathbf{x}t, \mathbf{x}'t'). \tag{6.2}$$

The negative sign is required according to the Fermion sign rule of Feynman diagrams since $\mathbf{X}_0$ is one closed Fermion loop.

From now on, we will connect the building blocks $\mathbf{X}_0$ and $\mathbf{V}$ in series. In the time domain, this corresponds to convolutions while it corresponds to simple products in the frequency domain. Thus, we transform $\mathbf{X}_0$ into the frequency domain with respect to the time difference, giving

$$\mathbf{X}_0(\omega) = \int \mathrm{d}(t-t')\, \mathrm{e}^{+\mathrm{i}\omega(t-t')}\, \mathbf{X}_0(t-t').$$

We use $\mathrm{e}^{+\mathrm{i}\omega(t-t')}$ for the forward Fourier transform into the frequency domain. Using this convention, the poles of the polarizability as a function of ω coincide with the positive elementary excitation energies $\varepsilon_a - \varepsilon_i$ of $\hat{H}_0$. See (6.42) for more details in the case of the uniform electron gas. The Coulomb propagator $\mathbf{V}$ is independent of the frequency.

We can now evaluate the diagrams of the Random Phase Approximation. In (5.44) we already derived an expression for the second order ring diagram in the time domain where $\mathrm{d}i = \mathrm{d}\mathbf{x}_i\, \mathrm{d}t_i$:

$(-\mathrm{i})$ 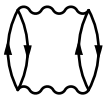

$$= \frac{1}{4} \iiiint \mathrm{d}1\, \mathrm{d}2\, \mathrm{d}3\, \mathrm{d}4\, \delta(t_1)\, \underbrace{G_0(1,3)\, G_0(3,1)}_{=-\chi_0(1,3)}\, V(3,4)\, \underbrace{G_0(4,2)\, G_0(2,4)}_{=-\chi_0(4,2)}\, V(2,1).$$

[1] A matrix with continuous indices is actually an operator. However, for numerical evaluation the coordinates will be discretized justifying a matrix notation for the practical application.

In the frequency domain, there is only one frequency ω to integrate over, since we have only one loop and the frequency is conserved at every vertex. The integral over all frequencies corresponds to a convolution of all time differences rather than absolute times. Therefore, we do not need to anchor the diagram at a certain time anymore, here done by $\delta(t_1)$. Using the matrix notation for the integrals over space we get

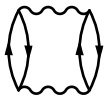

$$= \frac{\mathrm{i}}{4}\int\frac{\mathrm{d}\omega}{2\pi}\,\mathrm{tr}\Big\{\mathbf{X}_0(\omega)\mathbf{V}\mathbf{X}_0(\omega)\mathbf{V}\Big\} = \frac{\mathrm{i}}{4}\int\frac{\mathrm{d}\omega}{2\pi}\,\mathrm{tr}\Big\{(\mathbf{X}_0(\omega)\mathbf{V})^2\Big\}. \tag{6.3}$$

This diagram has two reflection symmetries of order 2. Thus, the symmetry factor of this diagram is 4 giving rise to the factor 1/4 as discussed in Section 5.8. The next diagram in the RPA is the third order ring diagram. It has one reflection symmetry of order 2 and one rotational symmetry of order 3 indicated by the dotted lines. It is therefore given by

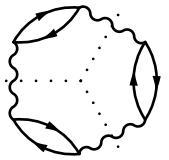

$$= \frac{\mathrm{i}}{2\cdot 3}\int\frac{\mathrm{d}\omega}{2\pi}\,\mathrm{tr}\Big\{(\mathbf{X}_0(\omega)\mathbf{V})^3\Big\}. \tag{6.4}$$

All ring diagrams have a reflection symmetry due the symmetry of the independent particle polarizability $\mathbf{X}_0$. Additionally, each ring diagram of order n has a rotational symmetry of order n, allowing us to evaluate any given order

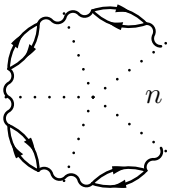

$$= \frac{\mathrm{i}}{2n}\int\frac{\mathrm{d}\omega}{2\pi}\,\mathrm{tr}\Big\{(\mathbf{X}_0(\omega)\mathbf{V})^n\Big\}. \tag{6.5}$$

We can now do the resummation, summing over the orders before evaluating the frequency integration and the trace:

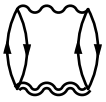

$$= \frac{\mathrm{i}}{2}\int\frac{\mathrm{d}\omega}{2\pi}\,\mathrm{tr}\left\{\sum_{n=2}^{\infty}\frac{1}{n}(\mathbf{X}_0(\omega)\mathbf{V})^n\right\}. \tag{6.6}$$

For the diagrammatic notation of the series we use the *screened interaction* W in RPA given by

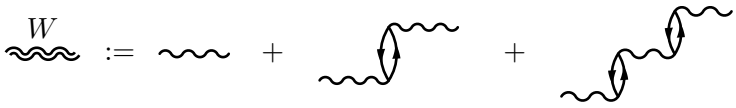

(6.7)

Note that the graphical appearance of a diagram containing the screened interaction W might be deceptive. The eye suggests a simple reflection symmetry of this diagram but in fact the symmetry factor must be considered for each order separately, as we have done it here.

Instead of carrying out the matrix products in (6.6) order by order we search for a matrix function having the same series expansion. The function $\log(1-x)$ has the power series $-x - x^2/2 - x^3/3 - \ldots$ so we can write the RPA energy as

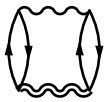

$$= -\frac{\mathrm{i}}{2}\int_{-\infty}^{\infty}\frac{\mathrm{d}\omega}{2\pi}\,\mathrm{tr}\Big\{\log\Big(\mathbf{1}-\mathbf{X}_0(\omega)\mathbf{V}\Big)+\mathbf{X}_0(\omega)\mathbf{V}\Big\}. \tag{6.8}$$

$\mathbf{X}_0(\omega)$ has poles along the real frequency axis making a numerical integration difficult. We can rotate the integration contour as long as we do not cross any poles and use the imaginary frequency instead. This rotation is called *Wick rotation* and it is discussed in more detail for the uniform electron gas in Section 6.4. Given $\mathbf{X}_0(\mathrm{i}\nu)$ in imaginary frequency we can substitute $\omega = \mathrm{i}\nu$ in (6.8) and finally get

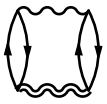

$$= \frac{1}{2}\int_{-\infty}^{\infty}\frac{\mathrm{d}\nu}{2\pi}\,\mathrm{tr}\Big\{\log\Big(\mathbf{1}-\mathbf{X}_0(\mathrm{i}\nu)\mathbf{V}\Big)+\mathbf{X}_0(\mathrm{i}\nu)\mathbf{V}\Big\}. \tag{6.9}$$

For the uniform electron gas (UEG) we can evaluate $\mathbf{X}_0(\mathrm{i}\nu)$ and $\mathbf{V}$ analytically and use (6.9) to evaluate the RPA energy for the UEG numerically. This is done in Section 6.4. For a molecule or a solid $\mathbf{X}_0(\mathrm{i}\nu)$ has to be computed from the Hartree-Fock or DFT spin-orbitals $\psi_p(\mathbf{x})$. Instead of calculating $\mathbf{X}_0(t-t')$ in real time according to (6.2), one can already perform the Wick rotation in the time domain and evaluate

$$\mathbf{X}_{0\mathbf{x}\mathbf{x}'}(\mathrm{i}\tau) = -\mathbf{G}_{0\mathbf{x}\mathbf{x}'}(\mathrm{i}\tau)\mathbf{G}_{0\mathbf{x}'\mathbf{x}}(-\mathrm{i}\tau) \tag{6.10}$$

in imaginary time $\mathrm{i}\tau$. Note that the matrices are multiplied elementwise. The particle/hole propagator in imaginary time is given by

$$\mathbf{G}_{0\mathbf{x}\mathbf{x}'}(\mathrm{i}\tau) = \begin{cases} -\sum_i \psi_i(\mathbf{x})\psi_i^*(\mathbf{x}')\mathrm{e}^{-(\varepsilon_i-\mu)\tau} & \text{for } \tau \leq 0 \\ +\sum_a \psi_a(\mathbf{x})\psi_a^*(\mathbf{x}')\mathrm{e}^{-(\varepsilon_a-\mu)\tau} & \text{otherwise,} \end{cases} \tag{6.11}$$

where μ is the Fermi energy. Evaluating the energies of second order Møller–Plesset Perturbation Theory using the imaginary time propagators is equivalent to the Laplace transformed MP2 approach proposed by Almlöf 1991. To evaluate the Random Phase Approximation $\mathbf{X}_0(\mathrm{i}\tau)$ needs to be Fourier transformed with respect to τ to arrive at the independent particle polarizability in imaginary frequency $\mathbf{X}_0(\mathrm{i}\nu)$ employed by (6.9). The Fourier transform from imaginary time to imaginary frequency, as well as the imaginary frequency integration in (6.9) can be done numerically on a non-equidistant grid to high accuracy with a only few integration points as proposed by Kaltak, Klimeš, and Kresse 2014b. To determine the employed quadrature frequencies and weights a function is chosen that resembles the RPA energy function and whose exact frequency integral is known. The proposed function of imaginary time is the direct MP2 term

$$\frac{1}{2}\int\frac{\mathrm{d}\nu}{2\pi}\,\frac{2(\varepsilon_a-\varepsilon_i)}{(\varepsilon_a-\varepsilon_i)^2+\nu^2}\,\frac{2(\varepsilon_b-\varepsilon_j)}{(\varepsilon_b-\varepsilon_j)^2+\nu^2} = \frac{1}{\varepsilon_i+\varepsilon_j-\varepsilon_a-\varepsilon_b},$$

which is the lowest order of the RPA expansion. The quadrature frequencies ν_k and weights w_k can then be fitted such that the dominant terms with $a=b$ and $i=j$ are best reproduced by the numeric integral

$$\frac{1}{\varepsilon_i+\varepsilon_i-\varepsilon_a-\varepsilon_a} \approx \frac{1}{2}\sum_k w_k\left(\frac{2(\varepsilon_a-\varepsilon_i)}{(\varepsilon_a-\varepsilon_i)^2+\nu_k^2}\right)^2. \tag{6.12}$$

This fit is done for all single particle excitation energies $\varepsilon_a-\varepsilon_i$ and the quality of the fit depends on the ratio of the largest and the smallest excitation energy $\max(\varepsilon_a-\varepsilon_i)/\min(\varepsilon_a-\varepsilon_i)$. For

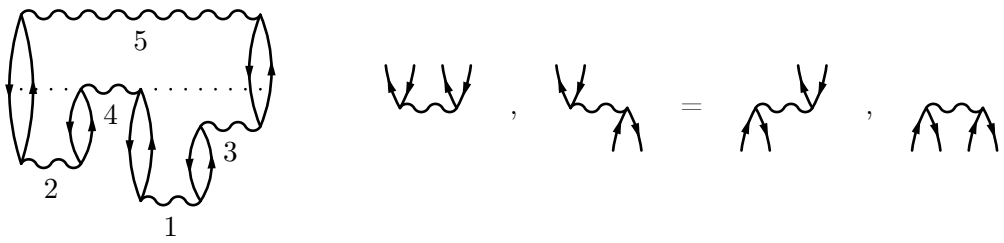

Figure 6.1: Goldstone diagram of an RPA ring diagram forming a closed loop. Each Coulomb interaction is connected to the ring in one of four possible ways of which three are distinct.

a non-metallic system the number of frequency points is negligible compared to the number of possible excitations, required in the conventional approach to calculate $\mathbf{X}_0$ from the Adler-Wiser formula (Adler 1962; Wiser 1963). The above frequency grid allows the RPA energy to be evaluated in $\mathcal{O}(N^3)$ steps, just like DFT but with a considerably higher prefactor (Kaltak, Klimeš, and Kresse 2014a). For a metallic system the behavior of the RPA energy for large imaginary frequencies is important for an accurate numerical quadrature. This is discussed in the end of Section 6.4.

6.2 Direct Ring Coupled Cluster Doubles

The Random Phase Approximation can also be evaluated using the matrix elements of the Coulomb integral

$$V_{sr}^{pq} = \iint \mathrm{d}\mathbf{x}\mathrm{d}\mathbf{x}'\, \psi_p^*(\mathbf{x})\psi_q^*(\mathbf{x}')\, \frac{1}{|\mathbf{r}-\mathbf{r}'|}\, \psi_r(\mathbf{x}')\psi_s(\mathbf{x})$$

rather than the propagators G_0 and V. This approach is not as efficient as the imaginary frequency approach, however, an important correction to the error remaining in the RPA is based on this approach.

The RPA ring diagrams form a closed loop and Figure 6.1 shows the Goldstone diagram of one such ring diagram. As discussed in Section 5.4, connected vertices represent contractions and we need to integrate over the time interval between Coulomb interactions. We will do that from bottom to top following the left and the right particle/hole pairs along the loop. In the diagram given as example in Figure 6.1 we start with interaction 1 following the left and the right particle/hole pairs to interaction 3. There, the right pair is contracted at one vertex and a new pair to follow on the right side emerges on the other vertex of interaction 3. Independently, we also follow the left and the right particle/hole pairs starting at interaction 2. At interaction 4 the two processes merge such that there is only one left pair and one right pair remaining after the time indicated by the dotted line. At interaction 5 both pairs are finally contracted and the loop is closed. This procedure is analogous to the one employed for deriving the Fermion sign of Goldstone diagrams in Subsection 5.4.3.

While following the left and the right particle/hole pairs we perform all occurring contractions and integrals over the respective time intervals and we keep the intermediate results in a matrix t_{ij}^{ab} depending on the states of two particle/hole pairs, diagrammatically denoted by

$$t_{ij}^{ab} \;=\; \overset{a\ \ i\ \ b\ \ j}{\vee\ \ \vee} \;.$$

t_{ij}^{ab} is called *direct ring Coupled Cluster Doubles (drCCD) amplitudes* and it contains the probability amplitude to arrive at two particle/hole pairs in the given states in any of the possible ways forming the ring diagrams. We will now go through all cases, shown on the right of Figure 6.1, that can occur following the left and the right particle/hole pair from bottom to top.

In the first case, a Coulomb interaction creates two new particle/hole pairs as in interaction 1 in Figure 6.1. This can occur at any time in the past so we need to integrate over the time interval between the Coulomb interaction and the time where we want to use the probability amplitudes t_{ij}^{ab}, which we always place at $t = 0$. One contribution to the drCCD amplitudes is thus

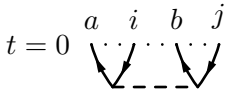

$$t_{ij}^{ab} = (-\mathrm{i}) \int_{-\infty}^{0} \mathrm{d}t\, \mathrm{e}^{\eta t}\, \mathrm{e}^{\varepsilon_a t}\, \mathrm{e}^{\varepsilon_b t}\, \mathrm{e}^{-\varepsilon_i t}\, \mathrm{e}^{-\varepsilon_j t}\, V_{ij}^{ab} + \ldots$$

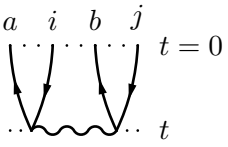

$$= \frac{V_{ij}^{ab}}{\varepsilon_i + \varepsilon_j - \varepsilon_a - \varepsilon_b + \mathrm{i}\eta} + \ldots \tag{6.13}$$

In the next case, a Coulomb interaction contracts the right particle/hole pair creating a new one. This is the case for interaction 3 in Figure 6.1. We can now use the drCCD amplitudes recursively containing all processes until the time of the interaction. The time interval between the interaction and the time where we want to use the updated drCCD amplitudes still needs to be integrated over as before. The second contribution to the drCCD amplitudes is thus

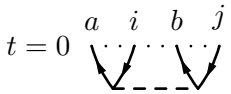

$$t_{ij}^{ab} = \ldots + \frac{\sum_{kc} t_{ik}^{ac} V_{cj}^{kb}}{\varepsilon_i + \varepsilon_j - \varepsilon_a - \varepsilon_b + \mathrm{i}\eta} + \ldots$$

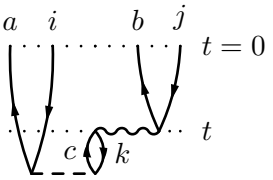

(6.14)

The Fermion sign of this contribution is positive since there is one more hole and one more closed Fermion loop. Note however, that the denominator is negative giving rise to the alternating sign when evaluating the RPA order by order. The same case can occur for the left particle/hole pair giving

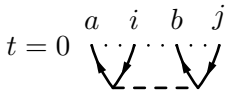

$$t_{ij}^{ab} = \ldots + \frac{\sum_{kc} V_{ic}^{ak} t_{kj}^{cb}}{\varepsilon_i + \varepsilon_j - \varepsilon_a - \varepsilon_b + \mathrm{i}\eta} + \ldots$$

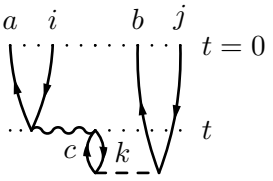

(6.15)

The last case occurs when two independent processes merge at a Coulomb interaction, as in interaction 4 of Figure 6.1. In this contribution, the drCCD amplitudes occur in a quadratic form on the right hand side

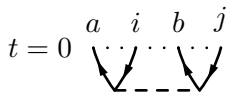

$$t_{ij}^{ab} = \ldots + \frac{\sum_{klcd} t_{ik}^{ac} V_{cd}^{kl} t_{lj}^{db}}{\varepsilon_i + \varepsilon_j - \varepsilon_a - \varepsilon_b + \mathrm{i}\eta}\,.$$

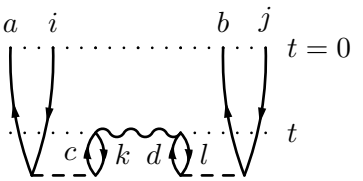

(6.16)

Taking all contribution (6.13) to (6.16) into consideration and taking the limit $\eta \to 0$ yields the drCCD amplitudes equation

$$(\varepsilon_i + \varepsilon_j - \varepsilon_a - \varepsilon_b)\, t_{ij}^{ab} = V_{ij}^{ab} + \sum_{kc} t_{ik}^{ac} V_{cj}^{kb} + \sum_{kc} V_{ic}^{ak} t_{kj}^{cb} + \sum_{klcd} t_{ik}^{ac} V_{cd}^{kl} t_{lj}^{db} \,. \tag{6.17}$$

This equation is quadratic and can only be solved by iteration. The convergence with respect to the number of iterations is, however, fast. Employing a Shanks transform to accelerate series convergence, 8 iterations are sufficient to yield a converged RPA energy to 5 significant digits of precision even for a system with a low band gap, such as a finite size uniform electron gas (Freeman 1977; Shanks 1955). Each iteration is still costly requiring $\mathcal{O}(N^5)$ steps. The iteration process also requires the amplitudes to be stored demanding $\mathcal{O}(N^4)$ of memory.

Given the drCCD amplitudes, we can evaluate the RPA energy by contracting both particle/hole pairs with the last Coulomb interaction, corresponding to interaction 5 in Figure 6.1. The drCCD amplitudes have a left/right reflection symmetry. The RPA energy is thus

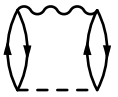

$$= \frac{1}{2} \sum_{ijab} t_{ij}^{ab} V_{ab}^{ij} \,, \tag{6.18}$$

where the two closing Fermion loops result in a positive Fermion sign.

In this approach the time order is always maintained by the way the drCCD amplitudes are recursively defined. Therefore, no particular symmetries have to be considered apart from the reflection symmetry. Ring diagrams that have more than two particle/hole pairs at some instances in time arise from the quadratic contribution (6.16). This is the case for the diagram in Figure 6.1 between interaction 2 and 4. Excluding the quadratic contribution (6.16) gives the *Tamm-Dancoff Approximation (TDA)*, which is the subset of all RPA ring diagrams where there are exactly two particle/hole pairs at all times between the first and the last interaction. From (6.16) and (6.13) follows that the lowest order diagram of RPA that is not part of TDA is of fourth order.

On the other hand, the drCCD amplitude equations are a subset of the amplitude equations including all possible ways to arrive at two particle/hole pairs. These amplitude equations are called *Coupled Cluster Singles Doubles (CCSD) amplitudes* and they contain processes such as

.

Unfortunately, it is computationally more time consuming to calculate the full CCSD amplitudes, scaling like $\mathcal{O}(N^6)$, since the employed tensor multiplications cannot be split into pieces, involving no more than 5 indices. For the calculation of the drCCD amplitudes this can be done since the matrix of the Coulomb interaction V_{sr}^{pq} can be decomposed into a product of two tensors with 3 indices in the momentum basis:

$$V_{sr}^{pq} = \int \frac{\mathrm{d}\mathbf{G}}{(2\pi)^3}\, \chi_s^p(\mathbf{G})\, \chi_q^{r*}(\mathbf{G}) \,, \quad \text{with } \chi_q^p(\mathbf{G}) = \int \mathrm{d}\mathbf{x}\, \frac{\sqrt{4\pi}}{|\mathbf{G}|}\, \psi_p^*(\mathbf{x}) \mathrm{e}^{\mathbf{i}\mathbf{G}\cdot\mathbf{r}} \psi_q(\mathbf{x}) \,. \tag{6.19}$$

This allows tensor products involving V_{sr}^{pq} to be "cut" at the Coulomb line, accelerating the evaluation of the direct ring Coupled Cluster Doubles amplitudes to $\mathcal{O}(N^5)$. For the first

non-trivial case in (6.17), this is done, for instance, by

$$\sigma_i^a(\mathbf{G}) = \sum_{ck} t_{ik}^{ac} \chi_c^k(\mathbf{G})\,, \qquad (\varepsilon_i + \varepsilon_j - \varepsilon_a - \varepsilon_b)\, t_{ij}^{ab} = \ldots + \int \frac{\mathrm{d}\mathbf{G}}{(2\pi)^3}\, \sigma_i^a(\mathbf{G}) \chi_b^{j*}(\mathbf{G}) + \ldots$$

The Coupled Cluster method was developed by Coester and Kümmel 1960 for the atomic nucleus and later adopted for electronic correlation by Čížek 1969.

6.3 RPA from the Adiabatic Connection

In the framework of many-body perturbation theory the derivation of the Random Phase Approximation is straight forward. According to the last two sections it can be done either in the frequency domain employing Feynman diagrams and regarding the symmetries of the ring diagrams or in the time domain employing Goldstone diagrams. In Chapter 5 the equivalence of the two approaches was discussed.

Despite the straight forward derivations and the general applicability of many-body perturbation theory to arbitrary reference systems, neither of the two previously discussed derivations are considered standard approaches to the Random Phase Approximation. In this section we discuss the framework of the Adiabatic Connection (AC) employed by Langreth and Perdew 1977, which is considered the standard approach to the RPA, at least in solid state physics.

In the Adiabatic Connection (AC) we define a Hamiltonian $\hat{H}(\lambda)$ depending on a coupling constant λ specifying the strength of the full electron-electron Coulomb interaction

$$\hat{H}(\lambda) = \hat{T} + \hat{V}_{\mathrm{ne}} + \hat{V}_{\mathrm{eff}}(\lambda) + \lambda \hat{V}_{\mathrm{ee}}\,, \quad \text{with } 0 \leq \lambda \leq 1\,. \tag{6.20}$$

The effective interaction $\hat{V}_{\mathrm{eff}}(\lambda)$ also depends on the coupling constant and we choose $\hat{V}_{\mathrm{eff}}(\lambda)$ such that the density of the system with the Hamiltonian $\hat{H}(\lambda)$ is for all λ equivalent to the density of the fully interacting system with the Hamiltonian $\hat{H}(1)$. This is in contrast to many-body perturbation theory where the effective interaction is simply scaled by the factor $1-\lambda$ according to (5.15) and where λ is time dependent. Requiring a constant density for all λ is a strong condition implying that the density of the reference system with the Hamiltonian $\hat{H}(0)$ is equivalent to the density of the fully interacting system. Although this condition is met to a good degree by using a DFT Hamiltonian for $\hat{H}(0)$, the Hohenberg-Kohn theorem only states the existence of such an effective potential $\hat{V}_{\mathrm{eff}}(\lambda)$. For practical considerations no DFT density fully agrees with the density of the respective fully interacting system in general.

Let now $\Psi(\lambda)$ denote the normalized ground state of the respective Hamiltonian $\hat{H}(\lambda)$, being the solution of

$$\hat{H}(\lambda)\,|\Psi(\lambda)\rangle = E\,|\Psi(\lambda)\rangle\,.$$

The ground state energy E is equivalent for all λ since E is a functional of the density according to the Hohenberg-Kohn theorem and the density is the same for all λ. Even assuming that the density $n(\mathbf{x})$ of the DFT reference is exact, we can only directly evaluate the nuclei-electron potential energy E_{ne} as the functionals for the kinetic energy T and for the electron-electron potential energy E_{ee} are unknown:

$$E[n(\mathbf{x})] = T[n(\mathbf{x})] + E_{\mathrm{ne}}[n(\mathbf{x})] + E_{\mathrm{ee}}[n(\mathbf{x})].$$

However, we are only interested in the sum of the kinetic and the potential energy so we may as well use the known kinetic energy of the Kohn-Sham system

$$T_{\mathrm{S}} = \Big\langle \Psi(0) \Big| \sum_{n=1}^{N} \frac{-\nabla_n^2}{2} \Big| \Psi(0) \Big\rangle$$

and ask for the energy to be added to T_{S} and E_{ne} to arrive at the same total energy E. This energy is called *Hartree-exchange-correlation energy* and it is given by

$$E_{\mathrm{Hxc}} = E - E_{\mathrm{ne}} - T_{\mathrm{S}} \,.$$

Using (6.20) we can express the terms above by expectation values of the fully and the non-interacting Hamiltonian:

$$\begin{aligned} E - E_{\mathrm{ne}} &= \langle \Psi(1) | \hat{H}(1) | \Psi(1) \rangle - \langle \Psi(1) | \hat{V}_{\mathrm{ne}} + \hat{V}_{\mathrm{eff}}(1) | \Psi(1) \rangle \\ T_{\mathrm{S}} &= \langle \Psi(0) | \hat{H}(0) | \Psi(0) \rangle - \langle \Psi(0) | \hat{V}_{\mathrm{ne}} + \hat{V}_{\mathrm{eff}}(0) | \Psi(0) \rangle \,, \end{aligned}$$

noting that $\hat{V}_{\mathrm{eff}}(1) = \hat{0}$ and $\hat{V}_{\mathrm{eff}}(0)$ is the effective potential of the Kohn-Sham system. This allows us to make the connection between the fully interacting and the non-interacting system

$$E_{\mathrm{Hxc}} = \int_0^1 \mathrm{d}\lambda \, \frac{\mathrm{d}}{\mathrm{d}\lambda} \, \langle \Psi(\lambda) | \hat{H}(\lambda) - \hat{V}_{\mathrm{ne}} - \hat{V}_{\mathrm{eff}}(\lambda) | \Psi(\lambda) \rangle. \tag{6.21}$$

Since $\Psi(\lambda)$ is the ground state of $\hat{H}(\lambda)$, we can use the Güttinger 1932 theorem, also known as Hellman-Feynman theorem, to evaluate the total derivative of the expectation values involving the Hamiltonian:

$$\frac{\mathrm{d}}{\mathrm{d}\lambda} \, \langle \Psi(\lambda) | \hat{H}(\lambda) | \Psi(\lambda) \rangle = \Big\langle \Psi(\lambda) \Big| \frac{\mathrm{d}}{\mathrm{d}\lambda} \, \hat{H}(\lambda) \Big| \Psi(\lambda) \Big\rangle. \tag{6.22}$$

Furthermore, $\hat{V}_{\mathrm{ne}}$ and $\hat{V}_{\mathrm{eff}}(\lambda)$ are local potentials and their expectation value only depends on the electron density $n(\mathbf{x})$. Since the density is constant for all λ the total derivate of their respective expectation value simplifies to

$$\frac{\mathrm{d}}{\mathrm{d}\lambda} \, \langle \Psi(\lambda) | \hat{V}_{\mathrm{ne}} | \Psi(\lambda) \rangle = 0 \tag{6.23}$$

$$\frac{\mathrm{d}}{\mathrm{d}\lambda} \, \langle \Psi(\lambda) | \hat{V}_{\mathrm{eff}}(\lambda) | \Psi(\lambda) \rangle = \Big\langle \Psi(\lambda) \Big| \frac{\mathrm{d}}{\mathrm{d}\lambda} \, \hat{V}_{\mathrm{eff}}(\lambda) \Big| \Psi(\lambda) \Big\rangle \,. \tag{6.24}$$

Inserting the total derivatives into (6.21) yields the final expression for the Hartree-exchange-correlation energy in the Adiabatic Connection:

$$E_{\mathrm{Hxc}} = \int_0^1 \mathrm{d}\lambda \, \langle \Psi(\lambda) | \hat{V}_{\mathrm{ee}} | \Psi(\lambda) \rangle \,. \tag{6.25}$$

In other words, the Hartree-exchange-correlation energy is the coupling strength averaged potential electron-electron energy.

6.3.1 Fluctuation dissipation theorem

Equation (6.25) cannot be evaluated directly since the ground states $\Psi(\lambda)$ are not available for any λ except 0. However, the whole information of the many-body wave function $\Psi(\lambda)$ is not required to evaluate the Coulomb operator. The pair density $n^2(\mathbf{x}, \mathbf{x}')$ is sufficient:

$$\begin{aligned}\langle\Psi|\hat{V}_{\mathrm{ee}}|\Psi\rangle &= \int \mathrm{d}\mathbf{x}_1 \ldots \int \mathrm{d}\mathbf{x}_N \, \Psi^*(\mathbf{x}_1, \ldots, \mathbf{x}_N) \, \frac{1}{2} \sum_{n \neq m} \frac{1}{|\mathbf{r}_n - \mathbf{r}_m|} \, \Psi(\mathbf{x}_1, \ldots, \mathbf{x}_N) \\ &= \frac{1}{2} \int \mathrm{d}\mathbf{x} \int \mathrm{d}\mathbf{x}' \, \frac{1}{|\mathbf{r} - \mathbf{r}'|} \underbrace{\int \mathrm{d}\mathbf{x}_1 \ldots \int \mathrm{d}\mathbf{x}_N \, \Psi^*(\ldots) \sum_{n \neq m} \delta(\mathbf{x} - \mathbf{x}_n) \delta(\mathbf{x}' - x_m) \, \Psi(\ldots)}_{= n^2(\mathbf{x}, \mathbf{x}')}\end{aligned}$$

The pair density can be written in terms of unrestricted summations

$$\begin{aligned}n^2(\mathbf{x}, \mathbf{x}') &= \left\langle \Psi \middle| \sum_{n \neq m} \delta(\mathbf{x} - \mathbf{x}_n) \delta(\mathbf{x}' - \mathbf{x}_m) \middle| \Psi \right\rangle \\ &= \left\langle \Psi \middle| \sum_{nm} \delta(\mathbf{x} - \mathbf{x}_n) \delta(\mathbf{x}' - \mathbf{x}_m) \middle| \Psi \right\rangle - \underbrace{\left\langle \Psi \middle| \sum_{n} \delta(\mathbf{x} - \mathbf{x}') \delta(\mathbf{x} - \mathbf{x}_n) \middle| \Psi \right\rangle}_{= \delta(\mathbf{x} - \mathbf{x}') n(\mathbf{x})},\end{aligned}$$

which allows us to relate it to the density fluctuation operator $\delta\hat{n}(x) = \sum_n \delta(\mathbf{x} - \mathbf{x}_n) - n(x)$, since

$$\begin{aligned}\langle\Psi|\delta\hat{n}(\mathbf{x})\delta\hat{n}(\mathbf{x}')|\Psi\rangle &= \left\langle \Psi \middle| \sum_{n} \delta(\mathbf{x} - \mathbf{x}_n) \sum_{m} \delta(\mathbf{x}' - \mathbf{x}_m) \middle| \Psi \right\rangle + n(\mathbf{x}) n(\mathbf{x}') \\ &\quad - \underbrace{\left\langle \Psi \middle| \sum_{n} \delta(\mathbf{x} - \mathbf{x}_n) \middle| \Psi \right\rangle}_{= n(\mathbf{x})} n(\mathbf{x}') - n(\mathbf{x}) n(\mathbf{x}') \, .\end{aligned}$$

The pair density and the density fluctuation operator are thus related by

$$n^2(\mathbf{x}, \mathbf{x}') = \langle\Psi|\delta\hat{n}(\mathbf{x})\delta\hat{n}(\mathbf{x}')|\Psi\rangle + n(\mathbf{x}) n(\mathbf{x}') - \delta(\mathbf{x} - \mathbf{x}') n(\mathbf{x}) \, . \tag{6.26}$$

Note that although $\langle\Psi|\delta\hat{n}(\mathbf{x})|\Psi\rangle$ is zero, the expectation value of a quadratic form of the density fluctuation operator is in general non-zero. The fluctuation dissipation theorem (Callen and Welton 1951) links the density-density fluctuations at the two sites $\mathbf{x}$ and $\mathbf{x}'$ occurring in (6.26) to the density-density response function $\chi_\lambda(\mathbf{x}, \mathbf{x}', \mathrm{i}\nu)$ of the system with the coupling strength λ, here given in imaginary frequency (Harl 2008):

$$-\int \frac{\mathrm{d}\nu}{2\pi} \, \chi_\lambda(\mathbf{x}, \mathbf{x}', \mathrm{i}\nu) = \langle\Psi(\lambda)|\delta\hat{n}(\mathbf{x})\delta\hat{n}(\mathbf{x}')|\Psi(\lambda)\rangle \, . \tag{6.27}$$

With time dependent density functional theory (TDDFT) we can finally connect the density-density response function χ_λ of the system with a coupling strength λ to the density-density response function χ_0 of the DFT reference system (Gross and Kohn 1985; Harl 2008)

$$\begin{aligned}\chi_\lambda(\mathbf{x}_1, \mathbf{x}_4, \mathrm{i}\nu) = \; & \chi_0(\mathbf{x}_1, \mathbf{x}_4, \mathrm{i}\nu) \\ & + \iint \mathrm{d}\mathbf{x}_2 \mathrm{d}\mathbf{x}_3 \, \chi_0(\mathbf{x}_1, \mathbf{x}_2, \mathrm{i}\nu) \left(\frac{\lambda}{|\mathbf{r}_2 - \mathbf{r}_3|} + f_{\mathrm{xc}}^\lambda(\mathbf{x}_2, \mathbf{x}_3, \mathrm{i}\nu) \right) \chi_\lambda(\mathbf{x}_3, \mathbf{x}_4, \mathrm{i}\nu) \, ,\end{aligned} \tag{6.28}$$

where the Coulomb interaction is scaled by λ. f_{xc}^{λ} is called *exchange-correlation kernel* and it contains the change of the DFT effective potential with respect to a change in the electron density. f_{xc}^{λ} is not explicitly known and it is coupling strength dependent. (6.28) is an implicit integral equation for χ_λ called *Dyson-like equation*. It requires that the density response of the interacting system to a change of the external potential is the same as the density response of the DFT reference system to a change of the effective potential. This assumption is the TDDFT counterpart of the assumption that the DFT density is exact.

The response function of the DFT reference system χ_0 can be evaluated from the DFT spin-orbitals $\psi_p(\mathbf{x})$ with second order perturbation theory:

$$\chi_0(\mathbf{x}, \mathbf{x}', \mathrm{i}\nu) = -\sum_{ia} \left(\frac{\psi_a(\mathbf{x})\psi_a^*(\mathbf{x}')\psi_i(\mathbf{x}')\psi_i^*(\mathbf{x})}{\varepsilon_a - \varepsilon_i - \mathrm{i}\nu} + \text{c.c.} \right). \tag{6.29}$$

See (6.46) for an analogous derivation of the above result for the uniform electron gas. Note that the definition of χ_0 given in this section expects the Coulomb propagator to be $1/|\mathbf{r} - \mathbf{r}'|$. This differs from the convention used elsewhere in this work and has been chosen for consistency of this section with literature. In (6.52) this is discussed in detail. The above definition further assumes a spin-unrestricted reference and an imaginary frequency integration over the entire domain from $-\infty$ to ∞.

Using (6.25), (6.26) and (6.27) the Hartree-exchange-correlation energy is given by

$$\begin{aligned} E_{\text{Hxc}} &= \frac{1}{2}\int_0^1 \mathrm{d}\lambda \int \mathrm{d}\mathbf{x} \int \mathrm{d}\mathbf{x}' \frac{1}{|\mathbf{r} - \mathbf{r}'|} \left(n(\mathbf{x})n(\mathbf{x}') - \delta(\mathbf{x} - \mathbf{x}')n(\mathbf{x}) - \int \frac{\mathrm{d}\nu}{2\pi} \chi_\lambda(\mathbf{x}, \mathbf{x}', \mathrm{i}\nu) \right) \\ &= E_{\text{H}} + \frac{1}{2}\int_0^1 \mathrm{d}\lambda \int \mathrm{d}\mathbf{x} \int \mathrm{d}\mathbf{x}' \frac{1}{|\mathbf{r} - \mathbf{r}'|} \left(-\delta(\mathbf{x} - \mathbf{x}')n(\mathbf{x}) - \int \frac{\mathrm{d}\nu}{2\pi} \chi_\lambda(\mathbf{x}, \mathbf{x}', \mathrm{i}\nu) \right), \end{aligned} \tag{6.30}$$

where the Hartree energy E_{H} is readily factored out. To tackle the remaining Dirac delta function we rewrite $n(\mathbf{x}) = \sum_i \psi_i(\mathbf{x})\psi_i^*(\mathbf{x})$ in the context of the delta function and then use the completeness of the eigenstates $\psi_p(\mathbf{x})$:

$$\begin{aligned} \delta(\mathbf{x} - \mathbf{x}')n(\mathbf{x}) &= \delta(\mathbf{x} - \mathbf{x}') \sum_i \psi_i(\mathbf{x}')\psi_i^*(\mathbf{x}) \;=\; \sum_{pi} \psi_p(\mathbf{x})\psi_p^*(\mathbf{x}')\psi_i(\mathbf{x}')\psi_i^*(\mathbf{x}) \\ &= \sum_{ji} \psi_j(\mathbf{x})\psi_j^*(\mathbf{x}')\psi_i(\mathbf{x}')\psi_i^*(\mathbf{x}) + \sum_{ai} \psi_a(\mathbf{x})\psi_a^*(\mathbf{x}')\psi_i(\mathbf{x}')\psi_i^*(\mathbf{x}). \end{aligned} \tag{6.31}$$

The first sum over unexcited states can be inserted into (6.30) and factored out giving the *exact exchange* energy

$$E_{\text{x}} = -\frac{1}{2}\int \mathrm{d}\mathbf{x} \int \mathrm{d}\mathbf{x}' \sum_{ij} \frac{\psi_j(\mathbf{x})\psi_j^*(\mathbf{x}')\psi_i(\mathbf{x}')\psi_i^*(\mathbf{x})}{|\mathbf{r} - \mathbf{r}'|}.$$

The exact exchange energy corresponds to the first order diagram in many-body perturbation theory, given in (5.28), with the Kohn-Sham spin-orbitals $\psi_p(\mathbf{x})$ as reference system.

The second sum in (6.31) over excited and unexcited states is the integral of $\chi_0(\mathbf{x}, \mathbf{x}', \mathrm{i}\nu)$ given in (6.29) over all imaginary frequencies for real orbitals:

$$\int \frac{\mathrm{d}\nu}{2\pi} \chi_0(\mathbf{x}, \mathbf{x}', \mathrm{i}\nu) = -\sum_{ia} \psi_a(\mathbf{x})\psi_a^*(\mathbf{x}')\psi_i(\mathbf{x}')\psi_i^*(\mathbf{x}).$$

The above result can also be obtained evaluating $\chi_0(\mathbf{x}, \mathbf{x}', \mathrm{i}\tau)$ using imaginary time propagators according to (6.10) and (6.11) and then taking the limit $\tau \to 0^+$. Finally, we can insert the exact exchange energy and the above expression into (6.30) to arrive at an expression for the correlation energy:

$$E_\mathrm{c} = -\frac{1}{2}\int_0^1 \mathrm{d}\lambda \int \mathrm{d}\mathbf{x} \int \mathrm{d}\mathbf{x}' \frac{1}{|\mathbf{r}-\mathbf{r}'|} \int \frac{\mathrm{d}\nu}{2\pi} \left(\chi_\lambda(\mathbf{x}, \mathbf{x}', \mathrm{i}\nu) - \chi_0(\mathbf{x}, \mathbf{x}', \mathrm{i}\nu)\right), \tag{6.32}$$

where $E_\mathrm{Hxc} = E_\mathrm{H} + E_\mathrm{x} + E_\mathrm{c}$.

6.3.2 Random Phase Approximation of the polarizability

The Dyson-like equation (6.28) for the polarizability $\chi_\lambda(\mathbf{x}, \mathbf{x}', \mathrm{i}\nu)$ can be written in the matrix notation introduced in Section 6.1

$$\mathbf{X}_\lambda(\mathrm{i}\nu) = \mathbf{X}_0(\mathrm{i}\nu) + \mathbf{X}_0(\mathrm{i}\nu)\left(\lambda\mathbf{V} + \mathbf{F}_\mathrm{xc}^\lambda(\mathrm{i}\nu)\right)\mathbf{X}_\lambda(\mathrm{i}\nu)\,. \tag{6.33}$$

In the Random Phase Approximation one considers only the Hartree term in the time dependent Density Functional Theory derivation of the above Dyson-like equation, neglecting the exchange correlation kernel $\mathbf{F}_\mathrm{xc}^\lambda$. The polarizability can then be expanded to

$$\mathbf{X}_\lambda(\mathrm{i}\nu) = \mathbf{X}_0(\mathrm{i}\nu) + \lambda\mathbf{X}_0(\mathrm{i}\nu)\mathbf{V}\mathbf{X}_0(\mathrm{i}\nu) + \lambda^2\mathbf{X}_0(\mathrm{i}\nu)\mathbf{V}\mathbf{X}_0(\mathrm{i}\nu)\mathbf{V}\mathbf{X}_0(\mathrm{i}\nu) + \ldots$$

Writing (6.32) in the matrix notation and inserting the above expansion gives

$$\begin{aligned} E_\mathrm{c} =& -\frac{1}{2}\int_0^1 \mathrm{d}\lambda \int \frac{\mathrm{d}\nu}{2\pi} \mathrm{tr}\big\{\mathbf{X}_\lambda(\mathrm{i}\nu)\mathbf{V} - \mathbf{X}_0(\mathrm{i}\nu)\mathbf{V}\big\} \\ =& -\frac{1}{2}\int_0^1 \mathrm{d}\lambda \int \frac{\mathrm{d}\nu}{2\pi} \mathrm{tr}\left\{\lambda\big(\mathbf{X}_0(\mathrm{i}\nu)\mathbf{V}\big)^2 + \lambda^2\big(\mathbf{X}_0(\mathrm{i}\nu)\mathbf{V}\big)^3 + \ldots\right\}. \end{aligned} \tag{6.34}$$

The explicitly known λ dependency allows us to integrate λ analytically, which leads to the final expression of the correlation energy in the Random Phase Approximation:

$$\begin{aligned} E_\mathrm{c}^\mathrm{RPA} =& -\frac{1}{2}\int \frac{\mathrm{d}\nu}{2\pi} \mathrm{tr}\left\{\frac{1}{2}\big(\mathbf{X}_0(\mathrm{i}\nu)\mathbf{V}\big)^2 + \frac{1}{3}\big(\mathbf{X}_0(\mathrm{i}\nu)\mathbf{V}\big)^3 + \ldots\right\} \\ =& +\frac{1}{2}\int \frac{\mathrm{d}\nu}{2\pi} \mathrm{tr}\Big\{\log\Big(\mathbf{1} - \mathbf{X}_0(\mathrm{i}\nu)\mathbf{V}\Big) + \mathbf{X}_0(\mathrm{i}\nu)\mathbf{V}\Big\}. \end{aligned} \tag{6.35}$$

This result is formally equivalent to (6.9) although two very different approaches have been used in the respective derivations. The prescribed Hartree E_H and exact-exchange term E_x also correspond to the two first order diagrams in many-body perturbation theory using a non-Hartree-Fock reference. Note however, that the factors in the series expansion

$$\frac{1}{2}\big(\mathbf{X}_0(\mathrm{i}\nu)\mathbf{V}\big)^2 + \frac{1}{3}\big(\mathbf{X}_0(\mathrm{i}\nu)\mathbf{V}\big)^3 + \ldots$$

have different reasons in the two approaches. In the approach using many-body perturbation theory they originate from the rotational symmetry of the ring diagrams. In the Adiabatic Connection, on the other side, they stem from averaging the potential energy over all values of λ to arrive at the total energy.

6.4 RPA for the uniform electron gas

In this section we apply the framework of many-body perturbation theory as discussed in Chapter 5 to the uniform electron gas (UEG) and and use resulting propagators to calculate the Random Phase Approximation for this system.

We choose the free Hamiltonian as a reference only containing the kinetic energy

$$\hat{H}_0 = \sum_{n=1}^{N} \frac{-\nabla_n^2}{2}$$

for a system with N electrons in a cubic box of length a and volume $\Omega = a^3$. The solutions of the non-interacting Hamiltonian are plane waves commensurate with the box. The normalized spin orbitals and eigenenergies are

$$\psi_{\sigma\mathbf{k}}(\alpha\mathbf{r}) = \delta_{\sigma\alpha}\frac{1}{\sqrt{\Omega}}\mathrm{e}^{\mathrm{i}\mathbf{k}\cdot\mathbf{r}}, \qquad \varepsilon_{\sigma\mathbf{k}} = \frac{\mathbf{k}^2}{2}, \qquad \text{where } \mathbf{k} \in \frac{2\pi}{a}\mathbb{Z}^3, \text{ and } \sigma, \alpha \in \{\uparrow, \downarrow\}. \tag{6.36}$$

The uniform electron gas is the limit of this system taking its volume Ω to infinity while keeping the electron density N/Ω fixed. The average volume per electron is usually given by specifying the radius r_s of a sphere of equal volume

$$\Omega/N = \frac{4\pi r_s^3}{3}. \tag{6.37}$$

r_s is called *Wigner–Seitz radius*. In the non-interacting ground state the lowest N spin-orbitals are occupied and the wave numbers $\mathbf{k}$ of these states lie inside a sphere called *Fermi sphere* with radius k_F:

$$\sum_{\sigma,|\mathbf{k}|<k_\mathrm{F}} = N. \tag{6.38}$$

The density of the wave vectors $\mathbf{k} \in 2\pi\mathbb{Z}^3/a$ increases with increasing box volume so we can approximate the above sum by an appropriate integral

$$\sum_{\sigma,\mathbf{k}} = \sum_{\sigma} \int \frac{\Omega}{(2\pi)^3}\,\mathrm{d}\mathbf{k} \tag{6.39}$$

and use it together with (6.38) and (6.37) to find k_F as a function of the Wigner–Seitz radius r_s:

$$k_\mathrm{F}^3 = \frac{9\pi}{2\sum_\sigma}\frac{1}{r_s^3}\,. \tag{6.40}$$

In the non-spin polarized case $\sum_\sigma = 2$ and in the spin polarized case $\sum_\sigma = 1$.

6.4.1 Propagators

We can now evaluate the propagators for the uniform electron gas according to (5.43):

$$G_0(\alpha\mathbf{r}t, \alpha'\mathbf{r}'t') = \begin{cases} -\displaystyle\sum_{\sigma,|\mathbf{k}|<k_\mathrm{F}} \psi_{\sigma\mathbf{k}}(\alpha\mathbf{r})\psi^*_{\sigma\mathbf{k}}(\alpha'\mathbf{r}')\mathrm{e}^{(-\mathrm{i}\varepsilon_{\sigma\mathbf{k}}+\eta)(t-t')} & \text{for } t \leq t' \\ +\displaystyle\sum_{\sigma,|\mathbf{k}|\geq k_\mathrm{F}} \psi_{\sigma\mathbf{k}}(\alpha\mathbf{r})\psi^*_{\sigma\mathbf{k}}(\alpha'\mathbf{r}')\mathrm{e}^{(-\mathrm{i}\varepsilon_{\sigma\mathbf{k}}-\eta)(t-t')} & \text{otherwise.} \end{cases}$$

Inserting the spin orbitals and eigenenergies from (6.36) and approximating the sum over states by the appropriate integral from (6.39) gives

$$G_0(\alpha\mathbf{r}t,\alpha'\mathbf{r}'t') = \begin{cases} -\displaystyle\int\limits_{|\mathbf{k}'|<k_\mathrm{F}} \frac{\mathrm{d}\mathbf{k}'}{(2\pi)^3}\,\delta_{\alpha\alpha'}\,\mathrm{e}^{\mathrm{i}\mathbf{k}'\cdot(\mathbf{r}-\mathbf{r}')}\mathrm{e}^{(-\mathrm{i}\mathbf{k}'^2/2+\eta)(t-t')} & \text{for } t\le t' \\ +\displaystyle\int\limits_{|\mathbf{k}'|\ge k_\mathrm{F}} \frac{\mathrm{d}\mathbf{k}'}{(2\pi)^3}\,\delta_{\alpha\alpha'}\,\mathrm{e}^{\mathrm{i}\mathbf{k}'\cdot(\mathbf{r}-\mathbf{r}')}\mathrm{e}^{(-\mathrm{i}\mathbf{k}'^2/2-\eta)(t-t')} & \text{otherwise,} \end{cases}$$

which we can transform into momentum space $\mathbf{k}$ with respect to $(\mathbf{r}-\mathbf{r}')$. For the case $t\le t'$ this yields

$$\begin{aligned} & -\int \mathrm{d}(\mathbf{r}-\mathbf{r}')\mathrm{e}^{-\mathrm{i}\mathbf{k}\cdot(\mathbf{r}-\mathbf{r}')} \int\limits_{|\mathbf{k}'|<k_\mathrm{F}} \frac{\mathrm{d}\mathbf{k}'}{(2\pi)^3}\,\delta_{\alpha\alpha'}\,\mathrm{e}^{\mathrm{i}\mathbf{k}'\cdot(\mathbf{r}-\mathbf{r}')}\mathrm{e}^{(-\mathrm{i}\mathbf{k}'^2/2+\eta)(t-t')} \\ = & -\int\limits_{|\mathbf{k}'|<k_\mathrm{F}} \frac{\mathrm{d}\mathbf{k}'}{(2\pi)^3}\,(2\pi)^3\,\delta(\mathbf{k}'-\mathbf{k})\,\delta_{\alpha\alpha'}\,\mathrm{e}^{(-\mathrm{i}\mathbf{k}'^2/2+\eta)(t-t')} \\ = & -\theta(k_\mathrm{F}-|\mathbf{k}|)\,\delta_{\alpha\alpha'}\,\mathrm{e}^{(-\mathrm{i}\mathbf{k}^2/2+\eta)(t-t')}\,, \end{aligned}$$

where $\theta(x)$ is the Heaviside step function. In the general case, this gives

$$G_0(\mathbf{k},t-t') = \begin{cases} -\theta(k_\mathrm{F}-|\mathbf{k}|)\,\mathrm{e}^{(-\mathrm{i}\mathbf{k}^2/2+\eta)(t-t')} & \text{for } t\le t' \\ +\theta(|\mathbf{k}|-k_\mathrm{F})\,\mathrm{e}^{(-\mathrm{i}\mathbf{k}^2/2-\eta)(t-t')} & \text{otherwise,} \end{cases} \tag{6.41}$$

as a function of $\mathbf{k}$ and the time difference $(t-t')$, omitting the electron spins. Finally, we can transform the propagator into frequency space ω with respect to $(t-t')$. For the case $t\le t'$ this gives

$$\begin{aligned} & -\int_{-\infty}^{0} \mathrm{d}(t-t')\,\mathrm{e}^{+\mathrm{i}\omega(t-t')}\,\theta(k_\mathrm{F}-|\mathbf{k}|)\,\mathrm{e}^{(-\mathrm{i}\mathbf{k}^2/2+\eta)(t-t')} \\ = & -\frac{(1-0)\,\theta(k_\mathrm{F}-|\mathbf{k}|)}{\mathrm{i}(\omega-\mathbf{k}^2/2)+\eta} \;=\; \frac{\mathrm{i}\,\theta(k_\mathrm{F}-|\mathbf{k}|)}{\omega-\mathbf{k}^2/2-\mathrm{i}\eta}\,. \end{aligned}$$

Note that, unlike for the momentum, we use $\mathrm{e}^{+\mathrm{i}\omega(t-t')}$ for the forward Fourier transform into frequency space so that the poles of the propagator coincide with the positive eigenenergies. The particle/hole propagator is now quite compact, even for the general case:

$$G_0(\mathbf{k},\omega) = \frac{\mathrm{i}}{\omega-\mathbf{k}^2/2+\mathrm{i}\eta_\mathbf{k}}\,, \qquad \text{where } \eta_\mathbf{k} = \begin{cases} -\eta & \text{for } |\mathbf{k}|<k_\mathrm{F} \\ +\eta & \text{otherwise.} \end{cases} \tag{6.42}$$

In the space and time domain, we have to integrate over all spins, space and time coordinates of each vertex:

$$\sum_\alpha \int\limits_\Omega \mathrm{d}\mathbf{r}\int \mathrm{d}t\,.$$

In the momentum and frequency domain, we integrate over all spins, momenta and frequencies of all propagators connecting the vertices

$$\sum_\alpha \int \frac{\Omega}{(2\pi)^3}\,\mathrm{d}\mathbf{k}\int \frac{1}{2\pi}\,\mathrm{d}\omega\,, \tag{6.43}$$

respecting momentum and frequency conservation at each vertex. Next, we also want to transform the propagator for the Coulomb interaction

$$V(\alpha \mathbf{r} t, \alpha' \mathbf{r}' t') = \frac{-\mathrm{i}}{|\mathbf{r} - \mathbf{r}'|} \delta(t - t')$$

in the momentum and frequency domain. The transform with respect to $(t - t')$ is straight forward and simply gives a frequency independent propagator

$$V(\mathbf{r} - \mathbf{r}', \omega) = \frac{-\mathrm{i}}{|\mathbf{r} - \mathbf{r}'|},$$

omitting the spin coordinates. The transform into momentum space does not converge, however, the propagator for the Yukawa potential can be expressed by a Fourier integral for any parameter $m > 0$:

$$\frac{-\mathrm{i} \mathrm{e}^{-m|\mathbf{r}-\mathbf{r}'|}}{|\mathbf{r} - \mathbf{r}'|} = \int \frac{1}{(2\pi)^3} \mathrm{d}\mathbf{q}\, \mathrm{e}^{\mathrm{i}\mathbf{q}\cdot(\mathbf{r}-\mathbf{r}')} \frac{-4\pi\mathrm{i}}{\mathbf{q}^2 + m^2} = \int \frac{\Omega}{(2\pi)^3} \mathrm{d}\mathbf{q}\, \mathrm{e}^{\mathrm{i}\mathbf{q}\cdot(\mathbf{r}-\mathbf{r}')} \frac{-4\pi\mathrm{i}}{\Omega(\mathbf{q}^2 + m^2)}.$$

Taking the limit $m \to 0$ gives the propagator for the Coulomb interaction in momentum space:

$$V(\mathbf{q}, \omega) = -\frac{4\pi\mathrm{i}}{\Omega \mathbf{q}^2}. \tag{6.44}$$

Note that we use $\mathbf{k}$ for particle/hole propagators while we use $\mathbf{q}$ for Coulomb propagators. The spin coordinates remain omitted for brevity as the behavior of spin is intuitive in the UEG. A particle or a hole does not change spin during propagation while the Coulomb interaction mediates between particles or holes irrespective of the their spin.

6.4.2 Imaginary frequencies

G_0 as a function of ω with the momentum $\mathbf{k}$ as parameter has one pole on the positive real frequency axis. The pole is infinitesimally below or above the real axis depending on whether it is a particle, having $|\mathbf{k}| > k_\mathrm{F}$, or a hole. On which side of the real axis the pole lies determines whether there is forwards or backwards propagation in time. Figure 6.2 shows the pole of $G_0(\mathbf{k}, \omega)$ as a function of ω with $\mathbf{k}$ as parameter. The poles of the propagators make a numeric frequency integration along the real axis difficult. We can, however, smoothly deform the integration contour as long as we do not cross any poles. As indicated in Figure 6.2 we can rotate the contour $\mathcal{C}_1$ counterclockwise around the Fermi energy $\mu = k_\mathrm{F}^2/2$ to arrive at the contour $\mathcal{C}_2$. Substituting $\omega = \mu + \mathrm{i}\nu$ we obtain

$$\int_{-\infty}^{\infty} \mathrm{d}\omega = \oint_{\mathcal{C}_1} \mathrm{d}\omega = \oint_{\mathcal{C}_2} \mathrm{d}\omega = \int_{-\infty}^{\infty} \mathrm{i}\, \mathrm{d}\nu,$$

where we assume that the contribution of a contour at infinity vanishes. This rotation of the integral contour is called *Wick* rotation to *imaginary frequency*. When integrating in imaginary frequency, the side of the poles relative to the contour no longer depend on adiabatic switching constant η and we can as well take the limit $\eta \to 0$ before evaluating the imaginary frequency integrals. The particle/hole propagator in imaginary frequency is then given by

$$G_0(\mathbf{k}, \mathrm{i}\nu) = \frac{\mathrm{i}}{\mathrm{i}\nu - (\mathbf{k}^2/2 - \mu)} = \frac{1}{\nu + \mathrm{i}\Delta\varepsilon_\mathbf{k}}, \quad \text{where } \Delta\varepsilon_\mathbf{k} = \mathbf{k}^2/2 - k_\mathrm{F}^2/2. \tag{6.45}$$

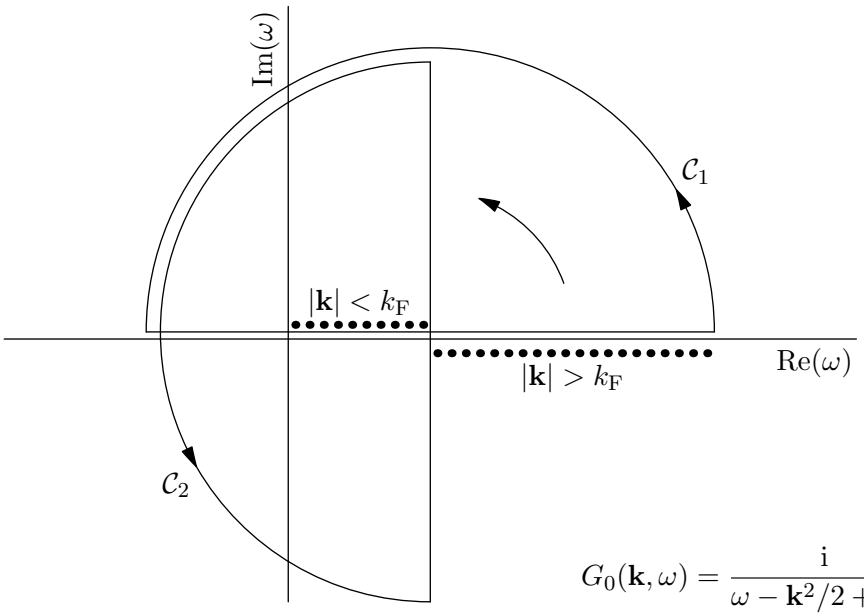

Figure 6.2: G_0 as a function of ω with $\mathbf{k}$ as parameter has one pole above the real axis for $|\mathbf{k}| < k_\mathrm{F}$ or below the real axis for $|\mathbf{k}| > k_\mathrm{F}$. We can smoothly rotate the integration contour from the real axis to a contour parallel to the imaginary axis without crossing any pole. The arcs indicate the contour at infinity.

6.4.3 Polarizability

Next, we can evaluate the independent particle polarizability. The polarizability diagram has two open vertices. Let $\mathbf{q}$ and ν denote the momentum and the imaginary frequency incident at the lower vertex shown in the diagram below. From the momentum and frequency conservation at every vertex follows that there is one pair of momentum $\mathbf{k}$ and frequency η to integrate over and that the outgoing momentum and frequency is equal to the incoming ones. In the context of this diagram part, $\mathbf{k}$ and η are called *internal* momentum and frequency, respectively, while $\mathbf{q}$ and ν are connected to other diagram parts and are therefore referred to as *external* momentum and frequency, respectively. We evaluate the diagram part by integrating over all internal momenta and frequencies starting with the analytic η integration:

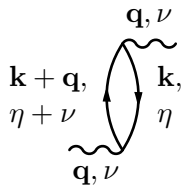

$$\begin{aligned}
\chi_0(\mathbf{q}, \mathrm{i}\nu) &= -\sum_\sigma \int \frac{\Omega\,\mathrm{d}\mathbf{k}}{(2\pi)^3} \int \frac{\mathrm{i}\,\mathrm{d}\eta}{2\pi}\, G_0(\mathbf{k}+\mathbf{q}, \mathrm{i}\eta + \mathrm{i}\nu)\, G_0(\mathbf{k}, \mathrm{i}\eta) \\
&= -\sum_\sigma \int \frac{\Omega\,\mathrm{d}\mathbf{k}}{(2\pi)^3} \int \frac{\mathrm{i}\,\mathrm{d}\eta}{2\pi}\, \frac{1}{\eta + \nu + \mathrm{i}\Delta\varepsilon_{\mathbf{k}+\mathbf{q}}}\, \frac{1}{\eta + \mathrm{i}\Delta\varepsilon_{\mathbf{k}}} \\
&= -\mathrm{i}\sum_\sigma \int \frac{\Omega\,\mathrm{d}\mathbf{k}}{(2\pi)^3} \left(\frac{\theta(|\mathbf{k}+\mathbf{q}| - k_\mathrm{F})\theta(k_\mathrm{F} - |\mathbf{k}|)}{\varepsilon_{\mathbf{k}+\mathbf{q}} - \varepsilon_{\mathbf{k}} - \mathrm{i}\nu} \right. \\
&\qquad \left. + \frac{\theta(|\mathbf{k}| - k_\mathrm{F})\theta(k_\mathrm{F} - |\mathbf{k}+\mathbf{q}|)}{\varepsilon_{\mathbf{k}} - \varepsilon_{\mathbf{k}+\mathbf{q}} + \mathrm{i}\nu} \right)
\end{aligned} \tag{6.46}$$

The conditions on $\mathbf{k}$ expressed by the Heaviside theta functions arise from the necessity to have one pole on either side of the integration contour for a non-vanishing result. The conditions in (6.46) can be unified by substituting $-\mathbf{k}' = \mathbf{k} + \mathbf{q}$ in the second sum. This gives

$$\chi_0(\mathbf{q}, \mathrm{i}\nu) = -\mathrm{i} \sum_\sigma \int_{|\mathbf{k}|<k_\mathrm{F}<|\mathbf{k}+\mathbf{q}|} \frac{\Omega \,\mathrm{d}\mathbf{k}}{(2\pi)^3} \left(\frac{1}{\varepsilon_{\mathbf{k}+\mathbf{q}} - \varepsilon_\mathbf{k} - \mathrm{i}\nu} + \frac{1}{\varepsilon_{\mathbf{k}+\mathbf{q}} - \varepsilon_\mathbf{k} + \mathrm{i}\nu} \right). \tag{6.47}$$

With some effort this expression can also be integrated analytically with respect to the momentum $\mathbf{k}$ and expressed in terms of a real valued function $R(q, u)$ where the Fermi momentum and the Fermi energy are normalized to 1 and $1/2$, respectively (Ziesche 2010):

$$\chi_0(\mathbf{q}, \mathrm{i}\nu) = -\,\mathrm{i}\, \frac{k_\mathrm{F}}{\pi^2}\, R\left(\frac{|\mathbf{q}|}{k_\mathrm{F}}, \frac{\nu}{|\mathbf{q}| k_\mathrm{F}} \right) \tag{6.48}$$

$$2R(q,u) = 1 - u \left(\arctan\left(\frac{1 + q/2}{u} \right) + \arctan\left(\frac{1 - q/2}{u} \right) \right) \tag{6.49}$$

$$+ \frac{1 + u^2 - q^2/4}{2q} \log\left(\frac{u^2 + (q/2+1)^2}{u^2 + (q/2-1)^2} \right). \tag{6.50}$$

Note that the imaginary units are often traded between the Coulomb kernel $V(\mathbf{q})$ and the polarizability $\chi_0(\mathbf{q}, \mathrm{i}\nu)$ since only their product occurs in the expression for the RPA correlation energy. Throughout this work, except in Section 6.3, imaginary units are used exactly as they emerge from Wick rotated imaginary frequency integrations:

$$V(\mathbf{q}) = -\frac{4\pi \mathrm{i}}{\Omega\, \mathbf{q}^2} \qquad \chi(\mathbf{q}, \mathrm{i}\nu) = -\mathrm{i} \sum_{\sigma \mathbf{k}} (\ldots) \qquad \text{used in this work,} \tag{6.51}$$

$$V(\mathbf{q}) = \frac{4\pi}{\Omega\, \mathbf{q}^2} \qquad \chi(\mathbf{q}, \mathrm{i}\nu) = -\sum_{\sigma \mathbf{k}} (\ldots) \qquad \text{also common in literature.} \tag{6.52}$$

6.4.4 Correlation energy

Finally, we can evaluate the correlation energy in the Random Phase Approximation for the uniform electron gas according to (6.9). In the space domain we needed to convolve the propagators connected in series which we denoted by the matrix product. In the momentum domain of a homogeneous system this simplifies to a product. The RPA energy per electron in the uniform electron gas is thus

$$\begin{aligned} E_\mathrm{c}^\mathrm{RPA}/N &= \frac{\Omega}{N} \frac{1}{2} \int \frac{\mathrm{d}\mathbf{q}}{(2\pi)^3} \int_{-\infty}^{\infty} \frac{\mathrm{d}\nu}{2\pi} \Big\{ \log\Big(1 - \chi_0(\mathbf{q}, \mathrm{i}\nu) V(\mathbf{q})\Big) + \chi_0(\mathbf{q}\mathrm{i}\nu) V(\mathbf{q}) \Big\} \\ &= \frac{4\pi r_s^3}{3} \int_0^\infty \frac{4\pi q^2 \mathrm{d}q}{(2\pi)^3} \int_0^\infty \frac{\mathrm{d}\nu}{2\pi} \Big\{ \log\Big(1 - \chi_0(q, \mathrm{i}\nu) V(q)\Big) + \chi_0(q, \mathrm{i}\nu) V(q) \Big\}. \end{aligned} \tag{6.53}$$

Note that the sum over all momenta $\mathbf{q}$ of the Coulomb propagator does not include a sum over spins. The given integral can be evaluated using a Gauss–Kronrod rule first in q, then in ν to yield the correlation energy in the Random Phase Approximation to 5 significant digits of precision for the non-spin polarized, paramagnetic case with $\sum_\sigma = 2$ and for the spin polarized, ferromagnetic case with $\sum_\sigma = 1$. The results are listed in Table 6.1 for

paramagnetic				ferromagnetic			
r_s [a.u.]	E_c^{RPA} [mE_h N]	$\pm$	E_c [mE_h N]	r_s [a.u.]	E_c^{RPA} [mE_h N]	$\pm$	E_c [mE_h N]
1	-78.799	0.001	-59.632	1	-51.893	0.002	-31.701
2	-61.801	0.001	-45.091	2	-42.416	0.001	-24.090
3	-52.759	<0.001	-37.214	3	-37.179	0.001	-20.048
4	-46.806	<0.001	-32.054	4	-33.633	<0.001	-17.415
5	-42.470	<0.001	-28.339	5	-30.992	<0.001	-15.520
6	-39.117	<0.001	-25.504	6	-28.911	<0.001	-14.071
7	-36.418	<0.001	-23.253	7	-27.209	<0.001	-12.916
8	-34.182	<0.001	-21.414	8	-25.778	<0.001	-11.969
9	-32.289	<0.001	-19.876	9	-24.551	<0.001	-11.174
10	-30.658	<0.001	-18.568	10	-23.482	<0.001	-10.495
12	-27.975	<0.001	-16.454	12	-21.698	<0.001	-9.391
15	-24.929	<0.001	-14.119	15	-19.629	<0.001	-8.160
20	-21.381	<0.001	-11.497	20	-17.156	<0.001	-6.758
30	-17.068	<0.001	-8.486	30	-14.044	<0.001	-5.112
40	-14.463	<0.001	-6.778	40	-12.099	<0.001	-4.156
50	-12.680	<0.001	-5.666	50	-10.736	<0.001	-3.521

Table 6.1: Correlation energy in the Random Phase Approximation for the uniform electron gas at different densities compared to Quantum Monte-Carlo (QMC) results obtained by Ceperley and Alder 1980 and parametrized by (Perdew and Zunger 1981). For RPA energies at intermediate spin polarizations see Vosko, Wilk, and Nusair 1980.

different densities and they include Quantum Monte Carlo results for comparison. RPA gives a good approximation to the correlation energy for most densities, although it systematically overestimates the correlation energy. Gell-Mann and Brueckner 1957 have shown that in the limit of $r_s \to 0$ the entire correlation energy is contained in the RPA ring diagrams. For low densities, however, the relative error becomes larger and other diagrams become important.

6.4.5 Large momentum behavior

The finite basis set, employed in a practical Hartree-Fock or DFT calculation, imposes an upper limit $G_{\max}$ for the evaluation of the independent particle polarizability χ_0. Therefore, we need to know the asymptotic behavior of the RPA correlation energy for sufficiently large values of $G_{\max}$ in order to extrapolate numerical results to $G_{\max} \to \infty$. Assuming that the system is sufficiently homogeneous at the length scale corresponding to a given $G_{\max}$, the asymptotic behavior of the RPA in a solid or in a molecule is the same as in the uniform electron gas. The latter can be derived analytically and will be outlined here.

Given the expression for the independent particle polarizability χ_0 of the uniform electron

gas from (6.47)

$$\begin{aligned}\chi_0(\mathbf{q},\mathrm{i}\nu) &= -\mathrm{i}\sum_\sigma \int\limits_{|\mathbf{k}|<k_\mathrm{F}<|\mathbf{k}+\mathbf{q}|} \frac{\Omega\,\mathrm{d}\mathbf{k}}{(2\pi)^3}\left(\frac{1}{\varepsilon_{\mathbf{k}+\mathbf{q}}-\varepsilon_\mathbf{k}-\mathrm{i}\nu}+\frac{1}{\varepsilon_{\mathbf{k}+\mathbf{q}}-\varepsilon_\mathbf{k}+\mathrm{i}\nu}\right)\\ &= -\mathrm{i}\sum_\sigma \int\limits_{|\mathbf{k}|<k_\mathrm{F}<|\mathbf{k}+\mathbf{q}|} \frac{\Omega\,\mathrm{d}\mathbf{k}}{(2\pi)^3}\,\frac{\Delta\varepsilon_{\mathbf{k},\mathbf{q}}}{\Delta\varepsilon_{\mathbf{k},\mathbf{q}}^2+\nu^2}\,,\end{aligned} \tag{6.54}$$

where $\Delta\varepsilon_{\mathbf{k},\mathbf{q}} = \varepsilon_{\mathbf{k}+\mathbf{q}} - \varepsilon_\mathbf{k} = \mathbf{k}\cdot\mathbf{q} + \mathbf{q}^2/2$, we can trivially integrate out $\mathbf{k}$ for large enough magnitudes of $\mathbf{q}$ since $|\mathbf{k}| < k_\mathrm{F} \ll |\mathbf{q}|$. This yields

$$\chi_0(q,\mathrm{i}\nu) \sim -\mathrm{i}\,k_\mathrm{F}^3\,\frac{q^2}{(q^2/2)^2+\nu^2}\,. \tag{6.55}$$

Next, we can insert this approximation into the RPA energy expression (6.53) for a given, large q and integrate out the imaginary frequency ν, getting

$$\begin{aligned}\int_0^\infty \frac{\mathrm{d}\nu}{2\pi}\left\{\log\Big(1-\chi_0(q,\mathrm{i}\nu)V(q)\Big)+\chi_0(q,\mathrm{i}\nu)V(q)\right\} &\sim \frac{\left(q^2/2\right)\sqrt{(q^2/2)^2+1}-\left(q^2/2\right)^2-1/2}{q^2}\\ &= -\frac{1}{q^6}+\frac{1}{q^{10}}+\mathcal{O}\left(\frac{1}{q^{14}}\right),\end{aligned}$$

where we expanded in the variable $u = 1/q$ at $u = 0$. The leading order term can finally be used to estimate the missing RPA energy per electron $\Delta E_\mathrm{c}^\mathrm{RPA}(G_\mathrm{max})$ when truncating the momentum integration at a finite momentum G_max:

$$\Delta E_\mathrm{c}^\mathrm{RPA}(G_\mathrm{max}) \sim \int_{G_\mathrm{max}}^\infty \mathrm{d}q\,q^2\left(\frac{1}{q^6}+\mathcal{O}\left(\frac{1}{q^{10}}\right)\right) \sim \frac{1}{G_\mathrm{max}^3}+\mathcal{O}\left(\frac{1}{G_\mathrm{max}^7}\right). \tag{6.56}$$

6.4.6 Large imaginary frequency behavior

Although most implementations of the RPA can evaluate the independent particle polarizability χ_0 at arbitrary imaginary frequencies, knowledge of the asymptotic behavior of the RPA energy for large frequencies ν is useful for choosing an appropriate variable transform for integrating the tail. This is relevant for metallic systems, where we can assume that the system behaves like a Uniform Electron Gas at times short enough.

Unlike in the case of large momenta q, $\mathbf{k}$ cannot be trivially integrated out. However, we can separate the momentum integration of q into three regions and show that they all come to an analogous form of the integrand for that momentum integration. In Subsection 6.4.5 we already have gotten an approximation of $\chi_0(q,\mathrm{i}\nu)$ for large q in (6.55). For small q, the volume of the momenta $\mathbf{k}$, such that $|\mathbf{k}| < k_\mathrm{F} < |\mathbf{k}+\mathbf{q}|$, is proportional to q, as shown in Figure 6.3. Therefore. the integral in (6.54) transforms as follows

$$\begin{aligned}-\mathrm{i}\sum_\sigma \int\limits_{|\mathbf{k}|<k_\mathrm{F}<|\mathbf{k}+\mathbf{q}|} \frac{\Omega\,\mathrm{d}\mathbf{k}}{(2\pi)^3}\,\frac{\Delta\varepsilon_{\mathbf{k},\mathbf{q}}}{\Delta\varepsilon_{\mathbf{k},\mathbf{q}}^2+\nu^2} &\sim -\,\mathrm{i}\,4\pi k_\mathrm{F}^2\,q\int_0^1 \mathrm{d}\cos\theta\,\cos\theta\,\frac{q^2/2+k_\mathrm{F}q\cos\theta}{(q^2/2+k_\mathrm{F}q\cos\theta)^2+\nu^2}\\ &\sim -\,\mathrm{i}\,k_\mathrm{F}^2\,\frac{q^3/4+k_\mathrm{F}q^2/6}{(q^2/2)^2+\nu^2} \sim -\mathrm{i}\,k_\mathrm{F}^3\,\frac{q^2+\mathcal{O}\left(q^3\right)}{(q^2/2)^2+\nu^2}\,,\end{aligned} \tag{6.57}$$

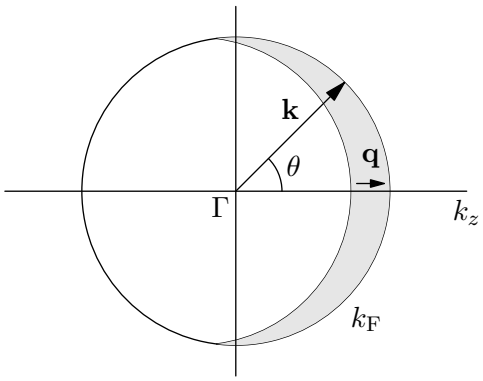

Figure 6.3: Cross section of the set of momenta $\mathbf{k}$ such that $|\mathbf{k}| < k_\mathrm{F} < |\mathbf{k}+\mathbf{q}|$ for small magnitudes of the excitation momentum $\mathbf{q}$. In this limit, the set covers half the surface of the Fermi sphere and its maximum thickness is $|\mathbf{q}|$.

where we used that $\Delta\varepsilon_{\mathbf{k},\mathbf{q}} = q^2/2 + k_\mathrm{F} q\cos\theta$ and that ν is large compared to $k_\mathrm{F} q$. This is the same behavior of $\chi_0(q, \mathrm{i}\nu)$ as for large momenta q. For intermediate q, where the integration volume for $\mathbf{k}$ is roughly independent of $\mathbf{q}$, the $\mathbf{k}$ integration merely averages the contributions to χ_0. For large ν we retrieve

$$-\mathrm{i}\sum_\sigma \int\limits_{|\mathbf{k}|<k_\mathrm{F}<|\mathbf{k}+\mathbf{q}|} \frac{\Omega\,\mathrm{d}\mathbf{k}}{(2\pi)^3}\,\frac{\Delta\varepsilon_{\mathbf{k},\mathbf{q}}}{\Delta\varepsilon_{\mathbf{k},\mathbf{q}}^2+\nu^2} \sim -\,\mathrm{i}\,\frac{4\pi k_\mathrm{F}^3}{3}\int_{-1}^{1}\mathrm{d}\cos\theta\,\frac{q^2/2+k_\mathrm{F} q\cos\theta}{\left(q^2/2+k_\mathrm{F} q\cos\theta\right)^2+\nu^2}$$
$$\sim -\,\mathrm{i}\,k_\mathrm{F}^3\,\frac{q^2+\mathcal{O}(q)}{\left(q^2/2\right)^2+\nu^2}\,, \tag{6.58}$$

Since the integrand has the same form for large ν in all cases, we can use it in the integral over the whole domain of q, getting

$$\int_0^\infty \frac{4\pi q^2\mathrm{d}q}{(2\pi)^3}\left\{\log\Big(1-\chi_0(q,\mathrm{i}\nu)V(q)\Big)+\chi_0(q,\mathrm{i}\nu)V(q)\right\}$$
$$\sim \frac{4\sqrt{\nu}\left(\nu^2+1\right)^{3/4}-4\nu^2-3}{6\sqrt{\nu}} = -\frac{1}{16}\frac{1}{\nu^{5/2}}+\frac{5}{192}\frac{1}{\nu^{9/2}}+\mathcal{O}\left(\frac{1}{\nu^{13/2}}\right),$$

which is expanded in the variable $u = 1/\nu$ at $u = 0$. The other orders in the terms (6.57) and (6.58) yield a leading order term of the form $\mathcal{O}(1/\nu^4)$ for the respective integration region of q and can therefore be neglected for sufficiently large frequencies ν. These terms can, however, contribute to the next-to-leading order. Finally, we can insert this expansion in the imaginary frequency integration to estimate the missing RPA energy per electron $\Delta E_\mathrm{c}^\mathrm{RPA}$ when truncating the frequency integration at some finite but large ν_max:

$$\Delta E_\mathrm{c}^\mathrm{RPA} \sim \int_{\nu_\mathrm{max}}^\infty \mathrm{d}\nu\left(\frac{1}{\nu^{5/2}}+\mathcal{O}\left(\frac{1}{\nu^{9/2}}\right)\right) \sim \frac{1}{\nu_\mathrm{max}^{3/2}}+\mathcal{O}\left(\frac{1}{\nu_\mathrm{max}^{7/2}}\right). \tag{6.59}$$

Summary

The Random Phase Approximation is the sum of all ring diagrams to infinite order. Momentum conservation dictates that every Coulomb interaction in a ring diagram mediates the same momentum giving rise to a $1/q^{2n}$ divergence in n-th order. This is the strongest divergence possible in n-th order, rendering the ring diagrams the most important contribution for low momenta, i.e. at long distances or in the high density regime. The divergence of each diagram when integrating over low momenta is referred to as *infrared catastrophe*. Evaluating the sum over all orders before integrating over the mediated momenta turns the $1/q^{2n}$ divergence of each order into a $\log(1 + 1/q^2)$ divergence, which yields a finite result in the subsequent momentum integration and solves the infrared catastrophe.

Within the framework of many-body perturbation theory, discussed in Chapter 5, the Random Phase Approximation can be readily derived using the independent particle polarizability  $= \chi_0$ as a building block. In the frequency domain this can be done using Feynman diagrams where the rotational symmetry of the ring diagrams gives rise to the factors in the expansion of the RPA energy

$$\frac{1}{2}\Big(\quad\Big)^2 + \frac{1}{3}\Big(\quad\Big)^3 + \ \ldots$$

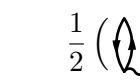

The RPA can also be derived in the frequency domain within the Adiabatic Connection (AC) arriving at a formally equivalent result for. In many-body perturbation theory the perturbation is slowly introduced to the system leaving it in its ground state. The sum over all connected diagrams, respecting their symmetry, yields the total correlation energy. In the Adiabatic Connection, the correlation energy is retrieved from averaging the potential energy over the coupling strength λ:

$$\int_0^1 \mathrm{d}\lambda \left(\lambda\Big(\quad\Big)^2 + \lambda^2\Big(\quad\Big)^3 + \ \ldots\right)$$

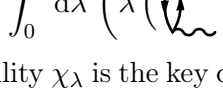

In the AC, the polarizability χ_λ is the key quantity of interest rather than connected diagrams. Therefore, there are no symmetries to consider and connected (closed) diagrams should be avoided for depicting the RPA within the Adiabatic Connection. It is important to remark that the AC derivation is tailored to a DFT reference system assuming an exact density of the reference for the Adiabatic Connection and an exact density response for the Dyson-like equation of the polarizability.

Finally, the RPA can also be derived in the time domain using Goldstone diagrams and the direct ring Coupled Cluster Doubles amplitudes

 .

In each iteration of the amplitude equation ring diagrams are added in all possible ways in a time ordered manner. The simple fact that rings have a left and a right side when building them bottom to top requires 4 open connections of this building block according to the left and the right particle/hole pair. Although this approach is numerically not as efficient as calculating the RPA in the imaginary frequency domain, it is easy to include a larger set of diagrams once the amplitudes are found. After all, Wick's theorem requires all contractions to be considered not just the ring diagrams. The additional set of diagrams available, given the direct ring Coupled Cluster Doubles amplitudes, is called *Second Order Screened Exchange* diagrams. They represent the lowest order correction to the Random Phase Approximation.

Chapter 7

Second Order Screened Exchange

The Random Phase Approximation (RPA) often improves considerably on Hartree-Fock or Density Functional Theory results. It is capable of describing van der Waals interactions and works well in a large variety of chemical environments (Harl, Schimka, and Kresse 2010). However, it tends to overestimate the negative correlation energy. In the previous chapter, we have seen that for the uniform electron gas and this has also been shown for various solids and molecules (Ángyán et al. 2011). It is not surprising that the Random Phase Approximation shows an error. Wick's theorem states that all contractions should be considered not just those forming the ring diagrams. That the RPA exhibits a systematic error, however, indicates a general reason behind this error which can serve as a guide to the next class of diagrams partially correcting RPA's error.

In second order the overestimation of the correlation energy is more evident. According to Figure 5.5 the second order (MP2) direct term is negative and reads

$$(-1)^{(2+2)}\,\frac{1}{2}\sum_{ijab}\frac{V_{ij}^{ab}V_{ab}^{ij}}{\varepsilon_i+\varepsilon_j-\varepsilon_a-\varepsilon_b}\,,$$

where the Fermion sign is explicitly given, depending on the number of loops and holes according to (5.38). This term contains contributions in violation of the Pauli exclusion principle, for instance as illustrated below on the left, where the state i occurs twice at the same instance in time. Such contributions are canceled exactly by the respective *exchange diagram* where the two offending states are crossed by anti-symmetrizing the affected interaction as shown on the right. The resulting diagram has one loop less giving an opposite sign:

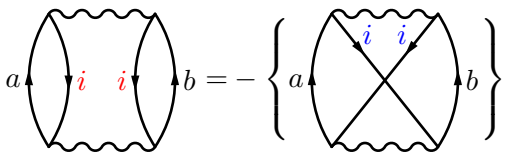

$$(-1)^{(2+2)}\,\frac{1}{2}\,\frac{V_{ii}^{ab}V_{ab}^{ii}}{\varepsilon_i+\varepsilon_i-\varepsilon_a-\varepsilon_b}=-\left\{(-1)^{(1+2)}\,\frac{1}{2}\,\frac{V_{ii}^{ab}V_{ab}^{ii}}{\varepsilon_i+\varepsilon_i-\varepsilon_a-\varepsilon_b}\right\}$$

As a consequence, contributions violating the Pauli exclusion principle would be canceled if all contractions were considered. Ignoring this exchange diagram leaves the respective contributions uncanceled resulting in a negative error. For the RPA the sign of the ring

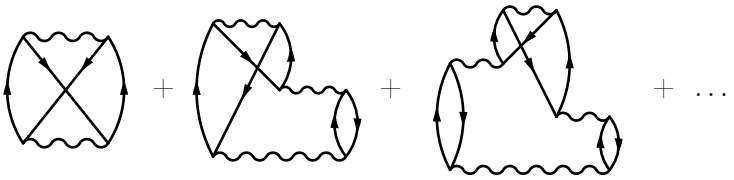

Figure 7.1: Exchanging only the last interaction in the ring diagrams leads to the Second Order Screened Exchange (SOSEX) correction to the Random Phase Approximation.

diagrams alternates with the order. However, the contributions of each order decay such that the error of the lowest order dominates, which is negative.

The systematic error can be alleviated by including exchange diagrams where violations of the Pauli exclusion principle can occur. The lowest order correction to the Random Phase Approximation anti-symmetrizes only one interaction of the RPA ring diagrams. The correction is termed *Second Order Screened Exchange (SOSEX)* if only the last interaction in time is anti-symmetrized. Figure 7.1 shows the additional diagrams included in the SOSEX.

7.1 SOSEX from Direct Ring Coupled Cluster Doubles

The lowest order correction anti-symmetrizes only one interaction of the RPA ring diagrams. This could be any interaction and not necessarily just the last one. However, when calculating the Random Phase Approximation using the direct ring Coupled Cluster Doubles amplitudes t_{ij}^{ab}, as discussed in Section 6.2, calculating the SOSEX corrections comes with hardly any additional costs. We simply close the amplitudes once with a direct interaction V_{ab}^{ij} and once with two indices swapped. Respecting the Fermion sign the RPA+SOSEX energy is then given by

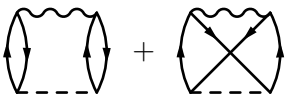

$$= \frac{1}{2} \sum_{ijab} t_{ij}^{ab} V_{ab}^{ij} - t_{ij}^{ab} V_{ab}^{ji} \,. \tag{7.1}$$

The Second Order Screened Exchange correction to the RPA was introduced by Freeman 1977, who applied it to the uniform electron gas. The term SOSEX was later coined by Grüneis et al. 2009, who studied this correction also for solids. Figure 7.2 shows the Second Order Screened Exchange correction per electron for the uniform electron gas as calculated by Freeman. The error of the Random Phase Approximation with respect to Quantum Monte Carlo (QMC) results of Ceperley and Alder 1980, parametrized by Perdew and Zunger 1981 is also given. Remarkably and certainly fortuitously RPA+SOSEX matches the QMC results at $r_s \approx 5$, which is in the density region of real metals. Anti-symmetrizing only the last interaction seems to give just the right correction to the RPA in the uniform electron gas. However, from a strictly *ab-initio* point of view, there is no reason to restrict the exchange diagrams to those where only the last interaction is anti-symmetrized, except technical convenience when having the drCCD amplitudes at hand.

Anti-symmetrizing each but still only one interaction in the ring diagrams gives worse agreement with QMC in the high density regime $r_s \leq 8$ but better agreement for low densities, where correlation effects are stronger. This is shown in Section 8.2. Note that in a spin-

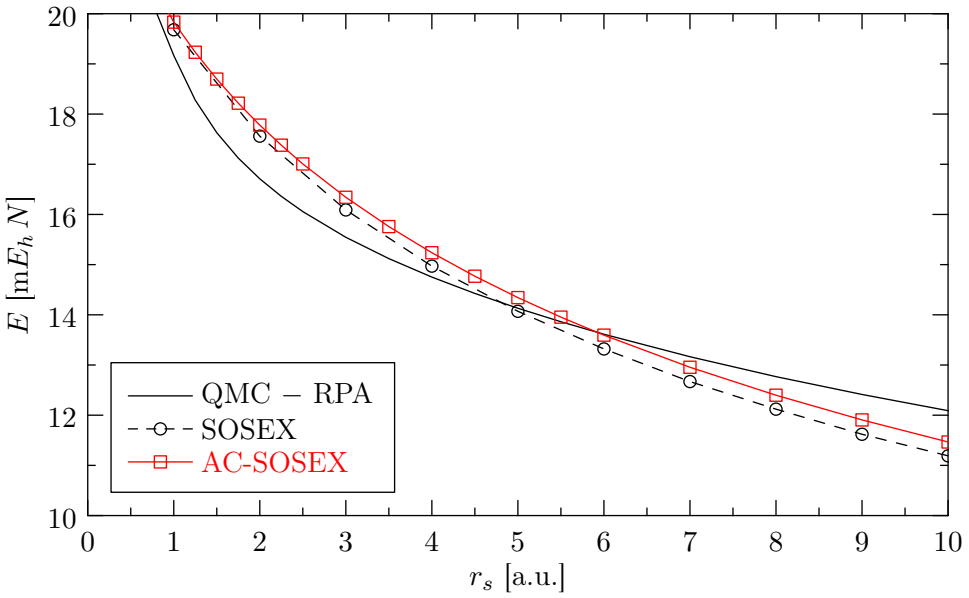

Figure 7.2: The Second Order Screened Exchange energy per electron obtained by Freeman 1977 for the uniform electron gas. It is compared to the error of the Random Phase Approximation with respect to Quantum Monte Carlo (QMC) calculations by Ceperley and Alder 1980, parametrized by Perdew and Zunger 1981. At $r_s \approx 5$ RPA+SOSEX fortuitously matches QMC results. The Adiabatic Connection-SOSEX according to (7.16), which is discussed later, is also shown here.

r_s [a.u.]	$(E_c - E_c^{RPA})$ [mE_h N]	E_c^{SOSEX} [mE_h N]	$E_c^{AC-SOSEX}$ [mE_h N]	$\pm$
1	19.167	19.680	19.832	0.009
2	16.710	17.560	17.780	0.003
3	15.545	16.090	16.342	0.003
4	14.752	14.970	15.237	0.003
5	14.131	14.070	14.343	0.003
6	13.613	13.320	13.595	0.003
7	13.165	12.670	12.955	0.003
8	12.768	12.120	12.398	0.003
9	12.413	11.620	11.906	0.003
10	12.090	11.190	11.466	0.003
12	11.521	—	10.712	0.003
15	10.810	—	9.806	0.003
20	9.884	—	8.679	0.003
30	8.582	—	7.201	0.003
40	7.685	—	6.246	0.003
50	7.014	—	5.564	0.003

Table 7.1: Data of Figure 7.2 including low densities.

polarized system SOSEX is less fortunate. While still improving on the RPA in the density range of interest, it cancels the RPA energy in the low density limit, as discussed in Subsection 8.2.3.

One can also include full anti-symmetrization in the amplitude equation, including terms such as

which lead to the full Coupled Cluster Doubles (CCD) amplitude equation. However, calculating the CCD amplitudes requires $\mathcal{O}(N^6)$ operations while the direct ring CCD amplitudes of RPA and SOSEX can be computed in $\mathcal{O}(N^5)$ steps. A major drawback of either method is the large memory requirement scaling like $\mathcal{O}(N^4)$ since the amplitudes t_{ij}^{ab} need to be stored for iterating the amplitude equation.

7.2 Adiabatic Connection-SOSEX

In contrast to calculating the drCCD amplitudes, evaluating the Random Phase Approximation in the frequency domain only requires $\mathcal{O}(N^2)$ memory. Calculating an exchange correction based on two point quantities, such as the independent particle polarizability χ_0 would therefore be favorable. Ángyán et al. 2011 suggested an approximation to the drCCD SOSEX within the framework of the Adiabatic Connection that can be implemented with a memory usage of $\mathcal{O}(N^2)$, which we will outline here (Ren et al. 2013; Ren et al. 2012).

Within the Adiabatic Connection one can define a screened interaction similar to the one defined in many-body perturbation theory in (6.7)

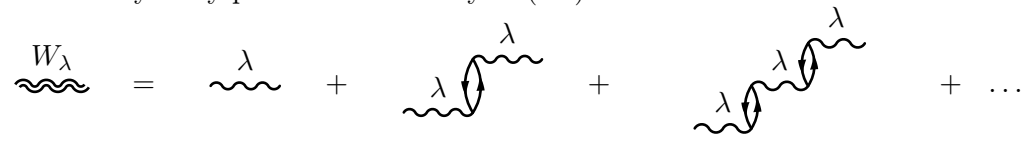

(7.2)

using the matrix notation introduced in Section 6.1. The only difference to (6.7) is the dependence on the coupling strength λ. Note that we explicitly write the coupling strength in all diagrams within the Adiabatic Connection to make a clear distinction from the diagrams within many-body perturbation theory discussed in Chapter 5.

We can now define the coupling strength averaged screened interaction

$$\overline{\mathbf{W}}(\mathrm{i}\nu) = \int_0^1 \mathrm{d}\lambda\, \mathbf{W}_\lambda(\mathrm{i}\nu) = \frac{1}{2}\mathbf{V} + \frac{1}{3}\mathbf{V}\mathbf{X}_0(\mathrm{i}\nu)\mathbf{V} + \dots$$

and write the RPA correlation energy found in (6.35) in terms of $\overline{\mathbf{W}}$:

$$E_\mathrm{c}^\mathrm{RPA} = -\frac{1}{2}\int \frac{\mathrm{d}\nu}{2\pi}\,\mathrm{tr}\Big\{\mathbf{X}_0(\mathrm{i}\nu)\mathbf{V}\mathbf{X}_0(\mathrm{i}\nu)\overline{\mathbf{W}}(\mathrm{i}\nu)\Big\}\,. \tag{7.3}$$

Next, we insert the independent particle polarizability given in (6.29),

$$\mathbf{X}_{0\mathbf{x}\mathbf{x}'}(\mathrm{i}\nu) = -\sum_{ia}\left(\frac{\psi_a(\mathbf{x})\psi_a^*(\mathbf{x}')\psi_i(\mathbf{x}')\psi_i^*(\mathbf{x})}{\varepsilon_a - \varepsilon_i - \mathrm{i}\nu} + \frac{\psi_i(\mathbf{x})\psi_i^*(\mathbf{x}')\psi_a(\mathbf{x}')\psi_a^*(\mathbf{x})}{\varepsilon_a - \varepsilon_i + \mathrm{i}\nu}\right),$$

into (7.3), giving

$$E_\mathrm{c}^\mathrm{RPA} = -\frac{1}{2}\int\frac{\mathrm{d}\nu}{2\pi}\sum_{ijab}\left(\frac{V_{ib}^{aj}\,\overline{W}_{ja}^{bi}(\mathrm{i}\nu)}{(\varepsilon_a-\varepsilon_i-\mathrm{i}\nu)(\varepsilon_b-\varepsilon_j-\mathrm{i}\nu)}+\frac{V_{ij}^{ab}\,\overline{W}_{ba}^{ji}(\mathrm{i}\nu)}{(\varepsilon_a-\varepsilon_i-\mathrm{i}\nu)(\varepsilon_b-\varepsilon_j+\mathrm{i}\nu)}+\right.$$
$$\left.\frac{V_{ab}^{ij}\,\overline{W}_{ji}^{ba}(\mathrm{i}\nu)}{(\varepsilon_a-\varepsilon_i+\mathrm{i}\nu)(\varepsilon_b-\varepsilon_j-\mathrm{i}\nu)}+\frac{V_{aj}^{ib}\,\overline{W}_{bi}^{ja}(\mathrm{i}\nu)}{(\varepsilon_a-\varepsilon_i+\mathrm{i}\nu)(\varepsilon_b-\varepsilon_j+\mathrm{i}\nu)}\right), \quad (7.4)$$

where we write $\overline{W}_{sr}^{pq}$ analogous to the matrix elements V_{sr}^{pq} of the Coulomb operator:

$$\overline{W}_{sr}^{pq}(\mathrm{i}\nu) = \iint \mathrm{d}\mathbf{x}_1\,\mathrm{d}\mathbf{x}_2\,\psi_p^*(\mathbf{x}_1)\psi_q^*(\mathbf{x}_2)\,\overline{\mathbf{W}}_{\mathbf{x}_1\mathbf{x}_2}(\mathrm{i}\nu)\,\psi_r(\mathbf{x}_2)\psi_s(\mathbf{x}_1)\,.$$

Although in the AC-FDT, the polarizability is the central quantity of interest rather than connected diagrams, we can use similar diagrams to depict the terms in (7.4):

$$E_\mathrm{c}^\mathrm{RPA} = -\frac{1}{2}$$

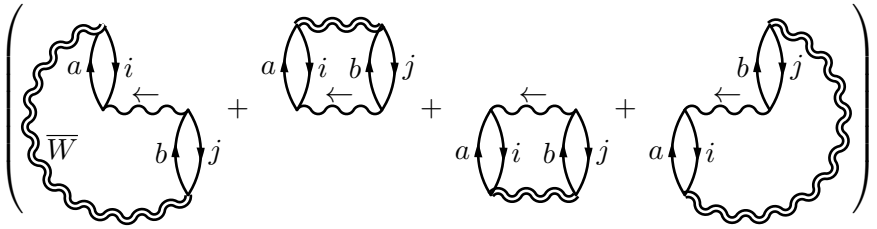

. (7.5)

The diagrams are drawn such that positive imaginary frequencies ν are defined right to left on the bare Coulomb interaction, as indicated by the arrow.

For real valued spin-orbitals $\psi_p(\mathbf{x})$ the Coulomb integrals exhibit time reversal symmetry at each vertex such that $V_{ij}^{ab} = V_{ib}^{aj} = V_{aj}^{ib} = V_{ab}^{ij}$. The same holds for the screened Coulomb integrals since the independent particle polarizability $\mathbf{X}_0(\mathrm{i}\nu)$ is real valued. This simplifies (7.4) to

$$E_\mathrm{c}^\mathrm{RPA} = -\frac{1}{2}\int\frac{\mathrm{d}\nu}{2\pi}\sum_{ijab}V_{ab}^{ij}\overline{W}_{ji}^{ba}(\mathrm{i}\nu)f_{ia}(\mathrm{i}\nu)f_{jb}(\mathrm{i}\nu)\,, \qquad \text{with } f_{ia}(\mathrm{i}\nu) = \frac{2(\varepsilon_a-\varepsilon_i)}{(\varepsilon_a-\varepsilon_i)^2+\nu^2}\,.$$

In this form, the frequency dependent RPA energy expression bears resemblance to the drCCD RPA expression $\frac{1}{2}\sum_{ijab}t_{ij}^{ab}V_{ab}^{ij}$ and we can define the *AC-SOSEX* by anti-symmetrizing the Coulomb interaction V in analogy to the drCCD SOSEX expression, arriving at

$$E_\mathrm{c}^\mathrm{AC-SOSEX} = +\frac{1}{2}\int\frac{\mathrm{d}\nu}{2\pi}\sum_{ijab}V_{ab}^{ji}\overline{W}_{ij}^{ab}(\mathrm{i}\nu)f_{ia}(\mathrm{i}\nu)f_{jb}(\mathrm{i}\nu)\,. \quad (7.6)$$

Above equation still requires $\mathcal{O}(N^4)$ of memory from the two interactions V_{ab}^{ij} and $\overline{W}_{ij}^{ab}$. We can, however, transform it back into the position basis as discussed in Section 5.7, to arrive at

$$E_\mathrm{c}^\mathrm{AC-SOSEX} = -\frac{1}{2}\int\frac{\mathrm{d}\nu}{2\pi}\,\mathrm{tr}\left\{\mathbf{P}_\mathrm{x}^\mathrm{AC}(\mathrm{i}\nu)\overline{\mathbf{W}}(\mathrm{i}\nu)\right\},$$

defining the imaginary frequency dependent exchange polarizability for the AC-SOSEX:

$$\mathbf{P}_\mathrm{x}^\mathrm{AC}{}_{\mathbf{x}_1\mathbf{x}_2}(\mathrm{i}\nu) = -\iint\mathrm{d}\mathbf{x}_3\,\mathrm{d}\mathbf{x}_4\,\frac{1}{|\mathbf{r}_3-\mathbf{r}_4|}\sum_{ia}\psi_i^*(\mathbf{x}_4)\psi_i(\mathbf{x}_1)\psi_a^*(\mathbf{x}_1)\psi_a(\mathbf{x}_3)f_{ia}(\mathrm{i}\nu)$$
$$\sum_{jb}\psi_j^*(\mathbf{x}_3)\psi_j(\mathbf{x}_2)\psi_b^*(\mathbf{x}_2)\psi_b(\mathbf{x}_4)f_{jb}(\mathrm{i}\nu)\,. \quad (7.7)$$

Note that the exchange polarizability is defined negative since it contains only one Fermion loop. We can give a closed form for the coupling strength averaged screened interaction finding a matrix function with the same series expansion. This yields the final expression for the AC-SOSEX:

$$E_{\mathrm{c}}^{\mathrm{AC-SOSEX}} = \frac{1}{2}\int \frac{\mathrm{d}\nu}{2\pi}\,\mathrm{tr}\left\{\mathbf{P}_{\mathrm{x}}^{\mathrm{AC}}(\mathrm{i}\nu)\Big(\mathbf{X}_0(\mathrm{i}\nu)\mathbf{V}\mathbf{X}_0(\mathrm{i}\nu)\Big)^{-1}\Big(\log\Big(\mathbf{1}-\mathbf{X}_0(\mathrm{i}\nu)\mathbf{V}\Big)+\mathbf{X}_0(\mathrm{i}\nu)\mathbf{V}\Big)\right\}. \tag{7.8}$$

The exchange polarizability is a quantity depending on two positions. Thus, evaluating the AC-SOSEX as given above requires only $\mathcal{O}(N^2)$ of memory rather than $\mathcal{O}(N^4)$, greatly broadening the applicability of the AC-SOSEX to larger systems. However, calculating the exchange polarizability still requires $\mathcal{O}(N^5)$ steps, which is equally time consuming as calculating the SOSEX from the direct ring Coupled Cluster Doubles amplitudes. In the Random Phase Approximation the respective polarizability analogous to $\mathbf{P}_{\mathrm{x}}^{\mathrm{AC}}(\mathrm{i}\nu)$ simply factors into $\mathbf{X}_0(\mathrm{i}\nu)\mathbf{V}\mathbf{X}_0(\mathrm{i}\nu)$, allowing for an evaluation in $\mathcal{O}(N^4)$ steps or better. This can not be done for the AC-SOSEX since $\mathbf{x}_3$ and $\mathbf{x}_4$ occur in both sums in (7.7). Reducing the memory consumption from $\mathcal{O}(N^4)$ to $\mathcal{O}(N^2)$ is still an important improvement since it is easier to allocate more CPUs to a calculation than it is to allocate more memory per CPU.

7.3 Difference between drCCD SOSEX and AC-SOSEX

Despite the similarity of (7.6) and the expression for the drCCD SOSEX (7.1) they are only identical in second order but not beyond. First, the drCCD amplitudes 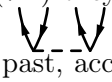 are constructed such that all interactions, contained in the amplitudes, lie in the past, according to (6.13)-(6.16). This guarantees that the closing Coulomb interaction in

is indeed the last interaction in time. In contrast, the averaged screened interaction $\overline{\mathbf{W}}(\mathrm{i}\nu)$ contains interactions that reach both, into the past and into the future. Thus, the left diagram shown in Figure 7.3 is contained in the AC-SOSEX while it is not contained in the drCCD SOSEX. Furthermore, anti-symmetrizing the first and the last case in (7.5) yields terms that have no correspondence in many-body perturbation theory. The AC-SOSEX introduces anti-symmetrization by simply swapping i and j at the unscreened interaction V. For the last term this yields for example

$$V_{ai}^{jb}\overline{W}_{bi}^{ja}\,.$$

This term, however, contradicts the requirement of many-body perturbation theory that upper indices must only match lower indices and vice-versa since upper and lower indices refer to creation and annihilation operators, respectively. This term can therefore not be drawn diagrammatically in the usual manner such that the upper/lower indices correspond to outgoing/incoming connections. We can, however, draw the term respecting the propagation direction of particles and holes. The resulting diagram is depicted on the right of Figure 7.3. It exhibits a particle a turning into a hole j at the left vertex of the Coulomb interaction and a hole i turning into a particle b at the right vertex. This diagram will be termed *improper ladder diagram* since it resembles a particle-hole ladder diagram where b and j are swapped.

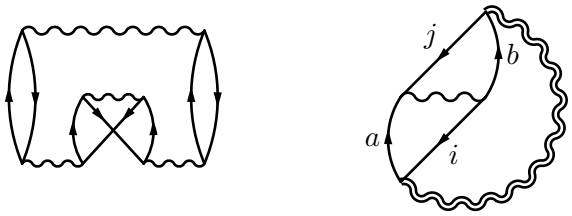

Figure 7.3: Diagrams contained in the AC-SOSEX that are not part of the SOSEX based on the drCCD amplitudes. The factors from the coupling strength integration are omitted. The right diagram shows a particle turning into a hole and vice-versa, which has no correspondence in many-body perturbation theory.

Employing the same notation of diagrams as in (7.5), the AC-SOSEX can be depicted diagrammatically by

$$E_{\mathrm{c}}^{\mathrm{AC-SOSEX}} = \frac{1}{2}$$

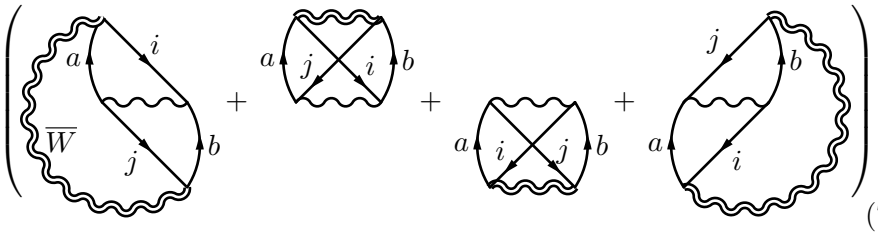

(7.9)

7.3.1 Diamond C(A4)

We can study the improper ladder diagram for a small test system consisting of diamond C(A4) with 128 states. It is based on a Hartree-Fock reference with 2×2×2 k-points in a primitive cell comprising 2 atoms with 4 electrons per atom, provided by Grüneis 2014. Although the system is only approximately described by 128 states it serves well as a benchmark for individual diagrams beyond second order. In this fairly large band gap system we can limit the order of the AC-SOSEX diagrams from (7.9) solely to third order while still getting finite results. This excludes all diagrams that are not contained in the drCCD SOSEX except the third order improper ladder diagram. The AC-SOSEX expression from (7.9) expands in third order to all possible permutations of the interaction times, analogous to Figure 5.9. Including the factor 1/3 from the coupling strength integration, this gives

$$E_{\mathrm{c}}^{\mathrm{AC-SOSEX}(3)} = \frac{1}{2 \cdot 3}$$

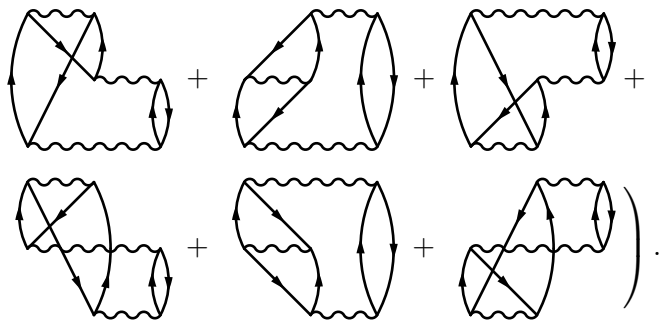

(7.10)

The lower diagrams are equivalent to the upper diagrams since each can be continuously deformed into the respective upper diagram without changing the order of the Coulomb interactions. The left two and the right two diagrams yield the same result due to time reversal

symmetry. This leaves two diagrams with distinct energies to evaluate, the exchange diagram and the improper ladder diagram:

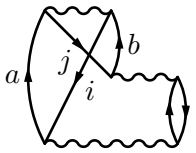

$$= (-1)^{2+3} \sum_{ijkabc} \frac{V_{ab}^{ji} V_{ik}^{ac} V_{jc}^{bk}}{(\varepsilon_i + \varepsilon_k - \varepsilon_a - \varepsilon_c)(\varepsilon_i + \varepsilon_j - \varepsilon_a - \varepsilon_b)} = -1.151\,\mathrm{m}E_h\,N, \tag{7.11}$$

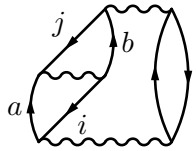

$$= (-1)^{2+3} \sum_{ijkabc} \frac{V_{ai}^{jb} V_{ik}^{ac} V_{bc}^{jk}}{(\varepsilon_i + \varepsilon_k - \varepsilon_a - \varepsilon_c)(\varepsilon_j + \varepsilon_k - \varepsilon_b - \varepsilon_c)} = -1.141\,\mathrm{m}E_h\,N. \tag{7.12}$$

Although the denominators differ, they yield almost the same energy per electron. Thus, the AC-SOSEX energy for the test system in third order hardly differs from the drCCD SOSEX energy in third order. The latter is simply given by the exchange diagram in (7.11):

$$\begin{aligned} E_\mathrm{c}^{\mathrm{AC-SOSEX}\,(3)} &= -\frac{1}{3}\big(2 \cdot 1.151 + 1.141\big) = -1.148\,\mathrm{m}E_h\,N, \\ E_\mathrm{c}^{\mathrm{SOSEX}\,(3)} &= -1.151\,\mathrm{m}E_h\,N. \end{aligned}$$

In fourth order, the AC-SOSEX expression from (7.9) expands to 24 possible permutations of the interaction times, 12 of which are distinct Goldstone diagrams. This cancels the factor 1/2 of (7.9). The factor from the coupling strength integration is 1/4, giving

$E_\mathrm{c}^{\mathrm{AC-SOSEX}\,(4)} = \frac{1}{4}\Bigg($

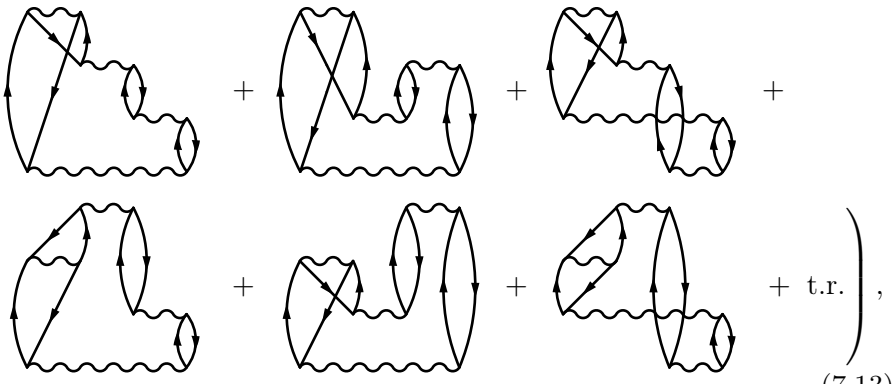

$\Bigg)$, (7.13)

where t.r. denotes the time reversed variants of the shown 6 diagrams. Note that the diagrams are drawn such that the permutations of the interaction times are evident and not according to a minimal number of intersections of the drawn edges. The diagrams can be evaluated by iterating the doubles amplitudes t_{ij}^{ab} employing only a subset of the direct ring Coupled Cluster Doubles amplitude equations. The following steps are for instance used to calculate the second diagram in (7.13) indicating the employed part of the drCCD amplitude equation

above each equal sign:

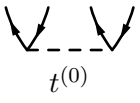

$$t_{ij}^{ab(0)} \overset{(6.13)}{=} \frac{V_{ij}^{ab}}{\varepsilon_i + \varepsilon_j - \varepsilon_a - \varepsilon_b},$$

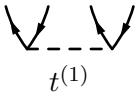

$$t_{ij}^{ab(1)} \overset{(6.16)}{=} \frac{\sum_{klcd} t_{ik}^{ac(0)} V_{cd}^{kl} t_{lj}^{db(0)}}{\varepsilon_i + \varepsilon_j - \varepsilon_a - \varepsilon_b},$$

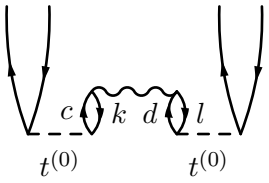

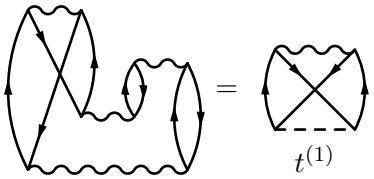

$$\overset{(7.1)}{=} -\frac{1}{2} \sum_{ijab} t_{ij}^{ab(1)} V_{ab}^{ji}.$$

Evaluating the second row of diagrams in (7.13) requires two additional parts of the doubles amplitude equation that are not part of the drCCD amplitude equation:

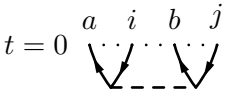

$$t_{ij}^{ab} = \frac{-\sum_{kc} V_{ia}^{ck} t_{kj}^{cb}}{\varepsilon_i + \varepsilon_j - \varepsilon_a - \varepsilon_b},$$

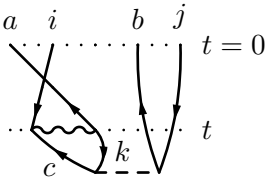

(7.14)

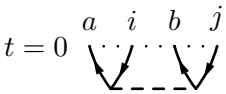

$$t_{ij}^{ab} = \frac{-\sum_{klcd} t_{ik}^{ac} V_{cd}^{lk} t_{lj}^{db}}{\varepsilon_i + \varepsilon_j - \varepsilon_a - \varepsilon_b}.$$

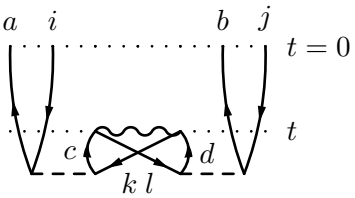

(7.15)

In the case of the improper ladder amplitude equation (7.14) there is one additional hole k but no additional loop, resulting in a negative sign. In the exchange amplitude equation (7.15) there are two additional holes and one additional loop also giving a negative sign. The latter is part of the full Coupled Cluster Doubles (CCD) amplitude equations while the improper ladder equation only occurs in the AC-SOSEX. Table 7.2 lists the energies per electron of all diagrams of the AC-SOSEX in third and fourth order modulo time reversal symmetry. The AC-SOSEX energy in fourth order is thus

$$E_{\mathrm{c}}^{\mathrm{AC-SOSEX}(4)} = \frac{1}{2}\big(0.212 + 0.105 + 0.208 + 0.208 + 0.103 + 0.209\big) = +0.522\,\mathrm{m}E_h\,N.$$

The drCCD SOSEX energy is formed by the diagrams of the first row in Table 7.2 only, yielding a very similar result:

$$E_{\mathrm{c}}^{\mathrm{SOSEX}(4)} = 0.212 + 0.105 + 0.208 = +0.525\,\mathrm{m}E_h\,N.$$

The top row in Table 7.2 shows diagrams where the last interaction is anti-symmetrized while in the second row it is the second last interaction that is anti-symmetrized. The table indicates that the energy of the SOSEX or AC-SOSEX diagrams hardly depends on which of the interactions is anti-symmetrized when using the improper ladder diagram instead of the

C(A4)	**3rd order**	**4th order** (a)	(b)	(c)
SOSEX	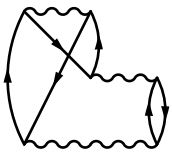	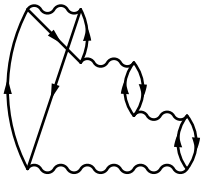	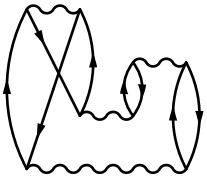	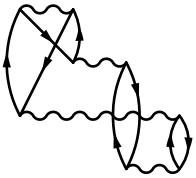
E [mE_h N]	-1.151	$+0.212$	$+0.105$	$+0.208$
AC-SOSEX	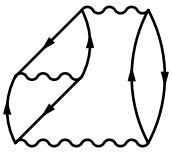	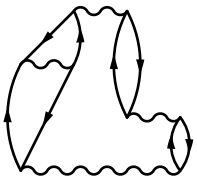	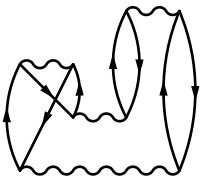	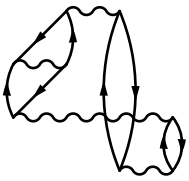
E [mE_h N]	-1.141	$+0.208$	$+0.103$	$+0.209$

Table 7.2: Goldstone diagrams forming the third and the fourth order of the drCCD SOSEX and the AC-SOSEX correction. The drCCD SOSEX consists of diagrams of the first row only. A weighted average of the first and second row yields the AC-SOSEX energy.

proper ladder diagram. Finally, the factor $1/n$ from the coupling strength integration simply averages the energies from anti-symmetrizing each of the n interactions, as shown in (7.10) for third order and in (7.13) for fourth order. Since the energies of the diagrams are very similar anti-symmetrizing each of the n interactions, the average is also very similar to the energy of the diagrams where only the last interaction is anti-symmetrized. The averaged energy forms the AC-SOSEX energy, while the latter forms the drCCD SOSEX originally proposed by Freeman. This argument holds at least up to fourth order in the diamond test system and the truncation at fourth order describes the drCCD SOSEX already to an accuracy of 5%.

7.3.2 Uniform electron gas

In a metallic system, it is not possible to truncate the AC-SOSEX expression at any finite order beyond the second order since all diagrams of SOSEX and AC-SOSEX diverge from third order on. It is, however, possible to study the AC-SOSEX diagrams of (7.9) numerically for the uniform electron gas (UEG) as the prototypical metal. In the UEG, we let spins and momenta denote the states i, j, a and b occurring in the diagrams. For the third and the fourth diagram of (7.9) we choose, for instance, the following definition of momenta:

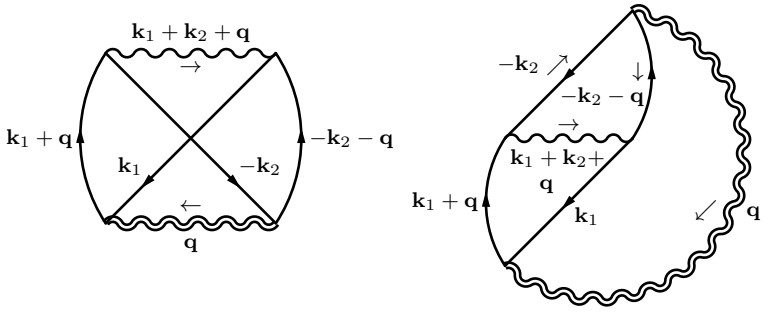

$\mathbf{k}_1$ and $-\mathbf{k}_2$ are required to be hole states while $\mathbf{k}_1 + \mathbf{q}$ and $-\mathbf{k}_2 - \mathbf{q}$ must be particle states. Thus, $\mathbf{k}_i$ must be below and $\mathbf{k}_i + \mathbf{q}$ must be above the Fermi momentum k_F for $i \in \{1, 2\}$. Note that in the improper ladder diagram on the right the momenta $-\mathbf{k}_2$ and $-\mathbf{k}_2 - \mathbf{q}$ are defined opposite to the propagation directions of the respective states, as indicated by the arrows next to the labels. The spins of all four states must be the same. In the UEG, the sum over the states is replaced by the sum over the spin and integrals over all internal momenta according to (6.39), arriving at

$$E_\mathrm{c}^{\mathrm{AC-SOSEX}}/N = + \frac{\Omega}{N}\frac{1}{2}\int \frac{\mathrm{d}\nu}{2\pi} \int \frac{\mathrm{d}\mathbf{q}}{(2\pi)^3} \sum_\sigma \iint\limits_{|\mathbf{k}_i|<k_\mathrm{F}<|\mathbf{k}_i+\mathbf{q}|} \frac{\Omega^2 \mathrm{d}\mathbf{k}_1 \mathrm{d}\mathbf{k}_2}{(2\pi)^6} V(\mathbf{k}_1 + \mathbf{k}_2 + \mathbf{q}) \overline{W}(\mathbf{q}, \nu)$$
$$\left(\frac{1}{(\Delta\varepsilon_{\mathbf{k}_1,\mathbf{q}} - \mathrm{i}\nu)(\Delta\varepsilon_{-\mathbf{k}_2,-\mathbf{q}} - \mathrm{i}\nu)} + \frac{1}{(\Delta\varepsilon_{\mathbf{k}_1,\mathbf{q}} - \mathrm{i}\nu)(\Delta\varepsilon_{-\mathbf{k}_2,-\mathbf{q}} + \mathrm{i}\nu)} + \right.$$
$$\left. \frac{1}{(\Delta\varepsilon_{\mathbf{k}_1,\mathbf{q}} + \mathrm{i}\nu)(\Delta\varepsilon_{-\mathbf{k}_2,-\mathbf{q}} - \mathrm{i}\nu)} + \frac{1}{(\Delta\varepsilon_{\mathbf{k}_1,\mathbf{q}} + \mathrm{i}\nu)(\Delta\varepsilon_{-\mathbf{k}_2,-\mathbf{q}} + \mathrm{i}\nu)} \right), \quad (7.16)$$

with $i \in \{1, 2\}$ and the single particle excitation energy $\Delta\varepsilon_{\mathbf{k}_i,\mathbf{q}} = (\mathbf{k}_i + \mathbf{q})^2/2 - \mathbf{k}_i^2/2$. The same expression can be derived using imaginary frequency propagators defined in (6.45) and integrating out the two additional imaginary frequencies analogous to the derivation of χ_0 in (6.46).

Integrating out $\mathbf{k}_1$ and $\mathbf{k}_2$ turns out to be a tedious task for the above equation. Although there are closed expressions for the second and the third case they are complicated. For the improper ladder diagrams in the first and the fourth case no such expressions were found (Ziesche 2014). However, a straight-forward Monte Carlo integration of $\mathbf{k}_1$ and $\mathbf{k}_2$ has proven to be sufficiently accurate when sampling the momenta $\mathbf{k}_i$ with a probability density function (PDF) given by

$$\mathrm{PDF}(\mathbf{k}_i) \propto \begin{cases} \left| \frac{1}{\Delta\varepsilon_{\mathbf{k}_i,\mathbf{q}} \pm \mathrm{i}\nu} \right| & \text{for } |\mathbf{k}_i| < k_\mathrm{F} < |\mathbf{k}_i + \mathbf{q}|\,, \\ 0 & \text{otherwise.} \end{cases}$$

Figure 7.2 and Table 7.1 show the resulting AC-SOSEX energies as a function of density given by the Wigner–Seitz radius, r_s. The uncertainties from the integrations are given the table. For the Monte Carlo integration of $\mathbf{k}_1$ and $\mathbf{k}_2$ a precision of 5 significant digits can be achieved with less than 30000 samples for each q and ν, depending on momentum, frequency and density. The error from the momentum and imaginary frequency integration is of similar magnitude. The differences between the two SOSEX variants are not as small as for an isolating system, however, they are still below 3% for the density range with $r_s \leq 10$. For lower densities, no drCCD SOSEX reference values were found.

Summary

The Random Phase Approximation (RPA) systematically overestimates the negative correlation energy. This originates, at least partially, from violations of the Pauli exclusion principle in the ring diagrams of the RPA such as

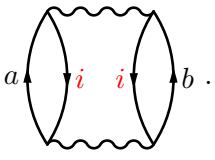

.

By the merit of Wick's theorem, violations of the Pauli exclusion principle do not have to be considered as long as all contractions of the occurring operators are included. The contractions correcting these violations are those from the respective exchange diagrams where the offending states are crossed by anti-symmetrizing an affected Coulomb interaction.

Thus, the lowest order correction to the Random Phase Approximation anti-symmetrizes one Coulomb interaction occurring in the ring diagrams. If this interaction is the last interaction in time the respective correction is termed Second Order Screened Exchange (SOSEX) containing the following diagrams:

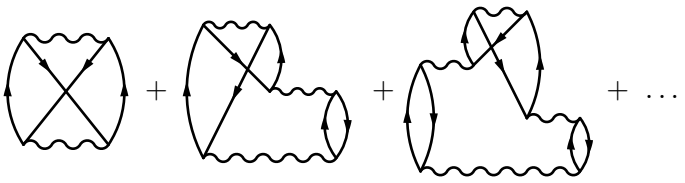

Currently, the SOSEX can only be computed from the direct ring Coupled Cluster Doubles (drCCD) amplitudes since monotonicity in time is required to be able to anti-symmetrize only the last interaction. When calculating the RPA using the drCCD amplitudes, the SOSEX can be easily computed with hardly any additional costs. However, calculating the drCCD amplitudes requires $\mathcal{O}(N^4)$ of memory limiting the applicability of RPA+SOSEX to rather small systems.

To overcome the limitations regarding memory consumption, the Adiabatic-Connection (AC) SOSEX can be used requiring only $\mathcal{O}(N^2)$ of memory. It yields very similar results compared to the SOSEX although it contains terms that have no correspondence in many-body perturbation theory where particles turn into holes and vice-versa, herein called improper ladder diagrams. This is due to the numerical oddity that it hardly matters which of the n occurring interactions in n-th order are anti-symmetrized, as long as improper ladder diagrams are used rather than actual ladder diagrams. In third order this means for instance:

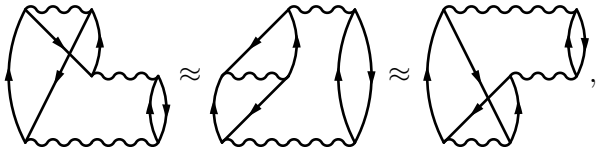

such that

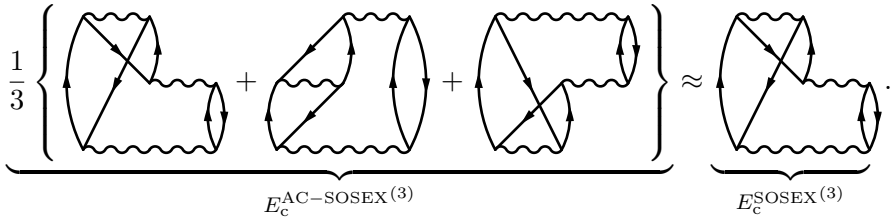

Thus, the AC-SOSEX can be considered a recipe for imitating the SOSEX energy, while reducing the memory requirements to $\mathcal{O}(N^2)$.

Apart from technical convenience when having the drCCD amplitudes at hand, there is however no reason to limit the considered exchange diagrams to those where only the last interaction is anti-symmetrized. From an *ab-initio* point of view, one should rather consider all diagrams where one interaction is anti-symmetrized and where violations of the Pauli principle can occur as the lowest order correction to the RPA. This is discussed in the next chapter.

Chapter 8

Adjacent Pairs Exchange

The Second Order Screened Exchange (SOSEX) correction to the Random Phase Approximation (RPA) arises from anti-symmetrizing only the last Coulomb interaction of RPA's ring diagrams as shown in Figure 7.1. When calculating the RPA using the direct ring Coupled Cluster Doubles (drCCD) amplitudes t_{ij}^{ab}, as introduced by Freeman 1977, this comes at virtually no extra costs and represents a natural choice for the lowest order correction to the RPA. However, when calculating the RPA in the frequency domain, which is more efficient, there is *a priori* no reason to choose this particular class of diagrams as the lowest order correction to the RPA. Furthermore, it is not possible to evaluate the SOSEX diagrams directly, since the last interaction in time cannot be explicitly addressed in the frequency domain. The AC-SOSEX approach, discussed in Section 7.2, offers an efficient alternative but it contains improper ladder diagrams that are not part of the many-body perturbation expansion. So the question remains, which diagrams that are actually part of the many-body perturbation expansion can be efficiently evaluated in the frequency domain and offer a good lowest order correction to the systematic error of the Random Phase Approximation.

8.1 Drivation of the Adjacent Pairs Exchange correction

As discussed in the beginning of Chapter 7, violations of the Pauli exclusion principle in RPA's ring diagrams suggest to anti-symmetrize the Coulomb interactions wherever such a violation can occur. In lowest order, it should be only one but not necessarily just the last Coulomb interaction that is anti-symmetrized. This is done by cutting out one Coulomb interaction including the adjacent particle/hole pair bubbles from the RPA ring diagrams and anti-symmetrizing that interaction. Which interaction are anti-symmetrized and which not will be studied in this section.

8.1.1 Two Sided Adjacent Pairs Exchange

Two adjacent particle/hole pair bubbles have four possible time orders with respect to the Coulomb interaction between them, shown in Figure 8.1(a). In the first and in the last case an anti-symmetrization of the contained Coulomb interaction only cancels contributions where the same states i and a occur in consecutive bubbles, as illustrated in Figure 8.1(b). In general, such contributions do not violate the Pauli exclusion principle. Following this argument, we exclude these cases and study a correction to the Random Phase Approximation where the

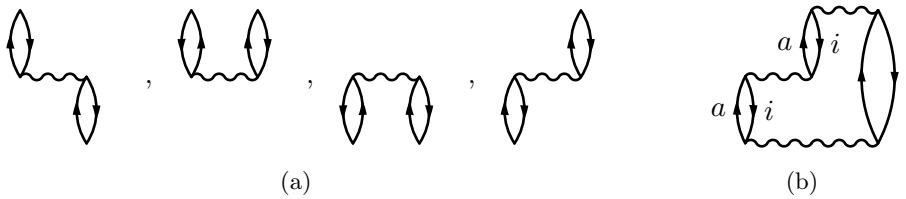

Figure 8.1: (a) The possible time orders of a Coulomb interaction and its two adjacent particle/hole pair bubbles. (b) Anti-symmetrizing the first and the last case only cancels contributions i and a as indicated here for example. In general, these contributions do not violate the Pauli exclusion principle.

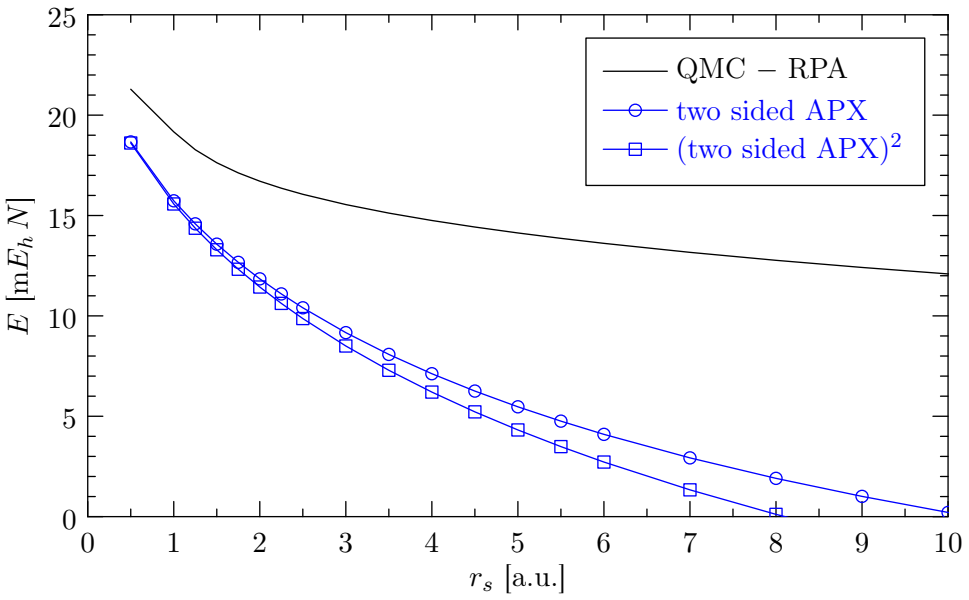

Figure 8.2: The Two sided Adjacent Pairs Exchange (2APX) energy per electron for the uniform electron gas compared to the error of the Random Phase Approximation with respect to Quantum Monte Carlo (QMC) calculations by Ceperley and Alder 1980, parametrized by Perdew and Zunger 1981. Anti-symmetrizing more than one interaction in the RPA ring diagrams by the application of (8.1) worsens the accuracy with respect to Quantum Monte Carlo results.

two remaining cases are anti-symmetrized to

(8.1)

and inserted into the RPA ring diagrams. Since these diagrams are polarization parts with two open vertices the memory requirement for calculating this correction scales like $\mathcal{O}(N^2)$ with the system size N. This is equivalent to the memory requirement of the AC-SOSEX and considerably less than $\mathcal{O}(N^4)$ of the conventional SOSEX, calculated from the direct ring Coupled Cluster Doubles (drCCD) amplitudes. We term this correction *two sided Adjacent Pairs Exchange (2APX)* and its expansion in terms of Goldstone diagrams is given by

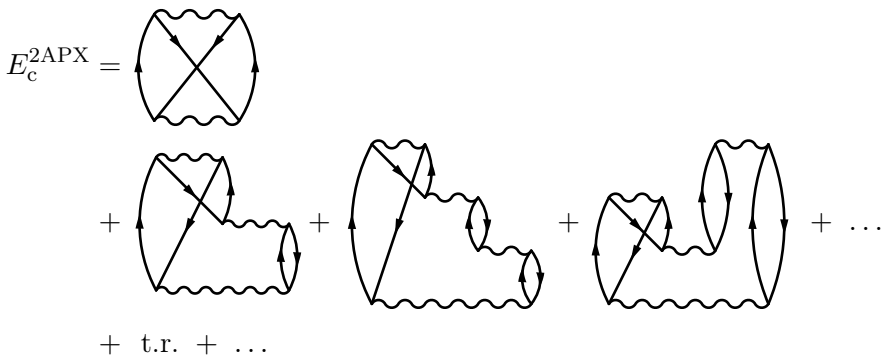

(8.2)

The second row contains only the right contribution of (8.1) and t.r. refers to diagrams emerging from the second row by time reversal, containing only the left contribution of (8.1).

In third order, the two sided Adjacent Pair Exchange correction yields twice the contribution of the SOSEX correction. In higher orders, there are even more diagrams contained in the two sided APX. Since the third order is the lowest order where the two sided APX and the SOSEX differ and since this order is in general negative, the two sided APX correction is expected to be smaller than the SOSEX correction. Evaluating the two sided APX for the Uniform Electron Gas, as discussed in Section 8.2, confirms this expectation. As shown in Figure 8.2 the two sided APX considerably underestimates the desired energy correction, given by the difference of the RPA and Quantum Monte Carlo results. At low densities, where $r_s > 10$, it even becomes negative, actually worsening the systematic error of RPA.

The two sided Adjacent Pairs Exchange correction seems the most plausible lowest order correction to the Random Phase Approximation. However, despite improving on the RPA in the UEG for densities with $r_s < 10$, it always underestimates, but never overestimates the missing correlation energy, which is herein referred to as *unbalanced*. One could include diagrams, where two, three or more of the RPA's Coulomb interactions are anti-symmetrized, in the fashion discussed above, as the next orders of the correction. These corrections are still forming a ring and can thus be efficiently evaluated in the frequency domain, once the two sided Adjacent Pairs Exchange polarization part $\mathbf{P}_{\mathrm{x}}^{\mathrm{2AXP}}$ has been calculated. In terms of Feynman diagrams and propagator matrices, the corrections with one or two Coulomb

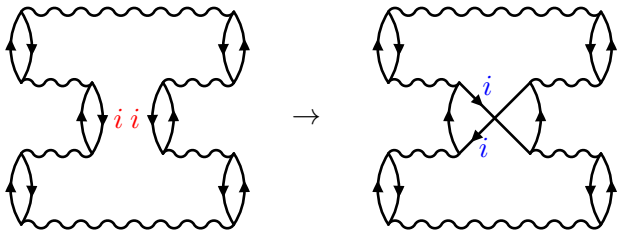

Figure 8.3: Exchange of pair bubbles that are non-adjacent

interactions anti-symmetrized are given by

$$E_{\mathrm{c}}^{\mathrm{2APX}} = \quad \mathbf{P}_{\mathrm{x}}$$

$$= \frac{1}{2}\left(\frac{1}{2}\mathbf{P}_{\mathrm{x}}\mathbf{V} + \mathbf{P}_{\mathrm{x}}\mathbf{V}\mathbf{X}_0\mathbf{V} + \mathbf{P}_{\mathrm{x}}\mathbf{V}\mathbf{X}_0\mathbf{V}\mathbf{X}_0\mathbf{V} + \ldots\right), \tag{8.3}$$

$$E_{\mathrm{c}}^{(\mathrm{2APX}^2)} = \quad \mathbf{P}_{\mathrm{x}} \quad + \quad \mathbf{P}_{\mathrm{x}} \quad \mathbf{P}_{\mathrm{x}}$$

$$= E_{\mathrm{c}}^{\mathrm{2APX}} + \frac{1}{2\cdot 2}\left(\mathbf{P}_{\mathrm{x}}\mathbf{V} + \mathbf{P}_{\mathrm{x}}\mathbf{V}\mathbf{X}_0\mathbf{V} + \mathbf{P}_{\mathrm{x}}\mathbf{V}\mathbf{X}_0\mathbf{V}\mathbf{X}_0\mathbf{V} + \ldots\right)^2, \tag{8.4}$$

with

$$\mathbf{P}_{\mathrm{x}} \quad = \quad + \quad ,$$

and where the superscript of $\mathbf{P}_{\mathrm{x}}^{\mathrm{2APX}}$, the trace, the imaginary time integration – including the sign – and the imaginary time arguments have been omitted for brevity. The RPA screened interaction is given by (6.7). All diagrams posses reflection symmetry but note that the symmetry factor differs in the case where only one occurrence of $\mathbf{P}_{\mathrm{x}}^{\mathrm{2APX}}$ is inserted into the ring diagrams compared to other case. This is due to a reflection symmetry introduced when closing $\mathbf{P}_{\mathrm{x}}^{\mathrm{2APX}}$ with only one Coulomb interaction $\mathbf{V}$. Figure 8.2 shows $E_{\mathrm{c}}^{\mathrm{2APX}}$ and $E_{\mathrm{c}}^{(2APX)^2}$ according to (8.3) and (8.4). More insertions of $\mathbf{P}_{\mathrm{x}}^{\mathrm{2APX}}$ into the ring diagrams of the Random Phase Approximation actually worsen the accuracy of the two sided APX with respect to Quantum Monte Carlo results. More than two insertions of $\mathbf{P}_{\mathrm{x}}^{\mathrm{2APX}}$ into the ring diagrams of the RPA offer no improvement either, so none of the two sided APX approximations ever overestimates the missing correlation energy and thus none is balanced.

We could investigate more complex exchange processes, for instance those correcting violations of the Pauli exclusion principle of pair bubbles in the RPA that are not adjacent, as sketched in Figure 8.3. However, the exclusion principle is only violated if the two affected pair bubbles propagate at overlapping times. This would require a time order which can only be provided when evaluating the Random Phase Approximation from the direct ring Coupled Cluster Doubles (drCCD) amplitudes, loosing the advantage of the reduced memory requirements of an RPA implementation in the frequency domain.

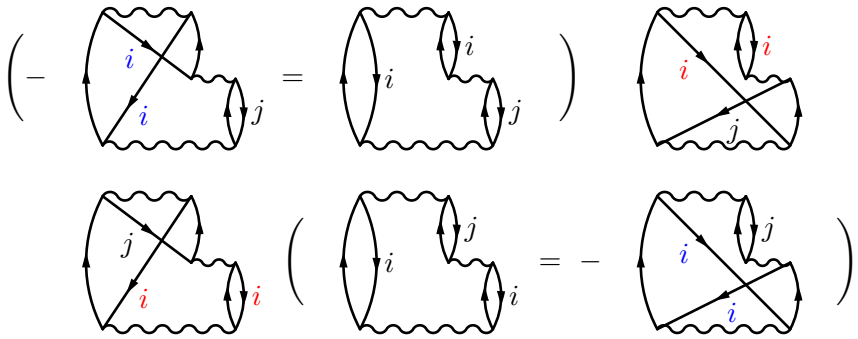

Figure 8.4: The two sided Adjacent Pairs Exchange correction introduces new violations of the Pauli exclusion principle, as shown here in third order in the case of two identical hole indices. One of the two exchange diagrams exactly cancels the offending contributions of the RPA diagram, put in parenthesis together with the RPA diagram. The other exchange diagram, however, introduces new violations.

8.1.2 Adjacent Pairs Exchange

The unbalanced performance of the two sided APX and its higher order variants rises the question whether really all Coulomb interactions should be anti-symmetrized if that can correct for violations of the Pauli exclusion principle. It turns out that the two sided APX, while indeed correcting for all violations occurring in adjacent pairs, introduces new violations. In third order this is most apparent and illustrated in Figure 8.4. The lower/upper row shows the case where the lower/upper two pair bubbles of the RPA propagate in the same hole state i. The exchange diagram contained in parenthesis together with the RPA diagram exchanges these two propagators and exactly cancels the offending contributions of the RPA. The other diagram, however, introduces new violations to the Pauli exclusion principle.

The key issue, in this case, is that the leftmost and longest particle/hole pair bubble of the RPA diagram is exchanged in both diagrams of the two sided APX corrections. While this guarantees that all possible violating contributions are canceled, it always introduces new violations. For a more balanced correction we therefore require that each pair bubble is exchanged at most once. The simplest correction satisfying this requirement is the (single sided) *Adjacent Pairs Exchange (APX)* correction, where only one case of (8.1) is contained. For a system with time reflection symmetry it is irrelevant which of the cases we choose and without loss of generality we choose to anti-symmetrize adjacent pair bubbles in the third case of time orders shown in Figure 8.1(a):

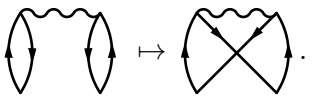

(8.5)

In terms of Feynman diagrams and the matrix notation of the propagators, introduced in

Section 6.1, the APX correction is then given by

$$E_{\mathrm{c}}^{\mathrm{APX}} =$$ 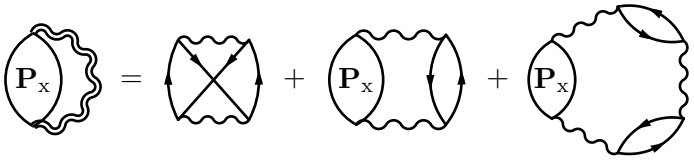 $$+ \ldots \tag{8.6}$$

$$\begin{aligned} &= -\frac{1}{2}\int \frac{\mathrm{d}\nu}{2\pi}\,\mathrm{tr}\Big\{\mathbf{P}_{\mathrm{x}}^{\mathrm{APX}}\mathbf{V} + \mathbf{P}_{\mathrm{x}}^{\mathrm{APX}}\mathbf{V}\mathbf{X}_0\mathbf{V} + \mathbf{P}_{\mathrm{x}}^{\mathrm{APX}}\mathbf{V}\mathbf{X}_0\mathbf{V}\mathbf{X}_0\mathbf{V} + \ldots\Big\} \\ &= -\frac{1}{2}\int \frac{\mathrm{d}\nu}{2\pi}\,\mathrm{tr}\Big\{\mathbf{P}_{\mathrm{x}}^{\mathrm{APX}}\mathbf{W}\Big\}, \end{aligned}$$

with

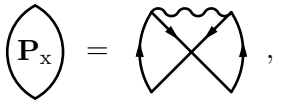

and where the imaginary time arguments as well as the superscript of $\mathbf{P}_{\mathrm{x}}^{\mathrm{APX}}$ in the diagrams have been omitted for brevity. All diagrams exhibit a single reflection symmetry but note that, unlike in the two sided APX case, there is no additional symmetry introduced when closing $\mathbf{P}_{\mathrm{x}}^{\mathrm{APX}}$ with one Coulomb interaction $\mathbf{V}$ since the $\mathbf{P}_{\mathrm{x}}^{\mathrm{APX}}$ contains only one of the two time orders contained in $\mathbf{P}_{\mathrm{x}}^{\mathrm{2APX}}$. Despite the ring form of the APX diagrams beyond second order, none of them has a rotational symmetry in contrast to the respective RPA diagrams. This simplifies the sum over all orders of the perturbation compared to the RPA since all orders have the same factor. We can use the infinite sum of a geometric series to give an explicit form for the APX energy:

$$E_{\mathrm{c}}^{\mathrm{APX}} = -\frac{1}{2}\int_{-\infty}^{\infty} \frac{\mathrm{d}\nu}{2\pi}\,\mathrm{tr}\left\{\mathbf{P}_{\mathrm{x}}^{\mathrm{APX}}(\mathrm{i}\nu)\mathbf{V}\Big(\mathbf{1} - \mathbf{X}_0(\mathrm{i}\nu)\mathbf{V}\Big)^{-1}\right\}, \tag{8.7}$$

where the imaginary frequency dependent exchange polarizability for the APX contains only one of the four time orders contained in $\mathbf{P}_{\mathrm{x}}^{\mathrm{AC}}$, which was given in (7.7):

$$\begin{aligned} \mathbf{P}_{\mathrm{x}}^{\mathrm{APX}}{}_{\mathbf{x}_1\mathbf{x}_2}(\mathrm{i}\nu) = -\iint \mathrm{d}\mathbf{x}_3\,\mathrm{d}\mathbf{x}_4\,\frac{1}{|\mathbf{r}_3-\mathbf{r}_4|}\sum_{ia}\psi_i^*(\mathbf{x}_4)\psi_i(\mathbf{x}_1)\psi_a^*(\mathbf{x}_1)\psi_a(\mathbf{x}_3)\frac{1}{\varepsilon_a-\varepsilon_i+\mathrm{i}\nu} \\ \sum_{jb}\psi_j^*(\mathbf{x}_3)\psi_j(\mathbf{x}_2)\psi_b^*(\mathbf{x}_2)\psi_b(\mathbf{x}_4)\frac{1}{\varepsilon_b-\varepsilon_j-\mathrm{i}\nu}\,. \end{aligned} \tag{8.8}$$

8.2 APX for the uniform electron gas

Evaluating the Adjacent Pairs Exchange (APX) energy for the Uniform Electron Gas (UEG) is very similar to evaluating the AC-SOSEX energy according to (7.16). In contrast to the AC-SOSEX expression, only one of the four time orders of two adjacent pair bubbles are contained in the APX. In the chosen order, the Coulomb interaction of the exchange polarizability $\mathbf{P}_{\mathrm{x}}^{\mathrm{APX}}$

occurs after both open vertices of $\mathbf{P}_{\mathrm{x}}^{\mathrm{APX}}$:[1]

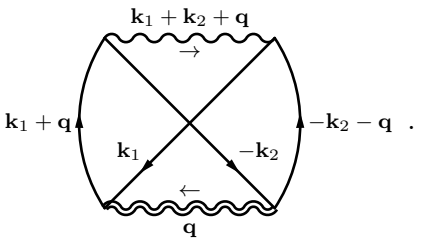

Furthermore, the APX uses the screened interaction W, represented by the double wiggly line, as given by (6.7) rather than the coupling strength averaged screened interaction $\overline{W}$, since all orders of the expansion have the same factor. The APX correction to the Random Phase Approximation per electron is thus given by

$$E_{\mathrm{c}}^{\mathrm{APX}}/N = +\frac{\Omega}{N}\frac{1}{2}\int\frac{\mathrm{d}\nu}{2\pi}\int\frac{\mathrm{d}\mathbf{q}}{(2\pi)^3}\sum_{\sigma}\iint\limits_{|\mathbf{k}_i|<k_{\mathrm{F}}<|\mathbf{k}_i+\mathbf{q}|}\frac{\Omega^2\mathrm{d}\mathbf{k}_1\mathrm{d}\mathbf{k}_2}{(2\pi)^6}\,V(\mathbf{k}_1+\mathbf{k}_2+\mathbf{q})W(\mathbf{q},\nu)$$
$$\frac{1}{(\Delta\varepsilon_{\mathbf{k}_1,\mathbf{q}}+\mathrm{i}\nu)(\Delta\varepsilon_{-\mathbf{k}_2,-\mathbf{q}}-\mathrm{i}\nu)}\,, \qquad (8.9)$$

with $i \in \{1,2\}$ and the single particle excitation energy $\Delta\varepsilon_{\mathbf{k}_i,\mathbf{q}} = (\mathbf{k}_i+\mathbf{q})^2/2 - \mathbf{k}_i^2/2$. As in the case of the AC-SOSEX, the above expression can be evaluated by a Monte Carlo integration for $\mathbf{k}_1$ and $\mathbf{k}_2$ using a probability density function (PDF) given by

$$\mathrm{PDF}(\mathbf{k}_i) \propto \begin{cases} \left|\dfrac{1}{\Delta\varepsilon_{\mathbf{k}_i,\mathbf{q}} \pm \mathrm{i}\nu}\right| & \text{for } |\mathbf{k}_i| < k_{\mathrm{F}} < |\mathbf{k}_i+\mathbf{q}|\,, \\ 0 & \text{otherwise.} \end{cases}$$

The momentum $\mathbf{q}$ and the imaginary frequency ν can be integrated using a Gauss–Kronrod rule, analogous to the evaluation of the Random Phase Approximation. However, the asymptotic behavior of the APX energy for large imaginary frequencies differs from that of the RPA and the AC-SOSEX, such that a different variable transform for integrating the frequency tail must be used. The asymptotic behavior for large frequencies is discussed Subsection 8.2.2.

For the lowest order of the APX, the accuracy of the numerical integrations can be benchmarked against the MP2 exchange energy, which is independent of the density and it is known *analytically* from the work of Onsager, Mittag, and Stephen 1966:

$$\frac{\log(2)}{6} - 3\frac{\zeta(3)}{(2\pi)^2} \approx 0.02417915891814441\ldots\, E_h\, N.$$

For the Monte Carlo integration of $\mathbf{k}_1$ and $\mathbf{k}_2$ a precision of 5 significant digits can be achieved with less than 30000 samples for each q and ν, depending on momentum, frequency and density. The error from the momentum and imaginary frequency integration is of similar magnitude. Figure 8.5 and Table 8.1 show the resulting APX energies as a function of density given by the Wigner–Seitz radius, r_s. The uncertainties from the integrations are given in Table 8.1.

[1] In the given diagram, the time order of the vertices is only relevant with respect to the Coulomb interaction. It is therefore neither a Goldstone nor a Feynman diagram. The proper Feynman diagram of APX is the leftmost diagram of (8.6).

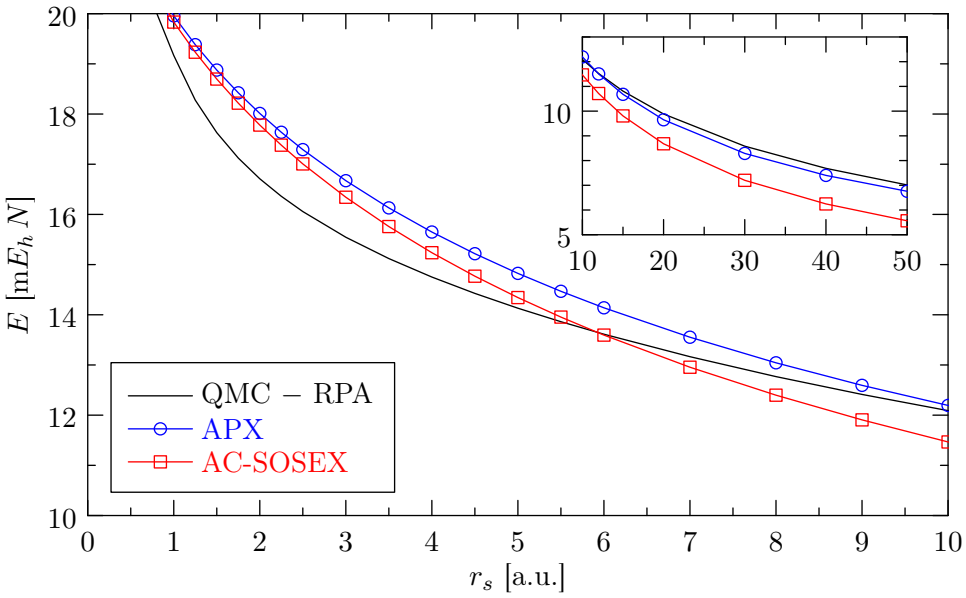

Figure 8.5: The Adjacent Pairs Exchange (APX) energy per electron for the uniform electron gas compared to the error of the Random Phase Approximation with respect to Quantum Monte Carlo (QMC) calculations by Ceperley and Alder 1980, parametrized by Perdew and Zunger 1981. RPA+APX also fortuitously matches the QMC results, but only at $r_s \approx 10$. In the low density regime, where correlation is stronger, RPA+APX is considerably closer to the QMC results than RPA+AC-SOSEX. For results of the spin-polarized uniform electron gas see Subsection 8.2.3.

r_s [a.u.]	$(E_c - E_c^{RPA})$ [mE_h N]	E_c^{APX} [mE_h N]	±	$E_c^{AC-SOSEX}$ [mE_h N]	±
1	19.167	19.956	0.005	19.832	0.009
2	16.710	18.012	0.005	17.780	0.003
3	15.545	16.672	0.005	16.342	0.003
4	14.752	15.649	0.005	15.237	0.003
5	14.131	14.825	0.004	14.343	0.003
6	13.613	14.139	0.004	13.595	0.003
7	13.165	13.553	0.004	12.955	0.003
8	12.768	13.043	0.004	12.398	0.003
9	12.413	12.594	0.004	11.906	0.003
10	12.090	12.194	0.004	11.466	0.003
12	11.521	11.506	0.004	10.712	0.003
15	10.810	10.680	0.004	9.806	0.003
20	9.884	9.650	0.004	8.679	0.003
30	8.582	8.289	0.004	7.201	0.003
40	7.685	7.400	0.004	6.246	0.003
50	7.014	6.757	0.004	5.564	0.003

Table 8.1: Data of Figure 8.5 including low densities.

8.2.1 Large momentum behavior

The finite basis set, employed in a practical Hartree-Fock or DFT calculation, imposes an upper limit $G_{\max}$ for the evaluation of the exchange polarizability $\mathbf{P}_{\mathrm{x}}^{\mathrm{APX}}$ and the independent particle polarizability $\mathbf{X}_0$. Assuming that the system is sufficiently homogeneous at that length scale, the asymptotic behavior for large momenta in the Uniform Electron Gas can be used to extrapolate results retrieved at finite $G_{\max}$ to the limit of an infinite basis set, where $G_{\max} \to \infty$.

We can write the APX correction in the UEG from (8.9) in terms an exchange polarizability $P_{\mathrm{x}}^{\mathrm{APX}}(q, \mathrm{i}\nu)$, analogous to the general APX expression (8.7):

$$E_{\mathrm{c}}^{\mathrm{APX}}/N = -\frac{\Omega}{N}\frac{1}{2}\int \frac{\mathrm{d}\nu}{2\pi} \int \frac{\mathrm{d}\mathbf{q}}{(2\pi)^3} P_{\mathrm{x}}^{\mathrm{APX}}(\mathbf{q}, \mathrm{i}\nu) V(\mathbf{q}) \Big(1 - \chi_0(\mathbf{q}, \mathrm{i}\nu) V(\mathbf{q})\Big)^{-1}, \tag{8.10}$$

$$P_{\mathrm{x}}^{\mathrm{APX}}(\mathbf{q}, \mathrm{i}\nu) = -\sum_{\sigma} \iint\limits_{|\mathbf{k}_i|<k_{\mathrm{F}}<|\mathbf{k}_i+\mathbf{q}|} \frac{\Omega^2 \mathrm{d}\mathbf{k}_1 \mathrm{d}\mathbf{k}_2}{(2\pi)^6} V(\mathbf{k}_1 + \mathbf{k}_2 + \mathbf{q}) \frac{1}{(\Delta\varepsilon_{\mathbf{k}_1,\mathbf{q}} + \mathrm{i}\nu)(\Delta\varepsilon_{-\mathbf{k}_2,-\mathbf{q}} - \mathrm{i}\nu)}\,. \tag{8.11}$$

To obtain an approximation $P_{\mathrm{x}}^{\mathrm{APX}}$ for large momenta q we can trivially integrate $\mathbf{k}_1$ and $\mathbf{k}_2$, since $|\mathbf{k}_i| < k_{\mathrm{F}} \ll q$, yielding

$$P_{\mathrm{x}}^{\mathrm{APX}}(q, \mathrm{i}\nu) \sim \frac{1}{q^2} \frac{1}{(q^2/2 + \mathrm{i}\nu)(q^2/2 - \mathrm{i}\nu)}\,. \tag{8.12}$$

Inserting this and the approximation of $\chi_0(q, \mathrm{i}\nu)V(q)$ for large q, given in (6.55), into the APX energy expression, we can integrate ν for a given, large momentum q:

$$\int \frac{\mathrm{d}\nu}{2\pi} \frac{1}{q^4} \frac{1}{(q^2/2 + \mathrm{i}\nu)(q^2/2 - \mathrm{i}\nu)} \left(1 - \frac{1}{(q^2/2)^2 + \nu^2}\right)^{-1} = \frac{1}{q^4\sqrt{q^4 - 4}}\,.$$

The missing energy $\Delta E_{\mathrm{c}}^{\mathrm{APX}}$ of the APX correction when truncating the momentum integration at a finite but large momentum $G_{\max}$ is thus

$$\Delta E_{\mathrm{c}}^{\mathrm{APX}}(G_{\max}) \sim \int_{G_{\max}}^{\infty} \frac{q^2}{q^4\sqrt{q^4 - 4}} \sim a_3 \frac{1}{G_{\max}^3} + a_7 \frac{1}{G_{\max}^7} + \mathcal{O}\left(\frac{1}{G_{\max}^{11}}\right), \tag{8.13}$$

where we have expanded the integrand in the variable $u = 1/q$ at $u = 0$. Hence, the APX energy and, similarly, the AC-SOSEX energy have the same asymptotic behavior with respect to large momenta $\mathbf{q}$ as the Random Phase Approximation. However, the convergence with respect to $G_{\max}$ is slower since the exchange corrections are more short ranged, which may require the use of more than the leading order term of the Taylor expansion for an accurate extrapolation to the infinite basis set limit.

8.2.2 Large imaginary frequency behavior

For the frequency integration of metallic systems, such as the Uniform Electron Gas, knowledge about the asymptotic behavior of the APX correction with respect to large imaginary frequencies is important for choosing an appropriate variable transform for the tail.

For large momenta q, we can use the approximation of $P_{\mathrm{x}}^{\mathrm{APX}}$ in (8.12), obtained in the previous subsection. Considering large frequencies ν, we can still use the same approximation

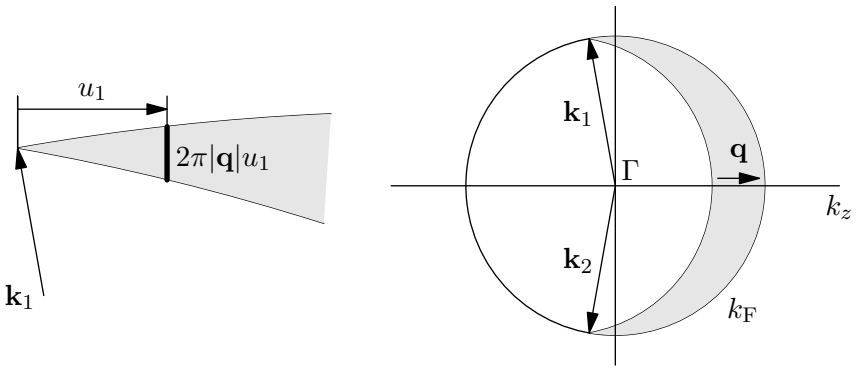

Figure 8.6: Cross section of the set of momenta $\mathbf{k}_i$ such that $|\mathbf{k}_i| < k_\mathrm{F} < |\mathbf{k}_i + \mathbf{q}|$ for excitation momenta $\mathbf{q} \leq 2$. The momentum of the Coulomb interaction $\mathbf{k}_1 + \mathbf{k}_2 + \mathbf{q}$ vanishes for the shown $\mathbf{k}_1$ and $\mathbf{k}_2$. The vicinity of the singular $\mathbf{k}_1$ is magnified on the left, showing the employed coordinates for the integration of this regions and a volume element in the form of a ring with area $2\pi|\mathbf{q}|u_1$.

for intermediate $q > 2k_\mathrm{F}$ since the denominator of the propagator $V(\mathbf{k}_1 + \mathbf{k}_2 + \mathbf{q})$ is non-vanishing and the volume of the integration region of $\mathbf{k}_1$ and $\mathbf{k}_2$ is independent of q. In this case, the integration of $\mathbf{k}_1$ and $\mathbf{k}_2$ merely averages the contributions. For $q \leq 2k_\mathrm{F}$, the volume of the integration region of $\mathbf{k}_1$ and $\mathbf{k}_2$ depends on q and there are also contributions where the propagator $V(\mathbf{k}_1 + \mathbf{k}_2 + \mathbf{q})$ becomes singular, as shown in Figure 8.6. In this case, we split the integration into two parts. In the first part both, $\mathbf{k}_1$ and $\mathbf{k}_2$ are in the vicinity of the singular contribution, shown for $\mathbf{k}_1$ on the left of Figure 8.6. In the remaining part either $\mathbf{k}_1$ or $\mathbf{k}_2$ or both are away from the singular contribution. For the first part, we can transform the integration of $\mathbf{k}_1$ and $\mathbf{k}_2$ into an integration of the respective distances u_1 and u_2 from the singular contribution in the direction of $\mathbf{q}$. In the remaining part, we approximate the integral assuming that $\mathbf{k}_1 + \mathbf{k}_2$ average out and taking into consideration that the integration volume of each $\mathbf{k}_i$ scales like $q^3 + q^2$. One obtains

$$\iint\limits_{|\mathbf{k}_i|<k_\mathrm{F}<|\mathbf{k}_i+\mathbf{q}|} \frac{\Omega^2 \mathrm{d}\mathbf{k}_1 \mathrm{d}\mathbf{k}_2}{(2\pi)^6} V(\mathbf{k}_1 + \mathbf{k}_2 + \mathbf{q}) \sim \iint_0^{k_\mathrm{F}-q/2} \mathrm{d}u_1 \mathrm{d}u_1 \, \frac{(2\pi)^2 q^2 u_1 u_2}{(u_1+u_2)^2} + \frac{(a_3 q^3 + a_2 q^2)^2}{q^2}$$
$$\sim q^2 + \mathcal{O}\left(q^3\right) . \tag{8.14}$$

Since $q \leq 2$ and ν is large, we can ignore the propagators of $P_\mathrm{x}^\mathrm{APX}$ containing the imaginary frequency for the integration of $\mathbf{k}_1$ and $\mathbf{k}_2$.

We can now insert the respective approximation of $P_\mathrm{x}^\mathrm{APX}$ for small q, intermediate q and large q into the expression for the APX energy (8.10) and integrate over q. For χ_0 we use the approximations (6.57), (6.58) and (6.55) for small, intermediate and large momenta q, respectively. The results are long and apart from their expansion in ν of no particular interest. For small and intermediate q the integration of q yields $1/\nu^2 + \mathcal{O}\left(1/\nu^4\right)$ and for large q we obtain $1/\nu^2 + \mathcal{O}\left(1/\nu^{5/2}\right)$. Finally, we can insert this expansion in the imaginary frequency integration of the APX energy and estimate the missing energy per electron $\Delta E_\mathrm{c}^\mathrm{APX}(\nu_\mathrm{max})$

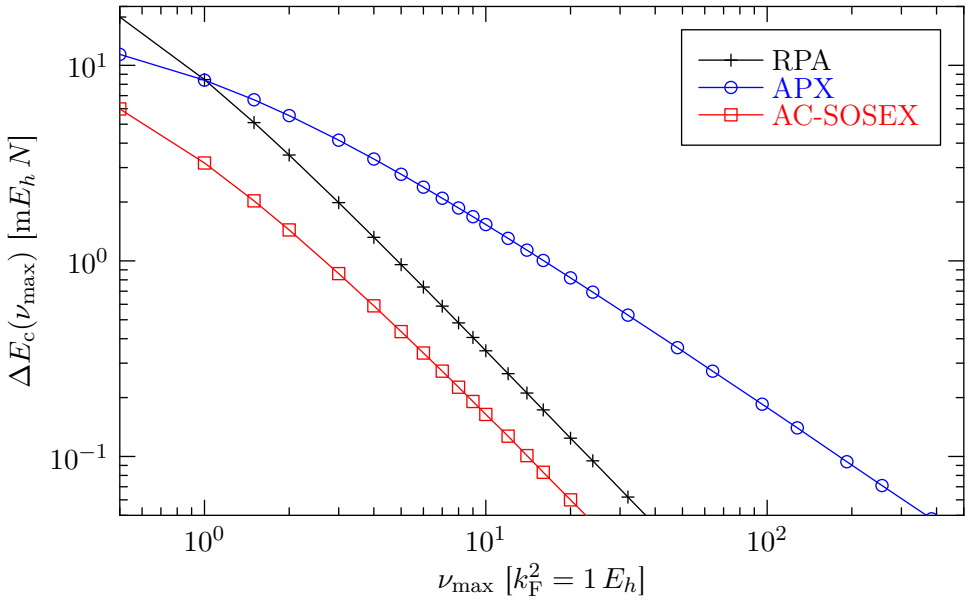

Figure 8.7: Numerical comparison of the missing correlation energy per electron for the Random Phase Approximation and its corrections when truncating the imaginary frequency integration at $\nu_{\max}$. $\nu_{\max}$ is given in units of k_{F}^2 and $k_{\mathrm{F}} = 1$.

when truncating the integration at some finite but large imaginary frequency $\nu_{\max}$:

$$\Delta E_{\mathrm{c}}^{\mathrm{APX}}(\nu_{\max}) \sim \int_{\nu_{\max}}^{\infty} \mathrm{d}\nu \left(\frac{1}{\nu^2} + \mathcal{O}\left(\frac{1}{\nu^{5/2}} \right) \right) \sim \frac{1}{\nu_{\max}} + \mathcal{O}\left(\frac{1}{\nu_{\max}^{3/2}} \right) . \tag{8.15}$$

The asymptotic behavior of the APX energy differs from that of the Random Phase Approximation and from that of the AC-SOSEX, which can be derived in an analogous fashion. This originates from the imaginary frequency behavior of $P_{\mathrm{x}}^{\mathrm{APX}}$, containing only one of the four time orders contained in the RPA and in the AC-SOSEX. Figure 8.7 compares the asymptotic behavior of RPA, AC-SOSEX and APX for the Uniform Electron Gas numerically.

8.2.3 Spin-polarized Uniform Electron Gas

We can readily evaluate the RPA and the Adjacent Pairs Exchange correction for the spin-polarized Uniform Electron Gas using only one spin in the sum over all spins $\sum_\sigma$, occurring in the expression of $P_{\mathrm{x}}^{\mathrm{APX}}(\mathbf{q}, \mathrm{i}\nu)$ in (8.11) and $\chi_0(\mathbf{q}, \mathrm{i}\nu)$ in (6.47). Considering that k_{F} also depends on whether the UEG is spin-polarized or not according to (6.40), yields correlation energies of RPA+APX shown in Figure 8.8 and Table 8.2. For comparison, the correlation energy of RPA+AC-SOSEX according to (7.16) is also given.

Unlike in the non-spin-polarized case, neither of the SOSEX variants offers a balanced correction to the Random Phase Approximation, overestimating the missing energy for the entire range of densities. The accuracy with respect to Quantum Monte Carlo results also worsens for low densities. For low densities we can assume $\mathbf{k}_1 + \mathbf{k}_2 + \mathbf{q} \approx \mathbf{q}$ since $|\mathbf{k}_i| < k_{\mathrm{F}} \ll 1$. In this limit, two adjacent RPA bubbles only differ from the respective exchange diagram in

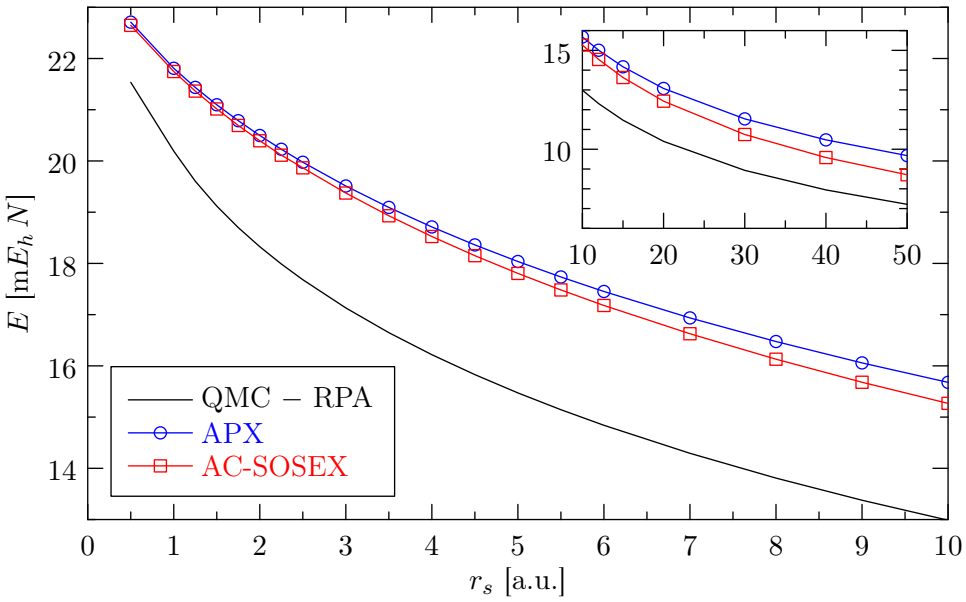

Figure 8.8: The Adjacent Pairs Exchange (APX) energy per electron for the spin-polarized uniform electron gas compared to the error of the Random Phase Approximation with respect to Quantum Monte Carlo (QMC) calculations by Ceperley and Alder 1980 fitted by Perdew and Zunger 1981. For low densities, anti-symmetrization of a ring diagram merely changes its sign, such that SOSEX or its variants simply remove the correlation energy already captured by the RPA.

r_s [a.u.]	$(E_c - E_c^{RPA})$ [mE_h N]	E_c^{APX} [mE_h N]	±	$E_c^{AC-SOSEX}$ [mE_h N]	±
1	20.192	21.809	0.005	21.746	0.033
2	18.326	20.497	0.005	20.394	0.017
3	17.131	19.511	0.005	19.374	0.006
4	16.218	18.712	0.005	18.525	0.003
5	15.472	18.037	0.005	17.805	0.003
6	14.840	17.452	0.005	17.179	0.003
7	14.293	16.936	0.005	16.627	0.003
8	13.809	16.475	0.005	16.130	0.003
9	13.377	16.058	0.005	15.680	0.003
10	12.987	15.678	0.005	15.268	0.003
12	12.307	15.007	0.005	14.541	0.003
15	11.469	14.169	0.004	13.628	0.003
20	10.398	13.073	0.004	12.431	0.003
30	8.932	11.536	0.004	10.745	0.003
40	7.943	10.474	0.004	9.580	0.003
50	7.215	9.678	0.004	8.710	0.003

Table 8.2: Data of Figure 8.8 including low densities.

the Fermion sign and the additional spin variable from having two loops instead of one:

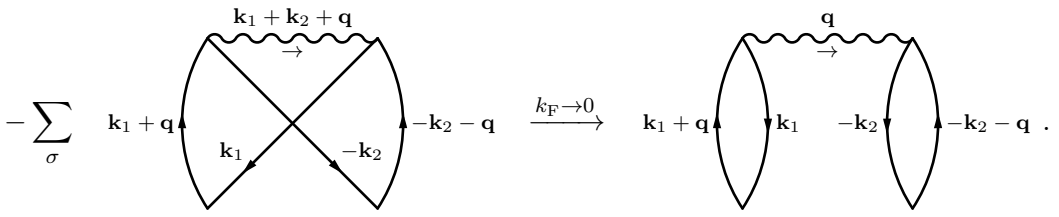

In the spin-polarized case, the exchange diagram entirely cancels the two pair bubbles for densities low enough and as a consequence RPA+SOSEX exactly cancels in the limit $k_\mathrm{F} \to 0$. RPA+APX becomes even positive, since APX contains more diagrams than RPA. This occurs, however, only at very low densities beyond $r_s \approx 88$.

8.3 APX for solids

In solids or in molecules the Adjacent Pairs Exchange correction can be evaluated in a similar fashion as the Random Phase Approximation. Collecting positive and negative imaginary frequencies and rotating the matrices cyclically converts all involved matrices into symmetric, real valued matrices:

$$E_\mathrm{c}^\mathrm{APX} = -\frac{1}{2}\int_0^\infty \frac{\mathrm{d}\nu}{2\pi}\,\mathrm{tr}\left\{\mathbf{V}^{\frac{1}{2}}\Big(\mathbf{P}_\mathrm{x}^\mathrm{APX}(\mathrm{i}\nu)+\mathbf{P}_\mathrm{x}^\mathrm{APX}(-\mathrm{i}\nu)\Big)\mathbf{V}^{\frac{1}{2}}\Big(\mathbf{1}-\mathbf{V}^{\frac{1}{2}}\mathbf{X}_0(\mathrm{i}\nu)\mathbf{V}^{\frac{1}{2}}\Big)^{-1}\right\}.$$

This makes the evaluation of the inverse more convenient. The independent particle polarizability $\mathbf{X}_0$ and the exchange polarizability $\mathbf{P}_\mathrm{x}^\mathrm{APX}$ can be evaluated in imaginary frequency and in real space according to (6.10) and (8.17) in $\mathcal{O}(N^3)$ and in $\mathcal{O}(N^4)$ steps, respectively, as described in Subsection 8.3.2. The memory requirement for both cases is $\mathcal{O}(N^2)$. Accepting a memory footprint of $\mathcal{O}(N^3)$, the prefactor in the evaluation of the APX and, similarly, of the AC-SOSEX correction might be lowered by storing the intermediate tensor $\mathbf{\Gamma}(\mathrm{i}\nu)$

$$\mathbf{\Gamma}_{\mathbf{x}\mathbf{x}'\mathbf{x}''}(\mathrm{i}\nu) = \int_0^\infty \mathrm{d}\tau\,\mathrm{e}^{+\mathrm{i}\nu\tau}\mathbf{G}_{0\mathbf{x}\mathbf{x}'}(\mathrm{i}\tau)\mathbf{G}_{0\mathbf{x}'\mathbf{x}''}(-\mathrm{i}\tau)$$

and then evaluating the exchange polarizability in terms of $\mathbf{\Gamma}$:

$$\mathbf{P}_\mathrm{x}^\mathrm{APX}{}_{\mathbf{x}_1\mathbf{x}_2}(\mathrm{i}\nu) = -\iint \mathrm{d}\mathbf{x}_3\,\mathrm{d}\mathbf{x}_4\,\frac{1}{|\mathbf{r}_3-\mathbf{r}_4|}\mathbf{\Gamma}_{\mathbf{x}_4\mathbf{x}_1\mathbf{x}_3}(+\mathrm{i}\nu)\mathbf{\Gamma}_{\mathbf{x}_3\mathbf{x}_2\mathbf{x}_4}(-\mathrm{i}\nu),$$

however, the required routines have not yet been implemented in `VASP`.

8.3.1 k-points and G_max convergence

In the diagrams for the Random Phase Approximation, each Coulomb interaction mediates the same momentum q according to momentum conservation at each vertex. This makes the RPA the most important contribution for small momenta or, equivalently, at long distances. The diagrams of the Adjacent Pairs Exchange correction contain one Coulomb interaction with a different momentum than all others. Thus, the APX correction is more short ranged

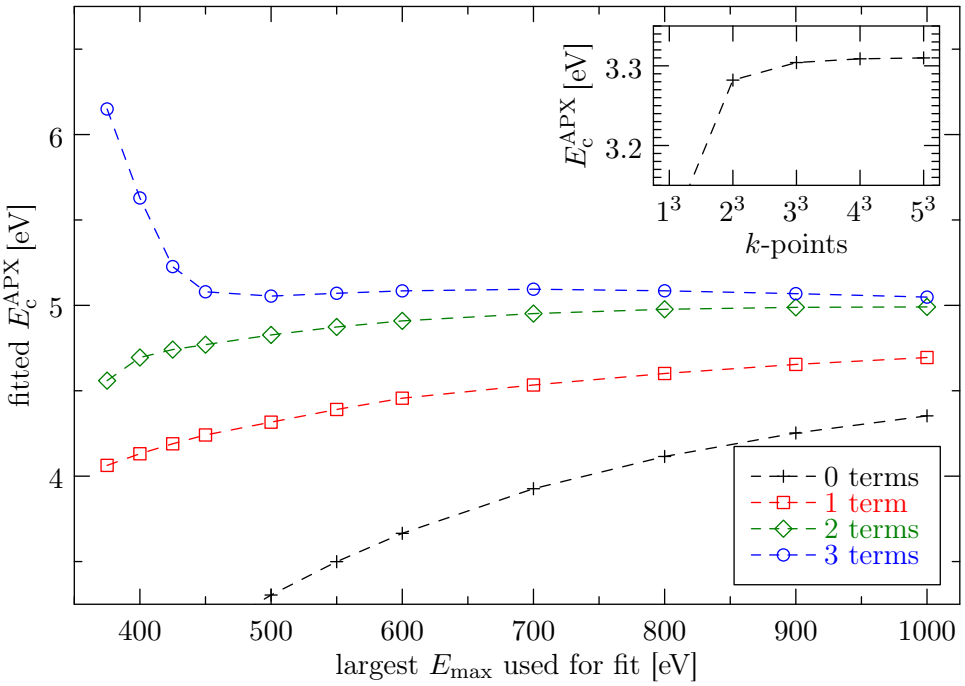

Figure 8.9: Basis set extrapolation of the APX energy for LiF with 10 electrons. The black points show the energies obtained at different cutoff energies E_{max}. The colored points show a fit using one, two or three orders in the expansion of the APX energy with respect to large cutoff momenta, according to (8.16). Each fit only uses data points with a cutoff energy below or equal to that of the fitted point. The inset shows the convergence of the APX energy with respect to different k point meshes.

than the Random Phase Approximation resulting in a faster k-point convergence, as shown in the inset of Figure 8.9.

The downside of the short ranged nature of the APX is that the convergence of the APX energy is slower with respect to the highest momentum G_{max} contained in $\mathbf{X}_0$ and $\mathbf{P}_{\text{x}}^{\text{APX}}$. Assuming that the system is homogeneous at distances short enough, the asymptotic behavior of the missing APX energy is equivalent to that of the Uniform Electron Gas, shown in Subsection 8.2.1. Figure 8.9 shows the convergence of the APX energy with respect to the employed energy cutoff $E_{\text{max}} = G_{\text{max}}^2/2$. `VASP` has an automatic finite basis set extrapolation implemented for the Random Phase Approximation, automatically evaluating the RPA energy for different cutoff energies and extrapolating according to the leading order term in the expansion of the asymptotic behavior, given in (8.16). However, this cannot be used for the APX correction for two reasons. First, unlike $\mathbf{X}_0$, $\mathbf{P}_{\text{x}}^{\text{APX}}$ changes with each considered cutoff momentum since the Coulomb kernel changes. Recalculating the exchange polarizability is, however, too time consuming. Second, it is often not sufficient to consider only the leading order term of the asymptotic behavior. For an accurate extrapolation to $G_{\text{max}} \to \infty$ it may be necessary to include the second, or higher order terms of the large momentum expansion

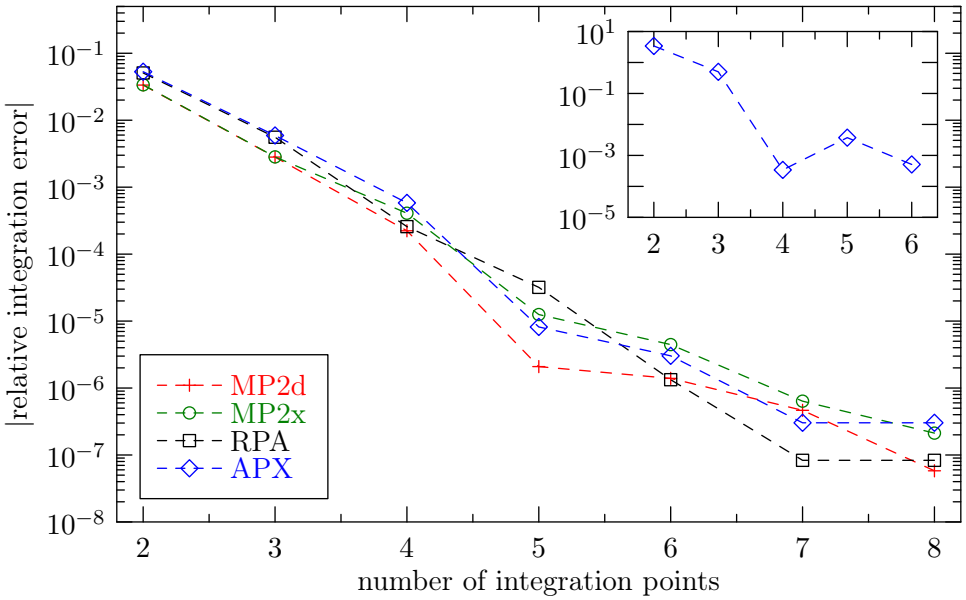

Figure 8.10: Relative error of the imaginary frequency integration for different approximations of the correlation energy of LiF, depending on the number of samples. The system contains 10 electrons and 384 bands. The inset shows the error for the difference of the APX energy for different unit cell volumes, once at 15.4 Å^3 and once at 15.9 Å^3. The error is below 1 μeV beyond the shown number of integration points.

for the Uniform Electron Gas. The asymptotic behavior can then be fitted to

$$\Delta E_{\mathrm{c}}^{\mathrm{APX}}(G_{\mathrm{max}}) \sim a_3 \frac{1}{G_{\mathrm{max}}^3} + a_7 \frac{1}{G_{\mathrm{max}}^7} + \mathcal{O}\left(\frac{1}{G_{\mathrm{max}}^{11}}\right), \tag{8.16}$$

derived in Subsection 8.2.1. The cutoff `ENMAX` $= G_{\mathrm{max}}^2/2$ needs to be manually increased and only the result without automatic extrapolation must be used. The number of bands, `NBANDS` should be close to the maximum number of bands permissible by the reference DFT or Hartree-Fock calculation for each respective value of `ENCUT`. Note that in `VASP` the number of bands must be a multiple of the number of cores employed for the APX calculation. To avoid strong shell effects it is therefore advantageous to choose `ENMAX` such that the reported maximum number of bands is as close as possible to `NBANDS`.

8.3.2 Frequency grid

A direct evaluation of (8.8) requires $\mathcal{O}(N^6)$ steps. However, $\mathbf{P}_{\mathrm{x}}^{\mathrm{APX}}$ can also be calculated in imaginary time using the imaginary time propagators given in (6.11). Subsequently, it can be Fourier transformed numerically to imaginary frequency on a non-equidistant grid, analogous to calculating the independent particle polarizability as proposed by Kaltak, Klimeš, and

Kresse 2014b:

$$\mathbf{P}_{\mathrm{x}}^{\mathrm{APX}}{}_{\mathbf{x}_1\mathbf{x}_2}(\mathrm{i}\nu) = -\iint \mathrm{d}\mathbf{x}_3\,\mathrm{d}\mathbf{x}_4\,\frac{1}{|\mathbf{r}_3-\mathbf{r}_4|}\int_0^\infty \mathrm{d}\tau_1\,\mathrm{e}^{+\mathrm{i}\nu\tau_1}\mathbf{G}_{0\mathbf{x}_3\mathbf{x}_1}(\mathrm{i}\tau_1)\mathbf{G}_{0\mathbf{x}_1\mathbf{x}_4}(-\mathrm{i}\tau_1) \int_0^\infty \mathrm{d}\tau_2\,\mathrm{e}^{-\mathrm{i}\nu\tau_2}\mathbf{G}_{0\mathbf{x}_4\mathbf{x}_2}(\mathrm{i}\tau_2)\mathbf{G}_{0\mathbf{x}_2\mathbf{x}_3}(-\mathrm{i}\tau_2). \quad (8.17)$$

The imaginary time propagators can be calculated in $\mathcal{O}(N^3)$ and since the convergence with the number of imaginary frequency and time samples is exponential, this evaluation of the APX scales like $\mathcal{O}(N^4)$. To reduce the memory requirements, the imaginary time propagators are not kept in memory in the current implementation in `VASP`, increasing the time complexity to $\mathcal{O}(N^5)$.

In the Random Phase Approximation the employed quadrature frequencies and weights are determined from a fit to the function of the direct MP2 energy, according to (6.12). This is well suited for the RPA, however, not necessarily also for the APX. Figure 8.10 shows the convergence of the APX energy in LiF containing 10 electrons with respect to the number of imaginary frequency points, using a grid that is optimized for the direct MP2 term. The convergence hardly differs for the different energies, justifying the use of the RPA optimized grid for calculating $\mathbf{P}_{\mathrm{x}}^{\mathrm{APX}}$ and subsequently the APX energy. For metallic systems, knowledge about asymptotic behavior of the APX with respect to large imaginary frequencies is important since the quality of the frequency grid degrades with vanishing band gap. APX has a different behavior for large frequencies in the Uniform Electron Gas than the Random Phase Approximation, as discussed in Subsection 8.2.2. However, since APX requires a different calculation setup with less k-points but higher plane wave cutoff momenta, evaluating APX and RPA on different frequency grids in metallic systems does not pose a considerable disadvantage.

8.3.3 Lattice constants

Calculating lattice constants beyond the Random Phase Approximation requires sub-meV accuracy for the energy differences at different volumes of the system under consideration. In this case, the basis set extrapolation of the APX energy differences does not require more than one term in the expansion of the large momentum behavior. In fact, the quality of the extrapolation deteriorates when using more than one term in the expansion since the higher order terms mostly cancel in the energy difference. Figure 8.11 shows the basis set convergence of the energy difference for LiF with 10 electrons. The volumes of the primitive cells are 15.9 Å^3 and 15.4 Å^3. The data contains considerable shell effects since the number of bands must be a multiple of the number of cores employed by the calculation, such that the number of bands is not always equally close to the maximum number of plane waves supported by the respective cutoff energy. All calculations were conducted with a $3 \times 3 \times 3$ k-points mesh, providing just sufficient accuracy, as indicated in the inset of Figure 8.11.

At each volume, the Adjacent Pairs Exchange correction is calculated and converged with respect to the cutoff energy using `VASP` with a PBE-DFT reference (Kresse and Furthmüller 1996; Blöchl 1994; Perdew et al. 2008). The Exact-Exchange+ RPA results were taken from the Birch–Murnaghan fit of previous converged RPA calculation by Grüneis et al. 2009; Harl, Schimka, and Kresse 2010, employing the same PAW potentials. The resulting RPA+APX energy is then fitted to a Birch–Murnaghan equation of state to retrieve the RPA+APX lattice constants. Table 8.3 lists lattice constants from RPA, SOSEX and APX in comparison with

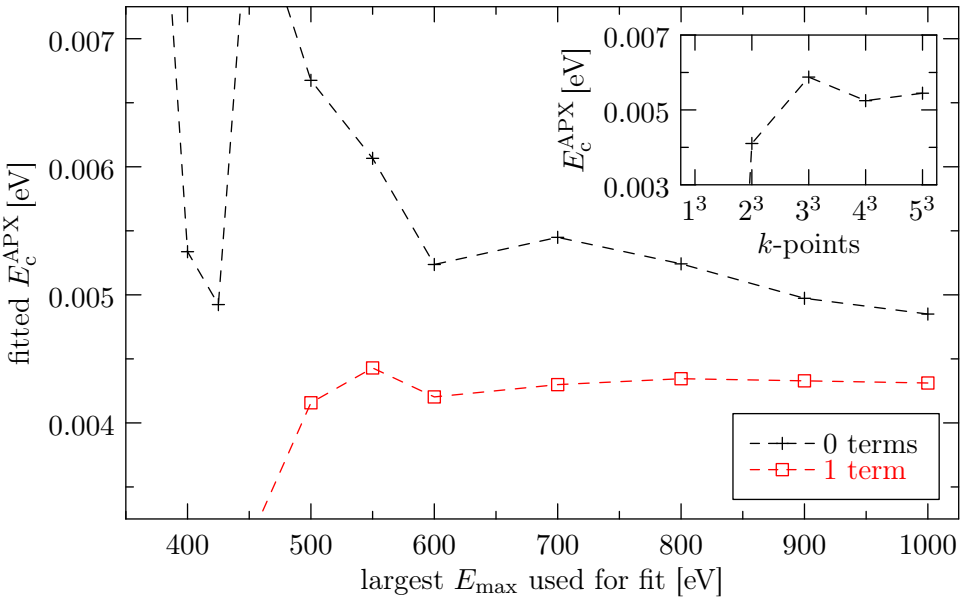

Figure 8.11: Basis set extrapolation of the APX energy difference at different volumes of LiF containing 10 electrons. The volumes of the primitive unit cell are 15.9 Å^3 and 15.4 Å^3. The black points show the energy differences obtained at different cutoff energies E_{max}. Aliasing effects can be clearly seen. The red points show a fit using in the leading order of the expansion of the APX energy with respect to large cutoff momenta. Each fit only uses data points with a cutoff energy below or equal to that of the fitted point. Higher order fits offer no improvement since they largely cancel in the difference. The inset shows the convergence of the APX energy difference with respect to different k point meshes.

Solid		a_0 [Å]						
		RPA	%	SOSEX	%	APX	%	exp.
C	(A4)	3.572	0.5	3.552	<0.1	3.550	−0.1	3.553
LiH	(B1)	3.983	0.1	3.989	0.3	3.992	0.4	3.979
LiF	(B1)	3.998	0.7	3.955	−0.4	3.974	<0.1	3.972

Table 8.3: Lattice constants from the Random Phase Approximation, SOSEX and the Adjacent Pairs Exchange correction compared to experiment. The uncertainties are about 0.1%. The experimental lattice constants were extrapolated to $T = 0\,\mathrm{K}$ and corrected for zero-point vibration effects (Harl, Schimka, and Kresse 2010).

experiment, extrapolated to $T = 0\,\mathrm{K}$ and corrected for zero-point vibration effects (Harl, Schimka, and Kresse 2010).

8.4 Summary and discussion

The Random Phase Approximation exhibits a systematic error which originates, at least partially, from violations of the Pauli exclusion principle, leading to a significant over correlation. As discussed at the beginning of Chapter 7, violating contributions are canceled by diagrams where the propagators of the offending states are exchanged. In the lowest order only one pair of propagators is exchanged.

The Adjacent Pairs Exchange (APX) correction to the RPA constitutes the largest set of Feynman diagrams correcting as many violations as possible in lowest order without introducing new violations and still forming one ring only:

$E_\mathrm{c}^\mathrm{APX} =$ 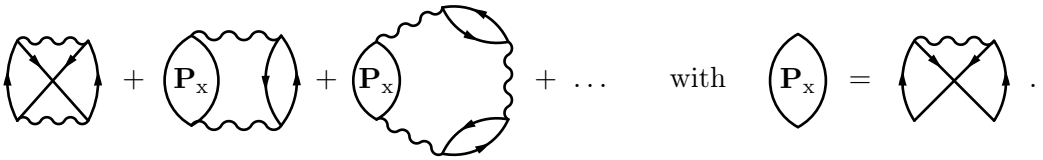 with

This makes the Random Phase Approximation plus the Adjacent Pairs Exchange correction a judicious choice of diagrams when the memory scaling for their evaluation must not exceed $\mathcal{O}(N^2)$, since the ring form of the APX allows its evaluation using only polarization parts with 2 open ends and RPA is the most important class of diagrams for high densities, becoming exact in the limit $r_s \to 0$.

Table 8.4 compares the SOSEX, the AC-SOSEX and the APX correction to the Random Phase Approximation in terms of included Goldstone diagrams, along with their current respective computational costs in time and memory. The diagrams of SOSEX constitute the largest set of Goldstone, rather than Feynman, diagrams correcting as many violations as possible under the same conditions as in the APX. In the case of SOSEX, forming a ring is necessary for the applicability of the direct ring Coupled Cluster Doubles amplitudes, which can be constructed in $\mathcal{O}(N^5)$ steps, as discussed in Section 6.2. Dropping the condition for the SOSEX diagrams to form a ring raises the time complexity for the construction of the amplitudes to $\mathcal{O}(N^6)$. Accepting this time complexity and the memory complexity of SOSEX, the full Coupled Cluster Singles and Doubles (CCSD) approximation can be employed. It includes considerably more diagrams, as indicated in Table 8.4, relieving the need of a correction to the Random Phase Approximation in general.

In the framework of the Adiabatic Connection, the unknown exchange-correlation kernel $\mathbf{f}_\mathrm{xc}^\lambda$, occurring in the Dyson-like equation (6.28) of the polarizability $\mathbf{X}_\lambda$, has to be included for a correction to the RPA. The AC-SOSEX contains the exchange-correlation kernel in lowest order:

$$\mathbf{X}_\lambda^\mathrm{AC-SOSEX} = \mathbf{X}_0 \tilde{\mathbf{f}}_\mathrm{xc}^\lambda \mathbf{X}_0 + \mathbf{X}_0 \tilde{\mathbf{f}}_\mathrm{xc}^\lambda \mathbf{X}_0 \lambda \mathbf{V} \mathbf{X}_0 + \dots ,$$

approximating the kernel by $\tilde{\mathbf{f}}_\mathrm{xc}^\lambda$, which is given implicitly by

$\mathbf{X}_0 \tilde{\mathbf{f}}_\mathrm{xc}^\lambda \mathbf{X}_0 = \lambda$ 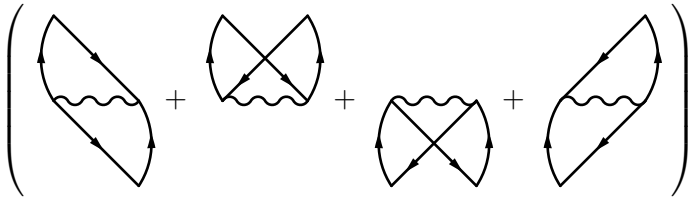 .

approximation	Goldstone diagrams	time	memory
SOSEX	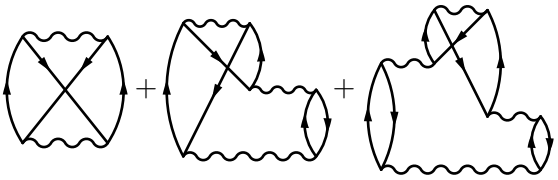	$\mathcal{O}(N^5)$	$\mathcal{O}(N^4)$
AC-SOSEX	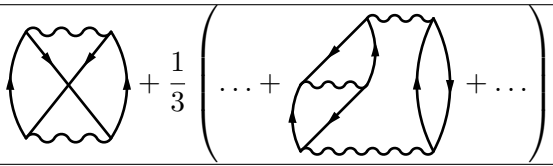	$\mathcal{O}(N^5)$	$\mathcal{O}(N^2)$
APX	SOSEX + 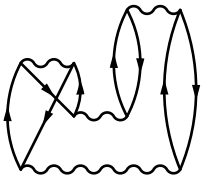	$\mathcal{O}(N^5)$	$\mathcal{O}(N^2)$
CCSD	RPA + APX + 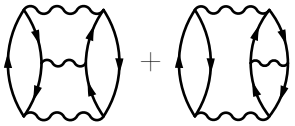	$\mathcal{O}(N^6)$	$\mathcal{O}(N^4)$

Table 8.4: Comparison of different approximations beyond the Random Phase Approximation, showing the lowest order Goldstone diagrams introduced by the respective approximation. The AC-SOSEX is not derived within the same many-body perturbation theory framework as the other approximations. It can, however, be translated into Goldstone diagrams when including improper ladder diagrams, as shown here in third order and which are discussed in Section 7.3.

In the first and in the last diagram, particles turn into holes and vice versa at the Coulomb interaction, which has no correspondence in many-body perturbation theory. It neither originates from time dependent DFT nor from many-body perturbation theory, which is employed by the AC-FDT RPA to calculate the independent particle polarizability $\mathbf{X}_0$. As discussed in Section 7.2, the above approximation rather comes from transforming the RPA energy expression into the particle/hole basis, applying the analogy of SOSEX to exchange two indices, ignoring the time order, and then transforming it back to the position basis. However, the results are very similar to those of SOSEX for reasons discussed in Section 7.3, which are in no obvious connection to its derivation. Owing to its similar results to SOSEX, the AC-SOSEX can be considered a numerical recipe to approximate the SOSEX energy, requiring only $\mathcal{O}(N^2)$ of memory.

The Adjacent Pairs Exchange correction contains more diagrams than the Second Order Screened Exchange correction since APX is the pendant of SOSEX in terms of Feynman diagrams rather than Goldstone diagrams. This does, however, not imply that APX is more accurate in any given situation. After all, the surprisingly high accuracy of SOSEX or APX in the case of the uniform electron gas is certainly fortuitous and no theory, involving only first and second order exchange diagrams can be expected to provide this accuracy for other systems than the UEG as well. The spin-polarized uniform electron gas is an example of

a system, where RPA+SOSEX or RPA+APX can yield zero or even positive correlation energies in the limit of dilute densities. For densities of real metals, the performance in the spin-polarized case is better, as indicated in Figure 8.8. It is assumed that AC-SOSEX is close to SOSEX since no SOSEX calculations for the spin-polarized UEG in the thermodynamic limit have been found. It is worth mentioning that finite spin-polarized systems often exhibit a (quasi)-degenerate ground state, rendering many-body perturbation theory, as discussed here and employed by most implementations, inaccurate at best. (Quasi)-degenerate many-body perturbation theory is discussed, for instance, in Shavitt and Bartlett 2009.

APX and SOSEX are identical up to third order resulting only in small differences. In the case of the non-spin-polarized uniform electron gas, RPA+SOSEX matches Quamtum Monte Carlo correlation energies already at $r_s \approx 5$, where RPA+APX still has an error of about $0.7\,\mathrm{m}E_h$ per electron, which is a relative error of 5%. For lower densities with $r_s > 8$, where correlation effects are more prevalent, APX improves on SOSEX and its accuracy is never worse than $0.3\,\mathrm{m}E_h$ per electron, even up to $r_s = 50$. Note, that the accuracy is given with respect to the Perdew and Zunger 1981 parametrization of the Ceperley and Alder 1980 QMC results. The Adjacent Pairs Exchange correction can be computed in $\mathcal{O}(N^4)$ or $\mathcal{O}(N^5)$ steps, depending on whether the propagator is stored or not. In the latter case, the time complexity is equivalent to SOSEX, however, it is considerably less memory demanding with its requirement scaling like $\mathcal{O}(N^2)$ instead of $\mathcal{O}(N^4)$. Both, APX and AC-SOSEX are implemented in `VASP` and first applications on lattice constants show excellent agreement with experiment. A more extensive survey could be done including atomization energies and a comparison to other SOSEX alternatives, such as the Approximate Exchange Kernel (AXK) suggested by Bates and Furche 2013.

Not all improvements beyond the Random Phase Approximation are based on the inclusion of exchange processes. After all, the effect of exchange decays with the distance d at finite temperature. It is proportional to $\exp(-k_\mathrm{B}Td^2/2)$ (Feynman, Hibbs, and Styer 2010). For room temperature this gives a typical 3σ distance of about 100 a.u., beyond which only direct diagrams are relevant. One improvement of the RPA including only direct diagrams is the *GW* approximation. In the *GW* approximation, the iterative scheme of RPA, used to build an effective interaction W from the Coulomb interaction V according to (6.7), is extended by an iterative scheme to improve the description of the propagator G_0 towards an effective propagator G of the fully interacting system, referred to as *dressed* propagator (Hedin 1965). The central quantity of interest in this approximation is the dressed propagator, rather than connected diagrams, as in the Goldstone approach of many-body perturbation theory, discussed here. This makes a comparison between the two approaches hard, as there is no consideration of symmetries. In most cases, the dressed propagator is used to retrieve excitation spectra but there are also total energy calculations within the *GW* approximation, usually employing the formula of Galitskii and Migdal 1958. In Appendix B, an alternative approach is suggested to evaluate the total energy in the G_0W_0 approximation within the many-body perturbation theory discussed here. The total energies retrieved by this approximation are expected to be more accurate than those of the RPA at computational costs that should not exceed $\mathcal{O}(N^4)$. However, this remains to be tested in the future. Also, G_0W_0 is only the least accurate variant of the *GW* approximation, depending on the reference such as DFT or HF.

Finally, it is worth mentioning that most of the time and memory requirements of high accuracy methods, such as Coupled Cluster Singles and Doubles (CCSD) depend on the number of unoccupied states ψ_a, needed for a convergent result. This number can sometimes be reduced without considerably sacrificing the accuracy such that CCSD or even higher accuracy

methods become feasible for larger systems. One way of reducing the number of unoccupied states is by means of natural orbitals, as introduced by Löwdin 1955. It is applicable in the case where large voids are between the atoms or molecules, such as in atomization energy calculations of solids. Another way of reducing the number of unoccupied states is by including explicit correction already in the description of the unperturbed system. This can be done by augmenting the Slater determinant, which is a product of functions depending on one electron position only, by a set of functions $f(\mathbf{x}_1, \mathbf{x}_2)$ explicitly depending on two electron positions, hence the name f_{12} methods. In all cases there is still an underlying perturbation expansion to be evaluated and the Adjacent Paris Correction as well as the AC-SOSEX can also profit from such a reduction of the number of unoccupied states.

Part III

Appendices

Appendix A

Periodic Table of Simple Liquids

Within Density Functional Theory most metallic elements exhibit isomorphic states to a large degree already at pressures close to the triple point. This simplifies the phase diagram to one effective dimension allowing, for instance, a prediction of the melting line of iron over a wide range of densities up to Earth core conditions from fluctuation data at the triple point. Theoretical considerations and details on the calculations are discussed in Chapter 4.

The following Periodic Table of Simple Liquids summarizes the results of the DFT study of 58 elements. The degree of simplicity is reflected by the correlation coefficient R between the fluctuations of the virial and the potential energy. All elements that were studied are colored according to their degree of simplicity. The studied state point close to the triple point is given by its temperature T and its density, once in terms of the mass density ρ and once in terms of the average volume per atom V/N.

The Periodic Table also includes the parameters σ and γ of an inverse power law fitted to the potential energy of the DFT at the studied state point. Assuming perfect inverse power law behavior, an element is expected to crystallize into a body centered cubic structure if the scaling exponent γ is below ≈ 2.5. For larger scaling exponents a close packed crystal structure is expected. For comparison, the experimental crystal structure at the triple point is given symbolically, colored according to the correlation coefficient R_{IPL} between the DFT and the fitted inverse power law potential energies. Note that the crystal structures at the triple point differ for some elements from the crystal structure at ambient conditions.

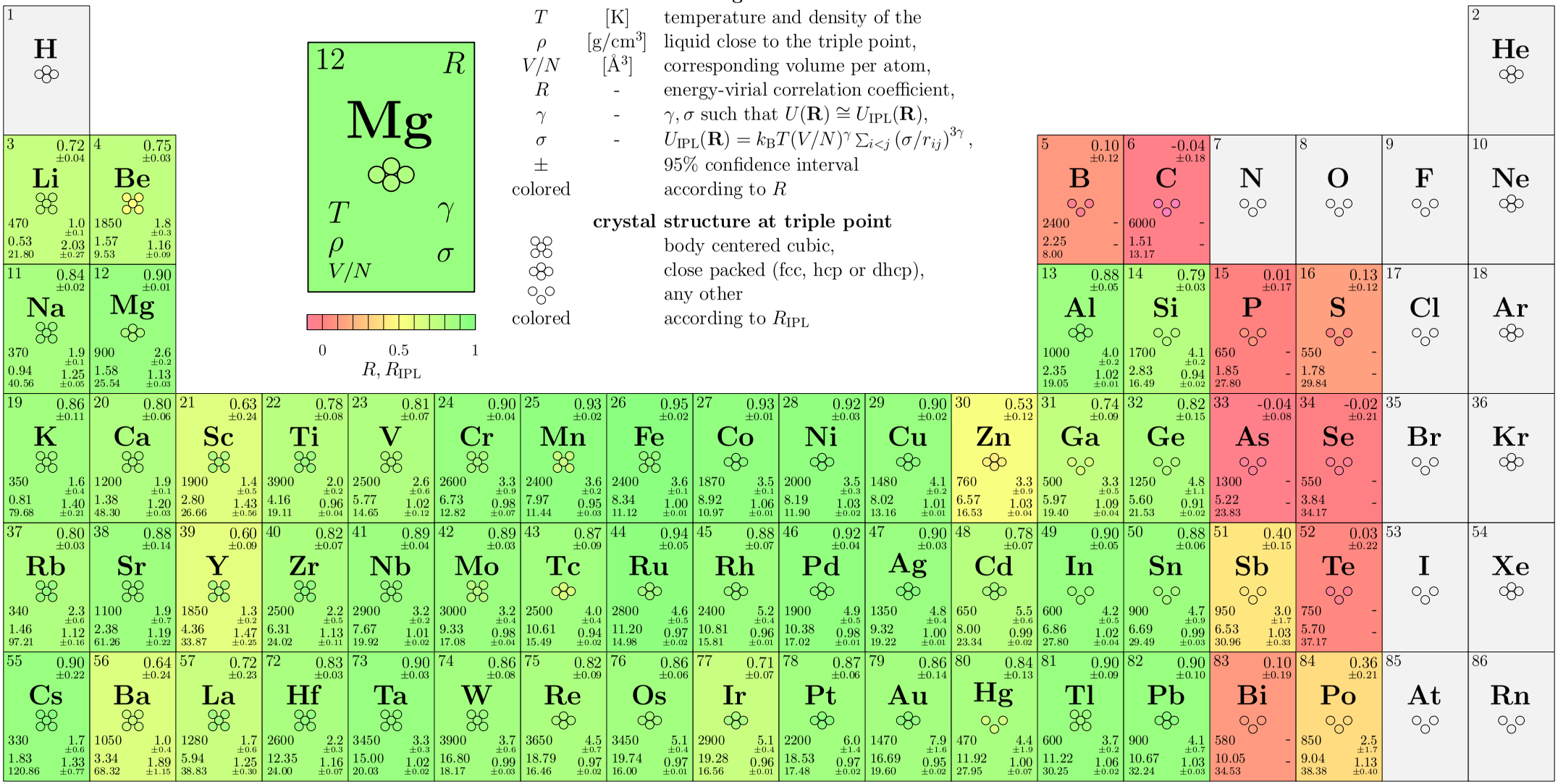
1
H
2
He
3
0.72 ±0.04
Li
470 1.0 ±0.1
0.53 2.03 ±0.27
21.80
4
0.75 ±0.03
Be
1850 1.8 ±0.3
1.57 1.16 ±0.09
9.53
5
0.10 ±0.12
B
2400 -
2.25 -
8.00
6
-0.04 ±0.18
C
6000 -
1.51 -
13.17
7
N
8
O
9
F
10
Ne
11
0.84 ±0.02
Na
370 1.9 ±0.1
0.94 1.25 ±0.05
40.56
12
0.90 ±0.01
Mg
900 2.6 ±0.2
1.58 1.13 ±0.03
25.54
13
0.88 ±0.05
Al
1000 4.0 ±0.2
2.35 1.02 ±0.01
19.05
14
0.79 ±0.03
Si
1700 4.1 ±0.2
2.83 0.94 ±0.02
16.49
15
0.01 ±0.17
P
650 -
1.85 -
27.80
16
0.13 ±0.12
S
550 -
1.78 -
29.84
17
Cl
18
Ar
19
0.86 ±0.11
K
350 1.6 ±0.4
0.81 1.40 ±0.21
79.68
20
0.80 ±0.06
Ca
1200 1.9 ±0.1
1.38 1.20 ±0.03
48.30
21
0.63 ±0.24
Sc
1900 1.4 ±0.5
2.80 1.43 ±0.56
26.66
22
0.78 ±0.08
Ti
3900 2.0 ±0.2
4.16 0.96 ±0.04
19.11
23
0.81 ±0.07
V
2500 2.6 ±0.6
5.77 1.02 ±0.12
14.65
24
0.90 ±0.04
Cr
2600 3.3 ±0.9
6.73 0.98 ±0.07
12.82
25
0.93 ±0.02
Mn
2400 3.6 ±0.2
7.97 0.95 ±0.03
11.44
26
0.95 ±0.02
Fe
2400 3.6 ±0.1
8.34 1.00 ±0.01
11.12
27
0.93 ±0.01
Co
1870 3.5 ±0.1
8.92 1.06 ±0.01
10.97
28
0.92 ±0.03
Ni
2000 3.5 ±0.3
8.19 1.03 ±0.02
11.90
29
0.90 ±0.02
Cu
1480 4.1 ±0.2
8.02 1.01 ±0.01
13.16
30
0.53 ±0.12
Zn
760 3.3 ±0.9
6.57 1.03 ±0.04
16.53
31
0.74 ±0.09
Ga
500 3.3 ±0.5
5.97 1.09 ±0.04
19.40
32
0.82 ±0.15
Ge
1250 4.8 ±1.1
5.60 0.91 ±0.02
21.53
33
-0.04 ±0.08
As
1300 -
5.22 -
23.83
34
-0.02 ±0.21
Se
550 -
3.84 -
34.17
35
Br
36
Kr
37
0.80 ±0.03
Rb
340 2.3 ±0.6
1.46 1.12 ±0.16
97.21
38
0.88 ±0.14
Sr
1100 1.9 ±0.7
2.38 1.19 ±0.22
61.26
39
0.60 ±0.09
Y
1850 1.3 ±0.2
4.36 1.47 ±0.25
33.87
40
0.82 ±0.07
Zr
2500 2.2 ±0.5
6.31 1.13 ±0.11
24.02
41
0.89 ±0.04
Nb
2900 3.2 ±0.2
7.67 1.01 ±0.02
19.92
42
0.89 ±0.03
Mo
3000 3.2 ±0.4
9.33 0.98 ±0.04
17.08
43
0.87 ±0.09
Tc
2500 4.0 ±0.4
10.61 0.94 ±0.02
15.49
44
0.94 ±0.05
Ru
2800 4.6 ±0.5
11.20 0.97 ±0.02
14.98
45
0.88 ±0.07
Rh
2400 5.2 ±0.4
10.81 0.96 ±0.01
15.81
46
0.92 ±0.04
Pd
1900 4.9 ±0.5
10.38 0.98 ±0.01
17.02
47
0.90 ±0.03
Ag
1350 4.8 ±0.4
9.32 1.00 ±0.01
19.22
48
0.78 ±0.07
Cd
650 5.5 ±0.6
8.00 0.99 ±0.02
23.34
49
0.90 ±0.05
In
600 4.2 ±0.5
6.86 1.02 ±0.04
27.80
50
0.88 ±0.06
Sn
900 4.7 ±0.9
6.69 0.99 ±0.03
29.49
51
0.40 ±0.15
Sb
950 3.0 ±1.7
6.53 1.03 ±0.33
30.96
52
0.03 ±0.22
Te
750 -
5.70 -
37.17
53
I
54
Xe
55
0.90 ±0.22
Cs
330 1.7 ±0.6
1.83 1.33 ±0.77
120.86
56
0.64 ±0.24
Ba
1050 1.0 ±0.4
3.34 1.89 ±1.15
68.32
57
0.72 ±0.23
La
1280 1.7 ±0.6
5.94 1.25 ±0.30
38.83
72
0.83 ±0.03
Hf
2600 2.2 ±0.3
12.35 1.16 ±0.07
24.00
73
0.90 ±0.03
Ta
3450 3.3 ±0.3
15.00 1.02 ±0.02
20.03
74
0.86 ±0.08
W
3900 3.7 ±0.6
16.80 0.99 ±0.03
18.17
75
0.82 ±0.09
Re
3650 4.5 ±0.7
18.79 0.97 ±0.02
16.46
76
0.86 ±0.06
Os
3450 5.1 ±0.4
19.74 0.97 ±0.01
16.00
77
0.71 ±0.07
Ir
2900 5.1 ±0.4
19.28 0.96 ±0.01
16.56
78
0.87 ±0.06
Pt
2200 6.0 ±1.4
18.53 0.97 ±0.02
17.48
79
0.86 ±0.14
Au
1470 7.9 ±1.6
16.69 0.95 ±0.02
19.60
80
0.84 ±0.13
Hg
470 4.4 ±1.9
11.92 1.00 ±0.07
27.95
81
0.90 ±0.09
Tl
600 3.7 ±0.2
11.22 1.06 ±0.02
30.25
82
0.90 ±0.10
Pb
900 4.1 ±0.7
10.67 1.03 ±0.03
32.24
83
0.10 ±0.19
Bi
580 -
10.05 -
34.53
84
0.36 ±0.21
Po
850 2.5 ±1.7
9.04 1.13 ±0.40
38.38
85
At
86
Rn
12
R
Mg
T
γ
ρ
σ
V/N
0
0.5
1
R, R_IPL
Legend
T [K] temperature and density of the
ρ [g/cm^3] liquid close to the triple point,
V/N [Å^3] corresponding volume per atom,
R - energy-virial correlation coefficient,
γ - γ, σ such that U(R) ≅ U_IPL(R),
σ - U_IPL(R) = k_B T (V/N)^γ Σ_{i<j} (σ/r_ij)^{3γ},
± 95% confidence interval
colored according to R
crystal structure at triple point
body centered cubic,
close packed (fcc, hcp or dhcp),
any other
colored according to R_IPL

Appendix B

Total energies in G_0W_0 from connected diagrams

Given the propagator G_0 in matrix form and in imaginary time according to (6.11)[1]

$$\mathbf{G}_{0\mathbf{x}\mathbf{x}'}(\mathrm{i}\tau) = \begin{cases} -\sum_i \psi_i(\mathbf{x})\psi_i^*(\mathbf{x}')\mathrm{e}^{-(\varepsilon_i-\mu)\tau} & \text{for } \tau \leq 0 \\ +\sum_a \psi_a(\mathbf{x})\psi_a^*(\mathbf{x}')\mathrm{e}^{-(\varepsilon_a-\mu)\tau} & \text{otherwise,} \end{cases}$$

we can Fourier transform it to imaginary frequency $\mathbf{G}_0(\mathrm{i}\eta)$. We also write the screened Coulomb interaction $\mathbf{W}_0$ in the Random Phase Approximation (RPA) in the same form

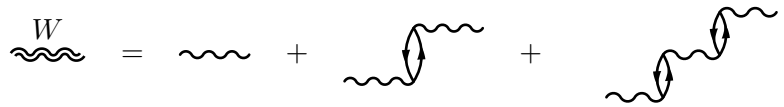

$$\begin{aligned} \mathbf{W}_0(\mathrm{i}\nu) &= \mathbf{V} + \mathbf{V}\mathbf{X}_0(\mathrm{i}\nu)\mathbf{V} + \mathbf{V}\mathbf{X}_0(\mathrm{i}\nu)\mathbf{V}\mathbf{X}_0(\mathrm{i}\nu)\mathbf{V} + \dots \\ &= \mathbf{V}\Big(\mathbf{1} - \mathbf{X}_0(\mathrm{i}\nu)\mathbf{V}\Big)^{-1}, \end{aligned} \tag{B.1}$$

where $\mathbf{X}_0$ is the independent particle polarizability in imaginary frequency as retrieved from a Fourier transform of (6.10). The correlation part of the *irreducible self energy* $\mathbf{\Sigma}$ can then be approximated in the RPA by

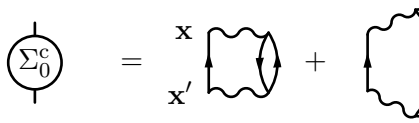

$$\begin{aligned} &= \\ &= \\ \mathbf{\Sigma}^{\mathrm{c}}_{0\mathbf{x}\mathbf{x}'}(\mathrm{i}\eta) &= \int_{-\infty}^{\infty} \frac{\mathrm{i}\,\mathrm{d}\nu}{2\pi}\, \mathbf{G}_{0\mathbf{x}\mathbf{x}'}(\mathrm{i}\eta + \mathrm{i}\nu)\Big(\mathbf{W}_{0\mathbf{x}\mathbf{x}'}(\mathrm{i}\nu) - \mathbf{V}_{\mathbf{x}\mathbf{x}'}\Big)\,. \end{aligned} \tag{B.2}$$

[1] Note that the propagator used here differs by a factor of i from the usual definition of the propagator, as discussed in the footnote of (5.42)

Note that the matrices are multiplied elementwise and that the exchange term G_0V is excluded since it cancels with the effective interaction in a Hartree-Fock reference, as discussed in Section 5.6. From now on we will write Σ_0 instead of Σ_0^c for convenience.

In the G_0W_0 approximation the full propagator $\mathbf{G}$ is approximated by inserting the above approximation to the correlation part of the irreducible self energy $\mathbf{\Sigma}_0$ into the propagator of the unperturbed system $\mathbf{G}_0$ arbitrarily many times

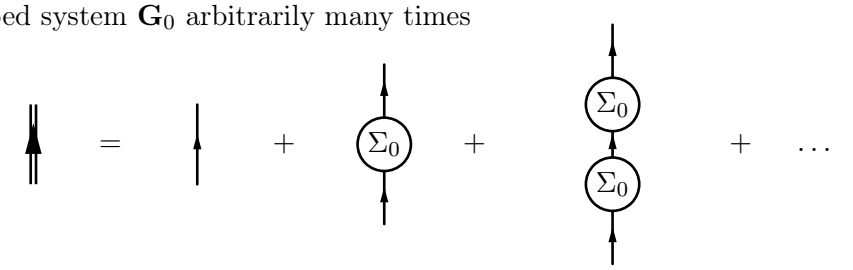

$$\mathbf{G} = \mathbf{G}_0 + \mathbf{G}_0\mathbf{\Sigma}_0\mathbf{G}_0 + \mathbf{G}_0\mathbf{\Sigma}_0\mathbf{G}_0\mathbf{\Sigma}_0\mathbf{G}_0 + \dots , \tag{B.3}$$

where we omit the imaginary frequency argument for brevity. Properties of the interacting system can then be extracted from this approximation to the full propagator $\mathbf{G}$. To get the total energy the formula of Galitskii and Migdal 1958 can be used on the full imaginary time propagator $\mathbf{G}(\mathrm{i}\tau)$, retrieved from an inverse Fourier transform of $\mathbf{G}(\mathrm{i}\eta)$ at $\tau \to 0$ from above:

$$E = -\frac{\mathrm{i}}{2}\int \mathrm{d}\mathbf{x} \lim_{\mathbf{r}'\to\mathbf{r}} \lim_{\tau\to 0^+} \left(\frac{\partial}{\mathrm{i}\,\partial\tau} - \mathrm{i}\,\hat{h}_{\mathbf{x}}\right) \mathbf{G}_{\mathbf{r}\alpha\,\mathbf{r}'\alpha}(\mathrm{i}\tau)\,, \tag{B.4}$$

where $\hat{h}_{\mathbf{x}}$ is the single body Hamiltonian of the unperturbed system acting on $\mathbf{G}_{\mathbf{x}}$. This can be interpreted as cutting out one occurrence of G_0 by the differential operator and then closing the remaining diagrams contained in G (Ziesche 2010).

Here, an alternative way to the Galitskii-Migdal formula is proposed for evaluating the total energy in G_0W_0, respecting the symmetries of all connected diagrams occurring in this approximation, as discussed in Subsection 5.8.2. Figure B.1 shows all diagrams order by order, where each row contains an order of the expansion of $\mathbf{W}_0$ contained in $\mathbf{\Sigma}_0$ according to (B.1) and each column contains an order of $\mathbf{G}$ according to (B.3). Note that the symmetries of the first column differ from the symmetries of all other columns since closing $\mathbf{\Sigma}_0$ with one $\mathbf{G}_0$ forms a bubble equivalent to $\mathbf{X}_0$. The diagrams of the first column form the ring diagrams of the RPA. All the remaining diagrams have rotational symmetry but no reflection symmetry and can be summed to infinite order in the same fashion as it was done in the RPA in (6.8), arriving at

$$\begin{aligned} E_{\mathrm{c}}^{G_0W_0} &= E_{\mathrm{c}}^{\mathrm{RPA}} + \mathrm{i}\int \frac{\mathrm{i}\,\mathrm{d}\eta}{2\pi}\mathrm{tr}\left\{-\frac{1}{2}\Big(\mathbf{G}_0(\mathrm{i}\eta)\Sigma_0(\mathrm{i}\eta)\Big)^2 - \frac{1}{3}\Big(\mathbf{G}_0(\mathrm{i}\eta)\Sigma_0(\mathrm{i}\eta)\Big)^3 - \dots\right\} \\ &= E_{\mathrm{c}}^{\mathrm{RPA}} - \int_{-\infty}^{\infty}\frac{\mathrm{d}\eta}{2\pi}\,\mathrm{tr}\Big\{\log\Big(\mathbf{1} - \mathbf{G}_0(\mathrm{i}\eta)\mathbf{\Sigma}_0(\mathrm{i}\eta)\Big) + \mathbf{G}_0(\mathrm{i}\eta)\mathbf{\Sigma}_0(\mathrm{i}\eta)\Big\}\,. \end{aligned} \tag{B.5}$$

This approach still has to be tested and compared to previous G_0W_0 total energies, as for instance retrieved by (Holm and Aryasetiawan 2000). The two approaches do differ after all. Conventional G_0W_0 uses a normalization factor for calculating $\mathbf{G}$ while this approach uses symmetry factors.

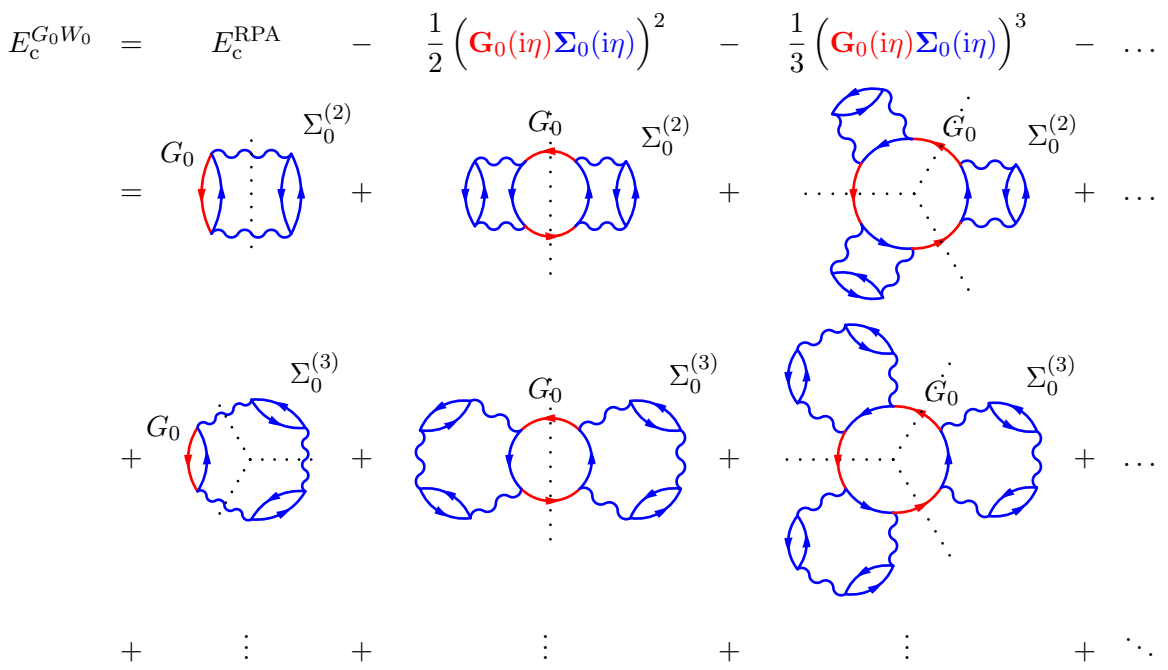

Figure B.1: Connected (closed) diagrams occurring in the G_0W_0 approximation of the correlation energy. The parts of the self energy are given in blue while the parts of the closing propagator are given in red. With each column the number of insertions of $\mathbf{\Sigma}_0\mathbf{G}_0$ into $\mathbf{G}$ increments, while the number of insertions of $\mathbf{X}_0\mathbf{V}$ into $\mathbf{\Sigma}_0$ increments with each row. The single Fermion loop in the center results in a negative Fermion sign of all diagrams beyond RPA. Imaginary units, the imaginary frequency integration and the trace are omitted for clarity.

Bibliography

Floquet, G. (1883). "Sur les équations différentielles linéaires à coefficients périodiques". *Annales de l'École Normale Supérieure*. 2nd ser. 12, pp. 47–88.

Bloch, F. (1929). "Über die Quantenmechanik der Elektronen in Kristallgittern". *Z. Physik* 52.7-8, pp. 555–600. DOI: 10.1007/BF01339455.

Güttinger, P. (1932). "Das Verhalten von Atomen im magnetischen Drehfeld". *Z. Physik* 73.3-4, pp. 169–184. DOI: 10.1007/BF01351211.

Møller, C. and M. S. Plesset (1934). "Note on an Approximation Treatment for Many-Electron Systems". *Phys. Rev.* 46.7, pp. 618–622. DOI: 10.1103/PhysRev.46.618.

Macke, W. (1950). "Über die Wechselwirkungen im Fermi-Gas, Polarisationserscheinungen, Correlationsenergie, Elektronenkondensation". *Z. Naturforsch.* 5a.8, pp. 192–208.

Wick, G. C. (1950). "The Evaluation of the Collision Matrix". *Phys. Rev.* 80.2, pp. 268–272. DOI: 10.1103/PhysRev.80.268.

Callen, H. B. and T. A. Welton (1951). "Irreversibility and Generalized Noise". *Phys. Rev.* 83.1, pp. 34–40. DOI: 10.1103/PhysRev.83.34.

Pines, D. and D. Bohm (1952). "A Collective Description of Electron Interactions: II. Collective vs Individual Particle Aspects of the Interactions". *Phys. Rev.* 85.2, pp. 338–353. DOI: 10.1103/PhysRev.85.338.

Metropolis, N., A. W. Rosenbluth, M. N. Rosenbluth, A. H. Teller, and E. Teller (1953). "Equation of State Calculations by Fast Computing Machines". *The Journal of Chemical Physics* 21.6, pp. 1087–1092. DOI: 10.1063/1.1699114.

Löwdin, P.-O. (1955). "Quantum Theory of Many-Particle Systems. I. Physical Interpretations by Means of Density Matrices, Natural Spin-Orbitals, and Convergence Problems in the Method of Configurational Interaction". *Phys. Rev.* 97.6, pp. 1474–1489. DOI: 10.1103/PhysRev.97.1474.

Shanks, D. (1955). "Non-linear transformation of divergent and slowly convergent sequences". *J. Math. Phys.* 34.1, pp. 1–42.

Gilvarry, J. J. (1956). "The Lindemann and Grüneisen Laws". *Phys. Rev.* 102.2, pp. 308–316. DOI: 10.1103/PhysRev.102.308.

Gell-Mann, M. and K. A. Brueckner (1957). "Correlation Energy of an Electron Gas at High Density". *Phys. Rev.* 106.2, pp. 364–368. DOI: 10.1103/PhysRev.106.364.

Goldstone, J. (1957). "Derivation of the Brueckner Many-Body Theory". *Proceedings of the Royal Society A: Mathematical, Physical and Engineering Sciences* 239.1217, pp. 267–279. DOI: 10.1098/rspa.1957.0037.

Galitskii, V. M. and A. B. Migdal (1958). "Application of quantum field theory methods to the many body problem". *Sov. Phys. JETP* 7.1, pp. 96–104.

Coester, F. and H. Kümmel (1960). "Short-range correlations in nuclear wave functions". *Nuclear Physics* 17, pp. 477–485. DOI: 10.1016/0029-5582(60)90140-1.

Adler, S. L. (1962). "Quantum Theory of the Dielectric Constant in Real Solids". *Phys. Rev.* 126.2, pp. 413–420. DOI: 10.1103/PhysRev.126.413.

Wiser, N. (1963). "Dielectric Constant with Local Field Effects Included". *Phys. Rev.* 129.1, pp. 62–69. DOI: 10.1103/PhysRev.129.62.

Hohenberg, P. and W. Kohn (1964). "Inhomogeneous Electron Gas". *Phys. Rev.* 136.3B, B864–B871. DOI: 10.1103/PhysRev.136.B864.

Hedin, L. (1965). "New Method for Calculating the One-Particle Green's Function with Application to the Electron-Gas Problem". *Phys. Rev.* 139.3A, A796–A823. DOI: 10.1103/PhysRev.139.A796.

Onsager, L., L. Mittag, and M. J. Stephen (1966). "Integrals in the Theory of Electron Correlations". *Ann. Phys.* 473.1-2, pp. 71–77. DOI: 10.1002/andp.19664730108.

Čížek, J. (1969). "On the Use of the Cluster Expansion and the Technique of Diagrams in Calculations of Correlation Effects in Atoms and Molecules". *Advances in Chemical Physics*. Ed. by R. LeFebvre and C. Moser. John Wiley & Sons, Inc., pp. 35–89.

Hastings, W. K. (1970). "Monte Carlo sampling methods using Markov chains and their applications". *Biometrika* 57.1, pp. 97–109. DOI: 10.1093/biomet/57.1.97.

Weeks, J. D., D. Chandler, and H. C. Andersen (1971). "Role of Repulsive Forces in Determining the Equilibrium Structure of Simple Liquids". *The Journal of Chemical Physics* 54.12, pp. 5237–5247. DOI: 10.1063/1.1674820.

Hoover, W. G. (1972). "Statistical Mechanics of Phase Diagrams. I. Inverse Power Potentials and the Close-Packed to Body-Centered Cubic Transition". *The Journal of Chemical Physics* 56.5, p. 2207. DOI: 10.1063/1.1677521.

Haaland, D. M. (1976). "Graphite-liquid-vapor triple point pressure and the density of liquid carbon". *Carbon* 14.6, pp. 357–361. DOI: 10.1016/0008-6223(76)90010-5.

Freeman, D. (1977). "Coupled-cluster expansion applied to the electron gas: Inclusion of ring and exchange effects". *Physical Review B* 15.12, pp. 5512–5521. DOI: 10.1103/PhysRevB.15.5512.

Langreth, D. C. and J. P. Perdew (1977). "Exchange-correlation energy of a metallic surface: Wave-vector analysis". *Physical Review B* 15.6, pp. 2884–2901. DOI: 10.1103/PhysRevB.15.2884.

Ceperley, D. M. and B. J. Alder (1980). "Ground State of the Electron Gas by a Stochastic Method". *Phys. Rev. Lett.* 45.7, pp. 566–569. DOI: 10.1103/PhysRevLett.45.566.

Vosko, S. H., L. Wilk, and M. Nusair (1980). "Accurate spin-dependent electron liquid correlation energies for local spin density calculations: a critical analysis". *Can. J. Phys.* 58.8, pp. 1200–1211. DOI: 10.1139/p80-159.

Parrinello, M. and A. Rahman (1981). "Polymorphic transitions in single crystals: A new molecular dynamics method". *Journal of Applied Physics* 52.12, pp. 7182–7190. DOI: 10.1063/1.328693.

Perdew, J. P. and A. Zunger (1981). "Self-interaction correction to density-functional approximations for many-electron systems". *Phys. Rev. B* 23.10, pp. 5048–5079. DOI: 10.1103/PhysRevB.23.5048.

Steinhardt, P. J., D. R. Nelson, and M. Ronchetti (1983). "Bond-orientational order in liquids and glasses". *Phys. Rev. B* 28.2, pp. 784–805. DOI: 10.1103/PhysRevB.28.784.

Gross, E. K. U. and W. Kohn (1985). "Local density-functional theory of frequency-dependent linear response". *Phys. Rev. Lett.* 55.26, pp. 2850–2852. DOI: 10.1103/PhysRevLett.55.2850.

Catlow, C. R. A., S. C. Parker, and M. P. Allen, eds. (1989). *Computer modelling of fluids, polymers, and solids*. NATO ASI series. Series C, Mathematical and physical sciences vol. 293. Dordrecht ; Boston: Kluwer Academic Publishers.

Almlöf, J. (1991). "Elimination of energy denominators in Møller—Plesset perturbation theory by a Laplace transform approach". *Chemical Physics Letters* 181.4, pp. 319–320. DOI: 10.1016/0009-2614(91)80078-C.

Perdew, J. P. and Y. Wang (1992). "Accurate and simple analytic representation of the electron-gas correlation energy". *Phys. Rev. B* 45.23, pp. 13244–13249. DOI: 10.1103/PhysRevB.45.13244.

Blöchl, P. E. (1994). "Projector augmented-wave method". *Physical Review B* 50.24, pp. 17953–17979. DOI: 10.1103/PhysRevB.50.17953.

Cao, J. and G. A. Voth (1994). "The formulation of quantum statistical mechanics based on the Feynman path centroid density. I. Equilibrium properties". *The Journal of Chemical Physics* 100.7, pp. 5093–5105. DOI: 10.1063/1.467175.

Peskin, M. E. and D. V. Schroeder (1995). *An introduction to quantum field theory*. Reading, Mass: Addison-Wesley Pub. Co.

Sugino, O. (1995). "Ab Initio Molecular Dynamics Study of First-Order Phase Transitions: Melting of Silicon". *Phys. Rev. Lett.* 74.10, pp. 1823–1826. DOI: 10.1103/PhysRevLett.74.1823.

Kresse, G. and J. Furthmüller (1996). "Efficient iterative schemes for ab initio total-energy calculations using a plane-wave basis set". *Phys. Rev. B* 54.16, pp. 11169–11186. DOI: 10.1103/PhysRevB.54.11169.

Holm, B. and F. Aryasetiawan (2000). "Total energy from the Galitskii-Migdal formula using realistic spectral functions". *Phys. Rev. B* 62.8, pp. 4858–4865. DOI: 10.1103/PhysRevB.62.4858.

Alfè, D. (2003). "First-principles simulations of direct coexistence of solid and liquid aluminum". *Phys. Rev. B* 68.6. DOI: 10.1103/PhysRevB.68.064423.

Barrat, J.-L. and J.-P. Hansen (2003). *Basic concepts for simple and complex liquids*. New York: Cambridge University Press.

Fetter, A. L. and J. D. Walecka (2003). *Quantum theory of many-particle systems*. Mineola, N.Y: Dover Publications.

Savvatimskiy, A. I. (2005). "Measurements of the melting point of graphite and the properties of liquid carbon (a review for 1963–2003)". *Carbon* 43.6, pp. 1115–1142. DOI: 10.1016/j.carbon.2004.12.027.

Tonkov, E. Y. and E. G. Ponyatovsky (2005). *Phase transformations of elements under high pressure*. Advances in metallic alloys v. 4. Boca Raton, Fla: CRC Press.

Bailey, N. P., U. R. Pedersen, N. Gnan, T. B. Schrøder, and J. C. Dyre (2008). "Pressure-energy correlations in liquids. I. Results from computer simulations". *The Journal of Chemical Physics* 129.18, p. 184507. DOI: 10.1063/1.2982247.

Harl, J. (2008). "The linear response function in density functional theory". PhD thesis. Vienna: University of Vienna.

Pedersen, U. R., N. P. Bailey, T. B. Schrøder, and J. C. Dyre (2008). "Strong Pressure-Energy Correlations in van der Waals Liquids". *Phys. Rev. Lett.* 100.1, p. 015701. DOI: 10.1103/PhysRevLett.100.015701.

Perdew, J. P., A. Ruzsinszky, G. I. Csonka, O. A. Vydrov, G. E. Scuseria, L. A. Constantin, X. Zhou, and K. Burke (2008). "Restoring the Density-Gradient Expansion for Exchange

in Solids and Surfaces". *Phys. Rev. Lett.* 100.13, p. 136406. DOI: 10.1103/PhysRevLett.100.136406.

Preparata, F. P. and M. I. Shamos (2008). *Computational geometry: an introduction*. 6. print. Texts and monographs in computer science. New York: Springer.

Gnan, N., T. B. Schrøder, U. R. Pedersen, N. P. Bailey, and J. C. Dyre (2009). "Pressure-energy correlations in liquids. IV. "Isomorphs" in liquid phase diagrams". *The Journal of Chemical Physics* 131.23, p. 234504. DOI: 10.1063/1.3265957.

Grüneis, A., M. Marsman, J. Harl, L. Schimka, and G. Kresse (2009). "Making the random phase approximation to electronic correlation accurate". *The Journal of Chemical Physics* 131.15, p. 154115. DOI: 10.1063/1.3250347.

Kutzelnigg, W. (2009). "How many-body perturbation theory (MBPT) has changed quantum chemistry". *International Journal of Quantum Chemistry* 109.15, pp. 3858–3884. DOI: 10.1002/qua.22384.

Shavitt, I. and R. J. Bartlett (2009). *Many-body methods in chemistry and physics: MBPT and coupled-cluster theory*. Cambridge; New York: Cambridge University Press.

Feynman, R. P., A. R. Hibbs, and D. F. Styer (2010). *Quantum mechanics and path integrals*. Emended ed. Mineola, N.Y: Dover Publications.

Harl, J., L. Schimka, and G. Kresse (2010). "Assessing the quality of the random phase approximation for lattice constants and atomization energies of solids". *Physical Review B* 81.11. DOI: 10.1103/PhysRevB.81.115126.

Pedersen, U. R., T. B. Schrøder, and J. C. Dyre (2010). "Repulsive Reference Potential Reproducing the Dynamics of a Liquid with Attractions". *Phys. Rev. Lett.* 105.15, p. 157801. DOI: 10.1103/PhysRevLett.105.157801.

Ziesche, P. (2010). "The high-density electron gas: How momentum distribution $n(k)$ and static structure factor $S(q)$ are mutually related through the off-shell self-energy $\Sigma(k, \omega)$". *Annalen der Physik* 522.10, pp. 739–765. DOI: 10.1002/andp.201000022.

Zykova-Timan, T., J. Horbach, and K. Binder (2010). "Monte Carlo simulations of the solid-liquid transition in hard spheres and colloid-polymer mixtures". *The Journal of Chemical Physics* 133.1, p. 014705. DOI: 10.1063/1.3455504.

Ángyán, J. G., R.-F. Liu, J. Toulouse, and G. Jansen (2011). "Correlation Energy Expressions from the Adiabatic-Connection Fluctuation–Dissipation Theorem Approach". *J. Chem. Theory Comput.* 7.10, pp. 3116–3130. DOI: 10.1021/ct200501r.

Assael, M. J., I. J. Armyra, J. Brillo, S. V. Stankus, J. Wu, and W. A. Wakeham (2012). "Reference Data for the Density and Viscosity of Liquid Cadmium, Cobalt, Gallium, Indium, Mercury, Silicon, Thallium, and Zinc". *Journal of Physical and Chemical Reference Data* 41.3, p. 033101. DOI: 10.1063/1.4729873.

Grimvall, G. (2012). "Lattice instabilities in metallic elements". *Rev. Mod. Phys.* 84.2, pp. 945–986. DOI: 10.1103/RevModPhys.84.945.

Ren, X., P. Rinke, V. Blum, J. Wieferink, A. Tkatchenko, A. Sanfilippo, Karsten Reuter, and M. Scheffler (2012). "Resolution-of-identity approach to Hartree–Fock, hybrid density functionals, RPA, MP2 and GW with numeric atom-centered orbital basis functions". *New J. Phys.* 14.5, p. 053020. DOI: 10.1088/1367-2630/14/5/053020.

Bates, J. E. and F. Furche (2013). "Communication: Random phase approximation renormalized many-body perturbation theory". *The Journal of Chemical Physics* 139.17, p. 171103. DOI: 10.1063/1.4827254.

Calvo, F., E. Pahl, M. Wormit, and P. Schwerdtfeger (2013). "Evidence for Low-Temperature Melting of Mercury owing to Relativity". *Angewandte Chemie International Edition* 52.29, pp. 7583–7585. DOI: 10.1002/anie.201302742.

Pedersen, U. R. (2013). "Direct calculation of the solid-liquid Gibbs free energy difference in a single equilibrium simulation". *The Journal of Chemical Physics* 139.10, p. 104102. DOI: 10.1063/1.4818747.

Pedersen, U. R., F. Hummel, G. Kresse, G. Kahl, and C. Dellago (2013). "Computing Gibbs free energy differences by interface pinning". *Physical Review B* 88.9. DOI: 10.1103/PhysRevB.88.094101.

Ren, X., P. Rinke, G. E. Scuseria, and M. Scheffler (2013). "Renormalized second-order perturbation theory for the electron correlation energy: Concept, implementation, and benchmarks". *Phys. Rev. B* 88.3, p. 035120. DOI: 10.1103/PhysRevB.88.035120.

Albrechtsen, D. E., A. E. Olsen, U. R. Pedersen, T. B. Schrøder, and J. C. Dyre (2014). "Isomorph invariance of the structure and dynamics of classical crystals". *Phys. Rev. B* 90.9, p. 094106. DOI: 10.1103/PhysRevB.90.094106.

CRC handbook of chemistry and physics (2014). Oakville, US: Apple Academic Press Inc.

Dyre, J. C. (2014). "Hidden Scale Invariance in Condensed Matter". *J. Phys. Chem. B* 118.34, pp. 10007–10024. DOI: 10.1021/jp501852b.

Grüneis, A. (2014). private communication.

Kaltak, M., J. Klimeš, and G. Kresse (2014a). "Cubic scaling algorithm for the random phase approximation: Self-interstitials and vacancies in Si". *Phys. Rev. B* 90.5, p. 054115. DOI: 10.1103/PhysRevB.90.054115.

— (2014b). "Low Scaling Algorithms for the Random Phase Approximation: Imaginary Time and Laplace Transformations". *J. Chem. Theory Comput.* 10.6, pp. 2498–2507. DOI: 10.1021/ct5001268.

Lancaster, T. and S. Blundell (2014). *Quantum field theory for the gifted amateur*. First Edition. Oxford: Oxford University Press.

Travesset, A. (2014). "Phase diagram of power law and Lennard-Jones systems: Crystal phases". *The Journal of Chemical Physics* 141.16, p. 164501. DOI: 10.1063/1.4898371.

Ziesche, P. (2014). private communication.

Cates, M. E. and V. N. Manoharan (2015). "Celebrating Soft Matter's 10th anniversary: Testing the foundations of classical entropy: colloid experiments". *Soft Matter* 11.33, pp. 6538–6546. DOI: 10.1039/C5SM01014D.

Coleman, P. (2015). *Introduction to Many-Body Physics*. New York, NY: Cambridge University Press.

Pedersen, U. R., F. Hummel, and C. Dellago (2015). "Computing the crystal growth rate by the interface pinning method". *The Journal of Chemical Physics* 142.4, p. 044104. DOI: 10.1063/1.4905955.

Index

Γ point, 8
k-vector, 8

Adjacent Pairs Exchange, 103

band index, 8
Brillouin zone, 8

chemical potential, 15
coexistence, 13
contraction, 49
correlation energy, 6
Coupled Cluster Singles Doubles, 71

diagram
    connected or linked -, 57
    Feynman -, 61
    Goldstone -, 51
    order, 53
direct isomorph check, 33
direct ring Coupled Cluster, 70
Dyson-like equation, 75

effective support, 13
entropy, 13
exchange
    diagram, 87
    exact -, 75
    term, 6
exchange-correlation
    kernel, 75
    potential, 7

Fermi sphere, 77
Fock
    operator, 6
    space, 44
    term, 6
frozen core approximation, 20

Gibbs free energy, 14
Green's function, 59, 60

Hartree, 3
    term, 6
Hartree-exchange-correlation energy, 73
Hartree-Fock approximation, 6
Helmholtz free energy, 14
Hilbert space, 5
hole, 45

imaginary frequency, 80
improper ladder diagram, 92
independent particle polarizability, 66
infrared catastrophe, 85
isomorph, 29, 31

Kohn-Sham orbital, 7

latent volume and entropy, 17
Local Density Approximation, 7

momentum
    external and internal -, 80
monotone polygon, 55

non-propagating, 52

order parameter, 18

particle, 44
phase diagram, 29
propagator, 59, 60
    dressed -, 114
Pulay stress, 37

renormalization, 58, 65
ring diagrams, 65

screened interaction, 67
Second Order Screened Exchange, 88
    Adiabatic Connection -, 91
self energy, 123

simple liquid, 29
Slater determinant, 5
spin orbital, 5
symmetry factor, 62

Tamm-Dancoff Approximation, 71

vertex, 51
virial, 32

Wick rotation, 68, 80
Wick's theorem, 49
Wigner–Seitz radius, 77

Acknowledgements

This thesis would not have been possible without help and support from many people. Particularly, I want to thank

my colleague Andreas Grüneis for fruitful as well as amusing discussions,
my partner Røsle for being with me, especially in demanding times,
my advisor Georg Kresse for a PhD in a really good and really nice group,
my friend and colleague Christian Kramberger-Kaplan for telling me about the group,
and all members of the group for their commitment and also their friendship.

Further, I want to express my gratitude to

Jeppe Dyre for constructive discussions and comments on the manuscript,
my colleague Ulf Pedersen for showing me an enjoyable way to do science,
my brother Marcus for his help whenever needed,
and last but not least, Rotte and Niels for their company.

The calculations were in part conducted at the Vienna Scientific Cluster (VSC) and I also want to thank their support team.

Curriculum Vitae

Peer reviewed articles

2013 U. R. Pedersen, F. Hummel, G. Kresse, G. Kahl, C. Dellago, *Computing Gibbs free energy differences by interface pinning*, Phys. Rev. B **88**, 094101.

2013 M. Hummel, F. Hummel, C. Brunner, J. Fluch, *Reducing Fuel Consumption in Industry*, Proceedings of the American Council for an Energy Efficient Economy.

2015 U. R. Pedersen, F. Hummel, C. Dellago, *Computing the crystal growth rate by the interface pinning method*, J. Chem. Phys. **142**, 044104.

2015 F. Hummel, G. Kresse, J. C. Dyre, U. R. Pedersen, *Hidden scale invariance of metallic melts*, submitted arXiv:1504.03627.

2015 F. Hummel, A. Grüneis, G. Kresse, *On the difference between SOSEX and the adiabatic connection-SOSEX*, drafted as Chapter 7.

2016 F. Hummel, G. Kresse, *Adjacent pairs exchange correction to the random phase approximation*, drafted as Chapter 8.

Invited talks

2014 F. Hummel, G. Kresse, *Exchange corrections to the random phase approximation: why SOSEX is better than it should be*, 14th International Conference on Computational and Mathematical Methods in Science and Engineering, Cadiz, Spain.

2015 F. Hummel, C. Dellago, U. R. Pedersen, *Computing solid-liquid Gibbs free energy difference by interface pinning*, Free energy workshop 2015, Münster, Germany.

Selected contributed talks

2013 F. Hummel, U. R. Pedersen, G. Kresse, G. Kahl, C. Dellago, *Computing melting temperatures of Na, Mg, Al and Si by pinning of solid-liquid interfaces in ab-initio calculations*, Verhandlungen der Deutchen Phys. Ges. DY25.1, Regensburg.

2014 F Hummel, G Kresse, J. C. Dyre, U. R. Pedersen, *Predicting crystal properties from melts: ab-initio results for all metals*, 12th Workshop on Viscous Liquids and the Glass Transition, Søminestationen, Holbæk, Denmark.

2015 F. Hummel, G. Kresse, *Variants of Second Order Screened Exchange using polarization parts*, ViCoM Spring Workshop 2015, Stadtschlaining, Austria.

Felix Hummel

University of Vienna, Faculty of Physics
Sensengasse 8/12,
1090 Wien, Austria

felix.hummel@univie.ac.at

Phone: +43-1-4277-51404
Fax: +43-1-4277-9514
cmp.univie.ac.at

Born: March 21, 1979, Salzburg, Austria
Nationality: Austrian

Current position

since 2015 Post Doc with A. Grüneis, Max-Planck-Institute for Solid State Research

Education

2005 BSc in Mathematics, University of Salzburg, Austria
2009 Dipl.-Ing. in Computer Science, University of Salzburg, Austria
2012-2015 PhD in Physics with Georg Kresse, University of Vienna, Austria

Teaching & work experience

1999-2003 Software developer, AGD Software GmbH, Austria
2005 Tutor, University of Salzburg, Austria
2006-2008 Scientific consultant and shareholder, SharpCam Ltd., United Kingdom
2007-2010 Co-founder and lead developer, Findologic GmbH, Austria
2008-2011 Lecturer and researcher, University of Applied Sciences, Salzburg, Austria
2013-2014 Lecturer, University of Vienna, Austria

Academic & teaching visits

2010 Arcada University of Applied Sciences, Helsinki, Finland
2011 University College London, United Kingdom
2014 Max-Planck-Institute for the Physics of Complex Systems, Dresden, Germany
2015 Roskilde University, Denmark

Awards & grants

1996 Honourable Mention, International Physics Olympiad, Oslo, Norway
1997 Honourable Mention, International Physics Olympiad, Sudbury, Canada
2007 Funded master's thesis, 6000 EUR
2014 Outstanding poster, Young Researchers Conference, Vienna

Last updated: October 12, 2015